Coupling Efficiency Improvement and Power Transfer Enhancement in Wireless Power Transfer System for Electric Vehicle Charging Applications

Gautam Rituraj

Coupling Efficiency Improvement and Power Transfer Enhancement in Wireless Power Transfer System for Electric Vehicle Charging Applications

A

Thesis submitted

for the award of the degree of

Doctor of Philosophy

by

Gautam Rituraj

Department of Electronics and Electrical Engineering

Indian Institute of Technology Guwahati

Guwahati -781039, Assam, India

February 2021

Dedicated

To

My **Guru**,

Lord Kṛṣṇá,

and

To

My dear **parents** and

to everyone who perseveres for wisdom.

Certificate

This is to certify that the thesis entitled "**Coupling Efficiency Improvement and Power Transfer Enhancement in Wireless Power Transfer System for Electric Vehicle Charging Applications**", submitted by **Gautam Rituraj** (136102005), a research scholar in the *Department of Electronics and Electrical Engineering, Indian Institute of Technology Guwahati*, for the award of the degree of **Doctor of Philosophy**, is a record of an original research work carried out by him under my supervision and guidance. The thesis has fulfilled all the requirements as per the regulations of the institute and in my opinion has reached the standard needed for submission. The results embodied in this thesis have not been submitted to any other University or Institute for the award of any degree or diploma.

Date: March 02, 2021

Place: Guwahati.

Dr.ing. Praveen Kumar
Professor
Dept. of Electronics and Electrical Engineering
Indian Institute of Technology Guwahati
Guwahati - 781 039, Assam, India.

Acknowledgements

First and foremost, I would like to express my deepest and sincere gratitude to my supervisor Prof. Praveen Kumar for giving me the opportunity to explorer this (WPT) technology. I want to thank him for providing excellent guidance throughout my study. His kindness, dedication, punctuality, and hard work have been a great inspiration to me. I would particularly like to thank you for all your help in patiently and carefully correcting all my manuscripts and this thesis.

I am also very grateful to my doctoral committee members Prof. Ratnajit Bhattacharjee, Prof. Pradeep G. Yammiyavar, and Dr. Sisir Kumar Nayak for sparing the valuable time to evaluate the progress of my work and provide constructive feedback.

I would also like to thank the Head of the Department and the other faculty members for their kind help in carrying out this work. I am also grateful to all the technical staff of the department who helped me to use the various equipment in their lab. I am also thankful to Mr. Dimpul Gogoi and Mr. Ridib Bharali for issuing hardware components in constructing the experimental setup.

I also wish to thank Computer and Communication Center, IIT Guwahati for providing high-performance parallel computing platform-Param-Ishan for rapid parametric simulation of 3-D FEA models.

Furthermore, I would like to thank IIT Guwahati and Patent Information Center (PIC)–Assam Science Technology and Environment Council, Guwahati, India, for its support for the patent application (201931003386). I especially wish to thank Mr. Siddhartha Devnath and his team (from PIC) for helping me till the filing of the patent application.

Thanks to my friends and PhD colleagues Dr. Ankit Dalal, Dr. Arghya Chakravarty, Dr. Ezhil Reena Joy, Dr. Himanshu S. Sahu, Dr. Samdarshi Khare, Dr. Saurabh Pandey, Dr. Venkata R. Kasi, Dr. Tousif Khan, Dr. Upendra Reddy, Dr. Kashyap K. Prabhakar, Dr. Brijesh K. Kushwaha, Rajendra Kumar, Jagath V. Missula, and Bikash Sah. They have always been around to provide useful suggestions and created a healthy research environment. They all have contributed directly or indirectly to this thesis. A special thanks to Dr. Mridul K. Malakar for always being available to do in-depth technical discussion.

I am also very thankful to Dr. Chintu Barman (physiotherapist) for his excellent treatment in my chronic pain, occurred at the beginning of my study. Moreover, I wish to thank Mr. Vinod Kumar for encouraging and motivating me during this study.

Furthermore, my deepest gratitude goes to my parents and my sisters for their love, patience, and support for my studies.

Finally, I thank the Almighty God for bestowing me this opportunity and showering his blessings on me to come out victorious against all the odds.

Gautam Rituraj

Abstract

In recent years, wireless power transfer (WPT) technology is gaining popularity for electric vehicle (EV) charging. This technology has advantages such as safety, reliability, ease of charging, and robustness over a conventional plug-in charging system. In the WPT system, transmitter and receiver coils (loosely coupled) play an essential role in power transfer. Since the power transfer happens through air-medium, the high leakage inductance results in reduced coupling coefficient (k). This reduced k decreases power transfer capability and transmission (coil-to-coil/coupling) efficiency. The transmission efficiency is also affected due to the varying nature of the load during battery charging (i.e., change in the equivalent load resistance due to change in the battery's state of charge). In this context, to improve the transmission efficiency, an experimental study is performed (using the developed experimental setup) while charging the battery bank (sealed lead-acid) using a series-parallel (SP) compensated WPT system. Charging of the battery bank is done using constant current (CC) and constant voltage (CV) modes. For these charging modes, the equivalent load resistance curve is experimentally determined. Moreover, an expression of optimum operating frequency is derived, which incorporated the load. At this frequency, the system is operated in both charging modes where it maintains the maximum possible transmission efficiency throughout the load variation compared with the operation at the resonant frequency. Furthermore, this optimum frequency gives a stable voltage waveform of the inverter in the CC charging mode compared with the resonant frequency. Besides that, it (optimum frequency) provides zero voltage switching throughout the charging process (i.e., in CC and CV charging modes). Moreover, the variation of transmission efficiency and the load phase angle for different operating frequencies in CC and CV charging modes are verified with the measurement to identify the possible

control parameters.

Furthermore, the power transfer capability and transmission efficiency (performance parameters) are enhanced by improving factor k. k of air-core coils can be improved by either doing modifications in the design of the coils or using the ferrite core (or by doing both). Since the ferrite core increases the weight and cost, it is not the first resort toward improving k; instead, an attempt to enhance k should involve modification in the design of the coils. For doing this, different conventional unipolar coils are investigated to find that approach of improving k, which enhances both performance parameters. Generally, the 3-D finite element analysis (FEA) software (ANSYS Maxwell or JMAG) is used to analyse the coils (i.e., magnetic field, self- and mutual inductance, and k). However, the simulation of various 3-D models with FEA software is a time-consuming process due to high mesh-density. Therefore, a 3-D analytical model is developed to analyse the air-core rectangular (or square) coils, used in the WPT systems. The developed 3-D analytical model calculates the magnetic field and k faster than 3-D FEA and also gives good accuracy (verified using the simulation and experimental results). Based on the observations obtained from the investigation, a unipolar coil arrangement method (UCAM) for improving k compared with conventional coils of the same self-inductance and outer dimensions is proposed. This method does not require ferrite materials and is applicable for different popular unipolar coils' geometry (i.e., rectangular, square, and circular) used in the static and dynamic WPT systems. Besides that, the developed 3-D analytical model (for rectangular and square coils) is extended for the coils designed using the proposed UCAM. For the unipolar rectangular coil system with 400 mm × 300 mm outer dimensions, 6.78%–27.04% improvement in k is achieved at the 150 mm air gap for the case 3 coil system compared with the different conventional unipolar coil systems. Moreover, the interoperability between the proposed and conventional coils, the impact of various misalignments of the receiver coil on improvement in k, and the impact of improved k on the performance parameters are examined. Prototypes of proposed and conventional coil systems are built to verify the factor k obtained from simulation and analytical model for

both vertical and horizontal misalignments and to confirm the improvement in k. Moreover, for the square and circular coil systems, up to 26.02% and 26.41% improvements in k at the 150 mm air gap have been found with the proposed UCAM for the outer dimensions of 350 mm × 350 mm and 400 mm × 400 mm, respectively, compared with conventional coil systems. Besides that, the second resort (using ferrite) of improving k is used to enhance the factor k of air-core coils (proposed and conventional). Traditionally, the ferrite core size is kept approximately equal to the outer dimensions of the coil, which increases the overall weight and volume of the system. With the traditional ferrite arrangement, the impact of improved k of the proposed coil system on performance parameters is examined in comparison to the proposed air-core coil system. To maintain the obtained enhancements in performance parameters and minimise the weight and volume of the system, a novel (and simple) ferrite arrangement of unipolar rectangular (and square) coils is proposed. The proposed arrangement maintains the maximum achievable k and minimises the volume of ferrite used compared with the traditional arrangement. The proposed arrangement uses Pythagoras' theorem that determines the position and length of the ferrite bars. Furthermore, various possible ferrite arrangements are studied and compared with the proposed ferrite arrangement. The proposed arrangement saves 81.24% volume of the ferrite used with a decrement of only 6.93% in k (for case 6) over the traditional ferrite arrangement. Thereafter, a prototype of the proposed ferrite arrangement is developed, and the results are verified (for misalignment also). Furthermore, the proposed arrangement is also tested with the conventional and other proposed coil systems. Thus, the presented method is elegant and obviates the need for computationally expensive optimisation.

Contents

List of Figures

List of Tables

List of Acronyms

2-D	Two Dimensional
3-D	Three Dimensional
AC	Alternating Current
AWG	American Wire Gauge
CC	Constant Current
CCAM	Conventional Coil Arrangement Method
CU	Configuration Update
CV	Constant Voltage
DC (or dc)	Direct Current
EMF	Electromotive Force
ESR	Equivalent Series Resistance
EV	Electric Vehicle
FEA	Finite Element Analysis
FPGA	Field Programmable Gate Array
HF	High-Frequency
IC	Integrated Circuit
InC	Inner Coil
MOSFET	Metal-Oxide Semiconductor Field-Effect Transistor
OuC	Outer Coil
PCB	Printed Circuit Board
PFA	Proposed Ferrite Arrangement
PP	Parallel-Parallel

PS	Parallel-Series
PWM	Pulse-Width Modulation
RMS	Root Mean Square
Rx	Receiver
SAE	Society of Automotive Engineers
SP	Series-Parallel
SS	Series-Series
Tx	Transmitter
UCAM	Unipolar Coil Arrangement Method
UFA	Traditional (Uniform) Ferrite Arrangement
WPT	Wireless Power Transfer
ZVS	Zero Voltage Switching

List of Symbols

$\langle * \rangle$	Spatial average over the turn's cross section
Ψ_{PS}	Magnetic flux linkage to the Rx coil
φ	Scalar magnetic potential
∇	Del operator
η_P	Efficiency of the equivalent primary
η_S	Efficiency of the secondary
$\eta_{t,cc}$	Transmission efficiency of compensated coils
$\eta_{t,cc_{max}}$	Maximum transmission efficiency of compensated coils
$\Im(*)$	Imaginary part of *
θ	Angle for placing the ferrite bar
ρ_c	Resistivity of copper
$\Re(*)$	Real part of *
τ_{X}	Coil pitch in X-direction
τ_{Y}	Coil pitch in Y-direction
μ_0	Permeability of free space
ω	Operating angular frequency
ω_o	Resonant angular frequency
$\mathbf{A}$	Magnetic vector potential
a_1	Half inner width of coil (conventional) in X-direction
a_1^{in}	Half innermost width of InC in X-direction
a_1^{out}	Half innermost width of OuC in X-direction
a_2	Half outer width of coil in X-direction

a_2^{in}	Half outermost width of InC in X-direction
a_2^{out}	Half outermost width of OuC in X-direction
A_{X}^{II}	Magnetic vector potential of Region II in X-direction
A_{Y}^{II}	Magnetic vector potential of Region II in Y-direction
A_{Z}^{II}	Magnetic vector potential of Region II in Z-direction
$\mathbf{B}$	Magnetic flux density (B-field)
b_1	Half inner width of coil in Y-direction
b_1^{in}	Half innermost width of InC in Y-direction
b_1^{out}	Half innermost width of OuC in Y-direction
b_2	Half outer width of coil in Y-direction
b_2^{in}	Half outermost width of InC in Y-direction
b_2^{out}	Half outermost width of OuC in Y-direction
B_{leak}	Leakage magnetic field
B_{peak}	Peak value of magnetic field across the turn generated by the peak current I_{peak}
B_{X}^{II}	X-component of B-field in Region II
B_{X}^{III}	X-component of B-field in Region III
B_{Y}^{II}	Y-component of B-field in Region II
B_{Y}^{III}	Y-component of B-field in Region III
B_{Z}^{II}	Z-component of B-field in Region II
B_{Z}^{III}	Z-component of B-field in Region III
C_{gx}	Gap between the last turn of InC and the first turn of OuC X-direction
C_{gy}	Gap between the last turn of InC and the first turn of OuC Y-direction
C_P	Primary compensation capacitor
C_S	Secondary compensation capacitor
$D_1 - D_4$	Hyperfast diodes in rectifier
d_s	Diameter of the strand
d_w	Wire diameter of the Tx and Rx coil
f	Operating frequency

f_0	Resonance frequency
$f_{optimum}$	Optimum operating frequency
h	Harmonic number
$\mathbf{H}$	Magnetic field intensity
I_{load}	Output (load) current
$i_p(t)$	Instantaneous current in the primary side
I_P	RMS value of the primary current
I_S	RMS value of the secondary current
I_{sc}	Short-circuit current that the Rx coil can source to the load
J	Equivalent current density in bars of conventional coil due to I_P
J_{in}	Equivalent current density in bars of InC due to I_P
J_{out}	Equivalent current density in bars of OuC due to I_P
$J_{\mathrm{X}}^{total}(\mathrm{X,Y})$	Current density distribution in X-direction
$J_{\mathrm{Y}}^{total}(\mathrm{X,Y})$	Current density distribution in Y-direction
$J\,(\mathrm{X, Y})$	Magnitude of current density distribution in both X- and Y-directions
k	Coupling coefficient (or factor) of the coil system
k_{X}	Spatial frequency in X-direction
k_{Y}	Spatial frequency in Y-direction
L_P	Self-inductance of primary (transmitter) coil
L_{req}	Required self-inductance
L_S	Self-inductance of secondary (receiver) coil
l_{coil}	Total required length of wire in a coil structure
l_t	Mean length of the turn
M	Mutual inductance between the primary and secondary coils
N	Number of turns in conventional Tx and Rx coils
N_{in}	Number of turns in InC
N_{out}	Number of turns in OuC
N_P	Number of turns in primary (transmitter) coil

N_S	Number of turns in secondary (receiver) coil
N_s	Total number of strands
P_{load}	Output active power transferred to the secondary side
$P_{P_{in}}$	Input power of the primary
$P_{P_{out}}$	Output power of the primary
$P_{S_{in}}$	Input power of the secondary
$P_{S_{load}}$	Output power of the secondary
Q_S	Quality factor of the secondary circuit (under load)
$R_{dc,P}$	Total dc resistance of the Tx coil
$R_{dc,S}$	Total dc resistance of the Rx coil
R_L	Equivalent load resistance of the battery
$R_{L,\text{eq}}$	Effective (or AC) load resistance referred to the input of rectifier (secondary side)
$R_{pe,P}$	Total proximity-effect resistance of Tx coil
$R_{pe,S}$	Total proximity-effect resistance of Rx coil
R_P	AC resistance of primary (transmitter) coil
R_S	AC resistance of secondary (receiver) coil
r_w	Radius of wire used in the Tx and Rx coils
$S_1 - S_4$	Power MOSFETs in inverter
$\mathbf{S}_S$	Area of the Rx coil
S_{in}	Total width occupied by N_{in} in InC
S_{max}	Maximum apparent power
S_{out}	Total width occupied by N_{out} in OuC
S_q	Surface area of q^{th} turn
S_w	Total width occupied by total number of turns (N)
T_g	Gap between the turns in conventional coil
T_{g-in}	Gap between the turns in InC
T_{g-out}	Gap between the turns in OuC
U	Number of harmonics in X-direction

V_{dc}	Value of DC voltage source
V_{oc}	Open-circuit voltage of the receiver coil
$v_p(t)$	Instantaneous output voltage of inverter (in the primary side)
$v_{p_1}(t)$	Instantaneous fundamental output voltage of inverter
V_P	RMS value of sinusoidal voltage source $v_{p_1}(t)$
W	Number of harmonics in Y-direction
X	One of the coordinates in Cartesian coordinate system
x	Outer dimension of coil (for OuC also) in X-direction
x_{o-in}	Outer dimension of InC in X-direction
y	Outer dimension of coil (for OuC also) in Y-direction
Y	One of the coordinates in Cartesian coordinate system
y_{o-in}	Outer dimension of InC in Y-direction
Z	One of the coordinates in Cartesian coordinate system
Z_r	Reflected impedance of secondary side impedance to the primary side
Z_S	Secondary side impedance
$Z_{S_{load}}$	Impedance of the load (having parallel RC branch)
Z_T	Total (or input) impedance seen from the source

भारतीय प्रौद्योगिकी संस्थान गुवाहाटी
Indian Institute of Technology Guwahati

1

Introduction

Contents

1.1 Background

In recent years, the Governments of major countries (such as India, China, and the United States) have initiated electrification of the public transport system to reduce air pollution and the effect of climate change. In this context, electric vehicles (EVs) (mainly two- and three-wheelers and buses) are being deployed and promoted in various cities of the countries. Currently, batteries are the primary source of energy in EVs, which requires charging to regain their energy. The commercialisation of EVs (in full fledge) needs charging infrastructure in every city. A charging station requires more numbers of the charger to meet the power demands of various types of EVs. Currently, the conventional plug-in charger is used to meet these demands. However, plug-in charger suffers from the risk of electric shocks (mainly in the rainy season), need to plug every time which reduces the connector lifetime, and the risk of injury while handling more than 20-kW charger due to the heavyweight of wires. Moreover, due to COVID-19 (coronavirus), people would like to avoid making physical contact with the plug-in chargers (to maintain the social-distancing) installed at public places. Therefore, wireless power transfer (WPT) charging system is a better option due to the advantages such as safety, reliability, ease of charging, robustness, and the fully automated charging process (supports social-distancing) [1, 5–9]. The fundamental elements and working of the WPT system are explained in the next subsection.

1.1.1 Fundamental Elements of the WPT System

The working principle of the WPT is governed by Ampere and Faraday's laws, which are briefly explained below:

(1) *Ampere's Law:* When electric current flows through a conductor in the permeability of free space, it generates a magnetic field [1, 10].

(2) *Faraday's Law:* When a time-varying magnetic flux links a loop, a voltage is induced in that loop, and it is directly proportional to the time rate of change of magnetic flux [1, 10].

Figure 1.1 shows the block diagram of the traditional WPT system. The explanation of each component used in the WPT system, as shown in Figure 1.1, is given as follows:

- At first, a single-phase or three-phase alternating current (AC) power source (that comes from

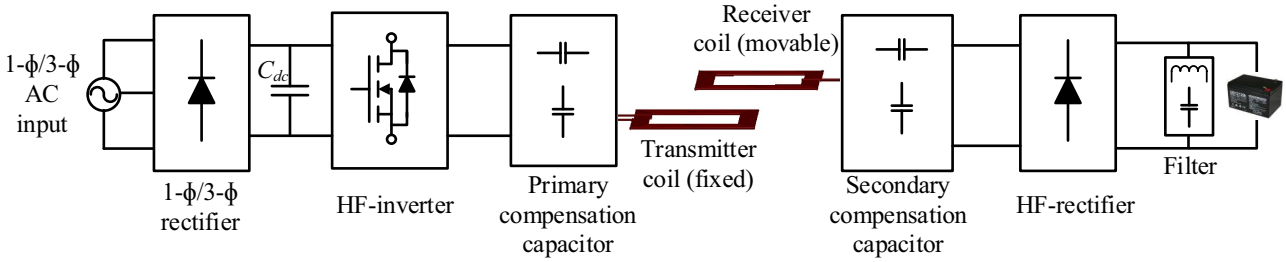

Figure 1.1: Block diagram of the traditional unidirectional (source to load) WPT system.

the grid) is converted to direct current (DC) power source through a full-wave rectifier (single-phase or three-phase, respectively).

- Then, the DC power source is converted to the high-frequency (HF) AC power source in the inverter stage. Usually, H-bridge inverter is used for this purpose. However, different topologies of the inverter, such as half-bridge and phase shift H-bridge inverters can also be used as per requirement. With this high-frequency current, the primary (transmitter) coil is excited through a primary compensation network and the magnetic field is generated according to Ampere's law.

- When this generated magnetic field links the secondary coils (installed at beneath the vehicle's chassis), a voltage is induced in the secondary coils according to Faraday's laws. The received high-frequency power is then fed to HF-rectifier through the secondary compensation network. This HF-rectifier converts the high-frequency AC power to DC power and the ripples present in it are filtered by the *C*/*LC* filter. Finally, DC power is available to charge the battery.

- It should be noted that there is an air gap, ranges from 100 to 250 mm in EV applications [1], present in between the primary and secondary coils. Due to this air gap, the primary and secondary coils have large leakage inductance. To compensate the same, compensation capacitors are used on both sides. Depending on the connections of the capacitor with the coil on both sides, there are four basic compensation topologies named series-series (SS), series-parallel (SP), parallel-series (PS), and parallel-parallel (PP) [11]. Figure 1.2 shows the circuit configuration of each compensation topology. In each topology, the secondary compensation capacitor (C_S) is generally designed to resonant with the secondary coil (L_S) to reduce the

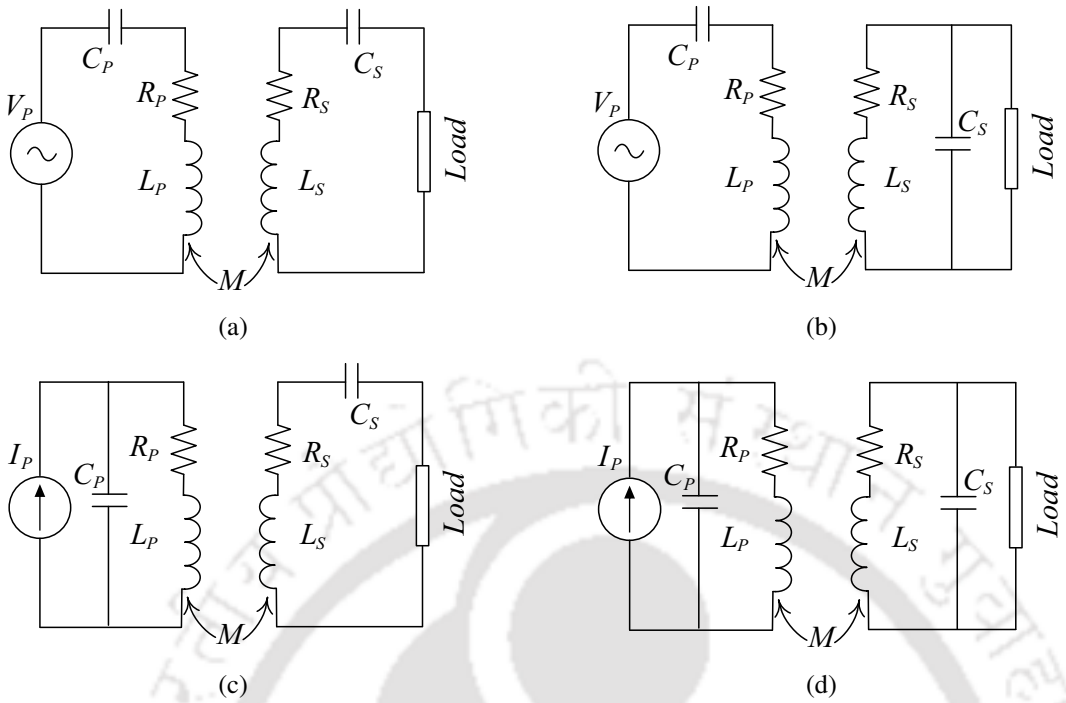

Figure 1.2: Circuit configuration of four basic compensation topologies used in the WPT system. (a) SS, (b) SP, (c) PS, and (d) PP. Here, the symbols V_P and I_P represent a high-frequency voltage source and current source, respectively. Moreover, L_P and L_S are the self-inductance of the primary (transmitter, Tx) and secondary (receiver, Rx) coils, respectively; M is the mutual inductance between the coils; R_P and R_S are the AC resistance of the Tx and Rx coils, respectively; and the primary and secondary compensation capacitors are represented with C_P and C_S, respectively.

reactive power demand of the coils. The expression of C_S (for both the series and parallel connections) can be given as

$$C_S = \frac{1}{\omega_o^2 L_S} \tag{1.1}$$

where ω_o is the resonant angular frequency. However, the primary compensation capacitor (C_P) is designed to compensate both the primary self-inductance (L_P) and the reflected impedance [11]. The expression of C_P is given in the following brief description of each topology.

(A) *Series-Series (SS) topology*: Figure 1.2(a) shows the circuit of SS compensation topology. Here, in each side, the capacitor is connected in series with the coil, and named series-series. Since the reflected impedance in this topology is zero [2, 11, 12], the expression of C_P remains the same as C_S, which is given below:

$$C_P = \frac{1}{\omega_o^2 L_P}. \tag{1.2}$$

From the expression of C_P, it can be seen that C_P does not depends on the mutual inductance (and

coupling coefficient k) between the coils, which is the main advantage of this topology. However, this topology has a significant drawback at light load condition or when the receiver is absent. At this scenario, the equivalent impedance seen from the source is zero, and only the parasitic impedance of the inductor and capacitor limits the current (i.e., current increases to infinity), which leads to an unsafe operation [1, 11]. Nevertheless, SS topology gives the unity power factor at the resonance frequency and maintains the high efficiency at low coupling [1, 11, 12].

(B) *Series-Parallel (SP) topology*: Figure 1.2(b) shows the SP compensation network. Here, on the primary side, the capacitor is connected in series with the Tx coil, whereas in the secondary side, it is connected in parallel with the Rx coil. Hence, it is named SP topology. Since this topology does not have zero reflected impedance, the expression of C_P is different from C_S, and given by [11]

$$C_P = \frac{1}{\omega_o^2\left(L_P - \dfrac{M^2}{L_S}\right)}. \tag{1.3}$$

From (1.3), it can be seen that C_P depends on the mutual inductance between the coils. Thus, any variation in coupling k detunes the primary side and reduces the power transfer capability. However, at light load condition, the equivalent impedance seen from the source is not zero at the resonance frequency and, hence, current does not increase to infinity. As a result, it gives safe operation when the Rx coil is absent (or light load condition happens) [11, 13].

(C) *Parallel-Series (PS) topology*: Figure 1.2(c) illustrates the circuit of PS topology. In this topology, on the primary side, the capacitor is connected in parallel with the Tx coil, whereas in the secondary side, it is connected in series with the Rx coil. The expression on C_P for PS topology is given by [11]

$$C_P = \frac{L_P}{\left(\dfrac{\omega_o^2 M^2}{R_{load}}\right)^2 + \omega_o^2 L_P^2} \tag{1.4}$$

where R_{load} is the equivalent load resistance. From (1.4), it is seen that C_P depends on both M and R_{load}. In the battery charging application, load resistance changes according to the change in the state of charge of the battery (occurs continuously). Therefore, this topology may not be suitable for the charging application with this C_P. However, different C_P can be used to tune the system according

to the load characteristics, but it makes the system bulky and complex. Another disadvantage of this topology is that it requires current source input to prevent any instantaneous change in voltage [1, 11].

(D) *Parallel-Parallel (PP) topology*: Figure 1.2(d) gives the circuit configuration of PP topology. Here, the capacitor is connected in parallel with the coil in each side. The expression of C_P for this topology is given by [11]

$$C_P = \frac{\left(L_P - \frac{M^2}{L_S}\right)}{\left(\frac{M^2 R_{load}}{L_S^2}\right)^2 + \omega_o^2\left(L_P - \frac{M^2}{L_S}\right)^2}. \tag{1.5}$$

From (1.5), it can be seen that C_P depends on both M and R_{load} (as in the PS topology). This compensation topology suffers from the low power factor, a high load voltage across the parallel secondary, and requires a large current source (in the primary-side) [1, 11]. Because of these disadvantages, this topology is not widely studied.

Finally, from Figure 1.1, the main parts of the WPT system can be summarised as:

(a) Loosely coupled transmitting and receiving coils (an essential part);

(b) Power electronics converters;

(c) Compensation network.

These three parts are widely researched for enhancing the power transfer capability and transmission (and system) efficiency and making the system compact. The upcoming section reviews the work reported in the literature related to the WPT charging system and developments in the coil design and modelling.

1.2 Literature Review

Currently, two types of batteries are widely used in EV application. These batteries are lead-acid and Lithium-ion. Usually, the charging process of these batteries comprise of two charging modes for extending the battery's lifecycle [14, 15]. These modes are constant current (CC), used in the beginning, and constant voltage (CV), used in the end [4, 14, 16]. Based on compensation capacitors, four basic topologies, as shown in Figure 1.2, are used in the WPT system [2, 17]. Among these topologies, SS and SP compensation topologies are widely used for charging the battery because both topologies can give CC and CV outputs (other advantages are given in Chapter 2).

For SS and SP compensations, a comparative study in terms of efficiency, load, and frequency control technique are reported in [18]. Here, authors have found that SS compensation topology is the best due to its peak efficiency and the fixed frequency control scheme. Moreover, some random resistance value is used in load for both the compensation topologies. However, doing so does not represent the actual load variation profile of the battery. In [12], the experimental comparison for various operating frequencies, different loads, various distances, and efficiency of SS and SP topologies is reported. The design of parameter values, analysis of the bifurcation frequencies, and corresponding output power for the SP compensated inductive power transfer system is given in [19]. For the SS compensated inductive charging system, an adaptive frequency control technique is used to achieve zero voltage switching (ZVS) throughout the charging process, is reported in [20]. For the SP compensated WPT system with a resistive load, a frequency tracking control method is explained in [21]. With SS or SP compensations in [12, 18–21], resistance is used as a load rather than battery.

The work on the design and control scheme for charging of the lithium iron phosphate battery using the WPT system is presented in [22]. Here, authors focused on the design of compensation capacitor, selection of the self-inductance based on the quality factor (Q), and the implementation of control strategies. Besides that, adjustment of the resonant circuit is done to achieve ZVS so that transmission efficiency can be enhanced. However, the reliability of the designed circuit was the primary concern of the authors. The variable frequency control for the SS compensated WPT system with an electronic load and battery is reported in [9, 23]. Furthermore, in [23], a closed loop scheme with the proportional-integral controller for CC and CV charging modes is presented. Here, the authors have given a design procedure to determine the optimal parameters for the coils and compensation capacitors. The frequency domain analysis of the SS compensated WPT system is also presented. Moreover, in [23], the selection procedure of switching frequency to minimise the circulating current is given based on voltage transfer gain and input impedance. In [16], the design of WPT battery charger for electric city-car using the SS compensation with the battery charging profile is presented. Here, the authors have presented a procedure for designing the power converter and systematically analysed the power losses of each component of the charging system. Moreover, in the designing of the SS compensated system, circular spiral coils are used.

In EV charging application, the coil system is one of the critical components, and the parameters that play a significant role in coil design are; available installation space, ground clearance, power transfer capability, transmission efficiency, and misalignment tolerance. The other influencing factors are the thermal performance, the weight of the coils, and manufacturing cost. The coil's size, power transfer capability, and transmission efficiency are dependent on the coupling coefficient k. Since the air-cored coil system has a lower value of k [12], it impacts the power transfer capability, and transmission efficiency and, hence, results in a larger coil system size [1,12,24]. Therefore, to enhance the power transfer capability and transmission efficiency, and to achieve a compact coil system, there is a need to improve k of the air-cored coil system [25–28] and, hence, the design of the coils is an area of extensive research.

Generally, a ferrite core is used to improve k of a unipolar air-cored coil system [24, 27, 29]. In recent years, multicoil topologies, such as bipolar, double-D quadrature, and mutually decoupled coils [30–32] are proposed to improve the value of k. However, the use of ferrite core in unipolar as well as multicoil topologies increases the cost and weight of the system [27, 33]. Thus, the ferrite is not the first resort towards improving k; instead, an attempt to improve k should involve modification in the design of the coils.

Few works have reported on improving the coupling factor k without using ferrite material for unipolar coils of different shapes in [28, 34, 35]. H. Li *et al.* [28] present an optimisation method for improving k for a tightly wounded circular coil structure. Here, the authors improve k by reducing the self-inductance of the coils. However, with this approach, the obtained maximum apparent power transferred to the receiver coil (expression can be seen in [36]) will be less than to the method where improvement in k is performed by keeping the self-inductance of the coils constant. An alternative to improve k of the square- and circular-shaped coils is to use intermediate coils [34, 35]. Here, authors have used two intermediate coils, which are placed one after another inside the source (Tx) coil (i.e., these three Tx coils are concentric and coplanar). These intermediate coils are acting as a resonator, which is tuned at two different frequencies using two different capacitors. These two coils can help to boost the flux generated by the source coil without electrically connected with the source power supply, if operated with the correct resonant frequency, as given in [34, 35]. However, the design

of intermediate coils and its tuning increases the complexity and cost of the system. A. B. Kurs *et al.* [37] focused to design high-frequency printed circuit board (PCB) resonator coils and these coils are printed on a thin substrate. Here, two differently sized resonator coils are used; a larger one acts as a Tx resonator coil and a smaller one as an Rx or device resonator coil. Due to differences in sizing and change in the relative position, the coupling of the coils changes. As a result, the system performance changes, and it is significant for low-power application devices. Moreover, Q of the PCB resonator coils is generally low and have higher losses compared to the resonator coil designed with traditional wire or Litz wire. Therefore, to minimise the variation in k and to increase Q of the coils, the number of loops, the width of each trace, and the spacing between the traces are adjusted mainly in the Tx resonator coil. In addition, different possible shapes of resonator coils with the previously mentioned adjustments are presented. However, no such coil design method is presented for improving k of the coils, which can enhance the transmission efficiency in the high/medium-power WPT system. Besides improving k, the design of the coil system should have an efficient cooling in long hours use because the temperature rise can increase the power loss of the copper wire [38], which decreases the transmission efficiency. Z. Zhang *et al.* [38] proposed multithread rectangular coils and performed the thermal analysis with the conventional rectangular coils. Here, the authors found multithread coil outperform in long hours of use.

Furthermore, the second resort for improving k is to use ferrite material in the air-core coils. Due to space limitation in EV charging, the size of the ferrite core is kept approximately equal to the coil dimensions, which is a traditional ferrite arrangement [39]. This arrangement gives the maximum possible k. However, the use of uniform ferrite core throughout the coil dimensions increases the weight and cost of the coil system. Therefore, the optimised ferrite arrangement (of the unipolar coil system) should consider the minimal use of ferrite core and maintain k obtained from the traditional ferrite arrangement.

The coil's geometry plays a critical role to minimise the use of ferrites. Usually, square-, circular-, and rectangular-shaped unipolar coils are used in both static and dynamic WPT systems [24, 27, 40]. However, the rectangular coils are mostly preferred due to the advantages of its shape [40, 41]. In the literature, the ferrite arrangement for the circular coil has been extensively researched and well

optimised by using different shapes of ferrite bars [27, 33, 42, 43]. But, the same ferrite arrangement (obtained for circular coils) may not be optimal for the rectangular coil because of the corners' effect [44]. Moreover, in [29], the work focuses on the modelling of square and circular coil system with the ferrite core. However, the authors have not shown any optimised ferrite arrangement.

The coil design is an iterative process, which requires multiple simulations. Usually, 3-D finite element analysis (FEA) software ANSYS Maxwell (or JMAG) is used to design the coils. However, due to the high mesh density, 3-D FEA is a time-consuming process [45, 46]. An alternate tool is to use analytical model. Analytical model is faster in calculation, but is slight less accurate compared to FEA. However, it can be useful in the initial design process. Few works are reported in the literature related to analytical modelling of various coil configurations [47–49]. 3-D analytical modelling for calculating k of air-cored rectangular coils, having an array of coils in the primary and a single coil in the secondary, is derived in [47]. In [48], 3-D analytical modelling for an array of air-cored coils with ferromagnetic boundaries is presented. Moreover, 3-D magnetic field modelling considering the ferromagnetic plate with cavities for an array of rectangular coils is described in [49].

1.3 Motivation

The literature shows that WPT charging system has several advantages, such as safety, reliability, ease of charging, and robustness over the conventional plug-in charging system [1, 12]. The WPT system uses loosely coupled coil system, which has a large leakage inductance. This leakage inductance results in a lower value of k [12]. Consequently, it impacts the power transfer capability and transmission (and system) efficiency, and also results in a larger coil system size [1, 12, 24]. Therefore, improvement in k of the coil system should be attempted to overcome these issues. The attempt of improving k should include both modifications in the design of coils and the optimal use of ferrite.

Moreover, in the WPT charging, different misalignments, such as vertical (due to different tyre pressures) and horizontal in X- and Y-directions (during parking) between the coils usually occurs. For understanding the effect of these misalignments on variation in k, different shapes of coils, such as unipolar circular, square, and rectangular are studied for finding the better misalignment tolerance and reports that rectangular coil outperforms [50]. Usually, a 3-D FEA software ANSYS Maxwell (or

JMAG) is used to design and study (calculating magnetic fields, self- and mutual inductance and k) the coils. However, the simulation of various 3-D models with 3-D FEA software is a time-consuming process due to the high mesh density [51]. Therefore, an analytical model is preferred for the same. In the literature, few works have modelled the air-core rectangular and square coils [47, 48, 50, 52]. In [47, 48], the authors presented the modelling for an array of the primary and a single secondary coils, which may not predict accurate results for a coil system where one primary coil and one secondary coil are present. In [50, 52], modelling of the square and rectangular coils are presented using the small-small sectors and by applying the Biot-Savart law in those sectors to enhance the accuracy. However, these sectors make the model time-consuming. Moreover, this modelling did not include circular corners. Therefore, a fast, accurate, and reliable analytical model for rectangular (and square) coils needs to be developed.

Furthermore, many works have used different values of a fixed resistor as a load for studying the various WPT systems. However, in the real charging scenario, the equivalent load resistance varies during the charging. From the literature, it is seen that SS and SP topologies can be used to charge the batteries. However, few works have used the battery (lithium iron phosphate) as a load with SS compensation topology. Nevertheless, SS compensated WPT system suffers from increasing in the primary-side current to a very high value at no load condition (secondary open) when operating at the resonant frequency. However, in the case of SP compensation topology, the current does not increase to a very high value for this scenario (thus, it is safer) [11]. Hence, it may be interesting to analyse (mainly transmission efficiency and proper ZVS during a charging cycle) the SP compensated WPT system with the battery (lead-acid or Lithium-ion batteries; widely used in two- and three-wheelers) as a load.

1.4 Objective of the Thesis

Based on the motivation and literature survey, the following are the objectives of this thesis:

(i) To analyse the SP compensated WPT system with the battery as a load (rather than resistance only), determine the charging profile(s), making improvement in the performance (if needed), and identifying the suitable control parameter(s). Moreover, to study the impact of coupling

variation on the power transfer capability and transmission efficiency in CC and CV charging modes.

(ii) To investigate the improvement in k of the coils so that power transfer capability and transmission efficiency can be enhanced: What are the ways available and how can it be done?

(iii) To develop a 3-D analytical model for the conventional air-core rectangular (and square) coils (incorporating circular corners) to fulfil the following needs so that faster calculation can be done compared to the 3-D ANSYS Maxwell (or JMAG) without affecting the accuracy:

A. it able to predict the magnetic fields generated by the transmitter coil, which can be used to understand the behaviour of the magnetic fields of the different designs of the air-core coil system.

B. it must have the capability to predict the self- and mutual inductances (and k) of the coils.

(iv) To develop a unipolar coil design method for improving k of different coils' geometry (such as rectangular, square, and circular) without using ferrite materials, compared with the conventional coils of the same self-inductance and outer dimensions.

(v) To extend the 3-D analytical model (developed for the conventional coils) for the coils designed using the proposed coil arrangement method.

(vi) To propose the new ferrite arrangement of the unipolar rectangular (and square) coil structures to minimise the ferrite volume while maintaining improved k (obtained from the traditional ferrite arrangement).

1.5 Contributions of the Thesis

The following are the main contributions of the work reported in this thesis.

(i) It investigates the SP compensated WPT system with the battery as a load and develops its experimental setup. Moreover, the charging profiles (obtained experimentally) are presented to show the load variation and output current and voltage variations for a complete charging cycle.

Furthermore, an expression of the optimum operating frequency is derived for achieving the maximum transmission efficiency throughout the load variation in the charging process. This frequency also gives the proper ZVS throughout the charging process.

(ii) It develops a 3-D analytical model for the conventional rectangular (and square) air-core coils (of any dimensions) to calculate the magnetic field densities, self- and mutual inductance, and k. This model also considers circular corners of rectangular (and square) coils. Furthermore, an expression for calculating the required wire length in a coil (or a coil system) is given.

(iii) Moreover, it investigates the various approaches of improving k of coils and suggests the best approach of improving k so that the power transfer capability and transmission efficiency can be enhanced. Based on this approach, the constraints of improving k is given.

(iv) It proposes a novel unipolar coil arrangement method (UCAM) for improving k compared with conventional coils of the same self-inductance and outer dimensions (without flux-guiding materials) in WPT systems. With the proposed UCAM, k of the different unipolar coil geometries, such as rectangular, square, and circular, can be improved. The proposed UCAM is also applicable for improving k of nonidentical (in terms of shape, dimensions, and self-inductance values) unipolar coils. Moreover, it studies the interoperability between the proposed and conventional coils and examines the peak leakage magnetic field nearby coil structures of the proposed and conventional coils. Furthermore, it investigates the impact of increased k on transmission efficiency and power transfer capability and the impact of different misalignments on improvement in the factor k.

(v) It also extends the developed 3-D analytical model for the conventional air-core coils to the proposed unipolar rectangular (and square) coil structures. Here, the extension includes the new expressions of current densities and change in the expressions of self- and mutual inductances. Moreover, the necessary modifications in the expression for calculating the used wire length in the proposed coil structures are also given. This length information is also used in the expression of the coils' AC resistance.

(vi) It proposes a new and simple ferrite arrangement of the rectangular (and square) coil structures (conventional and proposed) to minimise the ferrite volume while maintaining the improvement in k obtained from traditional ferrite arrangement.

1.6 Outline of the Thesis

This thesis contains six chapters. The organization of each chapter is as follows:

- **Chapter 1** first introduces the WPT along with its advantages over plug-in conventional charging system for EV charging applications. Then, it presents a brief introduction of the subsystems used in the WPT system along with the working principles involved. Moreover, this chapter reports the literature survey related to the different types of WPT system, efficiency enhancement, and developments in the loosely coupled coils of various popular shapes (mainly focused on modelling methods and approaches for improving the factor k). Furthermore, it describes the motivation behind the work and set the objectives for this thesis. Finally, it summarises the thesis contribution and presents a brief outline of the thesis.

- **Chapter 2** analyses the SP compensated WPT system with the battery as a load. Governing equations are derived to evaluate the performance of this system during the CC and CV charging modes. An expression for optimum operating frequency is derived, which gives maximum possible efficiency in both charging modes. Experimental setup of the SP compensated WPT system is developed to find the charging profiles of the battery (lead-acid) and verify the theoretical analysis. Furthermore, it investigates ZVS operation in both charging modes. Finally, this chapter examines the impact of k on the power transfer capability and transmission efficiency in the CC and CV charging modes.

- **Chapter 3** investigates on coupling improvement of conventional air-core coils. For analysing the magnetic fields, self- and mutual inductance (and k) of coils, a 3-D analytical model for the conventional air-core rectangular (and square) coils is developed, which incorporates circular corners. The analytical results are verified with those obtained from 3-D FEA simulation and experiments. Moreover, it derives the expression for calculating the wire length required in a coil system and presents the analytical calculation of the coils' AC resistance. With this

developed model, various approaches are investigated to improve k of a coil system so that both transmission efficiency and power transfer capability can be enhanced. Thereafter, the constraints for improving k are given based on the obtained (suitable) approach. With these constraints, various conventional air-core rectangular coils are analysed to understand the improvement in k. Finally, the obtained observations are used to develop the new coil design method, which is discussed in Chapter 4.

✍ **Chapter 4** proposes a novel unipolar coil arrangement method (UCAM) for improving k (without ferrites) compared with conventional coils of the same self-inductance and outer dimensions. Moreover, the developed 3-D analytical model in Chapter 3 is extended for the coils designed using the proposed UCAM. Furthermore, the modifications in the expression of the required wire length in the proposed coil system(s) and AC resistance of the proposed coils are given. With the rectangular coils, the proposed UCAM is explained and investigated thoroughly. Besides that, this chapter studies the interoperability between the proposed and conventional coils, examines the impact of increased k on transmission efficiency and power transfer capability, analyses the peak B_{leak} nearby coil structures, and investigates the impact of different misalignments on improvement in the factor k. The prototypes of conventional and proposed coils are constructed to verify the improvement in k (in both aligned and misaligned conditions). Additionally, the improvement in k of other coil geometries (square and circular) are presented. Finally, the improvement in k of nonidentical unipolar coils is also given.

✍ **Chapter 5** uses second resorts (i.e., ferrites) to improve k of unipolar coils (both conventional and proposed). At first, it reviews the traditional ferrite arrangement. After that, it discusses the improvement in k for the different horizontal misalignments of the Rx coil arrangement compared with the proposed air-cored coil system and examines the impact of further improved k on the power transfer capability and transmission efficiency. Then, it proposes a new and simple ferrite arrangement of unipolar rectangular (and square) coils to minimise the ferrite uses while maintaining the improved k (obtained from traditional ferrite arrangement) so that the obtained enhancements in power transfer capability and transmission efficiency can be main-

tained. Moreover, this chapter compares the proposed ferrite arrangement with the other possible ferrite arrangements, including the reported one in the literature. Ferrite utilisation is also presented for each ferrite arrangement. Furthermore, a prototype of the proposed ferrite arrangement is developed to verify the ferrite usages and obtained k. Besides that, this chapter investigates the proposed ferrite arrangement with the various types of rectangular air-core coils (other proposed and conventional) having the same outer dimensions. Besides that, it also examines the proposed arrangement with the different outer dimensions of the air-core coil system (for example, square-shaped).

✍ **Chapter 6** summaries the objectives and highlights the key points of the work presented in the previous chapters. Moreover, the future work for extending the research reported in this thesis have been outlined.

2

Analysis of Series-Parallel Compensated WPT System with the Battery as a Load

Contents

2.1 Introduction

In recent years, the use of electric vehicles (EVs) has increased significantly in India, especially two- and three-wheelers [53]. These EVs use either lead-acid or lithium-ion batteries as an energy source to run the drivetrain. Generally, a conductive method (i.e., using cord) is used for the charging of these batteries. Wireless power transfer (WPT) technology is another way of charging the batteries and has several advantages in comparison to the conductive method, such as safety, reliability, ease of charging, and robustness [1].

In EV charging application, an air gap is required as per the ground clearance of the vehicle to transfer the power to the load (batteries). Contactless coils are used for transferring power through this air gap. However, these coils suffer from large leakage inductance, which demands reactive power from the source and, hence, increases the VA rating [6]. For efficient power transfer, these leakage inductance are compensated with the capacitors. Based on the connection of capacitors in the primary and secondary coils, four basic topologies are used [2]. These are series-series (SS), series-parallel (SP), parallel-series (PS), and parallel-parallel (PP). The circuit configurations of these topologies can be seen in the previous chapter (Figure 1.2). Usually, the charging process of the abovementioned batteries comprise of two charging modes, which extend the battery's lifecycle [14, 15]. These charging modes are constant current (CC) mode, used in the beginning, and constant voltage (CV) mode, used in the end [4, 14, 16]. Based on the literature, four basic compensation topologies are compared in Table 2.1 to find the suitable topology for charging. The comparison in Table 2.1 shows that SS and SP topologies are able to provide CC and CV outputs. However, only CV output is possible with the PS topology, whereas only CC output is possible with the PP topology [6, 54]. Hence, CC and CV charging modes can be realised with the SS and SP topologies.

In SS topology, at light load condition (occurs in CV charging mode) or when the secondary coil is absent (i.e., the case when $k \approx 0$), the total impedance seen by the source is approximately zero (only parasitic impedances of the switches used in inverter, primary capacitor, and primary inductor remains) at the resonance frequency. As a result, the current in the primary side increases to infinity (due to very less value of these parasitic impedances). Whereas, in SP topology, the primary compensation capacitor depends on the mutual inductance (can be seen in Table 2.1), hence, when the

Table 2.1: Comparison of four basic compensation topologies [1–4].

Parameter \ Topology		SS	SP	PS	PP
Possible output		CC and CV	CC and CV	Only CV	Only CC
Primary capacitance dependent on	Load resistance	No	No	Yes	Yes
	Mutual inductance	No	Yes	Yes	Yes
System operation at zero coupling		Not allowed	Allowed	Allowed	Allowed
Inverter device voltage rating		Lower dc link voltage (but higher than SP)	Lower dc link voltage	Higher voltage is needed in comparison to SS and SP	Higher voltage is needed in comparison to SS and SP
Total impedance with coil misalignment		Decreases	Decreases	Increases	Increases

secondary coil is absent, or the light load condition occurs, the primary side gets detune. Then, the total impedance seen by the source is comparatively higher than the SS topology. Therefore, the primary current does not increase to infinity (have a minimum circulating current) [13]. Thus, SP topology is safer than SS topology. Moreover, form Table 2.1, it is seen that SP topology requires less dc-link voltage compared with SS topology.

The variations of the parameters, such as efficiency, mutual inductance, load, and frequency for SP topology, is studied in [12, 18, 55]. However, it does not consider battery as a load for investigation. Very few works have been used the battery as a load [16, 22]. Huang *et al.* [22] use lithium iron phosphate battery and develop the charging circuit according to the charging profile of this battery. Buja *et al.* [16] use SS topology to charge the lead-acid battery in CC and CV modes.

Therefore, this chapter investigates the SP compensated WPT system with the battery as a load (it could be lead-acid or lithium-ion). The rest of the chapter is organised as follows. Section 2.2 explains the SP compensated WPT system for charging the battery. Further, it derives the governing equations for understanding the system behaviour in CC and CV charging modes (achieved using open-loop control). Section 2.3 describes the developed experimental setup of the SP compensated WPT system where the lead-acid battery is used as a load. Furthermore, it presents the battery charging profiles obtained from the experiment. Then, based on the obtained load profile, it theoretically examines the system behaviour in CC and CV charging modes. The theoretical observations are validated using the experiments. Based on the study, it identifies possible control parameters, which can be used to implement closed-loop control. Moreover, Section 2.4 investigates the impact of k on the transferred

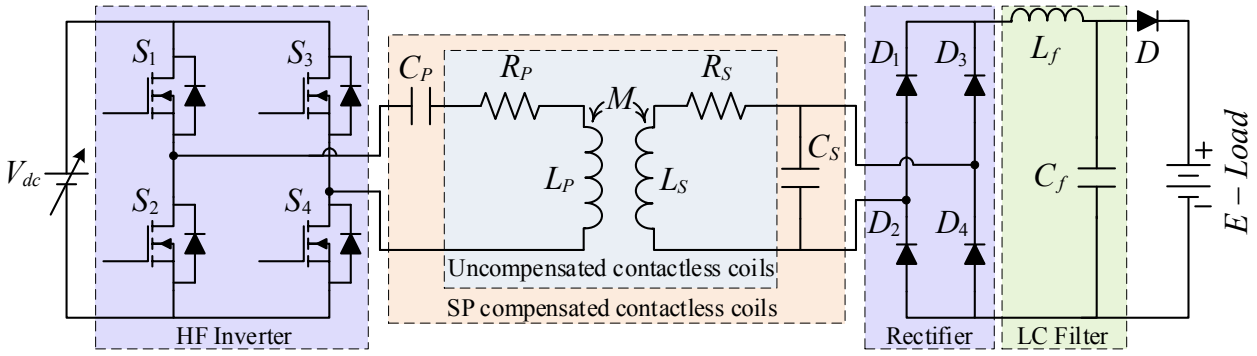

Figure 2.1: Schematic of wireless battery charging system with the SP compensation topology.

power and transmission efficiency in CC and CV charging modes. Finally, Section 2.5 presents a summary of this chapter.

2.2 Analysis of the SP Compensated WPT System for Battery Charging

In this section, a brief introduction about the SP compensated WPT system for battery charging in open-loop control is presented. Then, circuit equations of the system are derived with the help of different equivalent circuit models given in the subsequent subsections, to evaluate the system performance, such as efficiency and operation in CC and CV charging modes.

The circuit diagram of a wireless battery charging system with the SP compensation topology in open-loop control is depicted in Figure 2.1. From the input to output, the system consists of high-frequency (HF) voltage source inverter, SP compensated contactless coils, HF rectifier, and LC filter. A DC voltage source V_{dc} is applied to the input of HF H-bridge voltage source inverter, which converts DC voltage to HF square wave voltage. For the experimental purpose, a variable DC source is used to keep the current and voltage constant during charging of the battery bank in CC and CV modes, respectively. In the block of SP compensated contactless coils, the symbols L_P and L_S are the self-inductance, whereas R_P and R_S are the AC resistance of the primary (transmitter, Tx) and secondary (receiver, Rx) coils, respectively. The Tx and Rx coils, together with their AC resistances, make the coil system and it can also be referred to as uncompensated contactless coils. The magnetically coupled uncompensated contactless coils have the coupling coefficient k. This k is also called

coupling factor, and its value ranges from 0–1. The expression for the factor k of this coil system is

$$k = \frac{M}{\sqrt{L_P L_S}} \tag{2.1}$$

where M is the mutual inductance between the coils. To compensate the reactive power demand of the Tx and Rx coils, two compensation capacitors, C_P and C_S are connected in series with Tx coil and parallel to the Rx coil, respectively, as shown in Figure 2.1. The compensated Tx coil is excited with high-frequency (HF) current, generated by the HF H-bridge inverter. On the secondary side, a parallel compensated Rx coil is connected with a diode bridge rectifier (having HF diodes D_1–D_4), which converts HF AC voltage to DC voltage. In order to get ripple-free DC voltage and current, an LC filter is used. The battery bank is represented as *E–Load*. A diode D is used to connect the battery bank from the charger, which ensures charging of the battery bank only when the anode voltage is higher than the cathode voltage.

For understanding the circuit parameter variations of the system shown in Figure 2.1 during the battery charging, mathematical analysis is needed. In this context, to derive the circuit equations, the magnetically coupled coil system in Figure 2.1 should be replaced with their conductively coupled circuit. Further, the output of the rectifier connected to the DC load should be replaced with their AC equivalent load referred to the input of the rectifier. In other words, there is a need to develop the equivalent circuit models of this system, which are given in the next subsection.

2.2.1 Equivalent Circuit Models of SP Compensated WPT System

To analyse the SP compensated WPT system for battery charging, equations related to the system performance, such as transmission efficiency and waveforms of electrical quantities (voltage and current) at various stages during the operation in CC and CV modes, need to derive. These equations can be derived by making equivalent circuits of Figure 2.1 based on the **M**-model and **T**-model of uncompensated contactless coils. Hence, at first, the M-model and T-model of the uncompensated contactless coils are presented in this subsection. Further, based on these models, as per their applicability (discussed in Sections 2.2.1.1 and 2.2.1.2), different equivalent circuits are presented to derive the circuit equations for the SP compensated WPT system.

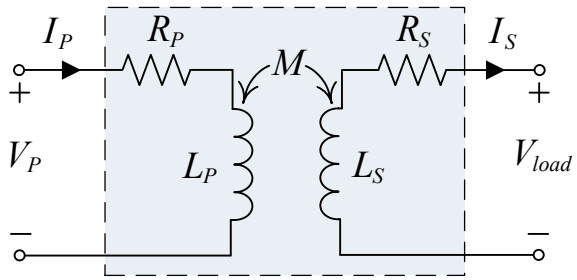

Figure 2.2: Magnetically coupled circuit of uncompensated contactless coils.

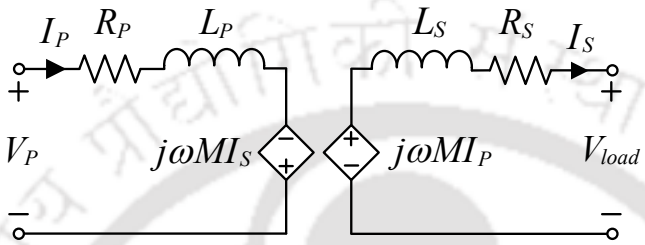

Figure 2.3: **M**-model of uncompensated contactless coils.

2.2.1.1 M-model of Magnetically Coupled Uncompensated Contactless Coils

Here, a mutually coupled model, named "**M**-model" [56], as shown in Figure 2.3 is derived from the magnetically coupled coils. A circuit diagram of magnetically coupled contactless coils is shown in Figure 2.2. By applying the Kirchhoff's law in Figure 2.2, the voltage equations of the primary and secondary sides are expressed as

$$V_P = R_P I_P + j\omega L_P I_P - j\omega M I_S \tag{2.2}$$

$$-j\omega M I_P + j\omega L_S I_S + R_S I_S + V_{load} = 0. \tag{2.3}$$

Equation (2.3) can be rewritten as

$$j\omega M I_P = j\omega L_S I_S + R_S I_S + V_{load}. \tag{2.4a}$$

In (2.2) and (2.4a), the voltages $-j\omega MI_S$ and $j\omega MI_P$ are dependent on the currents. Hence, the circuit shown in Figure 2.2 is modified as Figure 2.3 by adding the current dependent voltage source in the primary and secondary sides. The advantage of **M**-model, as shown in Figure 2.3, is its easiness. Further, this model can help in analysing the circuit independently at both sides.

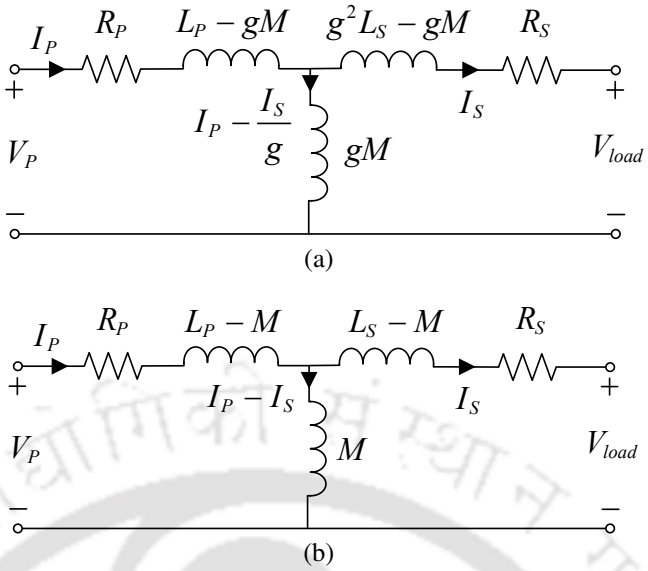

Figure 2.4: Conductively coupled circuit (i.e., **T**-model) of uncompensated contactless coils having (a) different number of turns (i.e., N_P and N_S) and (b) equal number of turns (i.e., $N_P = N_S$).

2.2.1.2 T-model of Magnetically Coupled Uncompensated Contactless Coils

T-model is preferred for circuit-based analysis [56]. It does not have dependent voltage sources, which makes the circuit-analysis simpler. Here, the magnetically coupled uncompensated contactless coils, as shown in Figure 2.3, are converted in three inductors. These three inductors in the circuit are arranged as the letter "**T**", hence, named "**T**-model". The inductance of three inductors in the **T**-model comprises a mutual inductance and two leakage inductances (primary and secondary sides). Thus, to get these inductances, (2.2) and (2.3) need to be modified.

By referring (2.3) to the primary side by multiplying it to the turns ratio $g = \dfrac{N_P}{N_S}$, where N_P and N_S are the numbers of turns in the primary and secondary sides, respectively, and it is given by

$$-jg\omega MI_P + jg^2\omega L_S I_S + g^2 R_S\left(\frac{I_S}{g}\right) + gV_{load} = 0. \tag{2.5a}$$

Adding $jg\omega M\left(\dfrac{I_S}{g}\right)$ to the first term and subtracting it from the second term to the left-hand side of (2.5a), and it can be written as

$$-jg\omega M\left(I_P - \frac{I_S}{g}\right) + j\omega\left(g^2L_S - gM\right)\left(\frac{I_S}{g}\right) + g^2R_S\left(\frac{I_S}{g}\right) + gV_{load} = 0. \tag{2.5b}$$

In the right-hand side of (2.2), multiplying and dividing the turns ratio in the third term and after

rearranging, it can be expressed as

$$V_P = R_P I_P + j\omega L_P I_P - jg\omega M\left(\frac{I_S}{g}\right). \tag{2.6a}$$

Subtracting $jg\omega M\left(\frac{I_P}{g}\right)$ from the second term and add it to the third term to the right-hand side of (2.6a) and after rearranging, it can be written as

$$V_P = R_P I_P + j\omega\left(L_P - gM\right)\left(\frac{I_P}{g}\right) - jg\omega M\left(I_P - \frac{I_S}{g}\right). \tag{2.6b}$$

A conductively coupled circuit of uncompensated contactless coils having different N_P and N_S, satisfying (2.6b) and (2.5b) is illustrated in Figure 2.4(a). However, in this thesis, N_P and N_S are taken equal (i.e., $g = 1$). Hence, the equations (2.6b) and (2.5b) are given as

$$-jg\omega M\left(I_P - I_S\right) + j\omega\left(L_S - M\right) I_S + R_S I_S + V_{load} = 0 \tag{2.7}$$

$$V_P = R_P I_P + j\omega\left(L_P - M\right) I_P - j\omega M\left(I_P - I_S\right). \tag{2.8}$$

For N_P equal to N_S (i.e., $g = 1$), the equivalent **T**-model of uncompensated contactless coils is shown in Figure 2.4(b), which satisfies (2.7) and (2.8). The **T**-model, as shown in Figure 2.4(b), is used in this chapter. Based on the discussed **M**-model and **T**-model, the different equivalent circuits are presented to derive the governing equations for the SP compensated WPT system in the subsequent subsections.

2.2.1.3 M-model Equivalent Circuit of the SP Compensated WPT System

The first equivalent circuit of Figure 2.1 is shown in Figure 2.5, which is based on **M**-model of the magnetically coupled coils (as shown in Figure 2.3), hence, named "**M**-model equivalent circuit of the SP compensated WPT System". Since the output voltage of HF H-bridge inverter is a square wave AC, the instantaneous output voltage of inverter in the primary side $v_p(t)$ can be expressed in Fourier series as

$$v_p(t) = \sum_{h=1,3,5..}^{\infty} \frac{4V_{dc}}{\pi h} \sin h\omega t \tag{2.9}$$

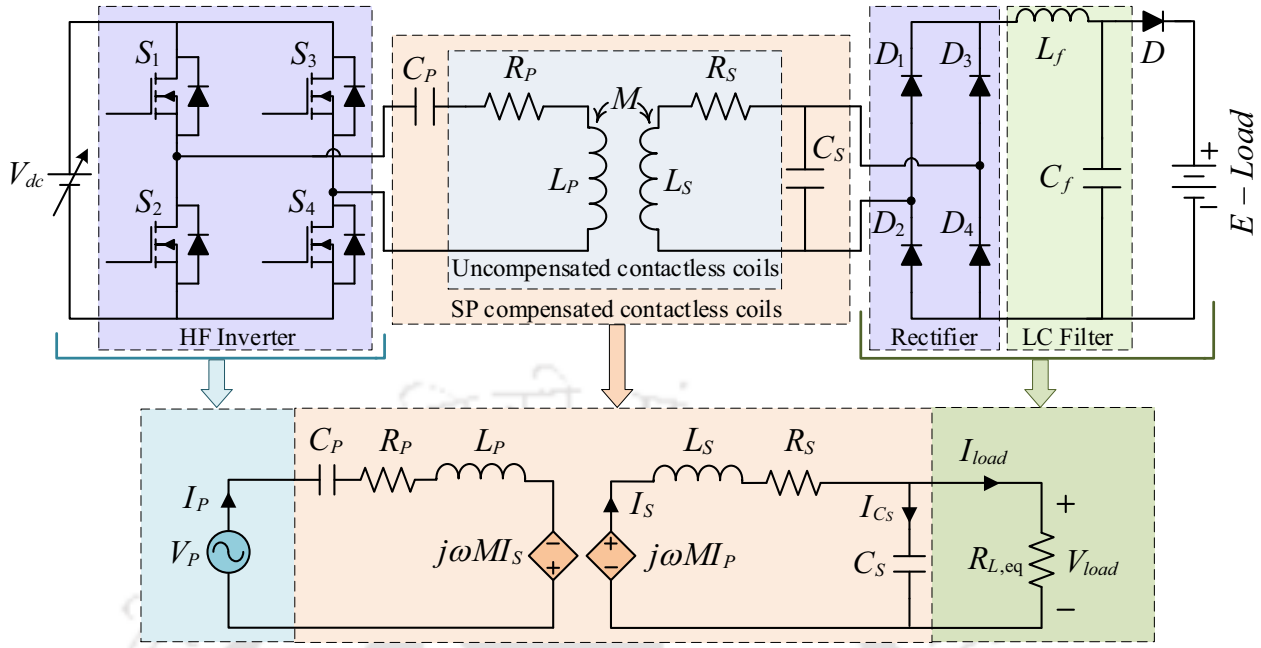

Figure 2.5: **M**-model equivalent circuit of Figure 2.1.

where h represents harmonics number and $\omega = 2\pi f$. Here, f is the operating frequency. By putting $h = 1$ in (2.9), the fundamental output voltage of the inverter v_{p_1} is given as

$$v_{p_1}(t) = \frac{4V_{dc}}{\pi} \sin \omega t \tag{2.10}$$

The RMS value of (2.10) is represented by V_P (= 0.9 V_{dc}). Hence, the output voltage of the inverter in the primary side can be replaced by a sinusoidal voltage source of V_P, as shown in Figure 2.5.

Moreover, at the load side, the equivalent load resistance (R_L) of the battery bank (*E–Load*) is referred to the input of rectifier and named effective load resistance ($R_{L,\text{eq}}$), as shown in Figure 2.5. Here, the value of R_L depends on the charging status of battery voltage and current (i.e., R_L is variable) [23]. The derivation of $R_{L,\text{eq}}$ is given in Appendix A. The relation between R_L and $R_{L,\text{eq}}$ is given as

$$R_{L,\text{eq}} = \frac{\pi^2}{8} R_L. \tag{2.11}$$

By using the equivalent circuit shown in Figure 2.5 for each harmonic component, one can calculate the currents, voltages, and other electrical quantities. Thus, by adding all the harmonics components until h^{th} harmonic of respective electrical quantities, one can get closest to the practical results compared with the consideration of only the fundamental component.

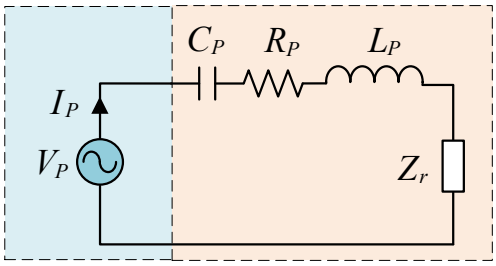

Figure 2.6: Simplified **M**-model of Figure 2.5.

From Figure 2.5, the secondary side impedance Z_S is given as

$$Z_S = R_S + j\omega L_S + \left(\frac{R_{L,\text{eq}}}{1 + j\omega C_S R_{L,\text{eq}}}\right). \tag{2.12}$$

The reflected impedance Z_r of Z_S to the primary side, as shown in Figure 2.6, is given by

$$Z_r = \frac{(\omega M)^2}{Z_S}. \tag{2.13}$$

From Figure 2.6, the total (or input) impedance Z_T, seen from the source, is given as

$$Z_T = R_P + j\left(\omega L_P - \frac{1}{\omega C_P}\right) + \frac{(\omega M)^2}{R_S + j\omega L_S + \left(\frac{R_{L,\text{eq}}}{1 + j\omega C_S R_{L,\text{eq}}}\right)} \tag{2.14}$$

where C_S and C_P are given in (2.15a) and (2.15b), respectively [2, 18, 21, 55].

$$C_S = \frac{1}{4\pi^2 {f_o}^2 L_S} \tag{2.15a}$$

$$C_P = \frac{1}{4\pi^2 {f_o}^2 \left(L_P - \frac{M^2}{L_S}\right)} \tag{2.15b}$$

For h^{th} harmonics, (2.14) can be modified as

$$Z_T = R_P + j\left(h\omega L_P - \frac{1}{h\omega C_P}\right) + \frac{(h\omega M)^2}{R_S + jh\omega L_S + \left(\frac{R_{L,\text{eq}}}{1 + jh\omega C_S R_{L,\text{eq}}}\right)} \tag{2.16}$$

The real and imaginary parts of (2.16) are given as

$$\Re\left(Z_T\right) = R_P + \frac{h^2\omega^2 M^2 \left(h^2 C_S^2 R_{L,\text{eq}}^2 R_S \omega^2 + R_S + R_{L,\text{eq}}\right)}{A} \tag{2.17a}$$

where $A = h^4 C_S^2 L_S^2 R_{L,\text{eq}}^2 \omega^4 + h^2 \left(C_S \left(C_S R_S^2 - 2L_S \right) R_{L,\text{eq}}^2 + L_S^2 \right) \omega^2 + \left(R_{L,\text{eq}} + R_S \right)^2$ and

$$\Im\left(Z_T\right) = h\omega L_P - \frac{1}{h\omega C_P} - \frac{h^3 \omega^3 M^2 \left(h^2 C_S^2 R_{L,\text{eq}}^2 L_S \omega^2 + L_S - C_S R_{L,\text{eq}}^2 \right)}{A}. \tag{2.17b}$$

By using (2.9) and (2.16), Fourier series expression of the instantaneous current in the primary side $i_p(t)$ is given by

$$i_p(t) = \sum_{h=1,3,5..}^{\infty} \frac{4V_{dc}}{\pi h |Z_T|} \sin\left(h\omega t - \theta_{Z_T}\right) \tag{2.18}$$

where θ_{Z_T} is the load phase angle of Z_T (i.e., the phase difference between $v_p(t)$ and $i_p(t)$.) and $\theta_{Z_T} = \tan^{-1}\left(\frac{\Im\left(Z_T\right)}{\Re\left(Z_T\right)}\right)$. This load phase angle is used (in Section 2.3) as one of the parameter to study the system performance during the CC and CV charging modes.

Generally, efficiency is one of the factors used to describe system performance. Therefore, an expression of transmission efficiency of compensated coils ($\eta_{t,cc}$) along with a condition to achieve its maximum value is derived using **T**-model equivalent circuit of SP compensated WPT System in the subsequent subsection.

2.2.1.4 T-model Equivalent Circuit of the SP Compensated WPT System

T-model of the magnetically coupled coils (as shown in Figure 2.4(b)) is used to make **T**-model equivalent circuit of Figure 2.1, as shown in Figure 2.7. This circuit is obtained by replacing **M**-model in Figure 2.5 with the **T**-model of the magnetically coupled coils. With the help of this equivalent circuit, $\eta_{t,cc}$ of the SP compensated WPT system is calculated. Then, a condition of optimum operating frequency is found to give the maximum transmission efficiency of compensated coils ($\eta_{t,cc_{max}}$) in CC and CV charging modes.

In the efficiency calculation, ESRs of C_P and C_S are not considered due to its insignificant effect [57]. Hence, the real power consumed in the capacitor is zero, and $\eta_{t,cc}$ of the SP compensated WPT system is given as

$$\eta_{t,cc} = \eta_P \cdot \eta_{mutual} \cdot \eta_S \tag{2.19}$$

where η_P, η_{mutual}, and η_S are the efficiencies of the equivalent primary, mutual, and secondary of the system, respectively. Since the mutual part (i.e., M) has only a reactive component, the active power

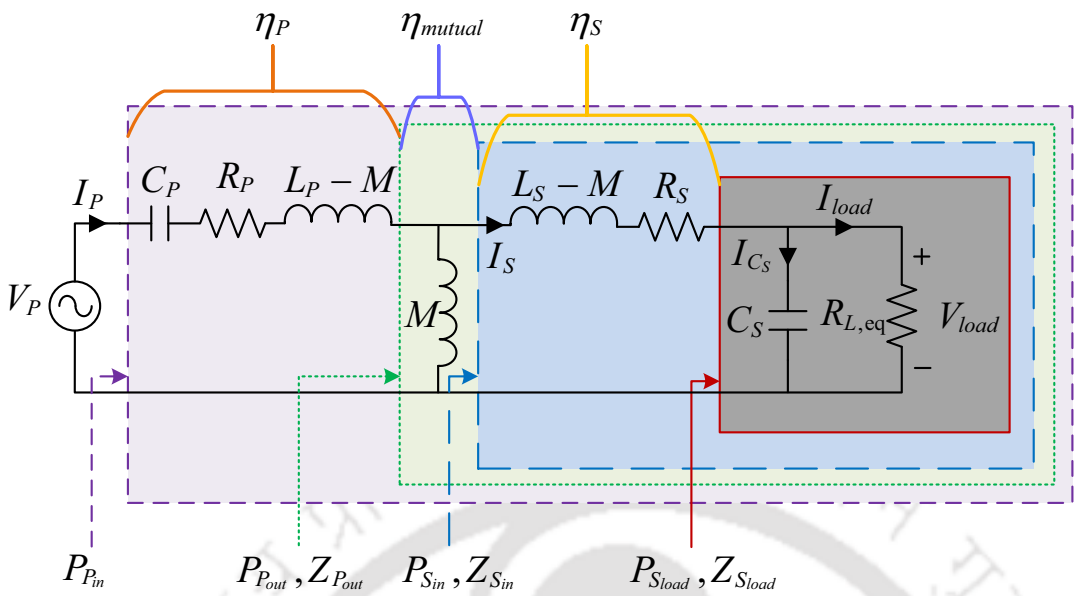

Figure 2.7: T-model equivalent circuit of Figure 2.1.

consumed is zero (hence, $\eta_{mutual} = 1$).

From Figure 2.7, $\eta_P = \dfrac{P_{P_{out}}}{P_{P_{in}}}$ and $\eta_S = \dfrac{P_{S_{load}}}{P_{S_{in}}}$, where the input power $P_{P_{in}} = (P_{P_{out}} + \text{loss in } R_P)$ and $P_{S_{in}} = (P_{S_{load}} + \text{loss in } R_S)$. Therefore, the equation (2.19) can be written as

$$\eta_{t,cc} = \frac{\Re(Z_{P_{out}})}{\Re(Z_{P_{out}}) + R_P} \cdot 1 \cdot \frac{\Re(Z_{S_{load}})}{\Re(Z_{S_{load}}) + R_S} \tag{2.20}$$

where the symbol $\Re$ represents the real part of the respective impedances (i.e., $Z_{P_{out}}$ and $Z_{S_{load}}$). From Figure 2.7, expressions of $Z_{S_{load}}$ and $Z_{P_{out}}$ are given by

$$Z_{S_{load}} = \frac{R_{L,\text{eq}}}{1 + j\omega C_S R_{L,\text{eq}}} \tag{2.21a}$$

$$Z_{P_{out}} = \frac{j\omega M Z_{S_{in}}}{j\omega M + Z_{S_{in}}} \tag{2.21b}$$

where $Z_{S_{in}} = j\omega(L_S - M) + R_S + Z_{S_{load}}$. Using (2.21a), (2.21b), real part of the impedances $Z_{S_{load}}$ and $Z_{P_{out}}$ are obtained as

$$\Re(Z_{S_{load}}) = \frac{R_{L,\text{eq}}}{1 + \omega^2 C_S^2 R_{L,\text{eq}}^2} \tag{2.22a}$$

$$\Re(Z_{P_{out}}) = \frac{\omega^2 M^2 \left(C_S^2 R_{L,\text{eq}}^2 R_S \omega^2 + R_{L,\text{eq}} + R_S\right)}{\left(C_S^2 L_S^2 \omega^4 + C_S\left(C_S R_S^2 - 2L_S\right)\omega^2\right) R_{L,\text{eq}}^2 + L_S^2 \omega^2 + \left(R_{L,\text{eq}} + R_S\right)^2}. \tag{2.22b}$$

Substituting $\Re(Z_{S_{load}})$ and $\Re(Z_{P_{out}})$ from (2.22a) and (2.22b), respectively, in (2.20) and the final

expression of $\eta_{t,cc}$ is given as

$$\eta_{t,cc} = \frac{M^2\omega^2 R_{L,\text{eq}}}{(C_S^2 R_{L,\text{eq}}^2 (L_S^2 R_P + M^2 R_S)\omega^4 + B\omega^2 + R_P\left(R_{L,\text{eq}} + R_S\right)^2} \tag{2.23}$$

where $B = \left(\left(\left(C_S^2 R_S^2 - 2C_S L_S\right) R_{L,\text{eq}}^2 + L_S^2\right) R_P + M^2\left(R_{L,\text{eq}} + R_S\right)\right)$.

To get $\eta_{t,cc_{max}}$ in CC and CV charging modes, an optimum operating frequency ($f_{optimum}$) needs to find because in (2.23), the operating frequency is only the parameter by which the system can be controlled during charging. Therefore, from (2.23), the optimum operating frequency ($f_{optimum}$) is obtained using (2.24), and the expression of $f_{optimum}$ is given in (2.25).

$$\left.\frac{\partial \eta_{t,cc}}{\partial f}\right|_{f_{optimum}} = 0. \tag{2.24}$$

$$f_{optimum} = \frac{1}{2\pi} \frac{R_P^{1/4}\sqrt{R_{L,\text{eq}} + R_S}}{\sqrt{R_{L,\text{eq}} C_S}\left(L_S^2 R_P + M^2 R_S\right)^{1/4}}. \tag{2.25}$$

Substituting (2.25) in (2.23), $\eta_{t,cc_{max}}$ can be expressed as

$$\eta_{t,cc_{max}} = \frac{M^2 R_{L,\text{eq}}\sqrt{R_P}}{\left(2C_S R_{L,\text{eq}} R_P\left(R_{L,\text{eq}} + R_S\right)\sqrt{L_S^2 R_P + M^2 R_S}\right) + B\sqrt{R_P}} \tag{2.26}$$

From the above analysis, (2.1), (2.15a), and (2.15b) are used to design the system in Section 2.3.1, whereas (2.9) (2.11), (2.18), (2.23), (2.25), and (2.26) are used to study the response of the system at the obtained equivalent resistance profile of the battery in CC and CV modes in Section 2.3.2. The following section explains the experimental setup and verifies the theocratical study of the system behaviour while charging in CC and CV modes.

2.3 Experimental Setup and Discussion

This section presents the developed experimental setup of the SP compensated WPT system. Here, the lead-acid battery is taken as a load. Moreover, it explains the charging profiles of the lead-acid battery in CC and CV modes, which is obtained experimentally. Furthermore, it discusses the effect of load variations during CC and CV modes on inverter waveforms, output waveforms, and $\eta_{t,cc}$), which is verified with the measurements. Finally, it identifies possible control parameters.

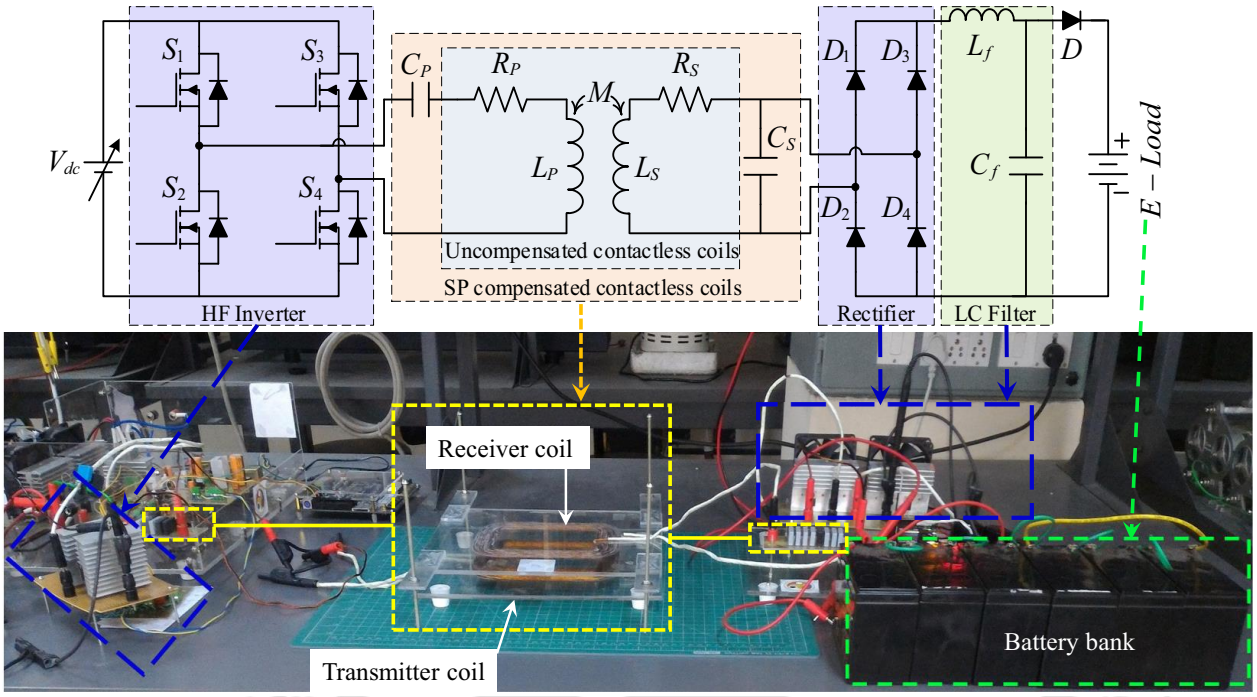

Figure 2.8: Experimental setup of the SP compensated WPT system for battery charging.

2.3.1 Experiment Setup

Figure 2.8 shows the experimental setup of the SP compensated WPT system for charging the battery bank. A total of six, 12 V sealed maintenance-free lead-acid batteries, connected in series, make a 72 V battery bank. The other technologies of batteries, such as lithium and sodium, can also be used to make a battery bank. Table 2.2 provides the specifications of the used power switches and the capacity of the battery bank. This thesis uses unipolar rectangular coils because of the advantages, such as excellent misalignment tolerance and similar to the shape of a vehicle's chassis [40, 41, 58]. The rectangular Tx and Rx coils (186 mm × 141.50 mm) are made using the Litz wire, having American wire gauge (AWG)#32 copper wire, and it is geometrically identical. The vertical distance (Z) between the Tx and Rx coils is measured from the bottom surface of the Tx coil to the bottom surface of the Rx coil. With the developed setup, the vertical distance can be adjusted up to 100 mm. However, it is kept at 20 mm [or equivalent to a 17.5-mm air gap (it is the distance measured from the top surface of the Tx coil to bottom surface of the Rx coil)] in the experiment. However, for the higher air gap, the same k can be achieved by increasing the outer dimensions of the coils [31]. A resonance frequency of 197.60-kHz is selected for the SP compensated WPT system. This selection

Table 2.2: Specifications of power components and battery bank.

Specification	Value
Power MOSFETs in inverter (S_1–S_4)	IRFP460
Hyperfast Diodes in rectifier (D_1–D_4)	RHRP30120
Half bridge gate driver IC	IR2110
Sealed Lead Acid Battery 7.2Ah	12×6 V

Table 2.3: Specifications of the SP compensated WPT system.

Symbol	Parameter	Value
N_P	Number of turns in Tx coil	11
N_S	Number of turns in Rx coil	11
L_P	Self-inductance of Tx coil	29.73 μH
L_S	Self-inductance of Rx coil	30.07 μH
R_P	AC resistance of Tx coil at 200 kHz	0.133 Ω
R_S	AC resistance of Rx coil at 200 kHz	0.137 Ω
k	Coupling coefficient at Z = 20 mm	0.51
C_P	Primary compensation capacitor	29.11 nF
C_S	Secondary compensation capacitor	21.51 nF
f_o	Resonance frequency	197.60 kHz

is because the higher resonance frequency gives a smaller value of compensation capacitors for fixed inductance values [from (2.15a) and (2.15b)]. Besides that, to minimise the ESRs of the capacitors and, hence, the losses, the operating frequency should be higher [57]. However, this higher resonance frequency is limited to the copper wire selection so that the power loss in the coil due to the skin effect can be eliminated. A PWM controller IC SG3525A is used to generate the gate pulses for the H-bridge inverter. With this IC, the output frequency of H-bridge inverter can be easily varied with the potentiometer. The remaining specifications of the SP compensated WPT system are given in Table 2.3. The upcoming subsection presents the charging profiles of the battery and discusses the system behaviour at the obtained load profile.

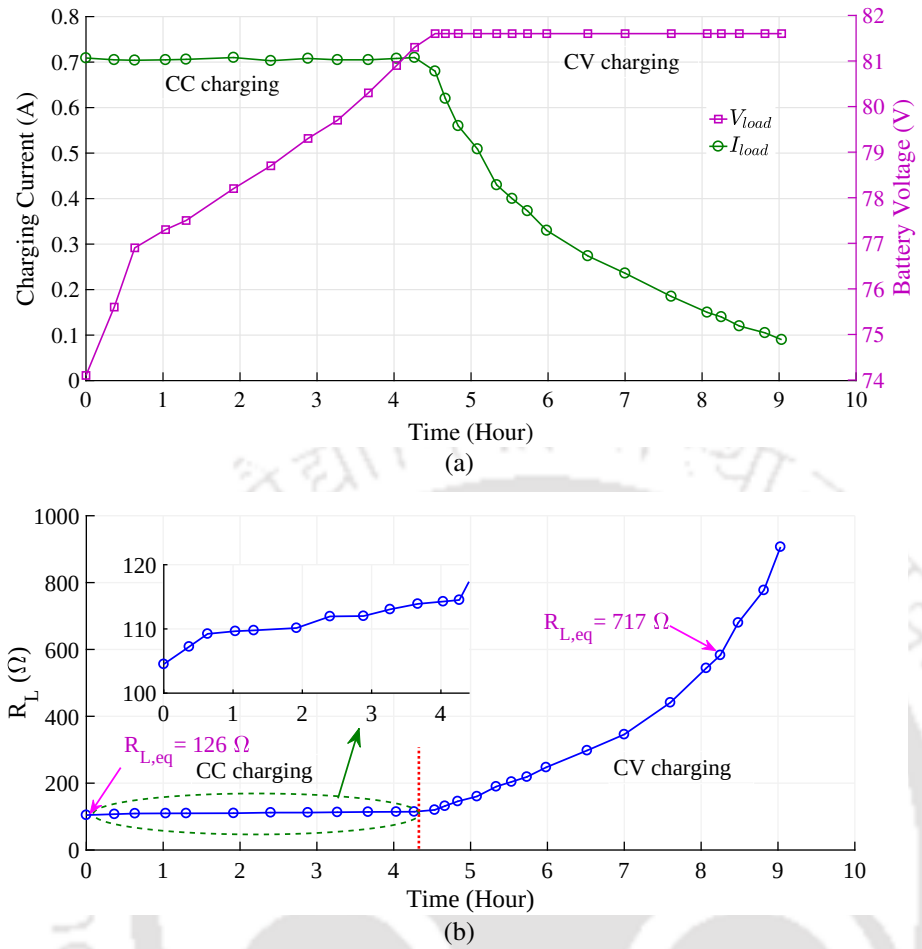

Figure 2.9: (a) Measured charging profile and (b) equivalent resistance profile of a lead-acid battery bank at resonance frequency.

2.3.2 Results and Discussion

In this subsection, the charging of lead-acid battery bank is performed in open-loop (by manually controlling the input DC voltage to maintain CC and CV modes) at the resonance frequency, and the related system parameters are studied. The varying range of input DC voltage is 49 V to 53 V. Figure 2.9 shows the measured charging profile and the equivalent resistance profile of a lead-acid battery bank. The initial voltage of the battery bank is 74.1 V, which is first charged in CC mode about four (4) hours after that in CV mode about five (5) hours, give a charging profile, as shown in Figure 2.9(a). The charging current in CC mode is set to a constant 700 mA (i.e., 0.1C-rate). To achieve this I_{load}, I_P is maintained at 1.4 A by varying the input DC voltage. Further, in CV mode, the voltage across the battery is maintained at 81.6 V by decreasing the input DC voltage (from 51 V to 49 V), which decreases the charging current, and when it reaches to approx 10% of the set charging current in CC

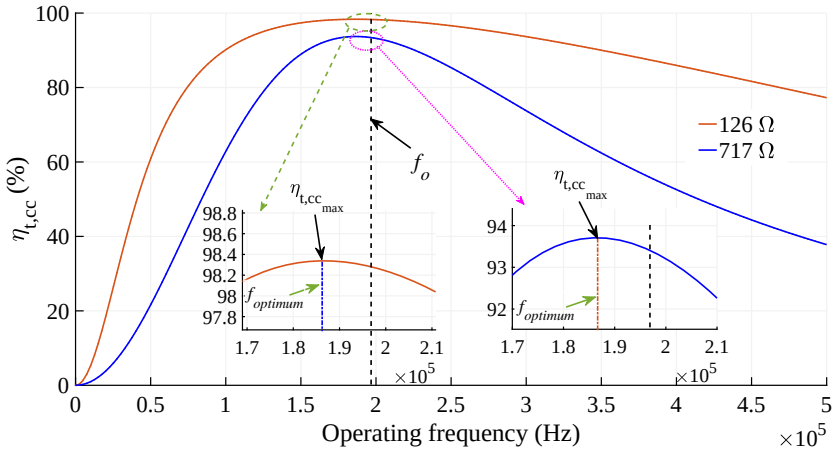

Figure 2.10: Variation of calculated $\eta_{t,cc_{max}}$ with respect to different operating frequencies for $R_{L,\text{eq}}$ = 126 Ω and 717 Ω.

mode, the charging gets completed. The equivalent resistance profile of battery bank, as shown in Figure 2.9(b), is obtained from Figure 2.9(a) by dividing V_{load} to I_{load} at each time interval. From Figure 2.9(b), it can be observed that R_L increases over the charging time and becomes high (lightly loaded condition) at the end of the charging.

Moreover, $\eta_{t,cc}$ is analysed in the CC and CV modes. Two cases of $R_{L,\text{eq}}$ are considered for the analysis of $\eta_{t,cc}$. One is for the CC mode ($R_{L,\text{eq}}$ = 126 Ω) and another is for the CV mode ($R_{L,\text{eq}}$ = 717 Ω). Figure 2.10 shows the variation of $\eta_{t,cc}$, calculated from (2.23), with respect to different operating frequencies (0 to 500 kHz) for $R_{L,\text{eq}}$ equal to 126 Ω and 717 Ω. For both the cases in Figure 2.10, $\eta_{t,cc_{max}}$ is shown by zooming the dotted circle area. From the zoomed view, it can be seen that $\eta_{t,cc_{max}}$ lies on the left side of f_o, marked as a $f_{optimum}$. Further investigation on $f_{optimum}$, $\eta_{t,cc_{max}}$, and various waveforms of voltage and current (input and output) at different operating frequencies in CC and CV modes are presented from the next paragraph onwards.

The voltage and current waveforms of the inverter and battery bank are observed at the time of CC and CV charging modes. In CC mode, the waveforms are recorded for the inverter output and battery bank, as shown in Figure 2.11. Since the current is constant in CC mode, an effective load resistance $R_{L,\text{eq}}$ changes only due to the voltage rise, which is less significant, as shown in Figure 2.9(b). In CC mode, at a particular instant of time, $R_{L,\text{eq}}$ is experimentally measured as 126 Ω (marked in Figure 2.9(b)). Since the electrical characteristics of the battery bank change over time, the battery bank is

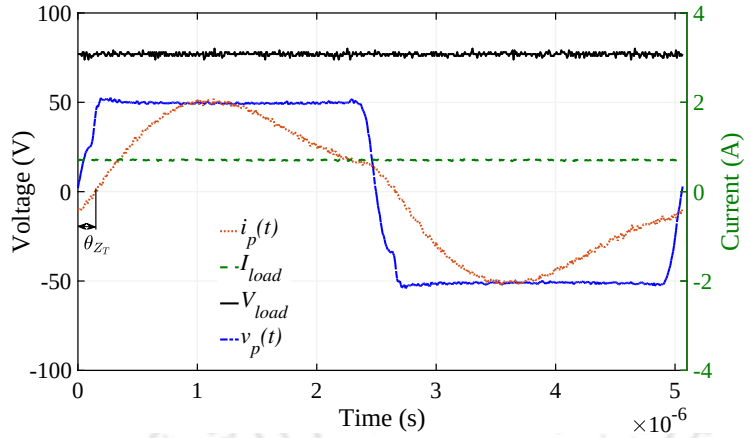

Figure 2.11: Experimental waveforms in CC mode at the resonance frequency.

replaced by an equivalent resistive load of 126 Ω to maintain the same $R_{L,\text{eq}}$ for further experiment.

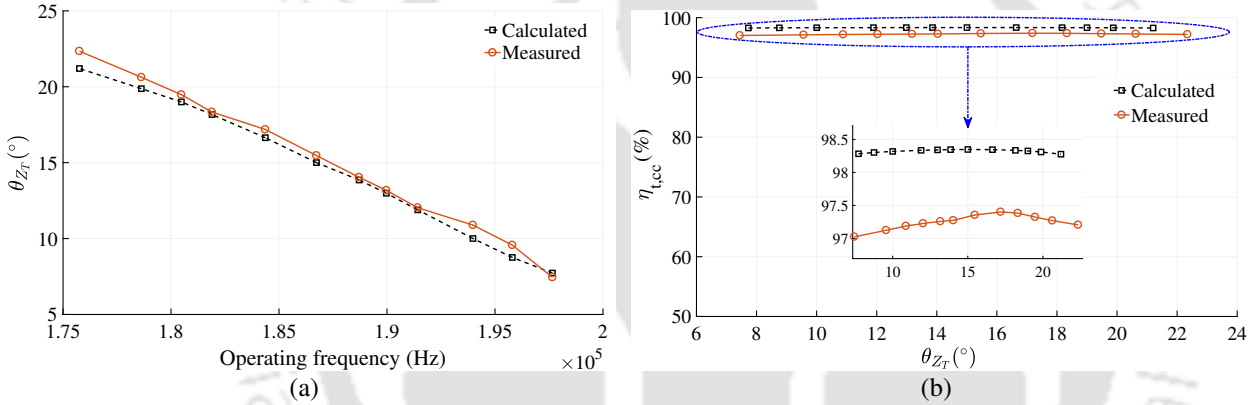

Figure 2.12: Experimental results at $R_{L,\text{eq}}$ = 126 Ω. (a) Load phase angle versus operating frequency. (b) $\eta_{t,cc}$ versus load phase angle.

Figure 2.12(a) shows the variation of load phase angle obtained from (2.18) for different operating frequencies when $R_{L,\text{eq}}$ equal to 126 Ω, which agrees well with the measured variation of the same. From Figure 2.12(a), it can be seen that the increase in load phase angle of the system is achieved by decreasing the operating frequency from its resonance frequency. Further, to examine the effect of the increase in the load phase angle of the system on $\eta_{t,cc}$, Figure 2.12(b) gives a variation of $\eta_{t,cc}$ with respect to the load phase angle obtained from (2.18) and (2.23), and from the measurement. From Figure 2.12(b), almost constant nature of $\eta_{t,cc}$ is seen with the variation in load phase angle. However, in zoomed view, a parabolic nature is seen with an increase in load phase angle. Hence, it has a maximum efficiency point about a load phase angle of 15° from the calculation and 17° from the measurement.

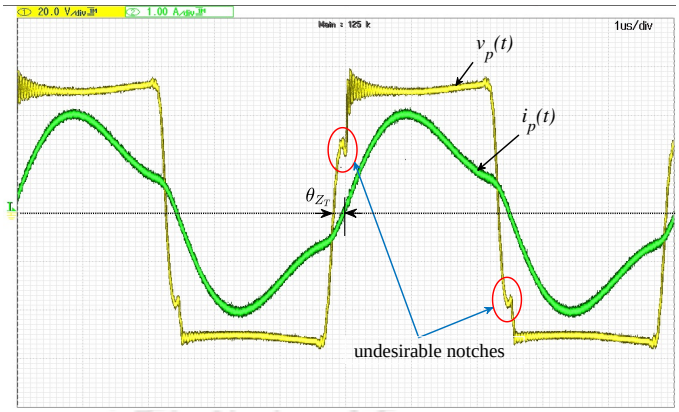

Figure 2.13: Experimental waveforms of primary voltage and current (inverter output) at the 197.6-kHz operating frequency (resonance frequency) and $R_{L,\text{eq}}$ = 126 Ω.

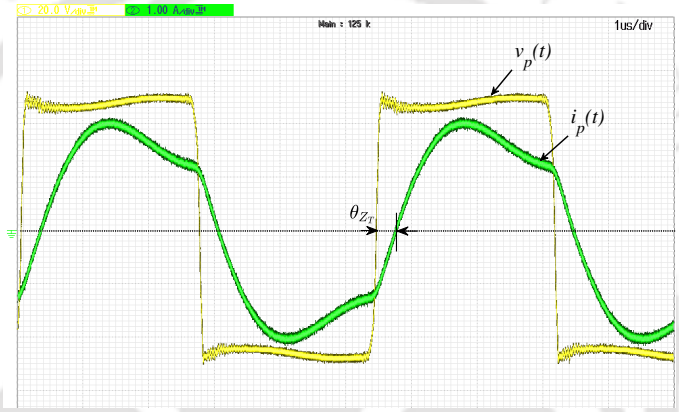

Figure 2.14: Experimental waveforms of primary voltage and current (inverter output) at the 184.3-kHz operating frequency and $R_{L,\text{eq}}$ = 126 Ω.

At the resonance frequency, Figure 2.13 shows the experimental waveforms of the primary voltage (inverter output) and current. In Figure 2.13, undesirable notches (due to inappropriate ZVS), marked in the red circle are noticed in the primary voltage waveform, which can affect the system stability. Figure 2.14 shows the improved waveform (due to proper ZVS) of the primary voltage, which is recorded at the 184.3-kHz frequency (measured $f_{optimum}$). The proper ZVS is noticed about 17° of the load phase angle. From Figures 2.12 to 2.14, it can be seen that to obtain a stable waveform, the load phase angle should be increased by decreasing the operating frequency to $f_{optimum}$. In this way, the system stability can be improved with maximum efficiency for a lower load resistance in CC mode.

In CV mode, the voltage and current waveforms of the inverter output and battery bank are recorded near the end stage of CV mode for a charging current of 140 mA, as shown in Figure 2.15. $R_{L,\text{eq}}$ is experimentally measured as 717 Ω (marked in Figure 2.9(b)), which is higher than to those

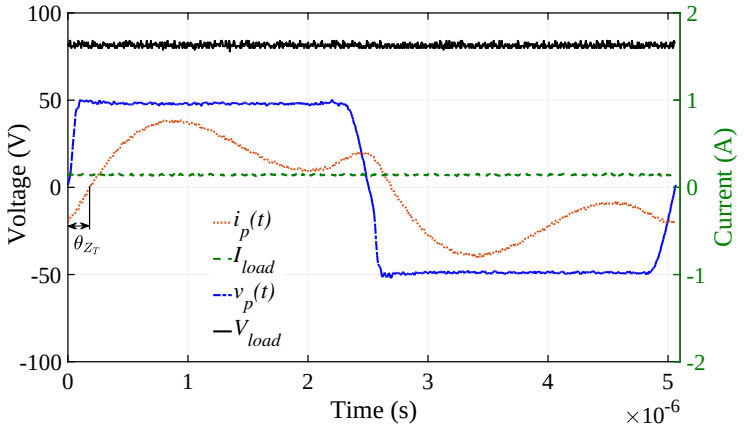

Figure 2.15: Experimental waveforms in CV mode at the resonance frequency.

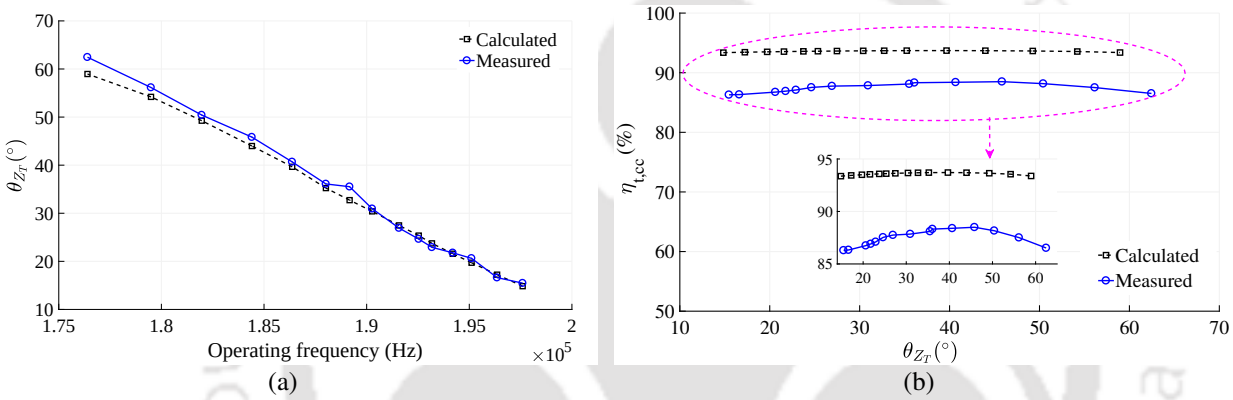

Figure 2.16: Experimental results at $R_{L,\text{eq}}$ = 717 Ω. (a) Load phase angle versus operating frequency. (b) Compensated coil efficiency versus load phase angle.

obtained in CC mode. The battery bank is replaced with a resistive load for the further experiment to maintain $R_{L,\text{eq}}$ (717 Ω).

At $R_{L,\text{eq}}$ equal to 717 Ω, again the operating frequency is varied to maintain ZVS along with the maximum efficiency. Figure 2.16(a) shows the variation of load phase angle for different operating frequencies obtained from (2.18) and measurement when $R_{L,\text{eq}}$ equal to 717 Ω. From Figure 2.16(a), it is found that both the curves are following the same pattern. In CV mode, the waveform of inverter voltage is stable throughout the variation, even at the resonance frequency, as shown in Figure 2.15. Figure 2.16(b) gives the variation in $\eta_{t,cc}$ against the load phase angle, calculated from (2.18) and (2.23). From Figure 2.16(b), it is observed that the $\eta_{t,cc}$ is maximum when the load phase angle is about 40° (obtained at $f_{optimum}$ = 186.5 kHz) from the calculation and about 45° (obtained at $f_{optimum}$ = 184.4 kHz) from the measurement. In addition, a parabolic nature of $\eta_{t,cc}$ curve is noticed with an

increase in the load phase angle.

From the above discussion, it is noticed that by controlling the load phase angle in both CC and CV modes, stable waveforms and maximum efficiency are achieved. Hence, based on the identified control parameters (load phase angle, operating frequency, and input DC voltage), a suitable closed-loop controller can be implemented.

The above analysis is performed at a fixed value of k. However, in wireless charging, the value of k can change due to several factors, such as different air gaps in the vehicles and different misalignments caused by the change in tyre pressure and imperfect parking [24]. Hence, to analyse the different values of k on the transferred power and $\eta_{t,cc}$, a theoretical analysis is presented in the next section.

2.4 Impact of Coupling Coefficient on Transferred Power and $\eta_{t,cc}$ in CC and CV Charging Modes: Theoretical Analysis

Usually, the air gap ranges from 100 to 250 mm in most of the vehicles [1], and it is determined based on the vehicle type. In most of the two- and three-wheelers, the air gap is kept 150 mm. At this air gap, k of the coils (taken in this chapter) is 0.041 (simulated value), which is a pretty low value. Therefore, the impact of k on the transferred power and $\eta_{t,cc}$ in the CC and CV charging modes (i.e., at different $R_{L,\text{eq}}$) should be studied. In this context, the subsequent subsections derive the expression of transferred power and $\eta_{t,cc}$ in terms of k and study its impact.

2.4.1 Impact of Coupling Coefficient on Transferred Power

In this subsection, an expression of transferred power in terms of k has been derived. Further, with the derived expression, the effect of different $R_{L,\text{eq}}$ at various k on power transfer has been investigated. From Figure 2.3, the maximum apparent power (S_{max}) that can be transferred to the Rx coil, irrespective of the compensation topology, is given by (2.1) [31, 33, 41]

$$S_{max} = V_{oc}\, I_{sc} \tag{2.27}$$

where V_{oc} is the open-circuit voltage of the Rx coil and I_{sc} is short-circuit current that the Rx coil can source to the load. For a current I_P in L_P at the operating angular frequency ω, V_{oc} and I_{sc} are given

as

$$V_{oc} = j\omega M I_P \tag{2.28a}$$

$$I_{sc} = \frac{V_{oc}}{R_S + j\omega L_S} \tag{2.28b}$$

Substituting (2.28a) and (2.28b) in (2.27), S_{max} can be given as

$$S_{max} = \frac{(j\omega M I_P)^2}{R_S + j\omega L_S} \tag{2.29}$$

The simplified form of the magnitude of (2.29) can be written as

$$S_{max} = \frac{(\omega M I_P)^2 \sqrt{R_S^2 + \omega^2 L_S^2}}{R_S^2 + \omega^2 L_S^2} = \frac{\omega^2 M^2 I_P^2}{\sqrt{R_S^2 + \omega^2 L_S^2}} \tag{2.30}$$

Substituting the value of M from (2.1) in (2.30), S_{max} in terms of k is given as

$$S_{max} = \frac{\omega^2 k^2 I_P^2 L_P L_S}{\sqrt{R_S^2 + \omega^2 L_S^2}} \tag{2.31}$$

For the compensated coils, the output active power (P_{load}) that can be transferred to the secondary side, is obtained by

$$P_{load} = S_{max} Q_S \tag{2.32}$$

where Q_S is the quality factor of the secondary circuit (under load), which depends on the way C_S is connected (series or parallel [12]) to the Rx coil. Here, for parallel resonance at the secondary side, Q_S is equal to $\frac{(R_S + R_{L,\text{eq}})}{\omega L_S}$. Hence, the final expression of P_{load} is given as

$$P_{load} = \frac{\omega k^2 I_P^2 \left(R_S + R_{L,\text{eq}}\right) L_P}{\sqrt{R_S^2 + \omega^2 L_S^2}} \tag{2.33}$$

As is evident from (2.33), it possible to enhance the power transfer capability by increasing either ω, I_P, k, L_P or Q_S. Practically, the operational value of Q_S is limited due to the component VA ratings, deterioration over time, tolerances, and Q of an individual unloaded component [30, 31]. The parameters ω and I_P are restricted by the availability and cost of appropriate power electronics devices and the Litz wire [30, 32]. Increasing the L_P leads to a higher resonant voltage across the coil, which

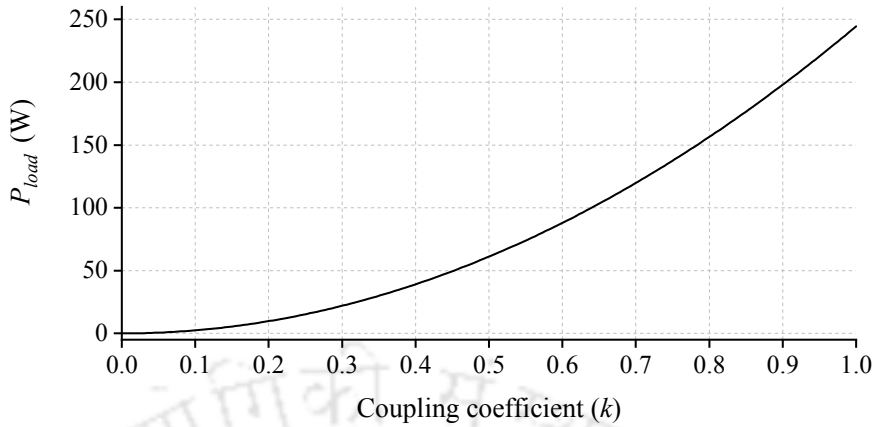

Figure 2.17: Variation of output power with respect to k for constant values of I_P, ω, and $R_{L,\text{eq}}$.

results in higher cost of C_P and C_S [25]. Due to these limitations, parameter k can be used to enhance the power transfer capability [30, 32, 33, 41], and it can be seen from (2.33), higher k results in higher P_{load}. The same could be seen in Figure 2.17 also. The curve in Figure 2.17 is shown for a constant value of I_P, ω, and $R_{L,\text{eq}}$. The value of I_P, ω, and $R_{L,\text{eq}}$ in (2.33) is chosen for the scenario presented for CC charging mode (i.e., $I_P = 1.4$ A and $R_{L,\text{eq}} = 126\ \Omega$), and the other parameters are selected from Table 2.3. Moreover, for different $R_{L,\text{eq}}$ (for the same I_P and ω), the pattern of the transferred power curves would remain unchanged. However, their magnitude would changes. The same is true for $R_{L,\text{eq}}$ in CV mode. The next subsection investigates the impact of various k on $\eta_{t,cc}$ for different $R_{L,\text{eq}}$.

2.4.2 Impact of Coupling Coefficient on the Transmission Efficiency of Compensated Coils

To examine the impact of various k on $\eta_{t,cc}$ at different $R_{L,\text{eq}}$, the expression of $\eta_{t,cc}$ in (2.23) is rewritten in terms of k as

$$\eta_{t,cc} = \frac{k^2\omega^2 R_{L,\text{eq}} L_P L_S}{C_S^2 R_{L,\text{eq}}^2 L_S \omega^4 \left(L_P R_S k^2 + L_S R_P\right) + H\omega^2 + R_P\left(R_{L,\text{eq}} + R_S\right)^2} \tag{2.34}$$

where $H = \left(\left(R_{L,\text{eq}} + R_S\right) L_P L_S k^2 + C_S R_P \left(C_S R_S^2 - 2L_S\right) R_{L,\text{eq}}^2 + L_S^2 R_P\right)$.

Figure 2.18(a) shows the efficiency map of the compensated coils. This efficiency map is obtained by varying k and $R_{L,\text{eq}}$ in (2.34) while keeping other parameters constant (the value of these parameters is given in Table 2.3). Here, k is varied from its minimum to maximum values (i.e., 0-1), whereas $R_{L,\text{eq}}$ is from 0 – 717 Ω. This range of $R_{L,\text{eq}}$ shows the load required in the CC (at different charging rates, i.e., 0.1C or 0.2C or 0.5C and so on) and CV charging modes. From Figure 2.18(a), it is seen

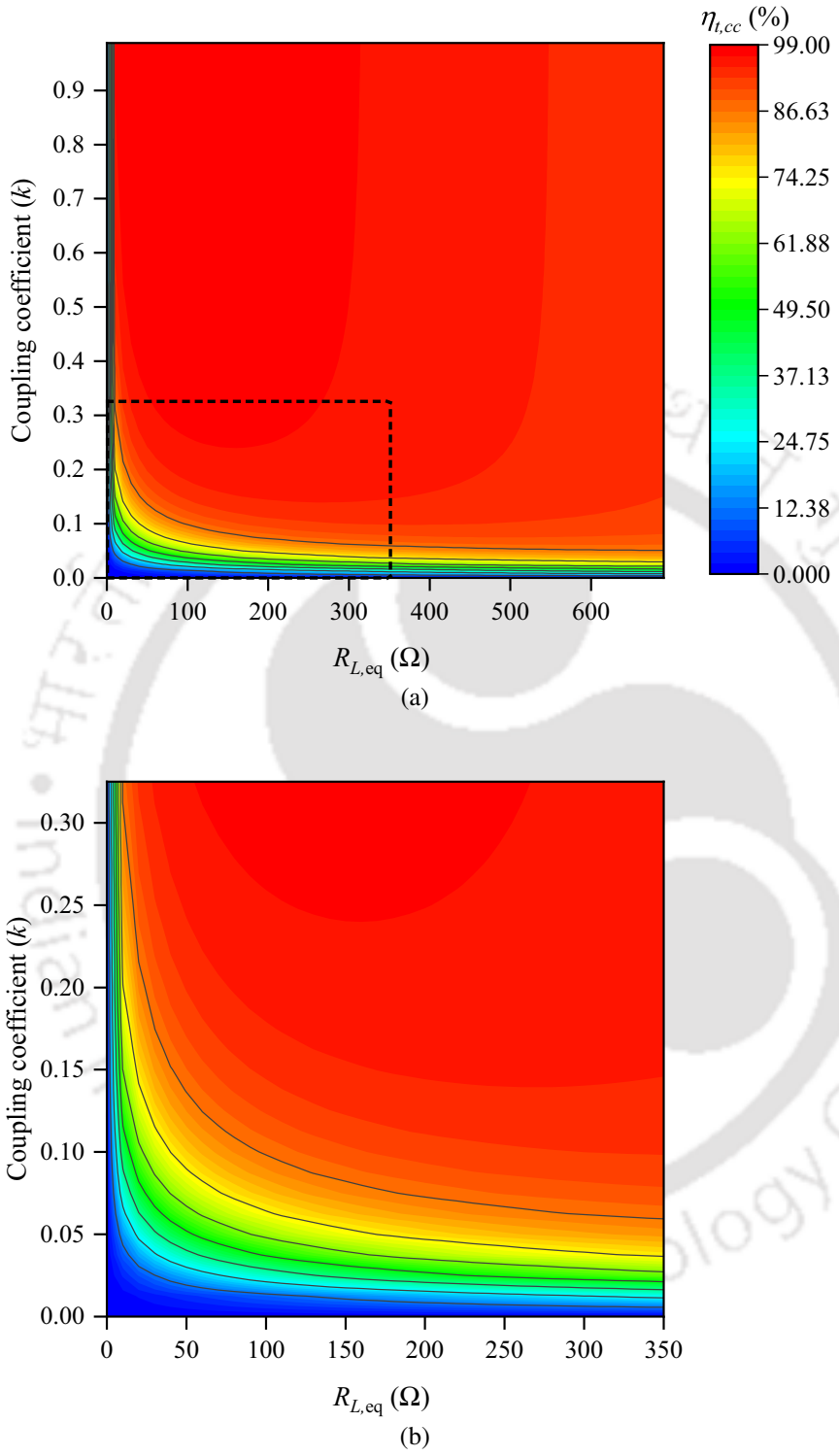

Figure 2.18: (a) Calculated efficiency map of the compensated coils and (b) zoomed view of dotted area shown in Figure 2.18(a).

that $\eta_{t,cc}$ is close to 99% for $R_{L,eq} < 10\ \Omega$ and $k \geqq 0.35$, whereas for $k < 0.35$, $\eta_{t,cc}$ is different according to $R_{L,eq}$. Furthermore, the variation of $\eta_{t,cc}$ of the dotted area in Figure 2.18(a) is zoomed and is shown

in Figure 2.18(b). From Figure 2.18(b), it is observed that for $k < 0.75$, $\eta_{t,cc}$ is between 0%–80% for all $R_{L,\text{eq}}$. For $0.75 < k < 0.35$, $\eta_{t,cc}$ is less than 90% for $R_{L,\text{eq}} < 50\ \Omega$, whereas for $R_{L,\text{eq}} > 50\ \Omega$, $\eta_{t,cc}$ is greater than 75%. Thus, it can be concluded that in CC charging mode where the $R_{L,\text{eq}} < 50\ \Omega$ (achieved at different charging rates), $\eta_{t,cc}$ has a lower value, whereas in CV charging mode $\eta_{t,cc}$ is comparatively high at $0.75 < k < 0.35$.

Further, at $k = 0.041$ (as calculated earlier at 150 mm), the transferred power is insufficient (can be seen in Figure 2.17) and $\eta_{t,cc}$ is less than 15%. Hence, to enhance the power transfer capability and $\eta_{t,cc}$ of the system, there is a need to enhance the factor k of the contactless coils for the required air gap.

2.5 Summary of the Chapter

In this chapter, an open-loop control for the lead-acid battery charging using the SP compensated WPT system is studied and presented. Various expressions (such as load phase angle, optimum operating frequency, and $\eta_{t,cc_{max}}$) are derived using different equivalent circuits of the SP compensated WPT system for analysing the performance in CC and CV charging modes. Measured charging profile and the equivalent resistance profile of the lead-acid battery bank are presented in the CC and CV modes. In CC charging mode, a slight increment in $R_{L,\text{eq}}$ is noticed over the charging time, whereas an exponential increment in $R_{L,\text{eq}}$ is observed in case of CV charging mode. Besides that, during the CC charging mode, undesirable notches are seen in the inverter voltage waveform at the resonance frequency due to inappropriate ZVS. This problem has been corrected while operating at the optimum operating frequency instead of the resonance frequency. Further, at this optimum operating frequency, $\eta_{t,cc_{max}}$ is achieved. In CV charging mode, a proper ZVS in the inverter voltage waveform is observed at the resonance frequency. However, operating at the optimum operating frequency has given $\eta_{t,cc_{max}}$. From the experimental results and discussion, control parameters are identified, which can be used to implement a suitable closed-loop robust controller.

Furthermore, the impact of k on $\eta_{t,cc}$, and transferred power is studied in the CC and CV charging modes. With this study, it is found that to enhance the power transfer capability and $\eta_{t,cc}$ of the WPT system, k needs to be enhanced. Therefore, the next chapter analyses and discusses the methods of

improving the factor *k* of the contactless coils.

Note: *The research findings of this chapter have been published in "Wireless Power Transfer," Cambridge University Press.*

3

3-D Analytical Modelling for Air-Core Rectangular Coils and Investigation on Improving the Coupling Coefficient

Contents

3.1 Introduction

In the previous chapter, it is found that in CC and CV charging modes, k of the coils needs to be enhanced at a given (for example, 150 mm) air gap to increase the transmission efficiency and power transfer capability. In this context, this chapter discusses and analyses the possible ways to improve k of air-cored coils. Factor k depends on magnetic design and alignment of the coils [33, 41]. For a fixed air gap, increasing the outer dimensions of the coils increase the factor k, but the applications restrict the outer dimensions. For example, in the EV application, the outer dimensions are restricted by the installation space available beneath the vehicle's chassis [59]. Therefore, improving k without changing the outer dimensions of the coils needs attention.

Generally, a ferrite core is used to improve k of a unipolar air-cored coil system [24, 27, 29]. In recent years, multi-coil topologies, such as bipolar coils [30], double-D quadrature coils [31], and mutually decoupled coils [32] are proposed to improve the value of k (multicoil topologies use unipolar coils and ferrite core). However, the use of ferrite core in unipolar as well as multicoil topologies increases the cost and weight of the system [27, 33]. Thus, the ferrite core is not the first resort toward improving k. Few works have reported on improving the factor k without using ferrite material for unipolar coils of different geometries in [34, 35]. Factor k of the square- and circular-shaped coils is improved by using intermediate coils [34, 35]. Still, the design of intermediate coils and its tuning increases the complexity and cost of the system. Therefore, an attempt to improve k should involve modification (the first resort) in the design of the coils.

Usually, 3-D FEA software is used to design the coils and calculate k. An FEA technique divides a continuous geometry into discrete elements, which is known as mesh and solves its governing equations to get the results. Therefore, the 3-D FEA model requires high-mesh density to generate accurate results. Further, when the parametric sweep is used to optimised the coils, then multiple simulations are needed, which require a large amount of memory to do massive mathematical calculations. Moreover, the mesh formation depends on the dimensions of the designed model, and any modification in the 3-D FEA model requires re-meshing. Hence, the FEA is a tedious and time-consuming process.

The analytical model is an another method to calculate the magnetic field and k of the coils. It is geometry specific and requires less number of equations in modelling, which makes it faster compared

with FEA. Moreover, the solving time is independent of the dimensions of the geometry. Generally, the assumptions are made to define the geometry and reduce the complexity in the analytical model. As a result, the analytical model is less accurate compared with FEA, but easier to implement and faster for the initial design and optimisation of the coils.

Many analytical models are reported in the literature to calculate the self- and mutual inductance of the rectangular- and square-shaped coils. However, the coils given in [60] have sharp edges at the corners, which generates eddy current and hot spots [44, 61]. In contrast, most of the WPT system uses the contactless coils with circular corners (used in the previous chapter also) to prevent the hot spots and eddy current generation [34]. If the rectangular or square coils with the circular corners are modelled by approximating the circular corners with the sharp edges at the corners, then it introduces significant error in the analytical results [48, 61]. Hence, the circular corners need to be considered in the modelling.

In this context, this chapter attempts to develop a 3-D analytical model for the rectangular and square coils by considering the effect of circular corners, which is used to study and analyse the different conventional coils for improving k. The organisation of the remainder of the chapter is as follows. Section 3.2 explains the geometry, assumptions, and the various steps used in the development of a 3-D analytical model. With this model, it is possible to describe the magnetic flux density (B-field, magnetic field) in any region of the coil. Furthermore, it provides the analytical expression to calculate the self-and mutual inductance of the coils. Section 3.3 explains the experimental setup used to measure the magnetic field generated by the Tx coil. Then, the obtained analytical results are compared with the 3-D FEA and measurements to verify the accuracy of the developed 3-D analytical model. Thereafter, by using this analytical model, Section 3.5 studies k of different possible conventional coils with the constraint(s) for the EV application (an electric scooter is taken as an example of EV application) and analyses the improvement in k. In the end, Section 3.6 summarises the work presented in this chapter.

3.2 3-D Analytical Modelling of Rectangular Coil System

This section presents a formulation of the 3-D analytical model for rectangular (and square) coils in the Cartesian coordinate system. This modelling is based on the harmonic modelling method

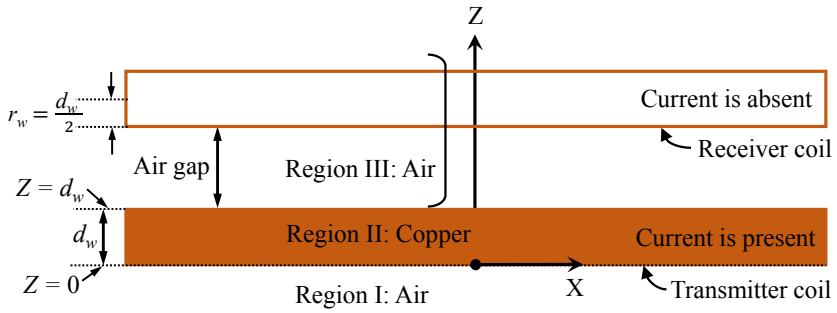

Figure 3.1: Side view (XZ plane view) of the air-cored coil system illustrating different regions.

[62], where Fourier analysis, magnetic vector potential, and magnetic scalar potential definitions are involved. Section 3.2.1 explains the geometry (which approximates the working rectangular coil) and assumptions used in the modelling. Further, Section 3.2.2 gives the current density definitions using Fourier series and discusses the number of harmonics to be used. Section 3.2.3 defines the magnetic vector and magnetic scalar potentials in the coil system. Moreover, it gives the expression for calculating the B-field in different regions of the coil system and self- and mutual inductance of the coils.

3.2.1 Geometrical Description and Assumptions

Figure 3.1 gives the XZ view of the air-cored coil system. Here, the Tx coil is excited with a current source, whereas the Rx coil is open-circuited. In the modelling, Rx coil is considered as air region because it is open-circuited and, hence, has no current in it. The coil system (geometry) is divided into horizontal regions, perpendicular to the direction of the spatial periodicity, due to the use of the harmonic modelling method [62]. The regions are differentiated from each other based on the properties of the medium. Here, the spatial periodicity is in the X- and Y-directions (Figure 3.3). Therefore, the coil system is divided into three regions based on the medium change along the Z-axis direction [63], as shown in Figure 3.1. Region II is the Tx coil, and Regions I and III, which are below and above to the Tx coil, are considered as air medium.

Figure 3.2(a) shows the top view of the working rectangular coil. The outer dimensions of the coil are defined as x mm and y mm in the X- and Y-directions, respectively. For the modelling of the coil shown in Figure 3.2(a), the approximated coil is depicted in Figure 3.2(b) that considers the effect of circular corners. Here, to closely mimic the circular corners, the coil in Figure 3.2(a) is divided into four finite rectangular bars that overlap at the corners. In each rectangular bar, the equivalent current

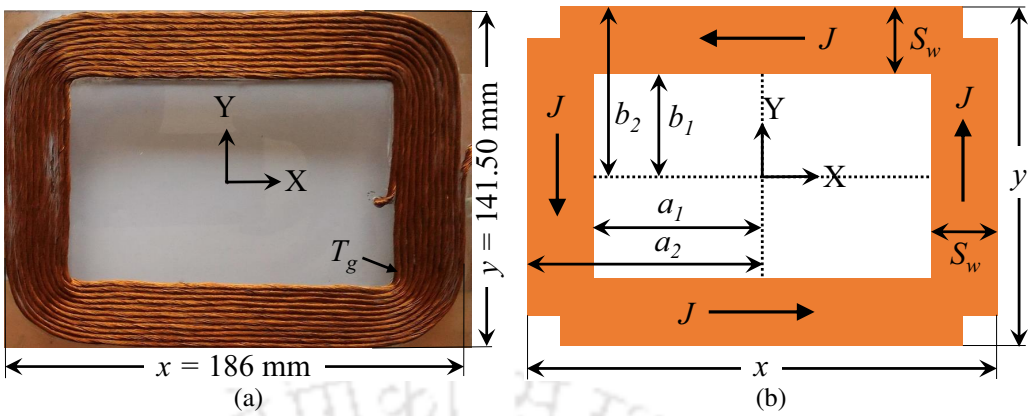

Figure 3.2: Top view (XY plane view) of (a) working coil and (b) modelling coil.

Table 3.1: Geometrical and modelling parameters.

Parameter	Description	Formula	Value	Unit
a_2	Half outer width of coil in X-direction	$x/2$	93.0	mm
b_2	Half outer width of coil in Y-direction	$y/2$	70.75	mm
d_w	Diameter of Litz wire (or height of coil in Z-direction)	-	2.5	mm
S_w	Total width occupied by total number of turns (N)	$(T_g + d_w)$N- T_g	27.5	mm
a_1	Half inner width of coil in X-direction	$(a_2 - S_w)$	65.5	mm
b_1	Half inner width of coil in Y-direction	$(b_2 - S_w)$	43.25	mm
τ_X	Coil pitch in X-direction	$5x$	930	mm
τ_Y	Coil pitch in Y-direction	$5y$	707.5	mm
J	Equivalent current density in bars due to I_P	$(NI_P)/(d_w S_w)$	0.713	Amm^{-2}
U	Number of harmonics in X-direction	-	140	-
W	Number of harmonics in Y-direction	-	140	-

T_g is the gap between the turns, and it is zero for the coil shown in Figure 3.2(a).

density is defined, which is produced in the working coil due to current I_P in N number of turns. With this approximation, the coils with different gaps between the conductors can be modelled (here, this gap is zero). The geometrical parameters, such as a_1, a_2, and ..., are also illustrated in Figure 3.2(b) to define the current densities in the rectangular bars. The description of the geometrical parameters and their values are given in Table 4.1.

The Litz wire is used to make the coils, and it is operated at the high-frequency as limited by the selected Litz wire. At this frequency, an uniform current distribution is assumed over the entire cross-section of the Litz wire in the inductance calculation due to the negligible effect of skin effect.

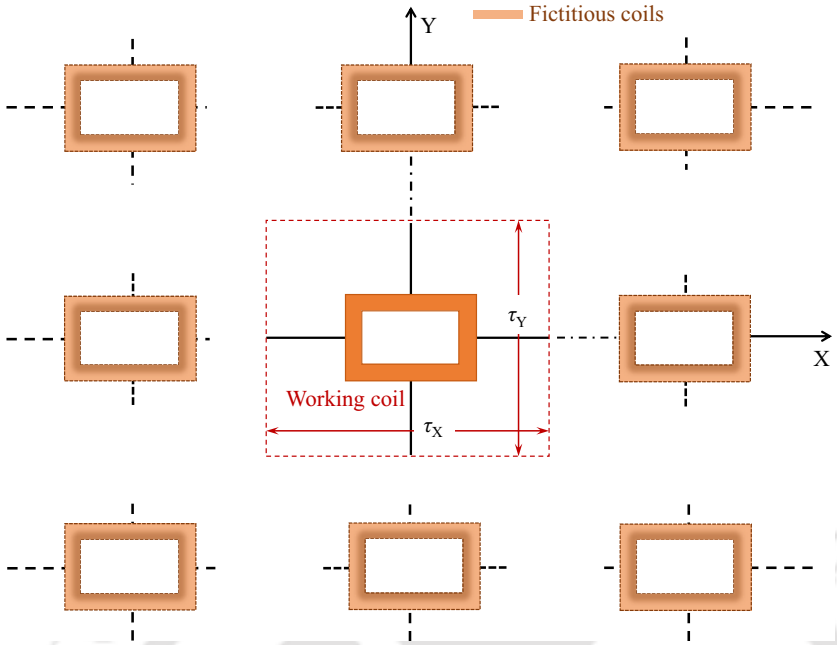

Figure 3.3: Periodic arrangement of air-core rectangular coil with period of τ_X and τ_Y in the X- and Y-directions.

The harmonics modelling method is applied in a periodic structure (divided into regions) for calculating the B-field in regions [62]. However, the presented WPT system in the previous chapter uses only a single coil system. Therefore, to model a single source (i.e., Tx) coil based WPT system, a periodic arrangement of the air-core rectangular coil is assumed with the period of τ_X and τ_Y in the X- and Y-directions, as shown in Figure 3.3. Here, two types of coils are shown; namely, the working coil and the fictitious coils. The working coil is a coil which is physically present, and the fictitious coils are physically absent. The fictitious coils are far away from the working coil so that the magnetic field of the fictitious coils does not influence the magnetic field of the working coil. Moreover, the magnetic vector potential formulation is used in the current-carrying region, whereas in all other regions, the magnetic scalar potential formulation is used [48]. The current density description, magnetic vector and magnetic scalar potential formulations are presented in the subsequent subsections.

3.2.2 Current Density Description

The coil, which has four finite rectangular bars, as shown in Figure 3.2(b), is modelled for the current flowing in the X- and Y-directions. For this, the current-carrying bars are expressed by a double Fourier series [47–49]. Figure 3.4 shows the XZ view of Figure 3.2(b) and its current density profile in the bars parallel to the Y-axis. It also shows the YZ view of Figure 3.2(b) and its current

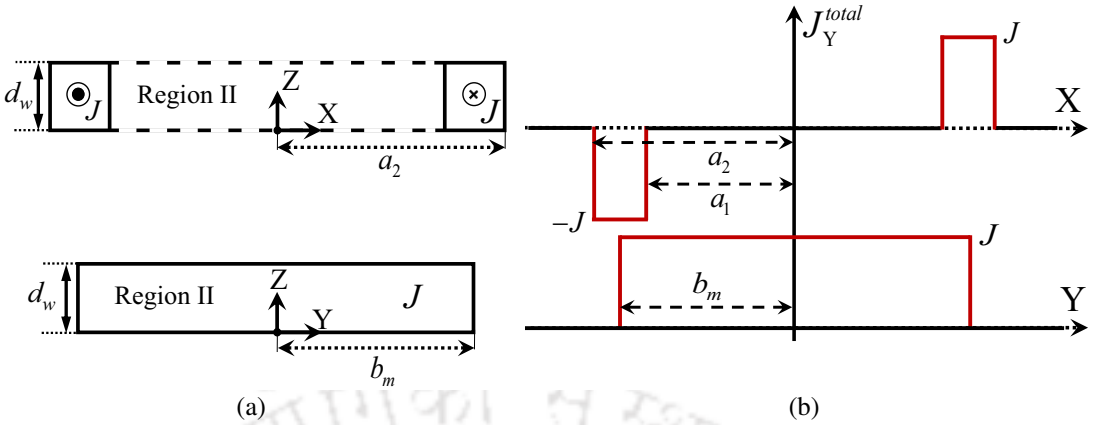

Figure 3.4: (a) XZ and YZ plane views (side views) of Figure 3.2(b) for defining the distribution of $J_Y^{total}(X,Y)$ in the bars parallel to the Y-axis. (b) Distribution of $J_Y^{total}(X,Y)$ along the X- and Y-directions.

density profile in the bars parallel to the Y-axis. Multiplying these two current density profiles gives the current density distribution in the Y-direction ($J_Y^{total}(X,Y)$), which is expressed as

$$J_Y^{total}(X,Y) = \sum_{u=1,3,5}^{U} \sum_{w=1,3,5}^{W} j_Y^{total} \sin(k_X X) \cos(k_Y Y) \tag{3.1}$$

where $k_X = \dfrac{u\pi}{\tau_X}$ and $k_Y = \dfrac{w\pi}{\tau_Y}$ are spatial frequencies in the X- and Y-directions with the period of τ_X and τ_Y, respectively. U and W are the maximum harmonics number in the X- and Y-directions, respectively. The term j_X^{total} depends on the geometrical parameters of the coil structure, and for the coil shown in Figure 3.2(b), it is given as

$$j_Y^{total} = \frac{16J}{uw\pi^2} ((\cos(k_X a_1) - \cos(k_X a_2)) \sin(k_Y b_m)) \tag{3.2}$$

where $b_m = 0.5(b_2 + b_1)$ and J is the value of equivalent current density in bars due to I_P, and its formula is given in Table 4.1.

Similarly, the current density distribution in the X-direction is given as

$$J_X^{total}(X,Y) = \sum_{u=1,3,5}^{U} \sum_{w=1,3,5}^{W} j_X^{total} \sin(k_Y Y) \cos(k_X X) \tag{3.3}$$

with

$$j_X^{total} = \frac{16J}{uw\pi^2} ((\cos(k_Y b_1) - \cos(k_Y b_2)) \sin(k_X a_m)) \tag{3.4}$$

where $a_m = 0.5(a_2 + a_1)$. The terms a_1, a_2, a_m, b_1, b_2, and b_m (in (3.4) and (3.2)) are the geometrical

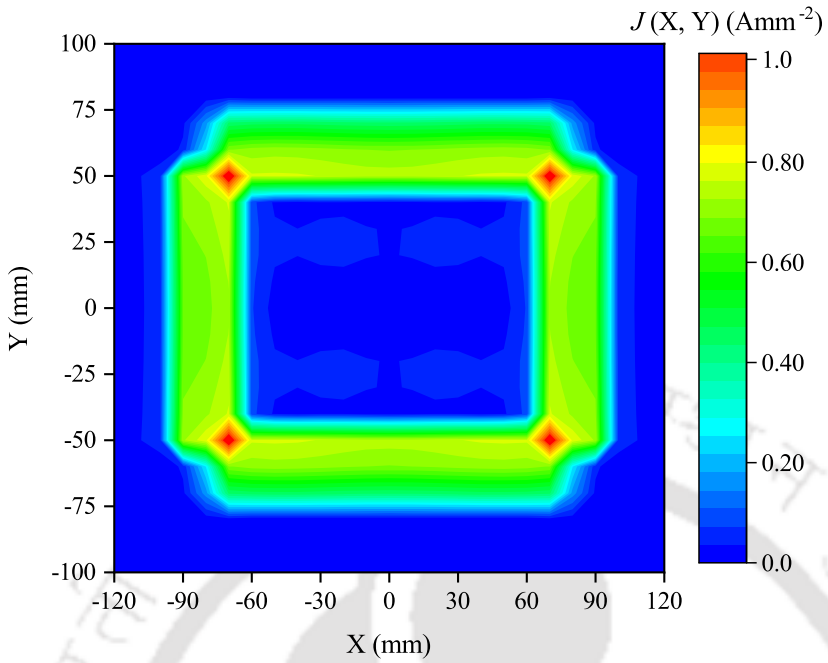

Figure 3.5: Magnitude of current density in the X- and Y- directions.

parameters, which are given in Table 4.1. The magnitude of current density distribution in the coil (i.e., in the X- and Y-directions) is given by

$$J(\mathrm{X},\mathrm{Y}) = \sqrt{\left(J_{\mathrm{X}}^{total}(\mathrm{X},\mathrm{Y})\right)^2 + \left(J_{\mathrm{Y}}^{total}(\mathrm{X},\mathrm{Y})\right)^2}. \tag{3.5}$$

Figure 3.5 shows the contour plot of $J(\mathrm{X},\mathrm{Y})$, which is obtained by putting the value of geometrical parameters from Table 4.1 in (3.5). From Figure 3.5, it can be seen that the magnitude of current density at the outside of each corner is zero, whereas it is $\sqrt{2}J$ at the inside of each corner. These magnitudes are due to the overlapping of the bars. The cross-section of the contour plot shown in Figure 3.5 along the X-axis at Y = 0 is shown in Figure 3.6(a). The effect of the limited number (140) of harmonics used in (3.5) can be seen in the current density profile in Figure 3.6(a). At the higher number of harmonics (560; four times of 140), the obtained current density profile in Figure 3.6(b) is near to the ideal profile, as shown in Figure 5.2. But, the overshoots (or ringing) are observed at the discontinuities due to the Gibbs phenomenon [64]. However, the use of higher harmonics increases the computational time significantly and has less impact on increment in accuracy. Thus, the selection of the number of harmonics is a trade-off between the required accuracy and computational time. Moreover, this selection also depends on the value of τ_{X} and τ_{Y}. For the higher value of τ_{X} and τ_{Y},

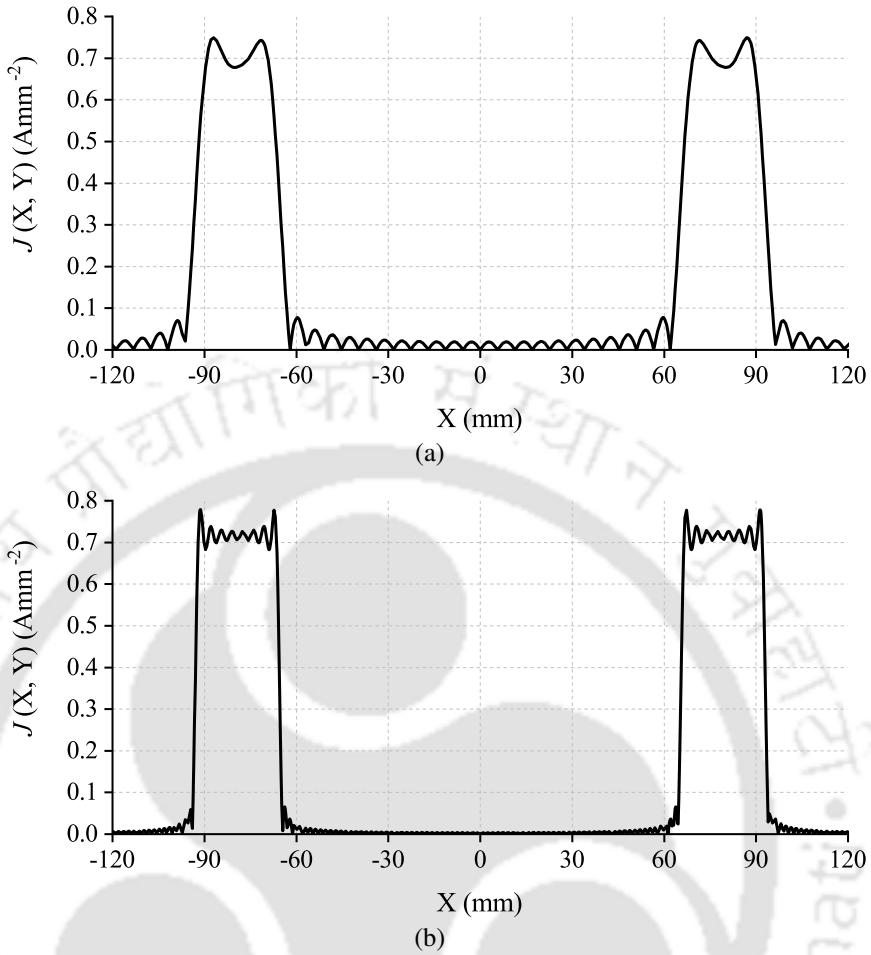

Figure 3.6: Cross section along the X-axis at Y = 0 of J (X, Y) shown in Figure 3.5 at the number of harmonics (a) $U = W = 140$ and (b) $U = W = 560$ (four times of 140). Here, an overshoot (or ringing) at a discontinuity is due to the Gibbs phenomenon [64].

the higher number of harmonics is required to achieve the ideal current density profile. Therefore, in this chapter, with $\tau_X = 5x$ and $\tau_Y = 5y$, the number of harmonics in the X- and Y-directions (i.e., U and W) are taken 140. By using these current density descriptions, the magnetic vector and magnetic scalar potentials are formulated in different regions in the next subsection.

3.2.3 Magnetic Field Description

This subsection presents the magnetic field description in Regions I, II and III. Further, it gives the expression to calculate the B-field in different regions.

3.2.3.1 Regions I and III

Regions I and III, which are below and above to the Tx coil, are the air medium, as shown in Figure 3.1. Since the current source is absent in these regions, the scalar magnetic potential is used

for describing the magnetic field density in both regions. The magnetic field intensity **H** is given by (3.6).

$$\mathbf{H} = -\nabla\varphi \tag{3.6}$$

where φ is a scalar magnetic potential. The solution of the scalar magnetic potential in Regions I and III are derived using the method of separation of variables and are given by (3.7) and (3.8), respectively.

$$\varphi_I = \sum_{u=1,3,5}^{U}\sum_{w=1,3,5}^{W} c_I e^{k_Z Z}\cos(k_X X)\cos(k_Y Y) \tag{3.7}$$

$$\varphi_{III} = \sum_{u=1,3,5}^{U}\sum_{w=1,3,5}^{W} c_{III} e^{-k_Z Z}\cos(k_X X)\cos(k_Y Y) \tag{3.8}$$

where $k_Z = \sqrt{{k_X}^2 + {k_Y}^2}$ and c_I and c_{III} are the unknown coefficients, which are determined using the boundary conditions (given in Section 3.2.4). The magnetic flux density **B** is obtain by (3.9)

$$\mathbf{B} = \mu_0\mathbf{H}. \tag{3.9}$$

where μ_0 is the permeability of free space, and its value is equal to $4\pi \times 10^{-7}$ henries per meter (H/m).

3.2.3.2 Region II

The current source is present in Region II; therefore, magnetic vector potential is used to describe the magnetic flux density **B** and is given by (3.10).

$$\mathbf{B} = \nabla \times \mathbf{A}. \tag{3.10}$$

The direction of the magnetic vector potential **A** is in the direction of the current. The Poisson and Laplace equations are solved using the method of separation of variables [47–49], as given in (3.11), to obtain the magnetic vector potential in this region.

$$\begin{cases} \nabla^2 A_X^{II}(X,Y,Z) = -\mu_0 J_X^{total}(X,Y) \\ \nabla^2 A_Y^{II}(X,Y,Z) = -\mu_0 J_Y^{total}(X,Y) \\ \nabla^2 A_Z^{II}(X,Y,Z) = 0. \end{cases} \tag{3.11}$$

Since the current source is absent in the Z-direction, the magnetic vector potential is zero. The

solution of (3.11) is given in (3.12) - (3.14).

$$A_{\mathrm{X}}^{II} = -\sum_{u=1,3,5}^{U}\sum_{w=1,3,5}^{W}\left(c_1^{II}\mathrm{e}^{k_{\mathrm{Z}}\mathrm{Z}} + c_2^{II}\mathrm{e}^{-k_{\mathrm{Z}}\mathrm{Z}} + \frac{\mu_0 j_{\mathrm{X}}^{total}}{{k_{\mathrm{Z}}}^2}\right)\sin\left(k_{\mathrm{Y}}\mathrm{Y}\right)\cos\left(k_{\mathrm{X}}\mathrm{X}\right) \tag{3.12}$$

$$A_{\mathrm{Y}}^{II} = \sum_{u=1,3,5}^{U}\sum_{w=1,3,5}^{W}\left(c_3^{II}\mathrm{e}^{k_{\mathrm{Z}}\mathrm{Z}} + c_4^{II}\mathrm{e}^{-k_{\mathrm{Z}}\mathrm{Z}} + \frac{\mu_0 j_{\mathrm{Y}}^{total}}{{k_{\mathrm{Z}}}^2}\right)\sin\left(k_{\mathrm{X}}\mathrm{X}\right)\cos\left(k_{\mathrm{Y}}\mathrm{Y}\right) \tag{3.13}$$

$$A_{\mathrm{Z}}^{II} = 0 \tag{3.14}$$

where A_{X}^{II}, A_{Y}^{II}, and A_{Z}^{II} are the magnetic vector potentials of Region II in the direction of X, Y, and Z, respectively. The coefficients c_1^{II}, c_2^{II}, c_3^{II}, and c_4^{II} are unknown, which are determined using the boundary conditions (given in Section 3.2.4).

By solving (3.9) and (3.10), the final expression of B-field in different regions is obtained and given in the next subsubsection.

3.2.3.3 Expression of Magnetic Field Density in Different Regions

The expression for X-, Y-, and Z-components of the B-field in Region II, i.e., B_{X}^{II}, B_{Y}^{II}, and B_{Z}^{II}, respectively, is given as

$$B_{\mathrm{X}}^{II} = \sum_{u=1,3,5}^{U}\sum_{w=1,3,5}^{W} k_{\mathrm{Z}}\left(c_4^{II}e^{-k_{\mathrm{Z}}\mathrm{Z}} - c_3^{II}e^{k_{\mathrm{Z}}\mathrm{Z}}\right)\sin\left(k_{\mathrm{X}}\mathrm{X}\right)\cos\left(k_{\mathrm{Y}}\mathrm{Y}\right) \tag{3.15}$$

$$B_{\mathrm{Y}}^{II} = \sum_{u=1,3,5}^{U}\sum_{w=1,3,5}^{W} k_{\mathrm{Z}}\left(c_2^{II}e^{-k_{\mathrm{Z}}\mathrm{Z}} - c_1^{II}e^{k_{\mathrm{Z}}\mathrm{Z}}\right)\sin\left(k_{\mathrm{Y}}\mathrm{Y}\right)\cos\left(k_{\mathrm{X}}\mathrm{X}\right) \tag{3.16}$$

$$B_{\mathrm{Z}}^{II} = \sum_{u=1,3,5}^{U}\sum_{w=1,3,5}^{W}\left(k_{\mathrm{X}}\left(c_1^{II}e^{k_{\mathrm{Z}}\mathrm{Z}} + c_2^{II}e^{-k_{\mathrm{Z}}\mathrm{Z}} + \frac{\mu_0 j_{\mathrm{Y}}^{total}}{k_{\mathrm{Z}}^2}\right) + k_{\mathrm{Y}}\left(c_3^{II}e^{k_{\mathrm{Z}}\mathrm{Z}} + c_4^{II}e^{-k_{\mathrm{Z}}\mathrm{Z}} + \frac{\mu_0 j_{\mathrm{X}}^{total}}{k_{\mathrm{Z}}^2}\right)\right) \cdot\cos\left(k_{\mathrm{X}}\mathrm{X}\right)\cos\left(k_{\mathrm{Y}}\mathrm{Y}\right) \tag{3.17}$$

and the same in Region III, i.e., B_{X}^{III}, B_{Y}^{III}, and B_{Z}^{III}, respectively, is given by

$$B_{\mathrm{X}}^{III} = \sum_{u=1,3,5}^{U}\sum_{w=1,3,5}^{W}\mu_0 c_{III}k_{\mathrm{X}}e^{-k_{\mathrm{Z}}\mathrm{Z}}\sin\left(k_{\mathrm{X}}\mathrm{X}\right)\cos\left(k_{\mathrm{Y}}\mathrm{Y}\right) \tag{3.18}$$

$$B_{\mathrm{Y}}^{III} = \sum_{u=1,3,5}^{U}\sum_{w=1,3,5}^{W}\mu_0 c_{III}k_{\mathrm{Y}}e^{-k_{\mathrm{Z}}\mathrm{Z}}\cos\left(k_{\mathrm{X}}\mathrm{X}\right)\sin\left(k_{\mathrm{Y}}\mathrm{Y}\right) \tag{3.19}$$

$$B_{\mathrm{Z}}^{III} = \sum_{u=1,3,5}^{U}\sum_{w=1,3,5}^{W}\mu_0 c_{III}k_{\mathrm{Z}}e^{-k_{\mathrm{Z}}\mathrm{Z}}\cos\left(k_{\mathrm{X}}\mathrm{X}\right)\cos\left(k_{\mathrm{Y}}\mathrm{Y}\right) \tag{3.20}$$

where the coefficients c_1^{II}, c_2^{II}, c_3^{II}, c_4^{II}, and c_{III} are determined using the boundary conditions, which are discussed in the next subsection.

3.2.4 Boundary Conditions

The unknown coefficients of magnetic scalar potential and magnetic vector potential in all regions are determined using the boundary conditions [48]. The boundary conditions are applied at the boundaries Z = 0 and Z = d_w, where medium changes, as shown in Figure 3.1. The set of the boundary conditions are listed in (3.21).

$$\begin{aligned} H_{\mathrm{X}}^{I}(\mathrm{X},\mathrm{Y},0) &= H_{\mathrm{X}}^{II}(\mathrm{X},\mathrm{Y},0) \\ H_{\mathrm{Y}}^{I}(\mathrm{X},\mathrm{Y},0) &= H_{\mathrm{Y}}^{II}(\mathrm{X},\mathrm{Y},0) \\ B_{\mathrm{Z}}^{I}(\mathrm{X},\mathrm{Y},0) &= B_{\mathrm{Z}}^{II}(\mathrm{X},\mathrm{Y},0) \\ H_{\mathrm{X}}^{II}(\mathrm{X},\mathrm{Y},d_w) &= H_{\mathrm{X}}^{III}(\mathrm{X},\mathrm{Y},d_w) \\ H_{\mathrm{Y}}^{II}(\mathrm{X},\mathrm{Y},d_w) &= H_{\mathrm{Y}}^{III}(\mathrm{X},\mathrm{Y},d_w) \\ B_{\mathrm{Z}}^{II}(\mathrm{X},\mathrm{Y},d_w) &= B_{\mathrm{Z}}^{III}(\mathrm{X},\mathrm{Y},d_w). \end{aligned} \tag{3.21}$$

Based on the boundary conditions given in (3.21), six equations are formed, which are given in Appendix B. By solving those six equations (see Appendix B), the final expression of unknown coefficients is obtained as

$$\begin{cases} c_I = 0.5k_{\mathrm{Z}}^{-3}(1-e^{-k_{\mathrm{Z}}d_w})\left(j_{\mathrm{X}}^{total}k_{\mathrm{Y}} + j_{\mathrm{Y}}^{total}k_{\mathrm{X}}\right) \\ c_1^{II} = 0.5\mu_0 k_{\mathrm{Y}}k_{\mathrm{Z}}^{-4}e^{-k_{\mathrm{Z}}d_w}\left(j_{\mathrm{X}}^{total}k_{\mathrm{Y}} + j_{\mathrm{Y}}^{total}k_{\mathrm{X}}\right) \\ c_2^{II} = 0.5\mu_0 k_{\mathrm{Y}}k_{\mathrm{Z}}^{-4}\left(j_{\mathrm{X}}^{total}k_{\mathrm{Y}} + j_{\mathrm{Y}}^{total}k_{\mathrm{X}}\right) \\ c_3^{II} = 0.5\mu_0 k_{\mathrm{X}}k_{\mathrm{Z}}^{-4}e^{-k_{\mathrm{Z}}d_w}\left(j_{\mathrm{X}}^{total}k_{\mathrm{Y}} + j_{\mathrm{Y}}^{total}k_{\mathrm{X}}\right) \\ c_4^{II} = 0.5\mu_0 k_{\mathrm{X}}k_{\mathrm{Z}}^{-4}\left(j_{\mathrm{X}}^{total}k_{\mathrm{Y}} + j_{\mathrm{Y}}^{total}k_{\mathrm{X}}\right) \\ c_{III} = 0.5k_{\mathrm{Z}}^{-3}(e^{k_{\mathrm{Z}}d_w}-1)\left(j_{\mathrm{X}}^{total}k_{\mathrm{Y}} + j_{\mathrm{Y}}^{total}k_{\mathrm{X}}\right). \end{cases} \tag{3.22}$$

The expression for calculating the self- and mutual inductance of (rectangular or square) coils is given in the next subsection.

3.2.5 Calculation of Self- and Mutual Inductance of Coils

To calculate the self-inductance of the coil, the B-field of Region II (obtained from (3.17)) is integrated over the surface of the Tx coil at Z = r_w for each turn:

$$L_P = \frac{1}{I_P} \sum_{q=1}^{\text{Total turns}} \int_{S_q} B_Z^{II} \, d\text{S}|_{Z=r_w} \tag{3.23}$$

where S_q is the surface area of q^{th} turn, and $q = 1$ represents the outermost turn of the coil. By applying integration limits in (3.23), it can be written in the following form

$$L_P = \frac{1}{I_P} \left[\sum_{q=1}^{\text{N}} \int_{-(b_2-G)}^{(b_2-G)} \int_{-(a_2-G)}^{(a_2-G)} B_Z^{II} \, d\text{X} d\text{Y} \right]_{Z=r_w} \tag{3.24}$$

where N is the total number of turns (since $N_P = N_S$, it is represented as N) and $G = (T_g + d_w)(q - 1) + 0.5d_w$. Here, T_g is the gap between the turns in conventional coil structures and is equal to $p \cdot d_w$, where p can be any integer or noninteger number.

The mutual inductance is calculated by integrating the B-field in Region III (obtained from (3.20)) over the surface of the Rx coil at Z = ($3d_w/2$ + Air gap) for each turn:

$$M = \frac{1}{I_P} \sum_{q=1}^{\text{Total turns}} \int_{S_g} B_Z^{III} \, d\text{S}|_{\text{Z}=(3d_w/2)+\text{Air gap}}. \tag{3.25}$$

Further, by applying integration limits in (3.31), (3.31) becomes

$$M = \frac{1}{I_P} \left[\sum_{q=1}^{\text{N}} \int_{-(b_2-G)}^{(b_2-G)} \int_{-(a_2-G)}^{(a_2-G)} B_Z^{III} \, d\text{X} d\text{Y} \right]_{\text{Z}=(3d_w/2)+\text{Air gap}}. \tag{3.26}$$

Thus, by using (4.6), the mutual inductance between the coils can be calculated at any air gap (or can say, at different ΔZ). Further, by using (4.5) and (4.6) in (2.1), the factor k of conventional coils can be calculated.

The accuracy of the developed 3-D analytical model is verified using the measurements and 3-D FEA in the next section.

3.3 Experimental Verification

This section explains the experimental setup used to measure the magnetic field generated by the Tx coil. Then, it compares the analytical results with the measurement and 3-D FEA simulation

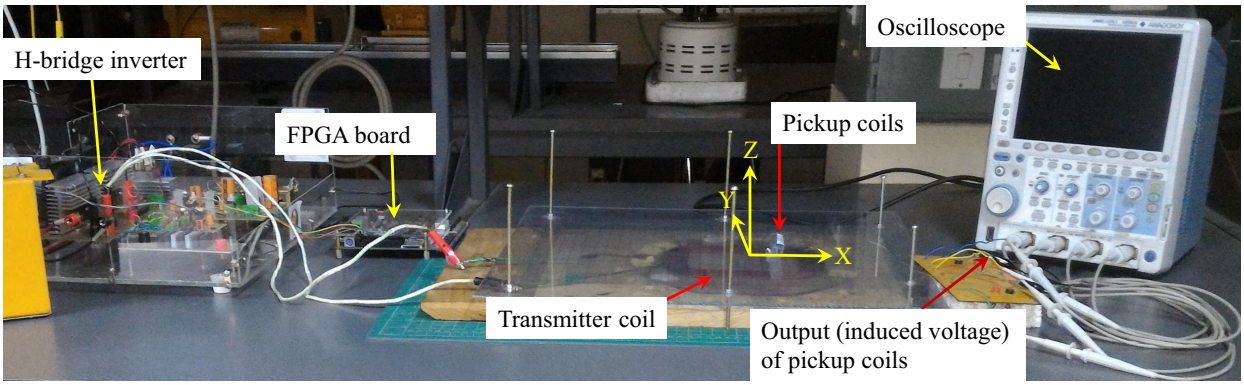

Figure 3.7: Experimental setup for the measurement of B_X, B_Y and B_Z in Region III.

results to verify the accuracy of the developed 3-D analytical model.

3.3.1 Experiment Setup

Figure 3.7 shows the developed experimental setup to measure the X-, Y-, and Z-components of B-field in Region III (Rx coil zone). The experimental setup consists of an HF H-bridge voltage source inverter, a rectangular coil, four pickup coils, an arrangement for measuring the coordinates of these pickup coils, and an oscilloscope (Yokogawa). The rectangular coil is made using the Litz wire (with 56 insulated strands), having 11 turns of AWG#32 copper wire. With this wire, the skin effect does not occur up to 400-kHz, hence, the uniform current distribution can be assumed over the cross-section of the Litz wire below the 400-kHz operating frequency. This coil is excited with a sinusoidal current of 150-kHz (other frequency up to 400-kHz can also be chosen), which is obtained using HF H-bridge inverter. The gate pulses of H-bridge inverter is given form Altera cyclone II field-programmable gate array (FPGA) board. The programming code to generate these pulses is provided in Appendix B. For measuring the generated magnetic field of this coil, induced EMF at different locations (in Region III) is recorded using the pickup coils. A total of four cylindrical pickup coils are used for this purpose due to available (four) channels in the oscilloscope to use at a time. All pickup coils are having a radius of 2 mm and a height of 4 mm. These pickup coils are made using AWG#40 copper wire. By using this wire, a total of 200 number of turns are wound on each pickup coil. The higher number of turns minimises the contribution of noise EMF during the induced EMF measurements, but at the same time, it increases the area of the pickup coils, which is undesirable. Therefore, a balance between the total number of turns (with the selected wire) and the area covered

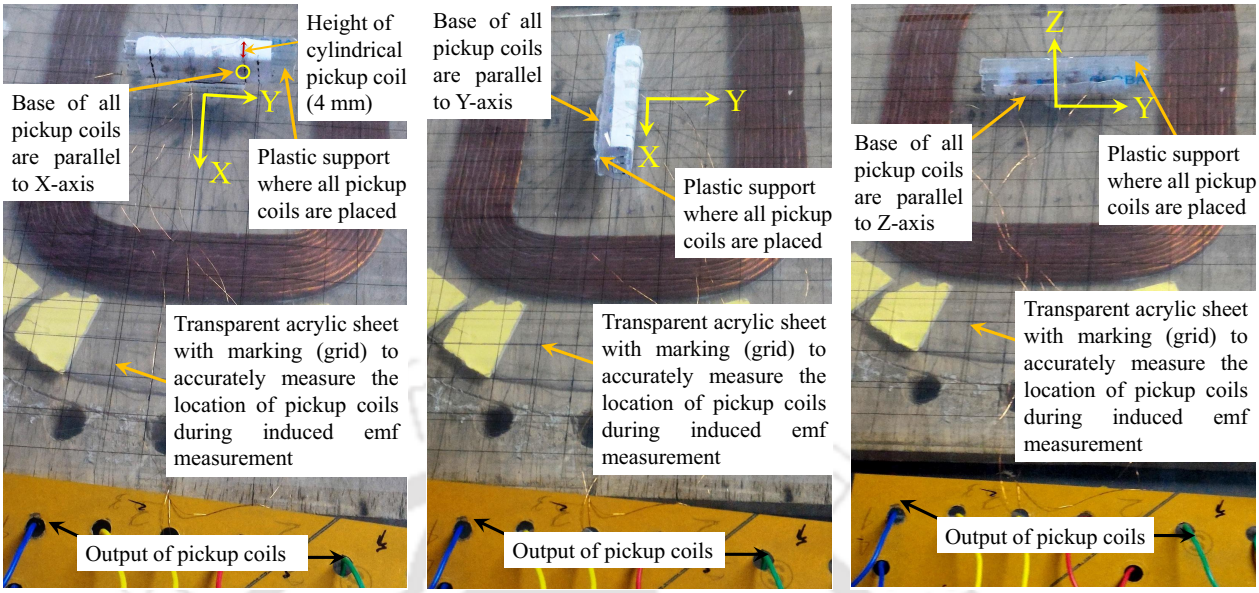

Figure 3.8: The arrangement for measuring the coordinates of pickup coils at which the induced EMF is recorded for (a) B_{X}^{III}, (b) B_{Y}^{III}, and (c) B_{Z}^{III} measurements.

is needed, which should be taken care of at the time of designing the pickup coils.

Figure 3.8 shows the constructed arrangement for measuring the coordinates of pickup coils while recording the induced EMF for the measurement of B_{X}^{III}, B_{Y}^{III}, and B_{Z}^{III}. The constructed arrangement has a grid with multiple cells, which is made on a transparent paper and has been glued on a transparent acrylic sheet. The size of each cell is designed in such a way that the coordinates of four pickup coils can be obtained together. For this, plastic support is used to mount all pickup coils, and the distance between each pickup coil is kept 10 mm. Thus, the possibility of error in the measurement of the coordinates is minimised at which the data are recorded. The main difference between Figure 3.8(a)-(c) is the orientation of pickup coils. According to the measurement of X-, Y-, and Z-components of B-field, the orientation of these pickup coils are chosen, as shown in Figure 3.8(a)-(c). The forthcoming subsection discusses the calculation of B-fields from the induced EMF and compares the 3-D analytical results with the measurements and 3-D FEA.

3.3.2 Experimental Results and Analytical Model Verification

The X-, Y-, and Z-components of B-field are calculated using the flowchart given in Figure 3.9. The explanation of this flowchart (Figure 3.9) is given in Appendix B. Here, for each component, induced EMF is measured at different points using the arrangements shown in Figure 3.8(a)-(c).

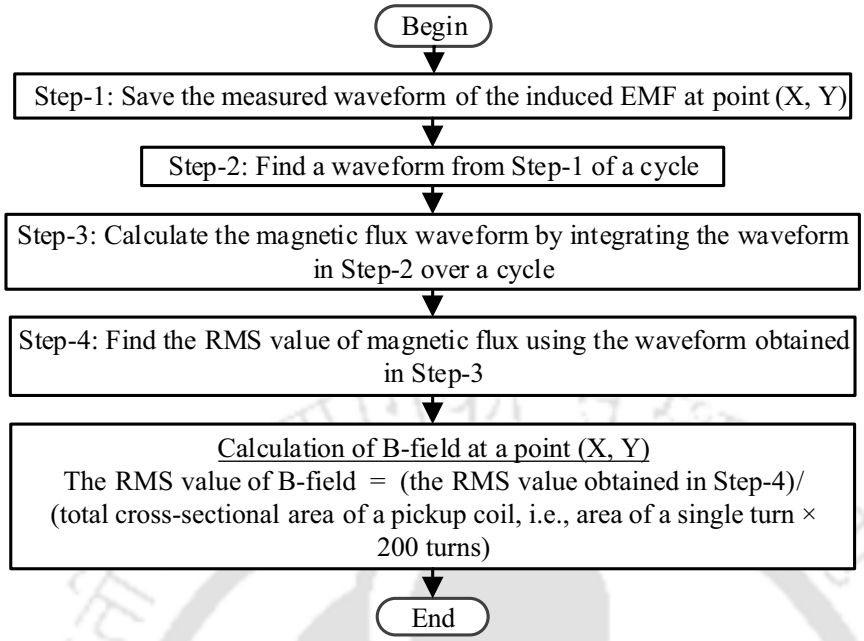

Figure 3.9: Flowchart for calculating the B-field at a point (X, Y) using the measured induced waveform. Note that, for different points, the given procedure needs to be repeated.

Figure 3.10 compares the 3-D graph of B_X at Z = 20 mm (i.e., in Region III) obtained from the calculation (using (3.19)), simulation, and measurement. The developed 3-D model of a rectangular coil for magnetic simulation in FEA software ANSYS Maxwell is explained in Appendix B. The 3-D graphs in Figure 3.10 are following the same pattern and magnitude as well. However, an uneven surface is seen in some places in the measured 3-D graph (Figure 3.10(c)). Since the data are recorded at a gap of 10 mm, fewer data points are received at the higher magnitude coordinates that form an uneven surface. Further, near the zero magnetic field (green part) area, the uneven surface is due to the more influence of noise EMF on the recorded induced EMF. Figure 3.11 shows the cross-section of B_X^{III} (given in Figure 3.10) along the X-axis at Y = 0. A good agreement can be seen among the analytical, simulation, and experimental results. In Figure 3.11, the analytical curve shows that B_X is zero within the τ_X limit. Moreover, from Figure 3.10(a), it can be seen that the B_X is zero along the Y-axis at X = 0. It shows that the fictitious coils do not influence the B-field of the working coil in the X-direction.

Figure 3.12 shows the comparison of the 3-D graph of B_Y at Z = 20 mm obtained from the calculation (using (3.20)), simulation, and measurement. Here, the 3-D graphs, obtained from analytical and simulation, are in good agreement, but in the measured 3-D graph, a slight variation in the mag-

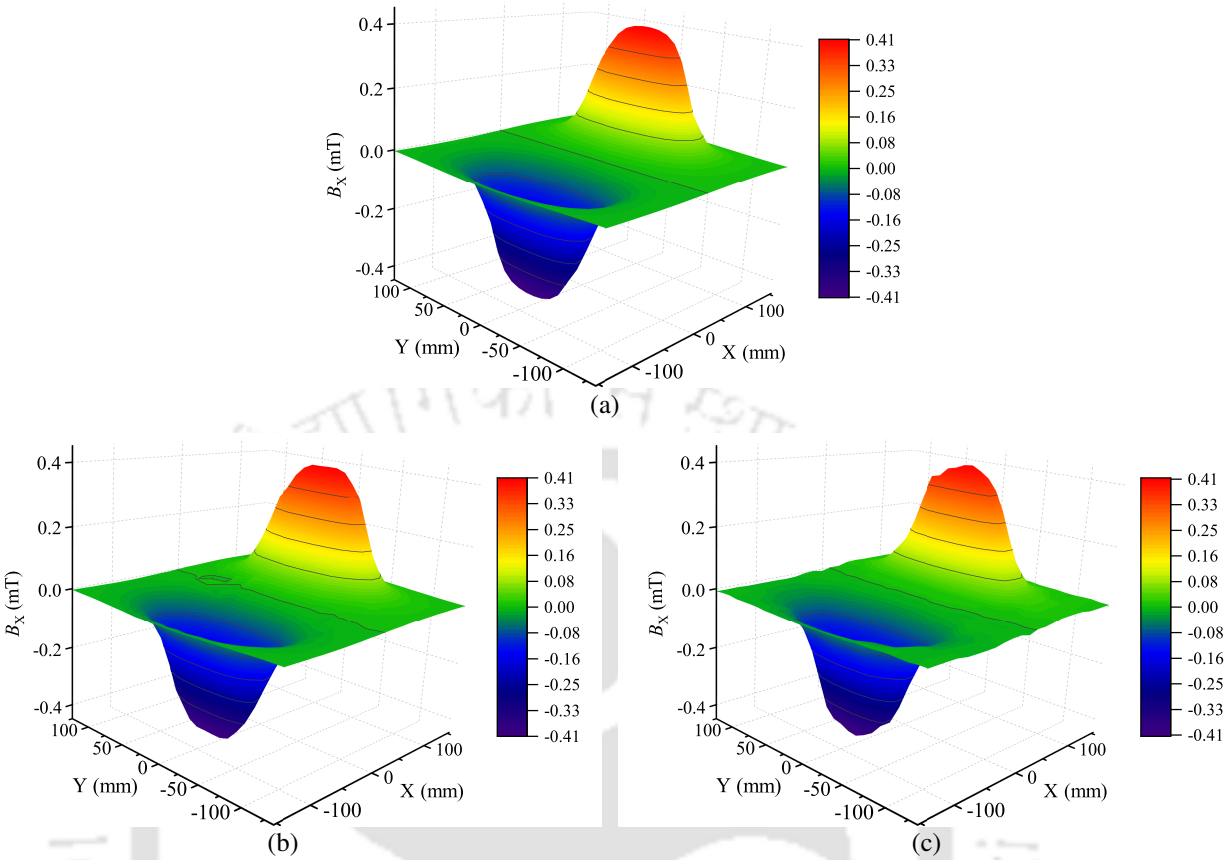

Figure 3.10: 3-D graph of B_X at Z = 20 mm (i.e., in Region III) obtained from (a) 3-D analytical model (using (3.19)), (b) 3-D FEA, and (c) measurement.

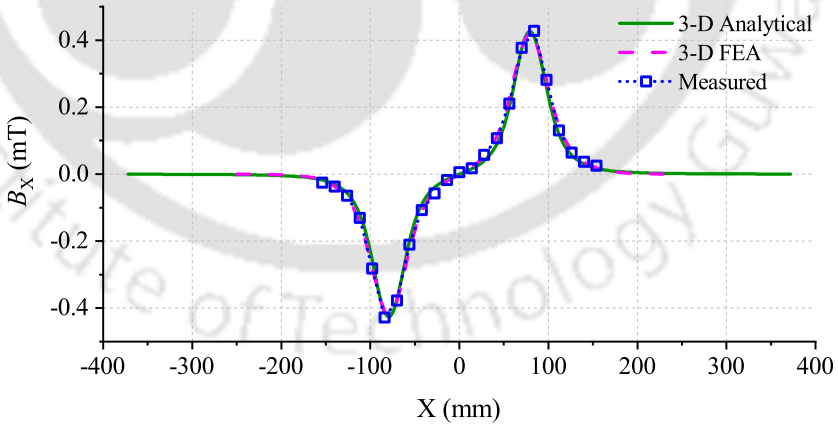

Figure 3.11: Cross-section of Figure 3.10 along the X-axis at Y = 0.

nitude is noticed at some points compared with the analytical graph. The reason for this difference is the same as that for measured B_X. The cross-section of Figure 3.12 along the Y-axis at X = 0 is depicted in Figure 3.13. In Figure 3.13, the analytical curve shows that B_Y is zero within the τ_Y limit. Moreover, from Figure 3.14(a), it can be seen that B_Y has a zero magnitude along the X-axis at Y =

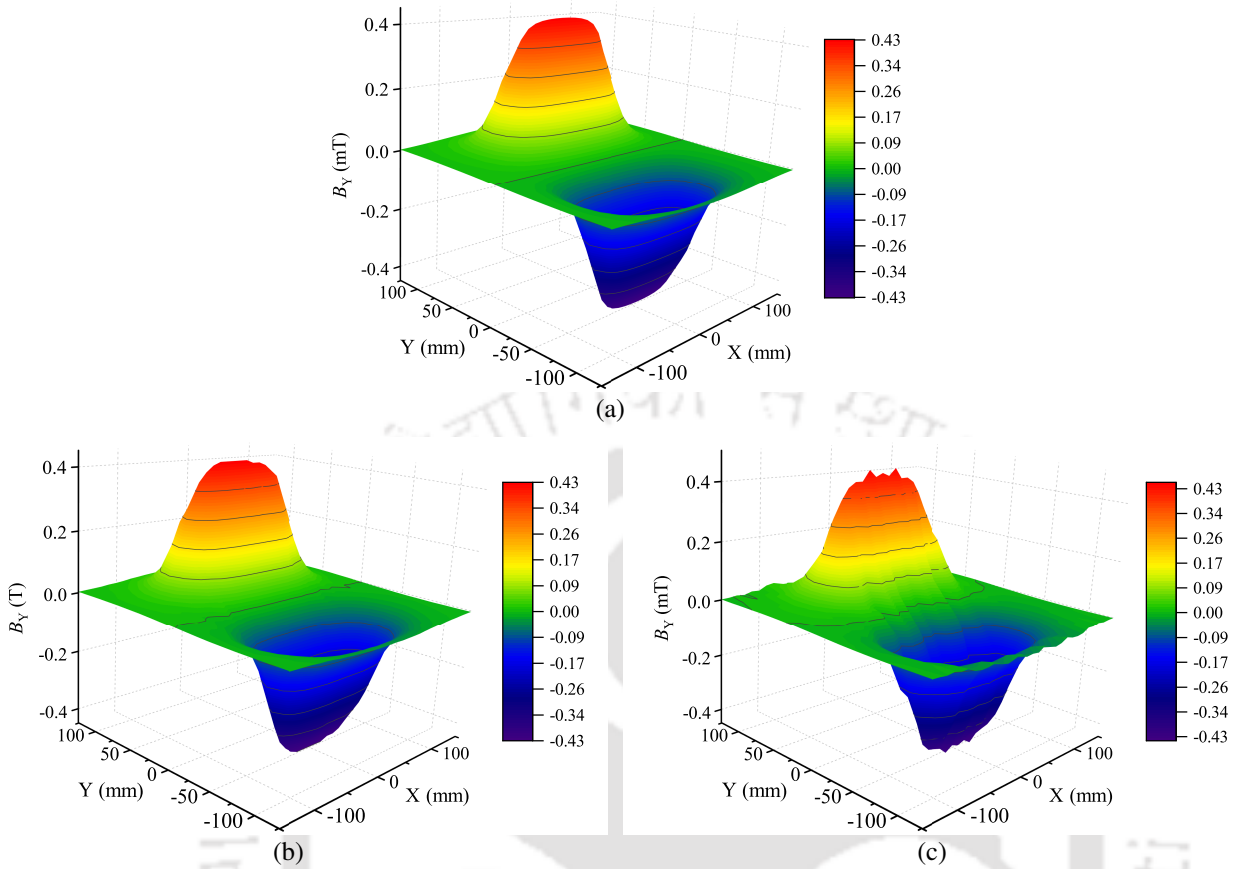

Figure 3.12: 3-D graph of B_Y at Z = 20 mm obtained from (a) 3-D analytical model (using (3.20)), (b) 3-D FEA, and (c) measurement.

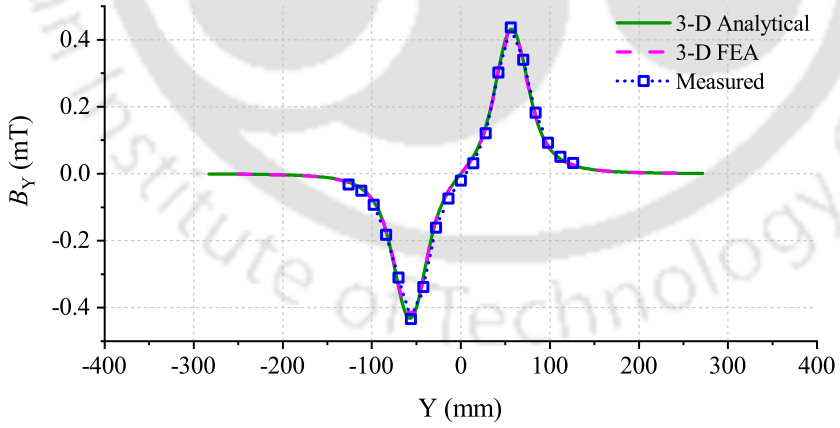

Figure 3.13: Cross-section of Figure 3.12 along the Y-axis at X = 0.

0. It shows that the fictitious coils do not influence the B-field of the working coil in the Y-direction.

Figure 3.14 gives the comparison of the 3-D graph of B_Z at Z = 20 mm obtained from the calculation (using (3.20)), simulation, and measurement. Again, the simulated and analytically calculated graphs show a good agreement. However, in the measured graph (Figure 3.14(c)), the increased mag-

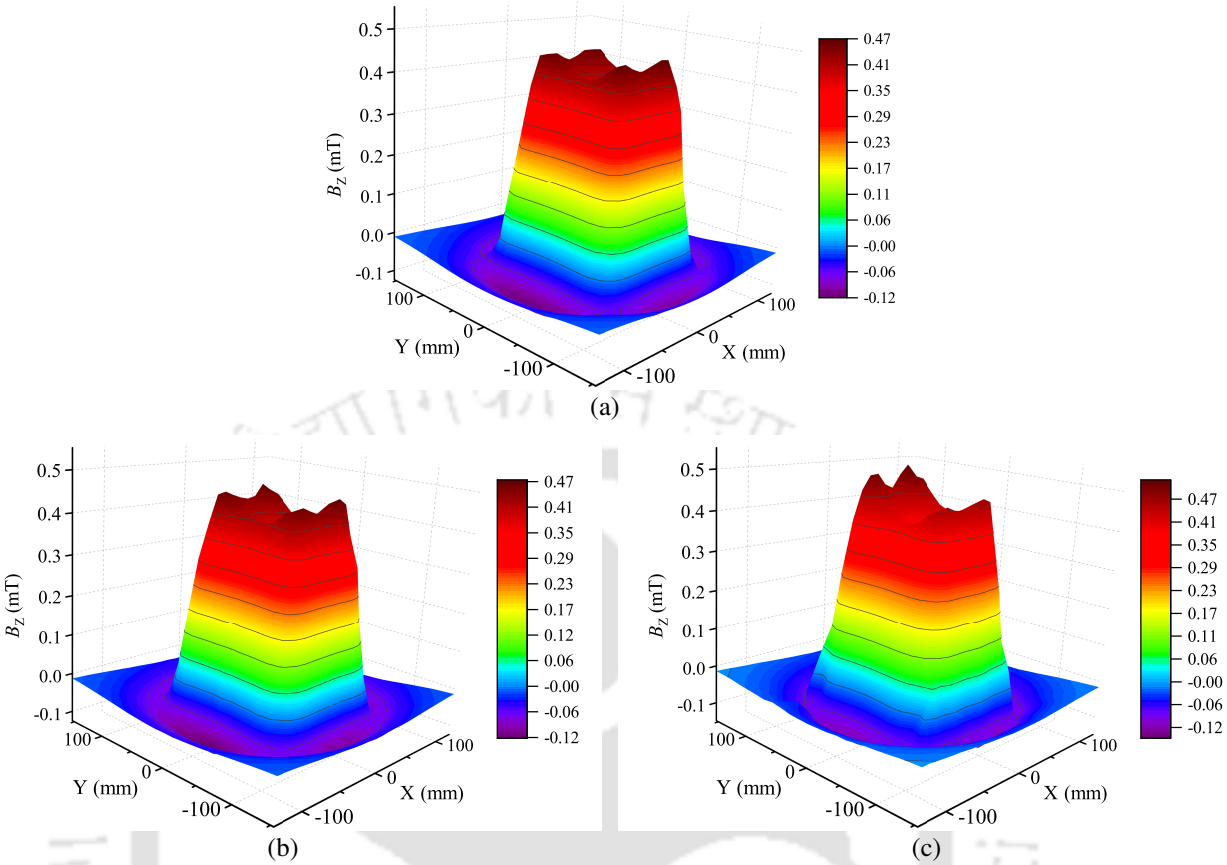

Figure 3.14: 3-D graph of B_Z at Z = 20 mm obtained from (a) 3-D analytical model (using (3.20)), (b) 3-D FEA, and (c) measurement.

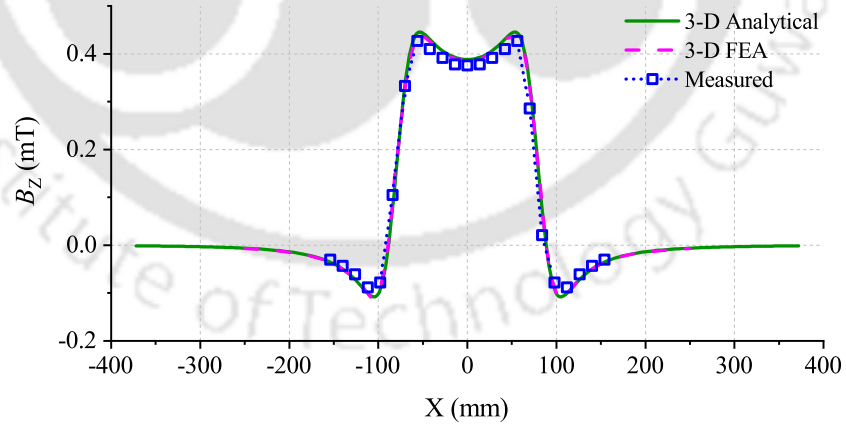

Figure 3.15: Cross-section of Figure 3.14 along the X-axis at Y = 0.

nitude at two corners is seen, which are located along X-axis at Y = 100 mm. Figure 3.15 shows the cross-section of Figure 3.14 along the X-axis at Y = 0. Here, the 3-D analytical and 3-D FEA curves are in good agreement, whereas measured has a slight deviation with respect to the other curves. Figure 3.16 gives the cross-section of Figure 3.14 along the Y-axis at X = 0. Here, all the curves are

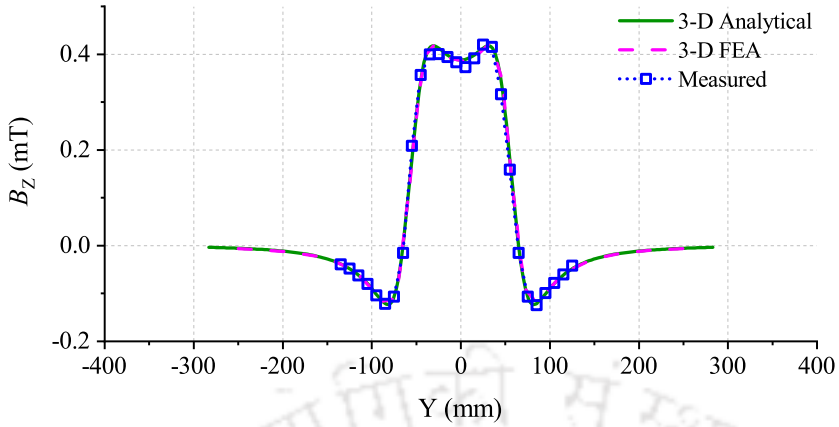

Figure 3.16: Cross-section of Figure 3.14 along the Y-axis at X = 0.

following the same pattern. From Figures 3.15 and 3.16, it can be seen that B_Z is zero within the τ_X and τ_Y limits, respectively. Hence, it can be said that the fictitious coils do not influence the B-field of the working coil in the X- and Y-directions with the chosen τ_X and τ_Y (given in Table 4.1).

Furthermore, the measured value of L_P is 29.73 μH, which matches with the calculated (3-D analytical using (4.5); 29.86 μH) and simulated (3-D FEA; 29.76 μH) results.

Apart from the inductance calculation, coil's AC resistance is also a part of the coil design, which is needed in evaluating the system performance. In this context, the calculation of the AC resistance of the coil is presented in the next section.

3.4 AC Resistance Calculation of the Coil

The AC resistance of a coil contains the dc resistance, skin-effect resistance, and proximity-effect resistance. The use of Litz wire eliminates the skin-effect loss in the winding, but the proximity-effect loss needs to consider [65]. Therefore, the AC resistance of the Tx (or Rx) coil R_P (or R_S) is given by

$$R_P = R_{dc,P} + R_{pe,P} \tag{3.27}$$

where $R_{pe,P}$ is the total proximity-effect resistance of the Tx coil and $R_{dc,P}$ is the total dc resistance of the Tx coil. The dc resistance (R_{dc}) of a turn is given by

$$R_{dc} = \frac{4\rho_c l_t}{\pi N_s d_s^2} \tag{3.28}$$

where N_s is the total number of strands, d_s is the diameter of the strand, ρ_c is the resistivity of copper, and l_t is the mean length of the turn, which is given by

$$l_t = 4\left(a_1 + b_1 + \frac{\pi}{2}\left(\left(T_g + d_w\right)(q_t - 1) + \frac{d_w}{2}\right)\right). \tag{3.29}$$

where $q_t = 1$ represents the innermost turn of the coil. Due to twisting in the Litz wire, the length of the individual strands per unit length is increased. Hence, l_t should be taken-up by $c\%$, which is determined based on the dc resistance measurement of a length of the Litz wire used (here, c is 5) [66]. The proximity-effect resistance R_{pe} (in strand level) of a turn is given by [65]

$$R_{pe} = \frac{\pi\omega^2 l_t N_s d_s^2}{128\rho_c I_{peak}^2} \cdot \langle B_{peak}^2 \rangle \tag{3.30}$$

where B_{peak} is the peak value of magnetic field across the turn generated by the peak current I_{peak} in the coil, and $\langle * \rangle$ is the spatial average over the turn's cross section [65]. In this work, $\langle B_{peak}^2 \rangle$ is calculated using simulation in ANSYS Maxwell.

With this 3-D analytical model and the given AC resistance calculation, the upcoming section studies the possible approaches to improve k of the conventional coils for EV applications and examines the impact of the improved k (obtained using different approaches) on the system performance of WPT.

3.5 Various Possible Approaches for Improving the factor k of the Conventional Coils: Study and Analysis

This section investigates the different possible approaches for improving the factor k of the conventional coils for EV applications. Section 3.5.1 presents the example of input parameters required in an EV application, which is used to study and analyse the improvement in k and examine the system performance. Section 3.5.2 explains the various possible approaches to improve the coupling k with the physical constraints applied in EV application (as discussed in Section 3.1). Section 3.5.3 analyses the impact of improved k (by different approaches) on the system performance to find the best approach(es). Further, it summarises the overall constraints, which need to be considered while attempting further improvement in k.

Table 3.2: Parameter values of the required coil system.

x mm × y mm	L_{req} (μH)	d_w (mm)	air gap (mm)
400 × 300	80.5	2.7	150

3.5.1 Input Parameters (taken for an EV application) for Improving the Factor k

For this study and analysis, this work uses unipolar rectangular coils for electric scooter (one of the EV application) charging because of the advantages of rectangular shape [40, 41, 58]. Since the same area of the Tx and Rx coils gives the best coupling [25], the outer dimensions of the Tx and Rx coils are taken same, which is 400 mm × 300 mm (due to the space limitation, as discussed in Section 3.1). The air gap (distance between Tx and Rx) is kept at 150 mm. The value of required self-inductance (L_{req}) is 80.5 μH for both Tx and Rx coils (for simplicity, assuming $L_P = L_S = L_{req}$). The Litz wire of 2.7-mm diameter (d_w) having 100 strands of 0.193-mm diameter that gives a total cross-sectional area of 2.93 mm^2 is used. The parameter values of the required coil system are summarised in Table 3.2. The parameter values in Table 3.2 could be different, and they depend on the designer's requirement (for their targeted application). I_P is set to 10 A by considering a current density of 4 A/mm^2 [31]. For showing the impact of improved k (using different approaches) on S_{max} and transmission efficiency, the 100-kHz operating frequency is selected. However, the operating frequency can also be taken according to SAE J2954 standards.

For the parameter values given in Table 3.2, the possible approaches for improving the factor k are studied and analysed in the next subsection.

3.5.2 Possible Approaches for Improving the Factor k

To understand the possible approaches of improving k, the expression (2.1) is simplified by replacing $L_P = L_S = L_{req}$ as

$$k = \frac{M}{L_{req}}. \tag{3.31}$$

From (3.31), for a fixed air gap (here, 150 mm), the factor k can be improved by following approaches:

(A). increasing the value of M while keeping the value of L_{req} constant;

(B). decreasing the value of L_{req} while keeping the value of M constant;

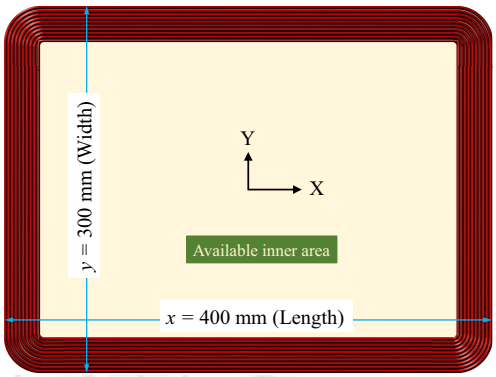

Figure 3.17: type-I conventional coil structure (of rectangular shape) of 400 mm × 300 mm outer dimensions.

(C). decreasing the value of L_{req} and increasing the value of M.

Before going into each approach, at first, a reference coil system is built using a conventional coil arrangement method (CCAM) so that the percentage of improvement in k can be tracked. Generally, in CCAM, the wires are spirally wound in a planar coil structure, and each turn has equal spacing between turns. The unipolar coils, designed using this method, are categorised as conventional coils.

With the parameter values in Table 3.2, a conventional coil system is designed using CCAM with zero spacing between the turns (i.e., $T_g = 0 \cdot d_w$), as shown in Figure 3.17, and it is named type-I. This coil system is widely used in WPT [1, 24, 30, 32, 34, 35, 38, 40, 58, 59, 63, 67]. With this coil system, k at the 150-mm air gap is 0.1339. The other coil parameters of the type-I coil system are presented in tables of each approach of improving k for ease in comparison. In each approach (explained below), the wire diameter and physical constraints, such as outer dimensions of the coils and the selected air gap, are kept the same.

(A). Improving the Factor k by Increasing the Value of M while Keeping the Value of L_{req} Constant

For improving k with this approach, the self-inductance of the type-I coil system is taken as a reference, which is 80.50 μH. By keeping the self-inductance unchanged, the coupling k is improved by increasing the mutual inductance M. In this context, for the same outer dimensions, the number of turns is increased. However, increasing the number of turns increases the value of self-inductance. Therefore, to maintain the self-inductance, the gap between the turns has been increased for each increment in turn (N). The obtained coil systems using this approach is named type-S# (where # is

Table 3.3: Parameter values of the conventional coils obtained using the approach **(*A*).**

Parameter		Name of coil system						
		type-I	type-S1	type-S2	type-S3	type-S4	type-S5	type-S6
T_g (mm)		$0 \cdot d_w$	$0.4 \cdot d_w$	$0.76 \cdot d_w$	$1.01 \cdot d_w$	$1.21 \cdot d_w$	$1.37 \cdot d_w$	$1.58 \cdot d_w$
Number of turns (N)		10	11	12	13	14	15	18
L_P, L_S (μH)	3-D Anyl*	80.50, 80.50	80.49, 80.49	79.96, 79.96	80.49, 80.49	80.41, 80.41	80.37, 80.37	81.02, 81.02
	3-D FEA	80.30, 80.80	80.85, 80.70	80.18, 80.25	80.72, 80.68	80.76, 80.77	80.40, 80.45	80.70, 80.60
M (μH)	3-D Anyl	10.834	11.723	12.280	12.738	12.939	13.021	12.974
	3-D FEA	10.784	11.683	12.213	12.633	12.826	12.810	12.546
k at 150 mm air gap	3-D Anyl	0.1345	0.1456	0.1536	0.1583	0.1609	0.1620	0.1601
	3-D FEA	0.1339	0.1446	0.1523	0.1565	0.1588	0.1593	0.1556
Available inner area (%)		70.93	58.22	45.94	36.20	27.83	20.72	7.59
Required wire length in a coil structure (m)		12.69	13.18	13.57	13.92	14.17	14.32	14.70

* Analytical.

◊ Here, it is seen that with the increment in T_g, the 3-D analytical results deviate from the 3-D FEA results. Due to the increment in T_g, the size of four circular corners in the coil increases. As a result, the rectangular bars becomes curvilinear from the outer side, which partially fulfils the assumption of rectangular bars. However, the trend of k for the presented coil systems is similar in both methods.

numeric) for ease in referring. The parameter value of each conventional coil system designed with this approach is summarised in Table 3.3 along with the type-I coil system. From Table 3.3, it can be seen that the value of self-inductance of the obtained coil is the same (deviation is within ±1%) as in the type-I. Moreover, it is also seen that the type-S5 coil system gives the highest k among types-S1–S6 coil systems. This highest k is 0.1593, which is 18.96% higher than k of the type-I coil system.

(*B*). Improving the Factor k by Decreasing the Value of L_{req} while Keeping the Value of M Constant

There are two possible ways to decrease the self-inductance of the type-I coil by (almost) maintaining the value of M, which are given as:

(B-1) by keeping the same number of turns as in type-I;

(B-2) by keeping the same wire length as in type-I.

The detailed analysis of approaches (B-1) and (B-2) are as follows:

(*B*-1). Decreasing the Value of L_{req} by Keeping the same Number of Turns as in type-I

Table 3.4: Parameter values of the conventional coils obtained using the approach **(*B*-1).**

Parameter		Name of coil system				
		type-I	type-N1	type-N2	type-N3	type-N4
Number of turns (N)		10	10	10	10	10
T_g (mm)		$0 \cdot d_w = 0$	$1 \cdot d_w$	$2 \cdot d_w$	$3 \cdot d_w$	$4 \cdot d_w$
L_P, L_S (μH)	3-D Anyl	80.50, 80.50	57.90, 57.90	43.17, 43.17	32.22, 32.22	23.58, 23.58
	3-D FEA	80.30, 80.80	58.25, 58.21	43.56, 43.53	32.50, 32.61	24.75, 24.79
M (μH)	3-D Anyl	10.834	8.816	6.954	5.272	3.823
	3-D FEA	10.784	8.776	6.890	5.181	3.849
k at 150 mm air gap	3-D Anyl	0.1345	0.1523	0.1611	0.1636	0.1621
	3-D FEA	0.1339	0.1507	0.1582	0.1591	0.1554
Available inner area (%)		70.93	48.92	30.85	16.72	6.52
Required wire length in a coil structure (m)		12.69	11.51	10.33	9.15	8.18

Here, the number of turns of the type-I coil system is taken as a reference, which is 10. For decreasing the self-inductance by keeping the same number of turns (10 turns), the gap between the turns (T_g) has been increased with a difference of $1 \cdot d_w$. However, different values of T_g can also be taken. This process is repeated until the available inner area (shown in Figure 3.17) is fully occupied. The obtained coil systems using this approach is named type-N# (where # is numeric) for ease in referring. The parameter value of each conventional coil system obtained with this approach is summarised in Table 3.4, along with the type-I coil system. From Table 3.4, it can be seen that the value of mutual inductance is not constant; it decreases with the decrease in the value of self-inductance. Moreover, it is also seen that the type-N3 coil system gives the highest k among types-N1–N4 coil systems. This highest k is 0.1591, which is 18.82% higher than k of the type-I coil system.

(*B*-2). Decreasing the Value of L_{req} by Keeping the same Wire Length as in type-I

With this approach, the used wire length in the type-I coil is taken as a reference, which is 12.69 m. For decreasing the self-inductance by keeping the same wire length, the gap between the turns is increased at each increment in turn (N) (so that M can be maintained). Here, the gap between the turns is calculated using the formula given in Appendix C, keeping the length unchanged for each design. This process is repeated until the available inner area (shown in Figure 3.17) is fully occupied. The obtained coil systems using this approach is named type-L# (where # is numeric) for

Table 3.5: Parameter values of the conventional coils obtained using the approach **(*B*-2).**

Parameter		Name of coil system						
		type-I	type-L1	type-L2	type-L3	type-L4	type-L5	type-L6
Required wire length in a coil structure (m)		12.69	12.69	12.69	12.69	12.69	12.69	12.70
Number of turns (N)		10	11	12	13	14	15	16
T_g (mm)		$0 \cdot d_w = 0$	$0.76 \cdot d_w$	$1.3 \cdot d_w$	$1.65 \cdot d_w$	$1.86 \cdot d_w$	$1.99 \cdot d_w$	$2.06 \cdot d_w$
L_P, L_S (μH)	3-D Anyl	80.50, 80.50	71.15, 71.15	65.94, 65.94	62.93, 62.93	61.35, 61.35	60.12, 60.12	59.32, 59.32
	3-D FEA	80.30, 80.80	71.51, 71.39	66.21, 66.30	63.19, 63.17	61.38, 61.44	60.26, 60.22	59.04, 59.02
M (μH)	3-D Anyl	10.834	10.773	10.508	10.205	9.947	9.697	9.477
	3-D FEA	10.784	10.724	10.416	10.063	9.744	9.420	9.110
k at 150 mm air gap	3-D Anyl	0.1345	0.1514	0.1594	0.1622	0.1621	0.1613	0.1598
	3-D FEA	0.1339	0.1501	0.1572	0.1593	0.1587	0.1564	0.1543
Available inner area (%)		70.93	49.82	33.96	22.82	15.16	9.63	5.72

ease in referring. The parameter value of each conventional coil system designed using this approach is summarised in Table 3.5, along with the type-I coil system. From Table 3.5, it can be seen that the mutual inductance decreases as the self-inductance decreases but the decrement in M is lower compared with the previous approach (***B*-1**). Still, constant M is not achieved. Moreover, it is also seen that the type-L3 coil system gives the highest k among types-L1–L6 coil systems. This highest k is 0.1593, which is 18.96% higher than k of the type-I coil system.

(*C*). Improving the Factor k by Decreasing the Value of L_{req} and Increasing the Value of M

In the previous approaches (i.e., **(*B*-1)** and **(*B*-2)**), it is seen that while decreasing the self-inductance, M also decreases. Therefore, this approach is not possible with CCAM.

Form the above analysis; it can be seen that the same highest k is obtained in all the approaches. Now, the question is, will all the highest k coils (i.e., type-S5, type-N3, and type-L3) enhance the similar system performance as well? For answering this, a comparison of the system performance with the obtained coil systems of improved k (i.e., type-S5, type-N3, and type-L3) has been performed in the next subsection.

Table 3.6: Comparison of the uncompensated WPT system performance having type-S5, type-N3, and type-L3 coil systems with respect to the type-I coil system at the 100-kHz operating frequency and I_P = 10 A.

Parameter		Name of coil system			
		type-I	**type-S5**	type-N3	type-L3
k at 150 mm air gap		0.1339	0.1593	0.1591	0.1593
Required wire length in a coil structure (m)		12.69	14.30	9.15	12.68
ⓐ dc resistance $R_{dc,P} = R_{dc,S}$ (mΩ)		78.33	88.41	56.46	78.32
ⓑ proximity-effect resistance $R_{pe,P} = R_{pe,S}$ (mΩ)		30.83	16.30	9.07	13.94
(ⓐ + ⓑ) AC resistance $R_P = R_S$ (mΩ)		109.16	104.71	65.53	92.26
Q_S at $R_{L,\text{eq}}$ = 10 Ω for secondary series circuit		5.00	5.00	2.035	3.932
Q_S at $R_{L,\text{eq}}$ = 125 Ω for secondary parallel circuit		2.47	2.47	6.10	3.15
Change in Q_S with respect to type-I for the secondary	series circuit	—	unchanged	59.30% decreased	21.36% decreased
	parallel circuit	—	unchanged	146.96% increased	27.53% increased
S_{max} (VA)		90.46	128.19	51.81	100.75
Change in S_{max} with respect to type-I		—	41.71% increased	42.73% decreased	11.38% increased
$\eta_{t,uc}$ at different $R_{L,\text{eq}}$		see Figure 3.18			

3.5.3 Comparison of the System Performance with the Coils of Improved k (obtained by the Various Approaches) in Uncompensated WPT System

S_{max} and transmission efficiency of the uncompensated coils ($\eta_{t,uc}$) are the essential part to assess the system performance of the WPT. In this context, S_{max} and $\eta_{t,uc}$ are compared for the obtained coil systems (of improved k) from the various approaches. Moreover, this subsection also examines how the various approaches impact the predetermined loaded quality factor (Q_S) (obtained in type-I) for a series- or parallel-connected secondary circuits? This Q_S is used to determine the power transfer capability of the compensated WPT system and defines the bandwidth of the tuned circuit [5].

For calculating Q_S [$\{\omega L_S/(R_S+R_{L,\text{eq}})\}$ for series and $\{(R_S+R_{L,\text{eq}})/\omega L_S\}$ for parallel compensations] and $\eta_{t,uc}$ for the type-I, type-S5, type-N3, and type-L3 coils, the coil's AC resistance is required, which is calculated using (3.27) and tabulated in Table 3.6. Moreover, the dc resistance (R_{dc}) and proximity-effect resistance (R_{pe}) of these coils are also summarised in Table 3.6, which are calculated using (3.28) and (3.30), respectively. From Table 3.6, it can be seen that the obtained value of AC resistance for the type-S5, type-N3, and type-L3 coils are lower than those in the type-I coils. Among the type-S5, type-N3, and type-L3 coil systems, the type-N3 has the lowest AC resistance value. Q_S

for series- and parallel-connected secondary circuits are calculated for all the coil systems at $R_{L,\text{eq}}$ equal to 10 Ω and 125 Ω (as an example), respectively. The value of Q_S for each coil system is given in Table 3.6. Here, it can be seen that Q_S in type-S5 coil system remains the unchanged for both connections compared with the type-I coil system due to the same self-inductance. Whereas, it changes in type-N3 and type-L3 coil systems compared with the type-I coil system due to a decrease in the value of self-inductance. In comparison to the type-I coil system, the value of Q_S in type-N3 and type-L3 coil systems in the series-connected secondary circuit is decreased by 59.30% and 21.36%, respectively, whereas in the parallel-connected secondary circuit, it is increased by 146.96% and 27.53%, respectively. This increase in Q_S (in the parallel-connected secondary circuit) of type-N3 and type-L3 coil systems narrows the bandwidth of the tuned circuit, which makes the system challenging to tune [5]. Whereas, the decrease in Q_S of the type-N3 and type-L3 coil systems in the series-connected secondary circuit decreases the power transfer capability compared with the type-I coil system. Therefore, the predetermined value of Q_S should be unchanged while improving k (here, type-S5 has unchanged Q_S). For other values of $R_{L,\text{eq}}$, the obtained changes in Q_S for the type-S5, type-N3, and type-L3 coil systems with respect to type-I coil system (as given in Table 3.6) remains the same for the series- and parallel-connected secondary circuits.

Further, to calculate S_{max}, the expression of S_{max} in (2.31) is simplified by neglecting R_S because of its insignificant effect on S_{max} (since $R_S << \omega^2 L_S^2$). The simplified expression of S_{max} is given as

$$S_{max} = \omega {I_P}^2 k^2 L_P \tag{3.32}$$

From (3.32), it can be seen that for a constant ω, I_P, and L_P, any improvement in k enhances S_{max} proportional to k^2. By using (3.32), the value of S_{max} for the type-I, type-S5, type-N3, and type-L3 coil systems is calculated and given in Table 3.6. Here, it can be seen that for the same improvement in k (ω and I_P are also kept the same), type-S5 coil system gives the highest S_{max} among the presented coil systems. Compared with the type-I coil system, S_{max} in type-S5 coil system is increased by 41.71%, whereas with type-L3 coil system, it is increased by 11.38%. But, for the type-N3 coil system, it is decreased by 42.72%.

For the case of compensated WPT system, based on the obtained changes in Q_S and S_{max} (given

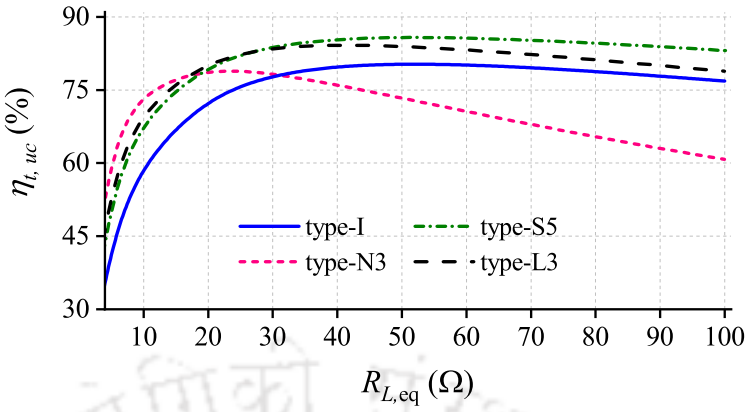

Figure 3.18: Comparison of transmission efficiency of uncompensated different coil systems for a wide load variation.

in Table 3.6), it can be concluded that the type-S5 coil system improves the power transfer capability in both series- and parallel-connected secondary circuits. However, the type-N3 and type-L3 coil systems improve the same only in the parallel-connected secondary circuit.

Furthermore, to calculate $\eta_{t,uc}$, the following expression is used [68].

$$\eta_{t,uc} = \frac{R_{L,\mathrm{eq}}}{\left(R_S + R_{L,\mathrm{eq}}\right)\left(1 + \dfrac{R_P\left(R_S + R_{L,\mathrm{eq}}\right)}{\omega^2 k^2 L_P L_S}\right) + \dfrac{R_P L_S}{k^2 L_P}}. \tag{3.33}$$

By using (3.33), $\eta_{t,uc}$ of type-I, type-S5, type-N3, and type-L3 coil systems are calculated for a wide variation of $R_{L,\mathrm{eq}}$, as shown in Figure 3.18. From Figure 3.18, it is seen that the type-S5 and type-L3 coil systems improve $\eta_{t,uc}$ throughout $R_{L,\mathrm{eq}}$ variation compared with the type-I coil system. Here, the type-S5 coil system maintains the improvement with a constant gap with respect to type-I coil system, whereas type-L3 does not; the gap between the curves of type-L3 and type-I becomes narrower after 30 Ω. Furthermore, the type-N3 coil system also improves $\eta_{t,uc}$, but up to 30 Ω compared with the type-I coil system; then after its value decreases. With the type-I and type-S5 coil systems, the maximum $\eta_{t,uc}$ is obtained at 50 Ω, which is 80.38% and 85.85%, respectively. Moreover, for the type-N3 coil system, it is obtained at 20 Ω, which is 79.51%, whereas for the type-L3 coil system, it is obtained at 40 Ω, which is 84.33%. Among all the coil systems, the maximum $\eta_{t,uc}$ is the highest in type-S5 coil system.

From the above study and analysis, it is concluded that for the same improvement in k (of type-S5,

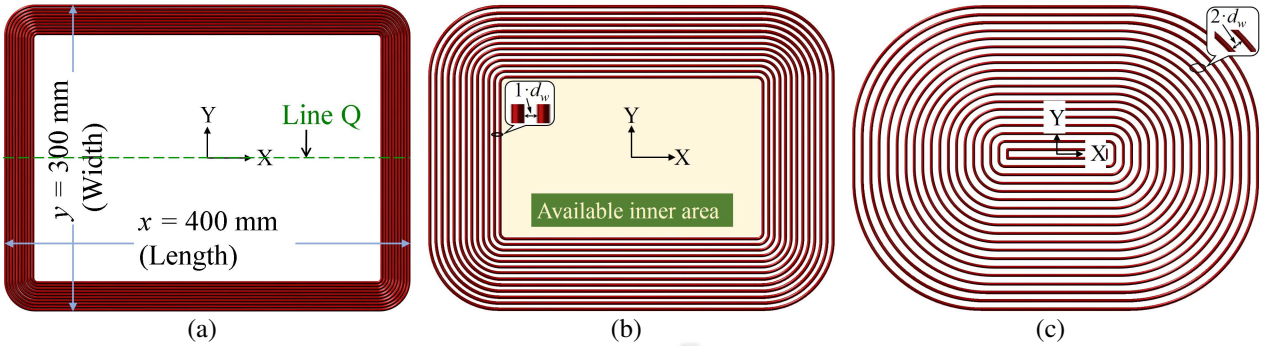

Figure 3.19: Conventional coil structures of rectangular shape with the same outer dimensions (400 mm × 300 mm) having different gaps between turns to obtain the L_{req} (80.5 μH). (a) type-I (L_{req} is achieved). (b) type-II (L_{req} is achieved). (c) type-III (L_{req} is not achieved).

type-N3, and type-L3 with respect to type-I), the type-S5 coil system gives 41.71% more S_{max} with the higher transmission efficiency for a wide load variation compared with the type-I coil system. This S_{max} is higher than the type-N3 and type-L3 coil systems. Therefore, the best approach of improving the factor k is the approach **(*A*)** (increasing M by keeping L_{req} constant), which enhances the system performance regardless of the secondary compensation circuits.

Therefore, for further attempts of improving the factor k at a given air gap should be performed by: 1) maintaining L_{req} of a coil system and 2) keeping the selected outer dimensions (x mm × y mm) unchanged. Thus, these two parameters are said to be constraints for improving the factor k, which can be expressed as

$$\max k, \quad \text{s. t.} \begin{cases} (x \text{ mm} \times y \text{ mm}) \rightarrow \text{unchanged} \\ L_{req} - 1\% \leq L_{req} \leq L_{req} + 1\%. \end{cases} \tag{3.34}$$

For a fixed air gap with the constraints given in (3.34) (values are in Table 3.2), how M increases by increasing the gap between the turns and the number of turns through CCAM, is analysed in the next subsection.

3.5.4 Analysis of Increment in M for the Constraints given in (3.34) using CCAM

To understand the variation of M, for the constraints given in (3.34) and the values are in Table 3.2, conventional coils are analysed here with different spacing between the turns. The spacing between the turns is considered as p times of the wire diameter ($p \cdot d_w$). These spacings are zero, one, and two

Table 3.7: Comparison of conventional coil structures.

Parameters	Calculated using	type-I (Figure 3.19(a))	type-II (Figure 3.19(b))	type-III (Figure 3.19(c))
Gap between turns T_g (mm)	–	$0{\cdot}d_w = 0$	$1{\cdot}d_w = 2.7$	$2{\cdot}d_w = 5.4$
Number of turns (N)	–	10	13	19
L_P, L_S (μH)	3-D Anyl	80.50, 80.50	80.80, 80.80	61.05, 61.05
	3-D FEA	80.30, 80.80	81.09, 81.11	60.45, 60.35
M at 150-mm air gap (μH)	3-D Anyl	10.834	12.780	–
	3-D FEA	10.784	12.677	–
k at 150-mm air gap	3-D Anyl	0.1346	0.1582	–
	3-D FEA	0.1339	0.1563	–

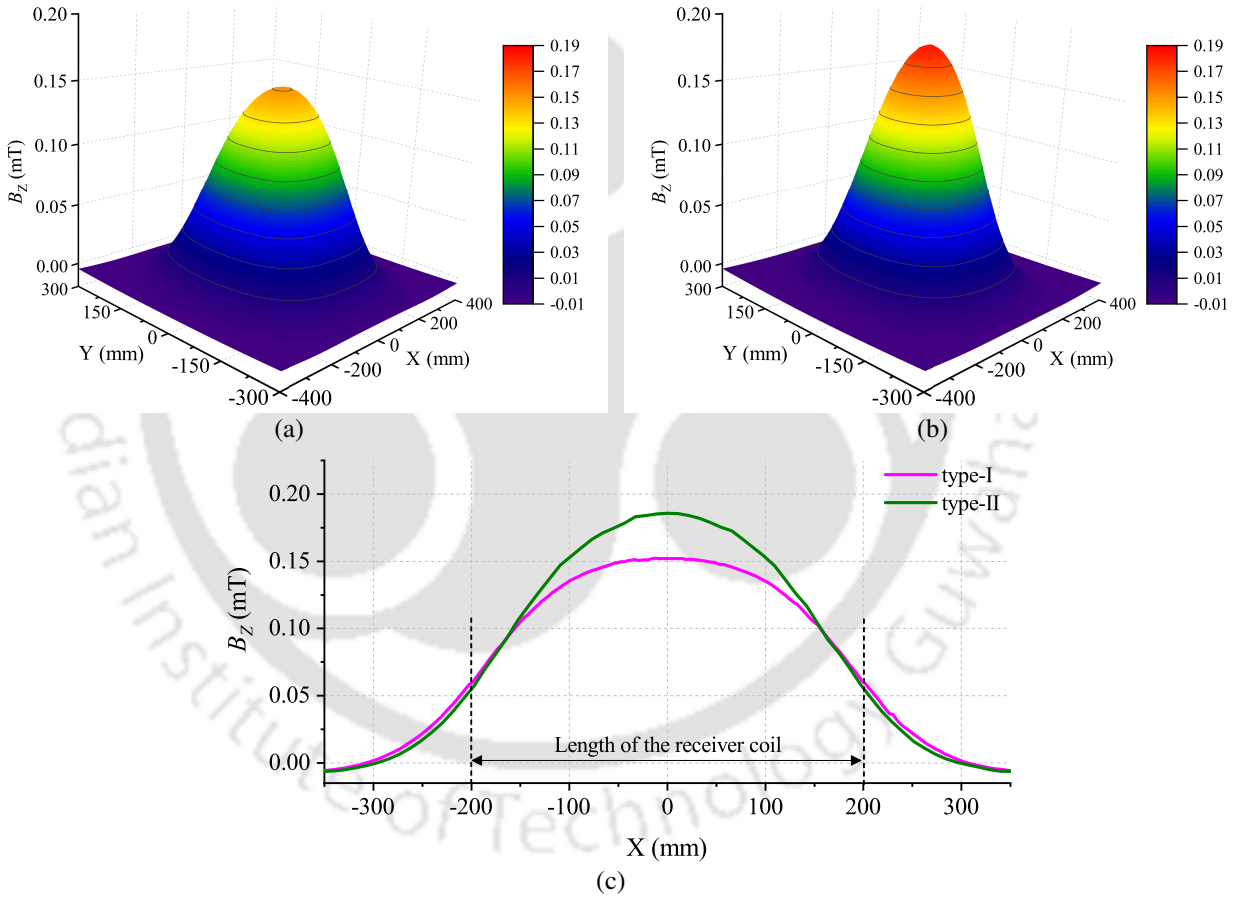

Figure 3.20: 3-D distribution of B_Z at Z = 152.7 mm (i.e., in Region III) at 10 A excitation current for (a) type-I and (b) type-II coils. (c) XZ plane view of Figures 3.20(a) and (b) along Line Q (Line Q is shown in Figure 3.19(a)).

times of the wire diameter (i.e., 0 times 2.7 = 0 mm, 1 times 2.7 = 2.7 mm, and 2 times 2.7 = 5.4 mm), and the coils are named type-I, type-II, and type-III, respectively, as shown in Figure 3.19(a)–(c). It should be noted that the considered spacings are chosen as a difference of $1{\cdot}d_w$ for winding

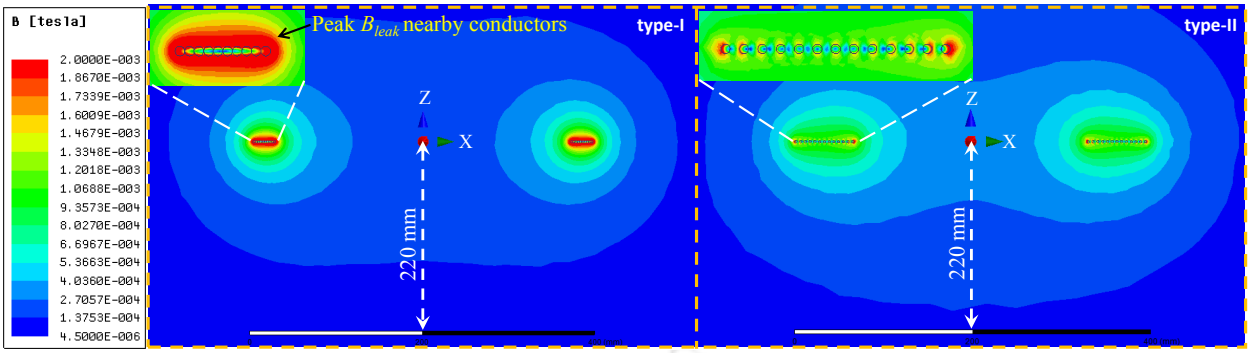

(a)

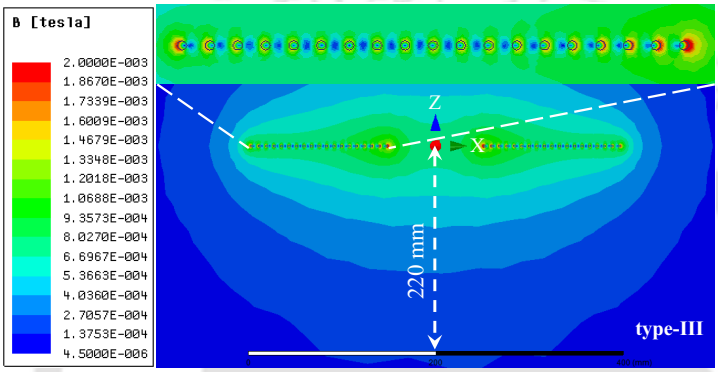

(b)

Figure 3.21: Magnetic field distribution for the excitation current of 10 A on XZ plane along Line Q for the (a) type-I and type-II coils, and for the (b) type-III coil (it is given here to show the effect of $2{\cdot}d_w$ gap between the turns on peak B_{leak} nearby conductors. However, it is not included in the analysis because it does not fulfil the given constraints in (3.34). Compared with type-I and type-II coils, reduced peak B_{leak} can be seen with $2{\cdot}d_w$ gap and approximately uniform magnetic field throughout the coil dimensions.).

ease in the prototyping. However, this difference can be selected as a noninteger value such as $0.8{\cdot}d_w$ (winding complexity may increase in prototyping). The self-inductances of these three conventional coils (types-I–III) are determined using 3-D analytical and 3-D FEA, and Table 3.7 shows L_P and L_S values. Due to different spacings between the turns, the number of turns is different for each coil type. As a result of this, the type-III coil does not achieve L_{req} value because the inner space is fully occupied, whereas type-I and type-II coils do achieve L_{req} value. Now, M and k values of type-I and type-II coils are determined using 3-D analytical and 3-D FEA, and Table 3.7 summarises the results. From Table 3.7, it is observed that the type-II coil system has a higher k in comparison to the type-I coil system. The higher value of k indicates that M of type-II coil system has increased (type-II–12.677 μH and type-I–10.784 μH).

M between the coils is the magnetic flux linkage to the Rx coil (Ψ_{PS}) by an excitation current I_P

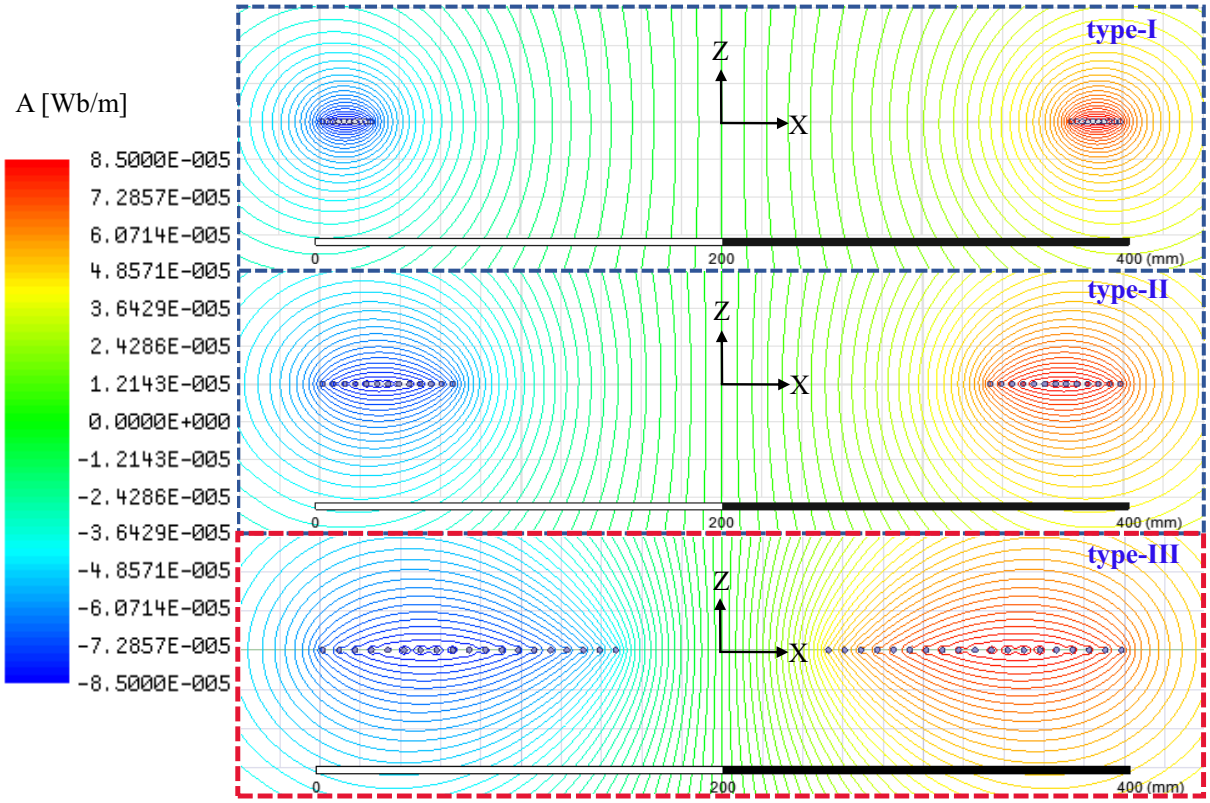

Figure 3.22: Magnetic flux distribution of conventional coils for the excitation current of 10 A, along Line Q. (Again, type-III is included here to show the effect of $2{\cdot}d_w$ gap between the turns on magnetic flux distribution. However, it is not included in the analysis because it does not fulfil the given constraints (3.34). Compared with type-I and type-II, higher flux concentration can be seen toward the centre of the coil with $2{\cdot}d_w$ gap (in type-III).)

and is given in the following equation:

$$M = \frac{\Psi_{PS}}{I_P} = \frac{1}{I_P} \iint \mathbf{B}^{III} \cdot d\mathbf{S}_S \tag{3.35}$$

where $\mathbf{B}^{III}$ $(= (B_{\mathrm{X}}^{III}\,\hat{i} + B_{\mathrm{Y}}^{III}\,\hat{j} + B_{\mathrm{Z}}^{III}\,\hat{k})$; the expression of B_{X}^{III}, B_{Y}^{III}, and B_{Z}^{III} can be found in (3.19)-(3.20)) is the magnetic flux density generated by the Tx coil, and $\mathbf{S}_S$ is the area of the Rx coil. From (3.35); for a fixed I_P, M is directly proportional to Ψ_{PS}. In the type-II coil system, Ψ_{PS} equal to 126.77 μWb, which is higher than the type-I coil system (i.e., 107.84 μWb). This increase in Ψ_{PS} eventually improves M for the type-II coil system. One of the main reasons behind the higher Ψ_{PS} in type-II coil system is better magnetic flux density profile of type-II Tx (higher in magnitude compared with the type-I Tx), as shown in Figure 3.20(c). This better profile is due to the increased gap between the turns and the number of turns. Increasing the gap between the turns reduces the peak B_{leak} nearby

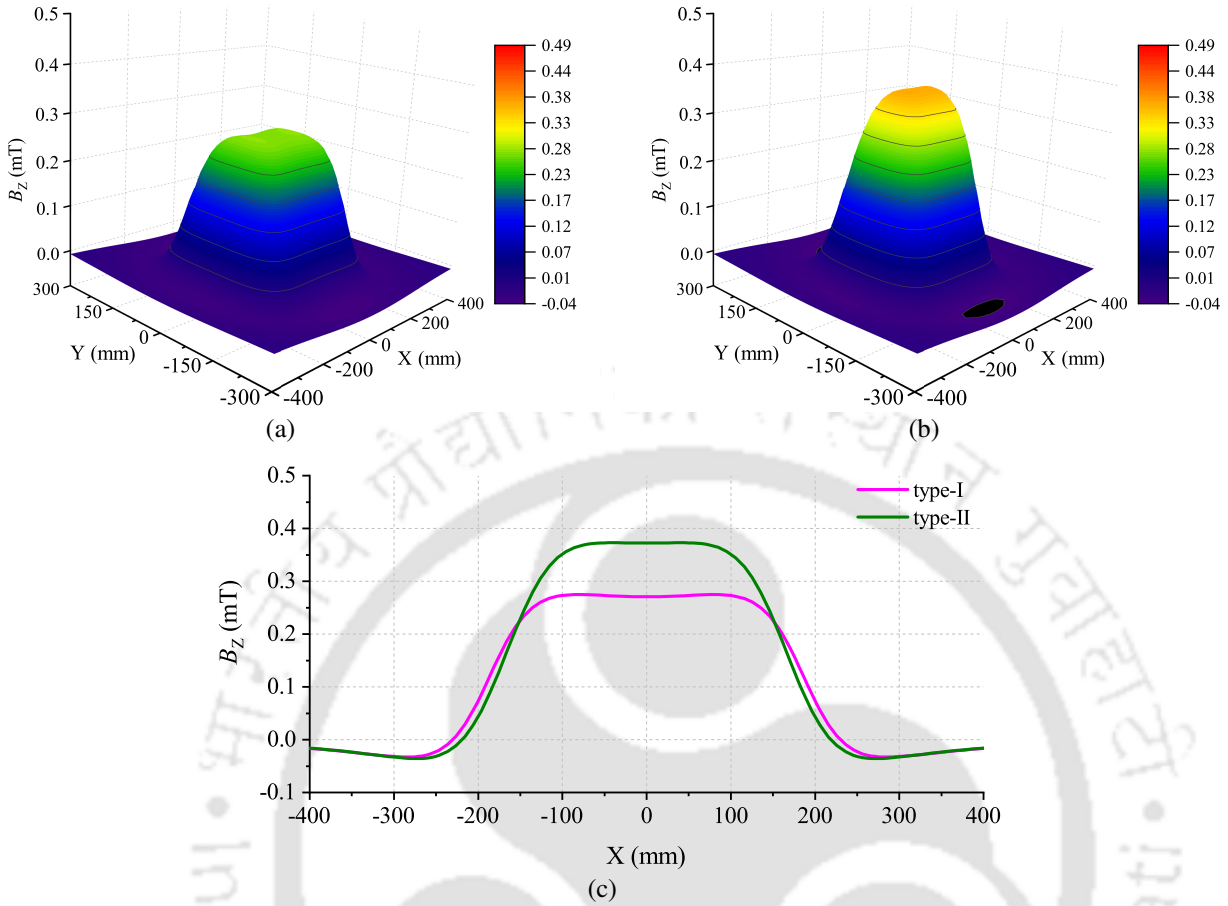

Figure 3.23: 3-D distribution of B_Z at Z = 80 mm at 10 A excitation current for the (a) type-I and (b) type-II coils. (c) XZ plane view of Figure 3.23(a) and (b) along Line Q.

conductors due to the cancellation of flux in between the turns, as shown in Figure 3.21(a) (type-II has a lower peak B_{leak} nearby conductors compared with type-I). The effect of the turns' layout resulted in the reshaping of magnetic flux lines. As a result of this, the concentration of flux increases toward the centre of the Tx coil compared with type-I, as shown in Figure 3.22, and, hence, giving better magnetic flux density profile in Z-direction (see Figure 3.20(c)). The second reason for the higher Ψ_{PS} could be the increased number of turns in the type-II Rx. To analyse the effect of the increased number of turns and gap between the turns in the type-II Rx, Ψ_{PS} is calculated for the coil system in which type-I is used as a Tx with type-II Rx. With this coil system (the outer dimensions of the Rx are fixed, and self-inductances are almost similar), Ψ_{PS} becomes 115.73 μWb for the same B_Z profile as in type-I coil system. Here, the obtained Ψ_{PS} (115.73 μWb) is higher than the type-I coil system (107.84 μWb). Hence, it can be concluded that increment in turns (of 3) and the gap between the turns

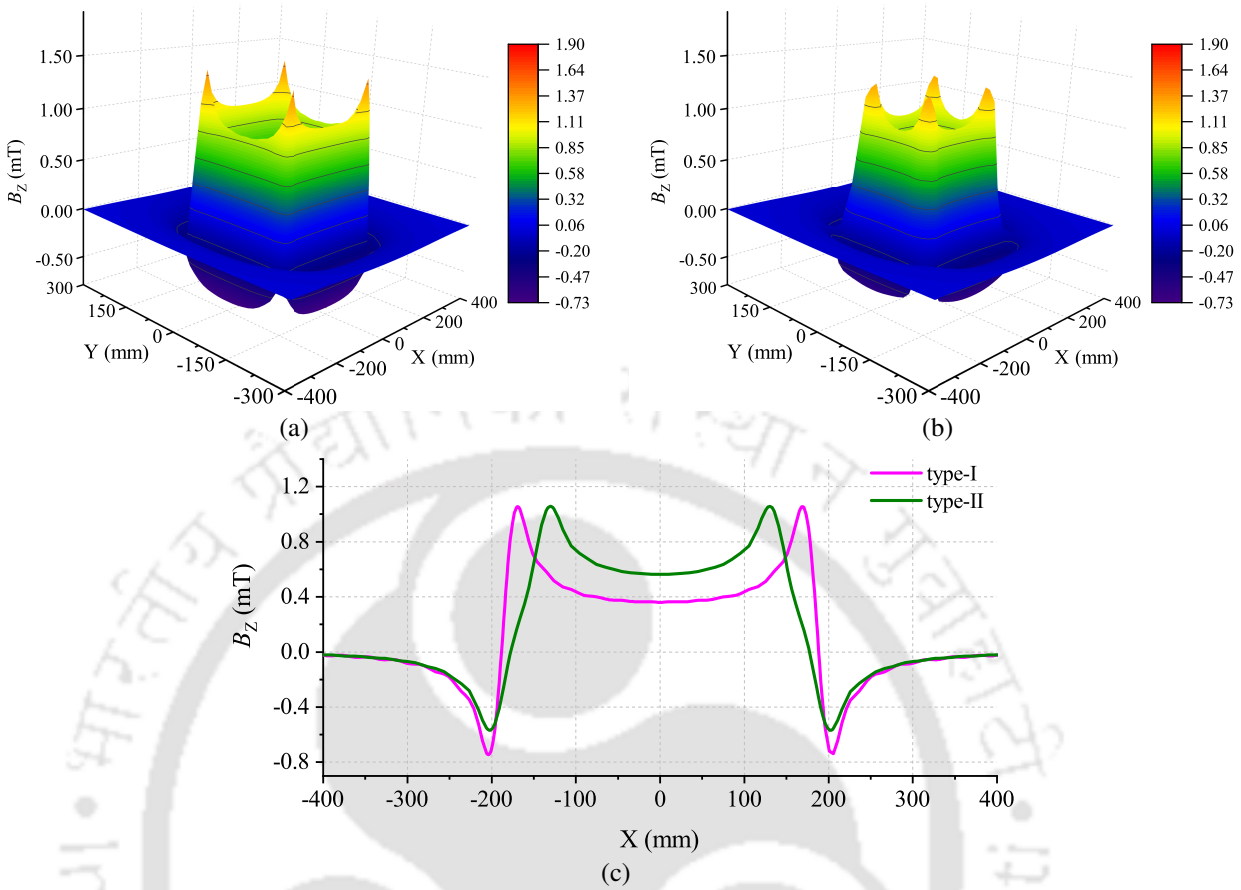

Figure 3.24: 3-D distribution of B_Z at Z = 10 mm at 10 A excitation current for the (a) type-I and (b) type-II coils. (c) XZ plane view of Figure 3.24(a) and (b) along Line Q.

have contributed in the increment of Ψ_{PS} in the type-II coil system. Thus, it is possible to conclude that a higher value of Ψ_{PS} results in higher k for the constraints in (3.34).

Furthermore, at different vertical heights, such as Z = 80 mm and 10 mm, the distribution of B_Z of type-I and type-II coils are shown in Figures 3.23 and 3.24, respectively. From Figures 3.23 and 3.24, the higher difference between the distribution of B_Z of type-I and type-II coils is seen. At Z = 10 mm, this difference is the highest compared with Z = 80 mm and 152.7 mm. The coupling k at Z = 80 mm and 10 mm is 0.3169 and 0.8079, respectively, for type-II coil system, which is higher than those in type-I coil system (k at Z = 80 mm and 10 mm is 0.2615 and 0.7255, respectively). Thus, the above analysis is also valid for different vertical heights.

3.6 Summary of the Chapter

In this chapter, an investigation for improving k of unipolar rectangular coils has been presented (the same is applicable to other geometry of the coils as well). From the discussion, it is found that

doing modification in the design of coils is the first resort toward improving k. In this context, a 3-D analytical model has been developed, which calculates the B-fields around the coil system and self- and mutual inductance of the coils (and k). In the modelling, Fourier analysis, magnetic scalar and magnetic vector potentials are used. For the modelling of a single source (Tx) coil based WPT system, fictitious coils (physically absent) are assumed to form a periodic structure, which allows using Fourier analysis. Fictitious coils are considered far away from the working coil (physically present) so that the fictitious coils do not influence the magnetic field of the working coil. An experimental setup is built to verify the accuracy of the developed 3-D analytical model. By using this experimental setup, X-, Y-, and Z-components of B-field in Region III have been measured. Then, the analytically calculated B-fields are compared with the measured and simulated (in 3-D FEA software) B-fields, which show a good agreement. From these results, it is also observed that the B-field of the modelled coil is not affected by the B-field of fictitious coils, which validates the assumption made. The calculate self-inductance of the modelled coil is also compared with the measurement and simulation, which matches well with the measured and simulated self-inductances. Thus, the developed model can be used to design and optimisation of the coil, which is a cost-effective and time-saving option compared with 3-D FEA software. This model is also valid for the square-shaped coil. Furthermore, the calculation of AC resistance of the coil is presented, which helps to assess the system performance.

By using this model, various possible approaches to improve the factor k of conventional coils for EV applications are studied and analysed. In all the approaches, the same highest k is obtained. Furthermore, the impact of improved k (using different approaches) on the system performance is examined to find the best approach(es). Form the investigation; it is found that with the approach of increasing M by keeping the self-inductance constant enhances the system performance regardless of the secondary compensation circuits. Based on this, the constraints for improving the factor k is summarised, which should be used for further improvement in k. Moreover, to understand the increment in M for the constraints given in (3.34), conventional coils are analysed with different spacing between the turns. From the analysis, it is found that a higher value of magnetic flux linkage to the Rx coil (Ψ_{PS}) results in higher k. This higher Ψ_{PS} is achieved due to the increased spacing between the turns and the number of turns. Doing this improved the generated magnetic field profile

by the Tx coil and increased the magnetic flux linkage to the Rx coil. From the observations of the presented analysis, the next chapter proposes a unipolar coil arrangement method for improving the factor k (with the same constraints) compared with the conventional coils through modification in the design of coils.

Note: *The research findings of this chapter have been published in "IECON 2016 - 42nd Annual Conference of the IEEE Industrial Electronics Society" and "IEEE Transactions on Transportation Electrification".*

Indian Institute of Technology Guwahati

4

A Unipolar Coil Arrangement Method for Improving the Coupling Coefficient Without Ferrites in WPT Systems

Contents

4.1 Introduction

As discussed in the previous chapter, modifying the design of coils is the first resort to improve the factor k. Improving k with this way reduces the weight and cost of the coil system in comparison to the second resort (i.e., with ferrite material). The various possible approaches to improve k of the conventional coils have been discussed in Section 3.5. From all the approaches, a similar improvement in k is obtained. Among them, the approach, which enhances the system performance regardless of the secondary compensation circuits, is increasing M by keeping the self-inductance constant. Based on this approach, the considered constraints of improving the factor k are summarised in (3.34).

Furthermore, to understand the increase in M for the constraints given in (3.34), the conventional coils have been analysed with different gaps between the turns and the number of turns in Section 3.5.4. It was seen that by increasing the gap between the turns and the number of turns increase the Ψ_{PS}. The increase in Ψ_{PS} results in higher M, which improves k. The discussion in Section 3.5.4 raises the following questions.

Q.1 Is it possible to use the first highest gap between the turns at which L_{req} is not achieved using CCAM (i.e., here, $2{\cdot}d_w$)?

Q.2 Is it possible to use different combinations (using $0{\cdot}d_w$, $1{\cdot}d_w$, $2{\cdot}d_w$, ...) of gaps between the turns?

Q.3 If Q.1 and Q.2 are possible, then how will the arrangement of turns in a coil be?

Q.4 While achieving Q.1, Q.2, and Q.3 for the constraints given in (3.34), does k improve compared with conventional coil structures?

For answering the abovementioned questions, a unipolar coil arrangement method (UCAM) for improving the factor k without using ferrite material compared with conventional coils of the same self-inductances and outer dimensions is developed and analysed in Section 4.2. Moreover, the developed 3-D analytical model in the previous chapter is extended for the proposed UCAM in Section 4.2. This section also studies the interoperability between the proposed and conventional coils, examines the impact of increased k on transmission efficiency and power transfer capability, analyses the peak

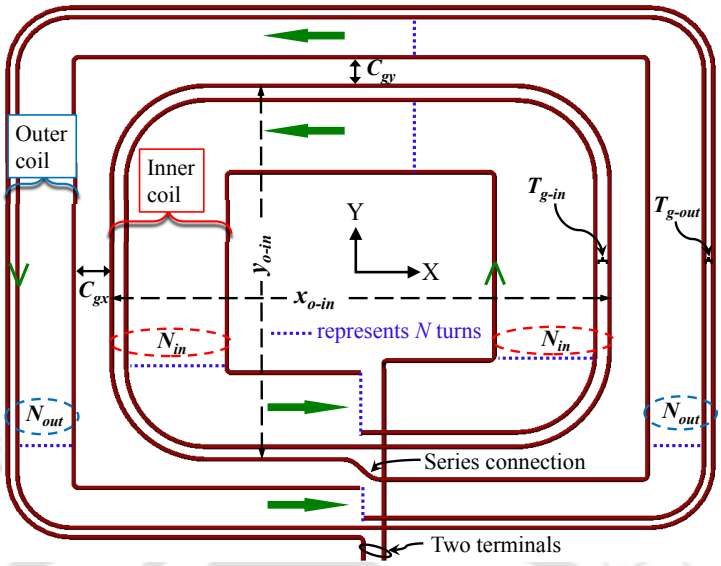

Figure 4.1: Schematic of the unipolar coil structure for describing the proposed UCAM.

B_{leak} nearby coil structures, and investigates the impact of different misalignments on improvement in the factor k. Section 4.3 presents the developed experimental setup and the verification of the results obtained using the proposed UCAM (through 3-D analytical model and simulations) and the measurements. Section 4.4 presents the improvement in k of the geometry having equal length and width using the proposed UCAM. Section 4.5 shows the improvement in k of nonidentical unipolar coils. Finally, Section 4.6 gives a summary of this chapter.

4.2 Proposed Unipolar Coil Arrangement Method

This section describes and analyses the proposed UCAM to answer the questions raised in Section 4.1. Initially, an overview of the proposed UCAM is presented, followed by the 3-D analytical model. Finally, the arrangement of turns in the coil structures at the maximum possible k for the constraints in (3.34) is presented.

Moreover, this section examines the impact of increased k on transmission efficiency and power transfer capability. It also studies the peak B_{leak} nearby coil structures and investigates the impact of different misalignments on improvement in k.

4.2.1 Overview of the Proposed UCAM

Figure 4.1 shows the conceptual diagram of the unipolar coil structure to describe the proposed UCAM. This coil structure comprises of two coil sets–outer coil (OuC) and inner coil (InC). OuC

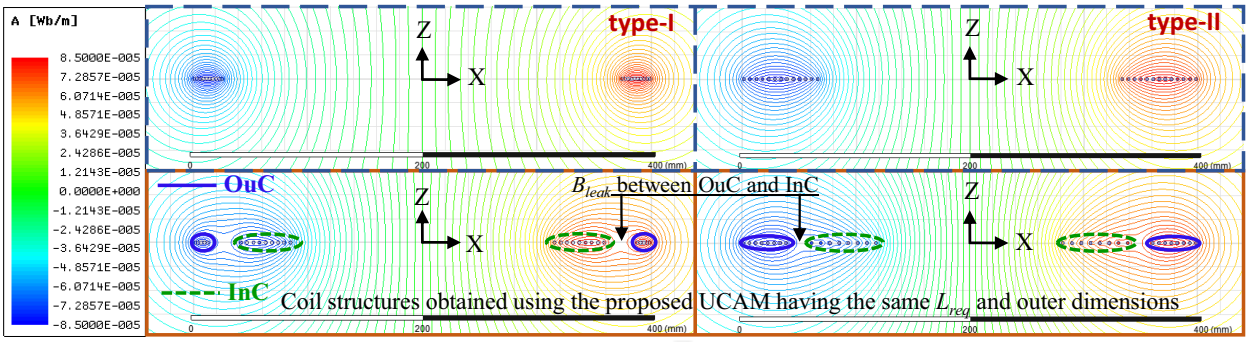

Figure 4.2: Flux lines distribution [having the same number of flux lines and excitation current (10 A)] of different coil structures (conventional and proposed) on the XZ plane along line Q. Here, the effect of introducing the InC on the flux lines concentration (toward the centre of the coil) and leakage flux (between the InC and OuC can be seen).

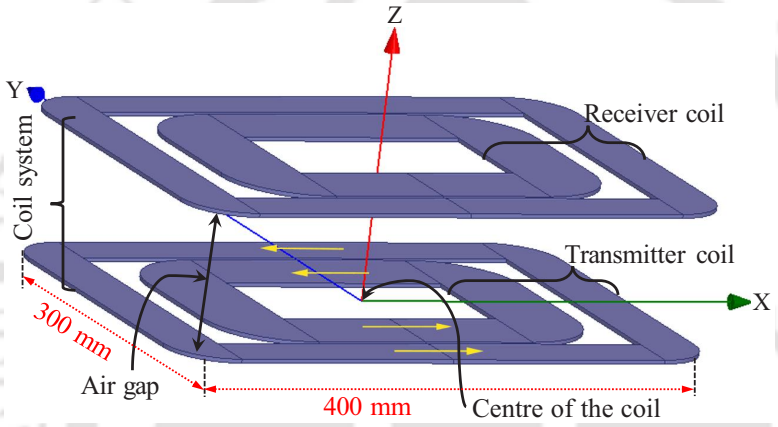

Figure 4.3: 3-D representation of a unipolar rectangular coil system (used in ANSYS Maxwell) derived from the proposed UCAM.

has N_{out} turns, and the gap between the turns is T_{g-out} mm, whereas InC has N_{in} turns, and the gap between the turns is T_{g-in} mm. OuC and InC are physically placed on the same axis (coaxial) and are in the same plane (coplanar). OuC and InC are connected in series, both electrically and magnetically (magnetic flux addition happens). The gaps between the last turn of InC and the first turn of OuC are C_{gx} mm and C_{gy} mm in the X- and Y-directions, respectively. The outer dimensions of OuC are x mm $\times$ y mm (same as conventional coils) whereas, for InC, x_{o-in} mm and y_{o-in} mm in the X- and Y-directions, respectively.

The use of InC helps to push the flux lines (increases the flux concentration) toward the centre of the coil structure that may increase Ψ_{PS}, as illustrated in Figure 4.2. Moreover, InC gives the freedom to use a different gap between the turns along with OuC (i.e., different combinations of T_{g-out} and T_{g-in} can be used). This arrangement allows generating a magnetic field by the Tx coil that results in

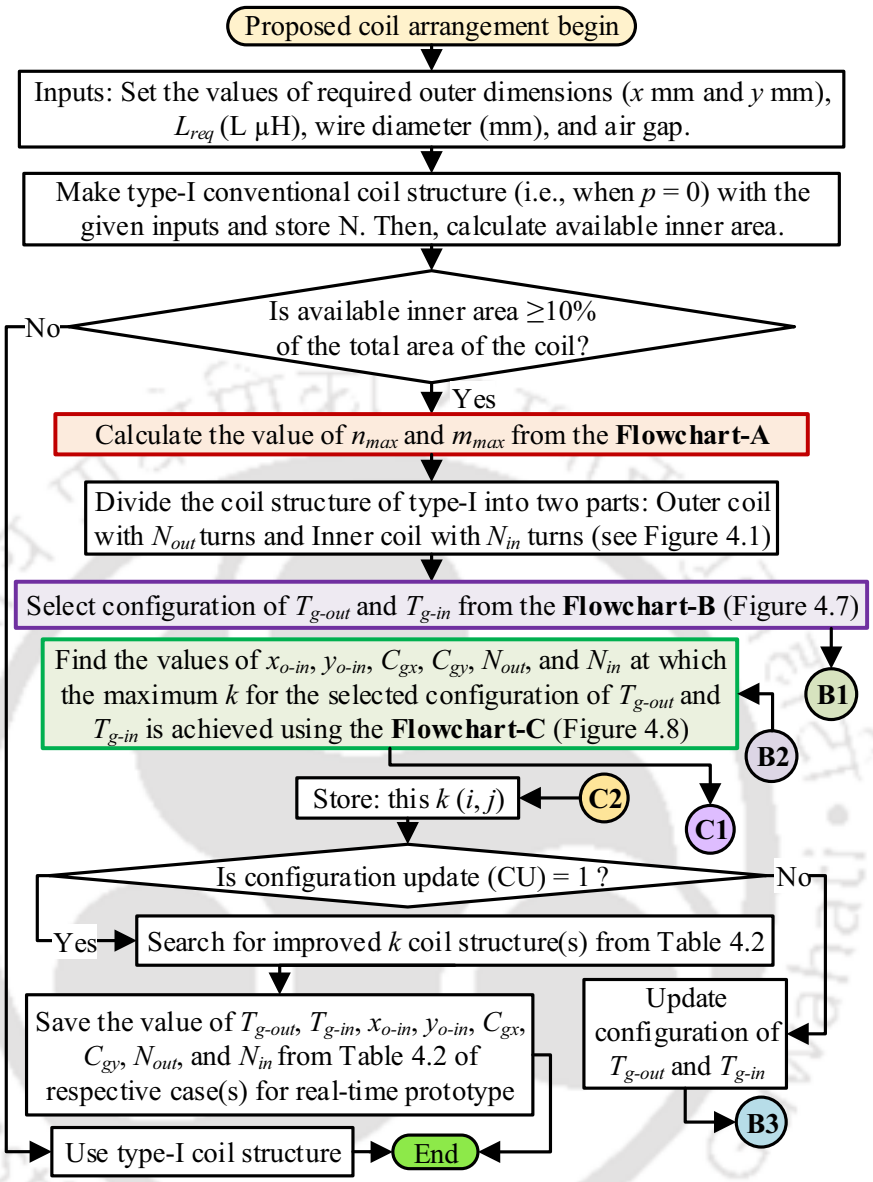

Figure 4.4: Flowchart of the proposed UCAM for improving *k* of unipolar coils. Here, **B1**–**B3**, **C1**, and **C2** are the nodes of flowchart-B and flowchart-C.

higher Ψ_{PS}. From Figure 4.2, it is also observed that conductors of InC and OuC (encircled in Figure 4.2) help further to reduce the peak B_{leak} between InC and OuC. This reduction is due to the change in the flux distribution between the OuC and InC. Furthermore, adjusting C_{gx} and C_{gy} helps to fine-tune the value of L_{req} even after finalising the $T_{g\text{–}out}$, $T_{g\text{–}in}$, N_{out}, and N_{in} due to the use of InC.

The 3-D representation of a unipolar rectangular coil system, according to Figure 4.1, is shown in Figure 4.3. For getting the maximum *k* for the selected configuration of $T_{g\text{–}out}$ and $T_{g\text{–}in}$, the unknown value of the coil parameters (N_{out}, N_{in}, C_{gx}, C_{gy}, $x_{o\text{–}in}$, and $y_{o\text{–}in}$) is calculated (for L_{req}) using the steps

given in the flowchart shown in Figure 4.4. Thus, it can be said that the factor k is a function of wire diameter, misalignments parameters (for example, ΔX, ΔY, and ΔZ), number of turns, gaps between turns, and the outer dimensions of OuC and InC. Hence, the factor k can be expressed as

$$k = f(T_{g-out}, N_{out}, T_{g-in}, N_{in}, x, y, x_{o-in}, y_{o-in}, d_w, \text{misalingment parameters}). \quad (4.1)$$

Here, k can be calculated using a 3-D analytical model that is presented in the next subsection.

4.2.2 3-D Analytical Modelling

In this section, the developed 3-D analytical model in Chapter 3, is extended for the coil structures obtained using the proposed UCAM. The necessary changes for this extension are presented here. These changes include the modification in the definition of current densities and integration limits in the equation of the self- and mutual inductances [i.e., in (3.2), (3.4), (3.20), and (3.22)].

Figure 5.2(b) shows the top view of the modelled air-cored coil (obtained from the proposed UCAM). For the modelling of proposed coil structures, the coil is assumed to have four finite rectangular bars in both OuC and InC that overlap at the corners, as shown in Figure 5.2(b) [24, 63]. The value of geometrical parameters is determined using Table 4.1. For the coil structure given in Figure 5.2(b), the current density distributions in the X- and Y-directions can be calculated using (3.1) and (3.3), respectively. However, in these equations, the terms j_{X}^{total} and j_{Y}^{total} are modified according to the geometrical parameters of the coil structure shown in Figure 5.2(b), and its expressions are given in the next sub subsection.

4.2.2.1 Expression of j_{Y}^{total} and j_{X}^{total} for the Proposed Coil Structures

Figure 5.2(c) shows the distribution of J_{Y}^{total}(X,Y) in the finite rectangular bars of OuC and InC (placed in Y-direction). For J_{Y}^{total}(X,Y), the term j_{Y}^{total} is obtained by superimposing the j_{Y} of OuC and InC, which can be expressed as

$$j_{\mathrm{Y}}^{total} = j_{\mathrm{Y}}^{\mathrm{OuC}} + j_{\mathrm{Y}}^{\mathrm{InC}} \quad (4.2)$$

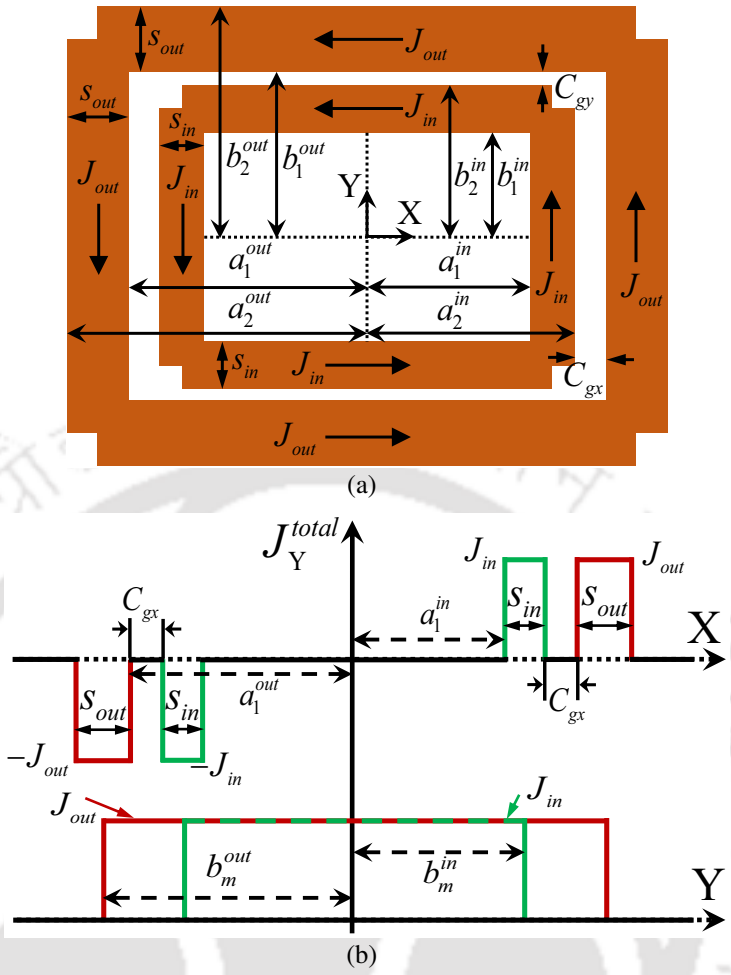

Figure 4.5: (b) Top view schematic of the modelled air-cored coil (having OuC and InC with coil parameters shown in Figure 4.1). (c) Distribution of J_{Y}^{total}(X,Y) along the X- and Y-directions.

In (4.2), putting the definition of $j_{\mathrm{Y}}^{\mathrm{OuC}}$ and $j_{\mathrm{Y}}^{\mathrm{InC}}$, which are similar to that explained in the previous chapter, and rewriting as

$$j_{\mathrm{Y}}^{total} = \frac{16}{uw\pi^2}\left(J_{out}\left(\cos\left(k_{\mathrm{X}}a_1^{out}\right) - \cos\left(k_{\mathrm{X}}a_2^{out}\right)\right)\sin(k_{\mathrm{Y}}b_m^{out}) + J_{in}\left(\cos\left(k_{\mathrm{X}}a_1^{in}\right) - \cos\left(k_{\mathrm{X}}a_2^{in}\right)\right)\sin(k_{\mathrm{Y}}b_m^{in})\right) \tag{4.3}$$

where $b_m^{out} = 0.5(b_2^{out} + b_1^{out})$, $b_m^{in} = 0.5(b_2^{in} + b_1^{in})$. Similarly, for J_{X}^{total}(X,Y), the term j_{X}^{total} is expressed as

$$j_{\mathrm{X}}^{total} = \frac{16}{uw\pi^2}\left(J_{out}\left(\cos\left(k_{\mathrm{Y}}b_1^{out}\right) - \cos\left(k_{\mathrm{Y}}b_2^{out}\right)\right)\sin(k_{\mathrm{X}}a_m^{out}) + J_{in}\left(\cos\left(k_{\mathrm{Y}}b_1^{in}\right) - \cos(k_{\mathrm{Y}}b_2^{in})\right)\sin(k_{\mathrm{X}}a_m^{in})\right) \tag{4.4}$$

where $a_m^{out} = 0.5(a_2^{out} + a_1^{out})$, $a_m^{in} = 0.5(a_2^{in} + a_1^{in})$. With these expressions, B_{Z}^{II} and B_{Z}^{III} can be obtained using (3.16) and (3.17), respectively. Furthermore, the required changes in the equation of self- and

Table 4.1: Geometrical parameters.

Parameter	Description	Value	Unit
a_2^{out}	Half outermost width of OuC in X-direction	$x/2$	mm
a_1^{out}	Half innermost width of OuC in X-direction	$a_2^{out} - s_{out}$ #1	mm
b_2^{out}	Half outermost width of OuC in Y-direction	$y/2$	mm
b_1^{out}	Half innermost width of OuC in Y-direction	$b_2^{out} - s_{out}$	mm
a_2^{in}	Half outermost width of InC in X-direction	$x_{o-in}/2$	mm
a_1^{in}	Half innermost width of InC in X-direction	$a_2^{in} - s_{in}$ #2	mm
b_2^{in}	Half outermost width of InC in Y-direction	$y_{o-in}/2$	mm
b_1^{in}	Half innermost width of InC in Y-direction	$b_2^{out} - s_{out}$	mm
J_{out}	Equivalent current density in OuC due to I_P	$(I_P N_{out})/(d_w s_{out})$	Amm^{-2}
J_{in}	Equivalent current density in InC due to I_P	$(I_P N_{in})/(d_w s_{in})$	Amm^{-2}

#1 $s_{out} = \left(T_{g-out} + d_w\right) N_{out} - T_{g-out}$.

#2 $s_{in} = \left(T_{g-in} + d_w\right) N_{in} - T_{g-in}$. Here, N_{out} and N_{in} cannot be zero, and the values of T_{g-out} and T_{g-in} can be found using Flowchart-B.

mutual inductances [i.e., (3.20), and (3.22)] are presented in the next subsection.

4.2.2.2 Calculation of Self- and Mutual Inductance and k of the Proposed Coil Structures

For the calculation of self- and mutual inductance of the proposed coils, the necessary changes are done in (3.20) and (3.22), respectively. In (3.20) and (3.22), by replacing $\int$ to $\left(\int_{\text{OuC}} + \int_{\text{InC}}\right)$ (i.e., integration over the surface of OuC and InC in a coil structure), the expression for self- and mutual inductance of the proposed coil structures is given in (4.5) and (4.6), respectively.

$$L_P = \frac{1}{I_P} \sum_{q=1}^{\text{Total turns}} \left(\int_{\text{OuC}}^{S_q} + \int_{\text{InC}}^{S_q} \right) B_Z^{II} \, d\text{S}|_{Z=r_w}. \tag{4.5}$$

$$M = \frac{1}{I_P} \sum_{q=1}^{\text{Total turns}} \left(\int_{\text{OuC}}^{S_q} + \int_{\text{InC}}^{S_q} \right) B_Z^{III} \, d\text{S}|_{\text{Z}=(3d_w/2)+\text{Air gap}}. \tag{4.6}$$

where $q = 1$ is the outermost turn in OuC and InC. Expanding (4.5) gives

$$L_P = \frac{1}{I_P} \left[\sum_{q=1}^{N_{out}} \int_{S_q} B_Z^{II} d\text{S} + \sum_{q=1}^{N_{in}} \int_{S_q} B_Z^{II} d\text{S} \right]_{Z=r_w}. \tag{4.7}$$

By applying integration limits in (4.7), it can be written in the following form as

$$L_P = \frac{1}{I_P} \left[\sum_{q=1}^{N_{out}} \int_{-B_{out}}^{B_{out}} \int_{-A_{out}}^{A_{out}} B_Z^{II} d\text{X} d\text{Y} + \sum_{q=1}^{N_{in}} \int_{-B_{in}}^{B_{in}} \int_{-A_{in}}^{A_{in}} B_Z^{II} d\text{X} d\text{Y} \right]_{Z=r_w} \tag{4.8}$$

where B_{out}, A_{out}, B_{in}, and A_{in} are given as

$$\begin{cases} B_{out} = b_2^{out} - G_{out} \\ A_{out} = a_2^{out} - G_{out} \\ B_{in} = b_2^{in} - G_{in} \\ A_{in} = a_2^{in} - G_{in}. \end{cases} \tag{4.9}$$

where b_2^{out}, a_2^{out}, b_2^{in}, and a_2^{in} can be seen in Figure 5.2(b). The terms G_{out} and G_{in} in (4.9) are the equivalent distances caused by the parameters q, d_w, and the gap between the turns. The expression of G_{out} and G_{in} is given as

$$\begin{cases} G_{out} = \left(T_{g-out} + d_w\right)(q-1) + 0.5d_w \\ G_{in} = \left(T_{g-in} + d_w\right)(q-1) + 0.5d_w. \end{cases} \tag{4.10}$$

Thus, the self-inductance of the rectangular- and square-shaped coil structures obtained using the proposed UCAM can be calculated using (4.8). Similarly, rewriting the mutual inductance expression (4.6) in the form of (4.8) as

$$M = \frac{1}{I_P}\left[\sum_{q=1}^{N_{out}} \int_{-B_{out}}^{B_{out}} \int_{-A_{out}}^{A_{out}} B_Z^{III} d\mathrm{X} d\mathrm{Y} + \sum_{q=1}^{N_{in}} \int_{-B_{out}}^{B_{out}} \int_{-A_{in}}^{A_{in}} B_Z^{III} d\mathrm{X} d\mathrm{Y}\right]_{\mathrm{Z}=(3d_w/2)+\text{Air gap}}. \tag{4.11}$$

By using (4.11), the mutual inductance between the coils at different ΔZ can be calculated. Furthermore, to calculate the mutual inductance for the horizontal misalignment in the X-direction at any air gap, integration limits in (4.11) are modified, and the expression is given as

$$M = \frac{1}{I_P}\left[\sum_{q=1}^{N_{out}} \int_{-B_{out}}^{B_{out}} \int_{-(A_{out}-\Delta\mathrm{X})}^{(A_{out}+\Delta\mathrm{X})} B_Z^{III} d\mathrm{X} d\mathrm{Y} + \sum_{q=1}^{N_{in}} \int_{-B_{in}}^{B_{in}} \int_{-(A_{in}-\Delta\mathrm{X})}^{(A_{in}+\Delta\mathrm{X})} B_Z^{III} d\mathrm{X} d\mathrm{Y}\right]_{\mathrm{Z}=(3d_w/2)+\text{Air gap}} \tag{4.12}$$

where ΔX is the change in position of the Rx coil structure in the X-direction from the perfect aligned place (i.e., from 0 mm). Similarly, the mutual inductance for the horizontal misalignment in the Y-direction at any air gap is calculated using (4.13).

$$M = \frac{1}{I_P}\left[\sum_{q=1}^{N_{out}} \int_{-(B_{out}+\Delta\mathrm{Y})}^{(B_{out}+\Delta\mathrm{Y})} \int_{-A_{out}}^{A_{out}} B_Z^{III} d\mathrm{X} d\mathrm{Y} + \sum_{q=1}^{N_{in}} \int_{-(B_{in}+\Delta\mathrm{Y})}^{(B_{in}+\Delta\mathrm{Y})} \int_{-A_{in}}^{A_{in}} B_Z^{III} d\mathrm{X} d\mathrm{Y}\right]_{\mathrm{Z}=(3d_w/2)+\text{Air gap}} \tag{4.13}$$

where ΔY is the change in position of the Rx coil structure in the Y-direction from the perfect aligned position (i.e., from 0 mm).

Thus, with (4.8) and (4.11)-(4.13), k of the proposed coils for different misalignments can be calculated analytically using (2.1). Here, the obtained expression of k contains all the parameters defined in (4.1).

Moreover, the total required length of wire in a coil structure (l_{coil}) is calculated by adding the length of wire used in OuC and InC, and the expression is given as

$$l_{\text{coil}} = 4\left[\left(a_1^{out}+b_1^{out}\right)N_{out}+\sum_{q_t=1}^{N_{out}}\frac{\pi}{2}\left(\left(T_{g-out}+d_w\right)(q_t-1)+\frac{d_w}{2}\right)\right]+4\left[\left(a_1^{in}+b_1^{in}\right)N_{in}+\sum_{q_t=1}^{N_{in}}\frac{\pi}{2}\left(\left(T_{g-in}+d_w\right)(q_t-1)+\frac{d_w}{2}\right)\right] \tag{4.14}$$

where $q_t = 1$ represents the innermost turn in OuC and InC. The derivation of (4.14) is given in Appendix C. The upcoming subsection explains flowchart-A, flowchart-B, and flowchart-C, which is used to calculate the coil parameters to obtain the coil system of improved k. Further, by using this 3-D analytical model, k is calculated (using the obtained coil parameters) and is verified with 3-D FEA.

4.2.3 Selection Procedure of T_{g-out}, T_{g-in} and Calculation of Coil Parameters

In this subsection, the coil parameters are calculated for the constraints (given in (3.34) and values in Table 3.2) to achieve the maximum possible k for the selected configurations of T_{g-out} and T_{g-in}, which gives the arrangement of a coil structure. The possible configurations of T_{g-out} and T_{g-in} depend on the maximum value of m and n, respectively, which are calculated using flowchart-A (based on Section 3.5.4), as shown in Figure 4.6. From flowchart-A, considering the value of Z_a is equal to one (for simplicity, during the winding in real-time), the condition to achieve L_{req} is not fulfilled at $p = 2$ due to inner space constraint (i.e., type-III). Hence, the maximum value of m and n is taken as two. With this m and n values in flowchart-B, as shown in Figure 4.7, a total of eight configurations of T_{g-out} and T_{g-in} is possible, which may give the improved k compared with conventional coils for the constraints given in (3.34). These eight configurations are named cases 1–8 (as listed in Table 4.2).

For each configuration of T_{g-out} and T_{g-in}, flowchart-C (as shown in Figure 4.8) calculates the

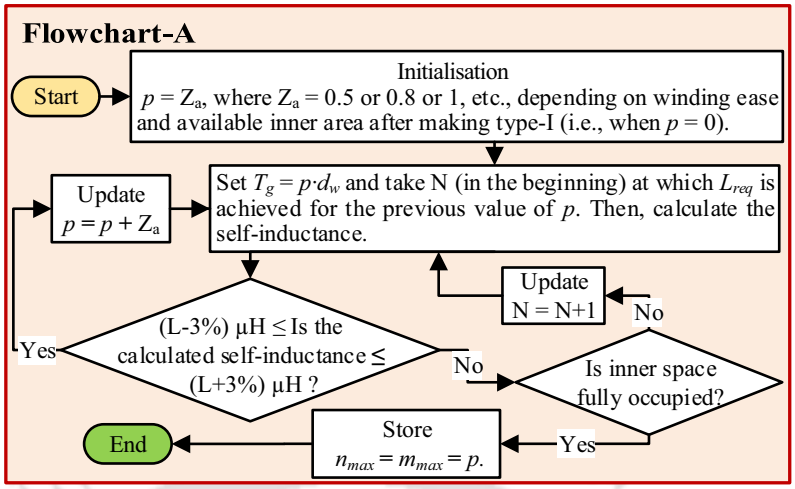

Figure 4.6: Flowchart for calculating the value of m_{max} and n_{max}.

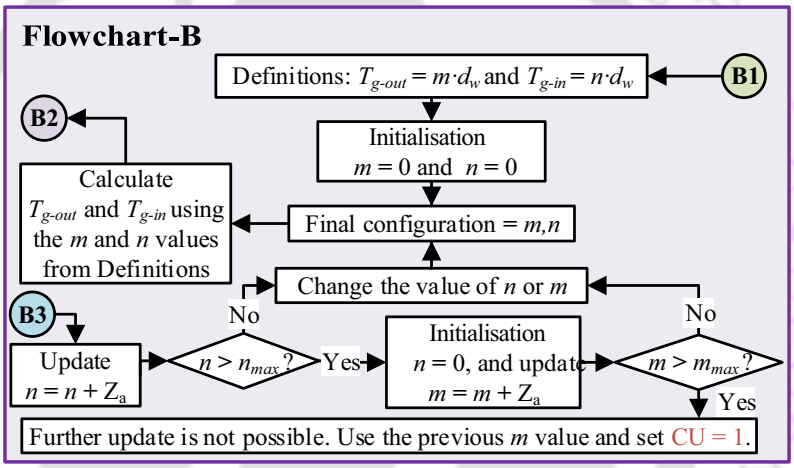

Figure 4.7: Flowchart for selecting the possible configurations of T_{g-out} and T_{g-in}. Here, **B1–B3** are the nodes of flowchart in Figure 4.4 and flowchart-C.

coil parameters to find the maximum value of k. Flowchart-C mainly has two parts–Outer loop and Inner loop. Outer loop deals with OuC, whereas inner loop with InC. These loops are based on the observations made for the conventional coils in Section 3.5.4. For each set of T_{g-out} and T_{g-in}, outer loop finds the possible N_{out} based on N. At each N_{out}, inner loop gives the possible N_{in}, and with chosen C_{gx}, C_{gy}, x_{o-in}, and y_{o-in} at each N_{in}, it verifies the considered constraints [given in (3.34)] and then calculates k. Finally, flowchart-C gives the highest k among the obtained maximum k at each N_{out}.

Now, for $T_{g-out} = 0 \cdot d_w$ and $T_{g-in} = 0 \cdot d_w$ (i.e., case 1), Figure 4.9 shows the variation of coil parameters to find the maximum possible k for the considered constraints according to the steps given in

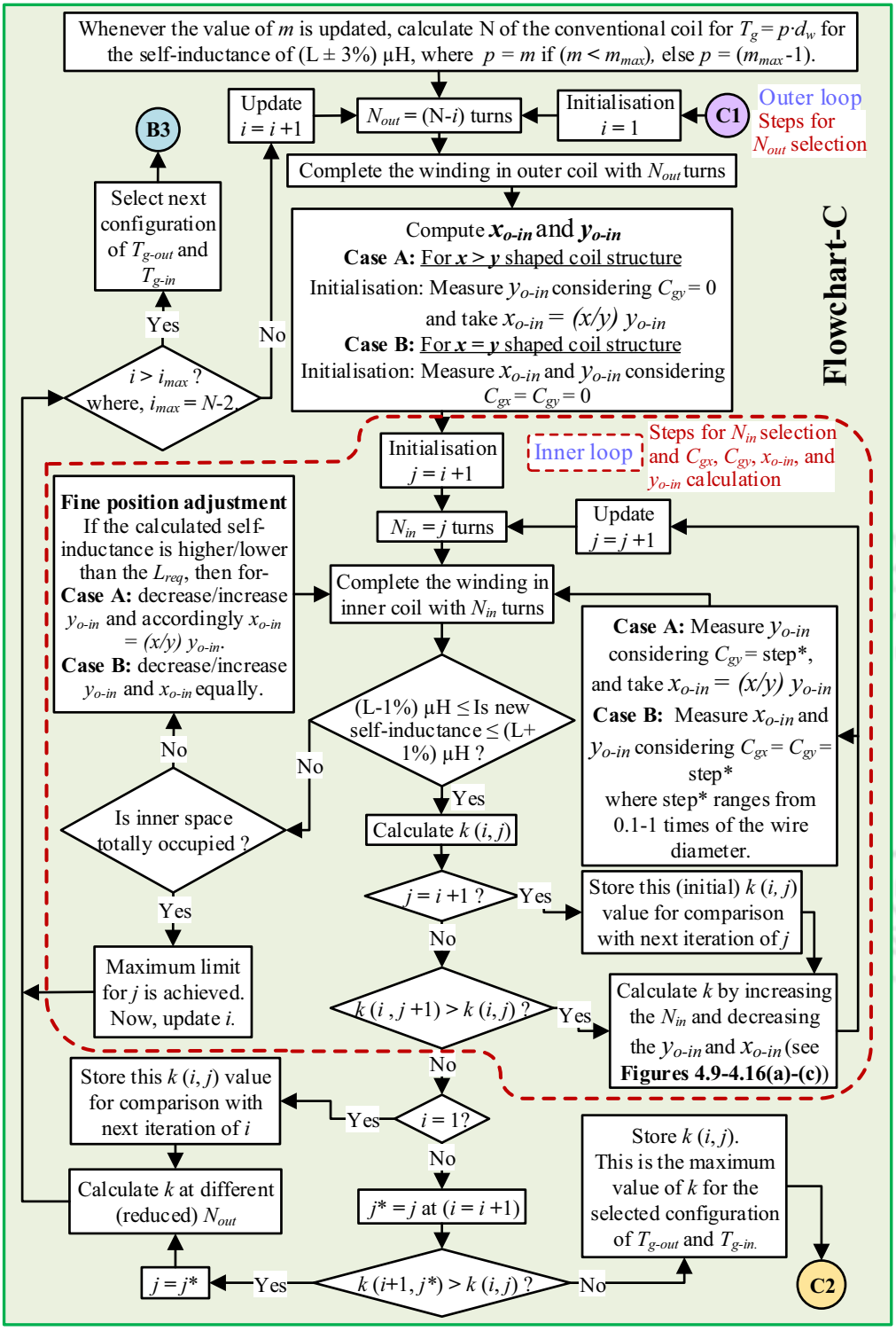

Figure 4.8: Flowchart for calculating the value of coil parameters to achieve maximum k for the selected configuration of $T_{g\text{–}out}$ and $T_{g\text{–}in}$. Here, **B3, C1**, and **C2** are the nodes of flowcharts in Figures 4.4 and 4.7.

flowchart-C. For getting L_{req} at different a N_{out} (selected from outer loop in flowchart-C), N_{in}, $x_{o\text{–}in}$, and $y_{o\text{–}in}$ are varied (according to inner loop in flowchart-C), as shown in Figure 4.9(a)–(c). From

Table 4.2: Specification of obtained coil structures using the proposed UCAM having outer dimensions of 400 mm × 300 mm.

Coil system	T_{g-out} $(m \cdot d_w)$	T_{g-in} $(n \cdot d_w)$	N_{out}	N_{in}	x_{o-in} (mm)	y_{o-in} (mm)	C_{gx} (mm)	C_{gy} (mm)	3-D Analytical L_P=L_S (μH)	3-D Analytical k at 150 mm	3-D FEA L_P, L_S (μH)	3-D FEA k at 150 mm	Error in k w.r.t. 3-D FEA (%)
case 1	$0{\cdot}d_w$	$0{\cdot}d_w$	7	5	144.5	109	36.6	22.1	79.75	0.1514	80.11, 80.90	0.1495	1.27
case 2	$0{\cdot}d_w$	$1{\cdot}d_w$	3	10	181	136	10.9	5.9	80.22	0.1617	80.66, 80.89	0.1596	1.32
case 3	$0{\cdot}d_w$	$2{\cdot}d_w$	4	11	182.5	137.5	6.7	1.7	81.18	**0.1710**	80.06, 80.66	**0.1701**	0.53
case 4	$1{\cdot}d_w$	$0{\cdot}d_w$	11	3	105	79	38.3	14.3	80.02	0.1618	80.44, 80.57	0.1597	1.31
case 5	$1{\cdot}d_w$	$1{\cdot}d_w$	9	6	121.5	91.5	32.6	12.6	80.12	0.1629	80.35, 80.46	0.1614	0.93
case 6	$1{\cdot}d_w$	$2{\cdot}d_w$	8	8	140	105	19.5	4.5	80.85	**0.1667**	80.51, 80.69	**0.1655**	0.73
case 7	$2{\cdot}d_w$	$0{\cdot}d_w$	9	8	105	79	27.5	3.5	80.31	0.1487	80.25, 80.48	0.1475	0.81
case 8	$2{\cdot}d_w$	$1{\cdot}d_w$	3	11	174	130.5	7.1	0.6	80.56	**0.1577**	80.29, 80.48	**0.1567**	0.64

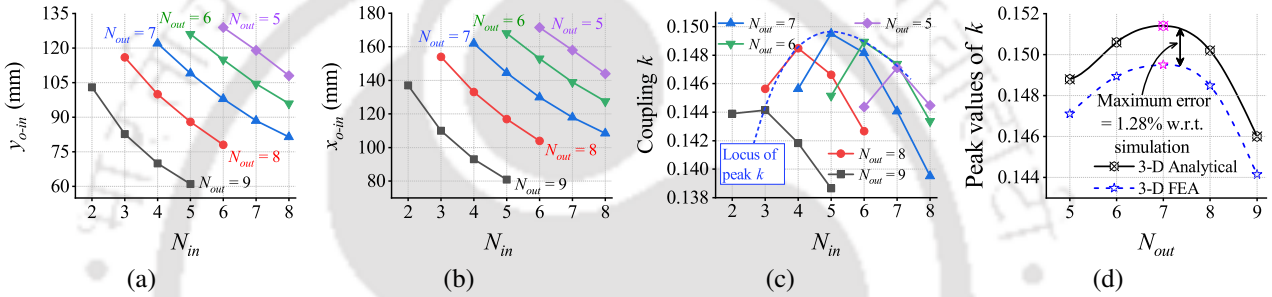

Figure 4.9: Coil parameters variations for finding the maximum value of k for case 1 coil structure. [(a) y_{o-in} versus N_{in}, (b) x_{o-in} versus N_{in}, (c) k versus N_{in}] for different N_{out} to get L_{req} and (d) Peak values of k [obtained from Figure 4.9(c)] versus N_{out}.

Figure 4.9(a) and (b), it can be seen that for each N_{out}, as N_{in} increases, a decrease in y_{o-in} and x_{o-in} is observed. This decrease is due to the use of more inner space by N_{in}. Figure 4.9(c) gives the variation of k with respect to N_{in} for each selected N_{out}, which helps to find the maximum k at each N_{out}. Finally, Figure 4.9(d) shows the locus of peak values of k obtained at each N_{out} where the peak of the curve is at N_{out} = 7. At this N_{out}, the obtained k is the highest k for case 1. The values of the remaining coil parameters at N_{out} = 7 [from Figure 4.9(a)–(c)] are tabulated in Table 4.2.

Similarly, for other configurations of T_{g-out} and T_{g-in} (i.e., cases 2–8), the value of coil parameters is calculated using flowchart-C, and its variations are given in Figures 4.10-4.16, respectively. From Figures 4.10(d)-4.16(d), a similar variation in k (with respect to N_{out}) can be seen for each case where the peak of these curves gives the maximum k. At this maximum k, the value of coil parameters for cases 2–8 is summarised in Table 4.2 from Figures 4.10-4.16, respectively. Figure 4.17 illustrates the obtained coil structures based on the coil parameters given in Table 4.2. The results presented

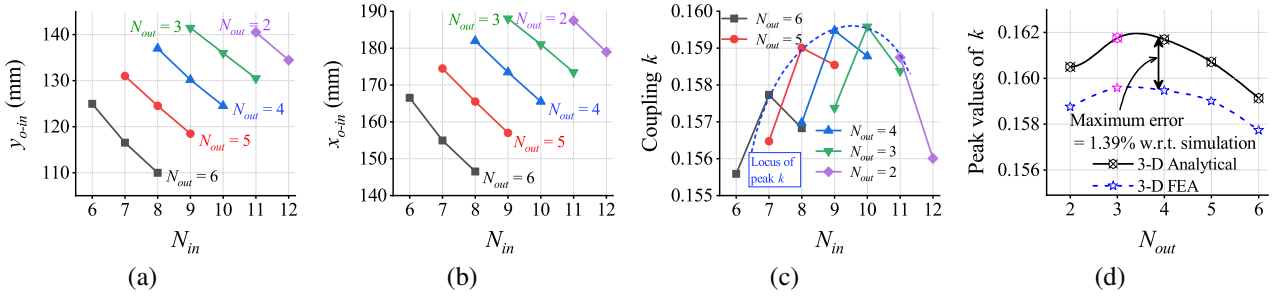

Figure 4.10: Coil parameters variations for finding the maximum value of k for case 2 coil structure. [(a) y_{o-in} versus N_{in}, (b) x_{o-in} versus N_{in}, (c) k versus N_{in}] for different N_{out} to get L_{req}. (d) Peak values of k [obtained from Figure 4.10(c)] versus N_{out}.

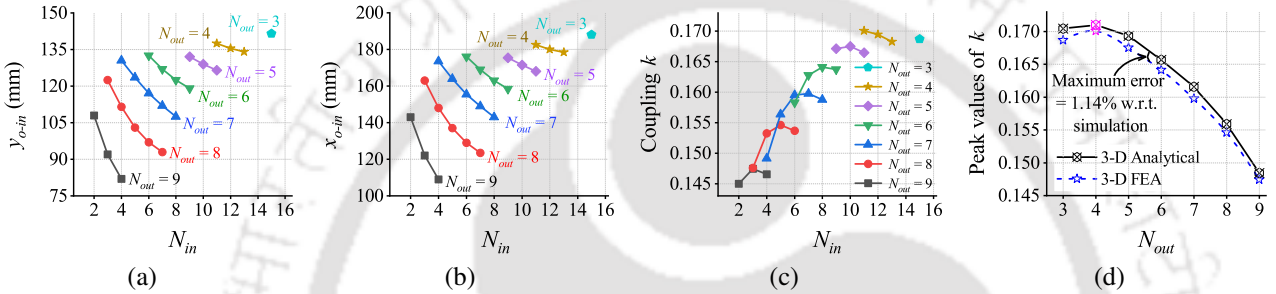

Figure 4.11: Coil parameters variations for finding the maximum value of k for case 3 coil structure. [(a) y_{o-in} versus N_{in}, (b) x_{o-in} versus N_{in}, (c) k versus N_{in}] for different N_{out} to get L_{req}. (d) Peak values of k [obtained from Figure 4.11(c)] versus N_{out}.

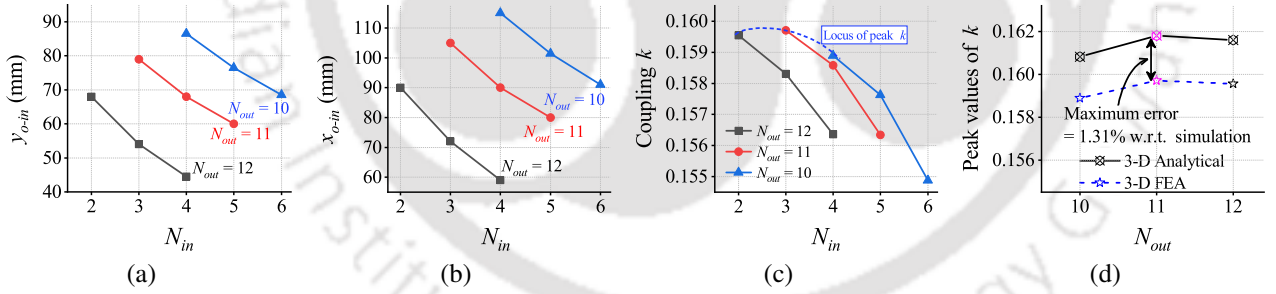

Figure 4.12: Coil parameters variations for finding the maximum value of k for case 4 coil structure. [(a) y_{o-in} versus N_{in}, (b) x_{o-in} versus N_{in}, (c) k versus N_{in}] for different N_{out} to get L_{req}. (d) Peak values of k (obtained from Figure 4.12(c)) versus N_{out}.

in Table 4.2 shows that the coil structure having the maximum possible value of n for each value of m gives higher k (i.e., cases 3, 6, and 8). Moreover, from Table 4.2, it is seen that the case 3 coil system has the highest k among all the cases. Furthermore, Table 4.2 shows the comparison of k obtained from 3-D analytical model and 3-D FEA, which are in good agreement with the error of 0.53%–1.32% for all the cases. Table 4.3 summarises the improvement in k (in %) for the obtained cases using the proposed UCAM with respect to type-I and type-II coil systems at the 150-mm air

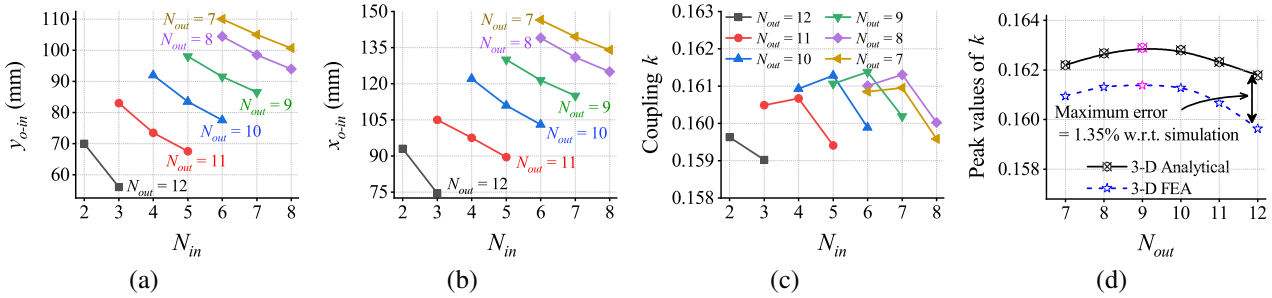

Figure 4.13: Coil parameters variations for finding the maximum value of k for case 5 coil structure. [(a) y_{o-in} versus N_{in}, (b) x_{o-in} versus N_{in}, (c) k versus N_{in}] for different N_{out} to get L_{req}. (d) Peak values of k [obtained from Figure 4.13(c)] versus N_{out}.

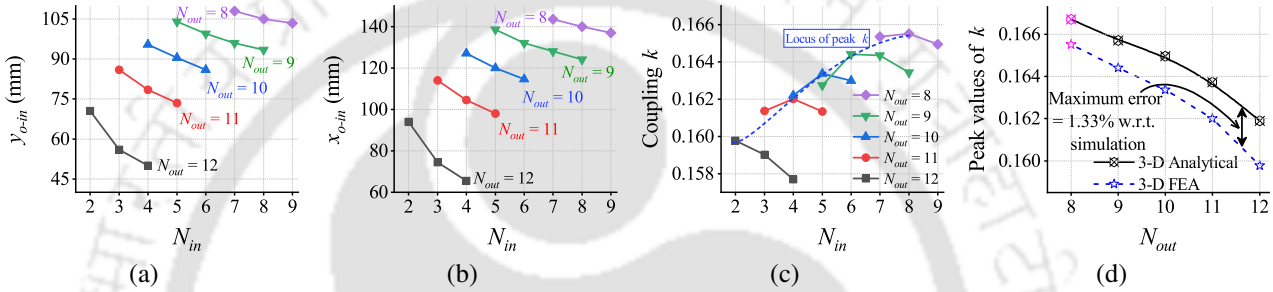

Figure 4.14: Coil parameters variations for finding the maximum value of k for case 6 coil structure. [(a) y_{o-in} versus N_{in}, (b) x_{o-in} versus N_{in}, (c) k versus N_{in}] for different N_{out} to get L_{req}. (d) Peak values of k [obtained from Figure 4.14(c)] versus N_{out}.

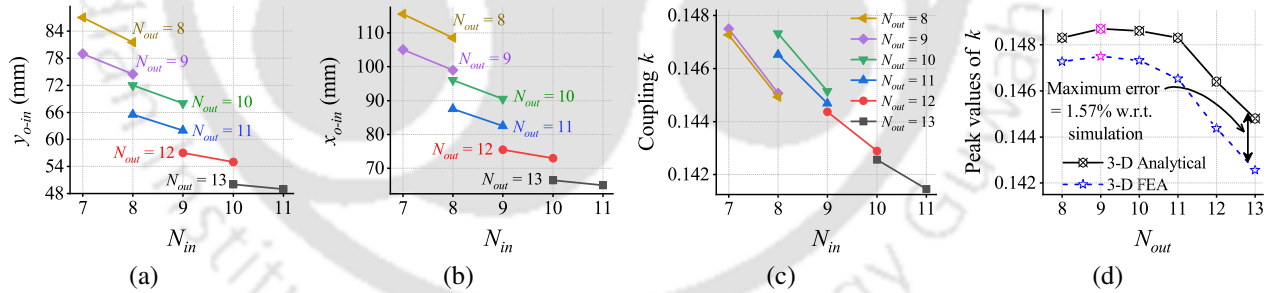

Figure 4.15: Coil parameters variations for finding the maximum value of k for case 7 coil structure. [(a) y_{o-in} versus N_{in}, (b) x_{o-in} versus N_{in}, (c) k versus N_{in}] for different N_{out} to get L_{req}. (d) Peak values of k [obtained from Figure 4.15(c)] versus N_{out}.

gap. Since in the proposed UCAM, a difference of one is considered in p (in flowchart-A, Z_a = 1 is selected) for winding ease, the conventional coils having the same difference of p-value (p = 0 and 1 that gives type-I and type-II coils, respectively) is chosen for a fair comparison. From Table 4.3, 10.16%–27.04% and 0.26%–8.83% improvements in k are observed for the obtained cases compared with type-I and type-II coil systems, respectively.

Now, if the noninteger p is also considered in the conventional coil design to find the highest

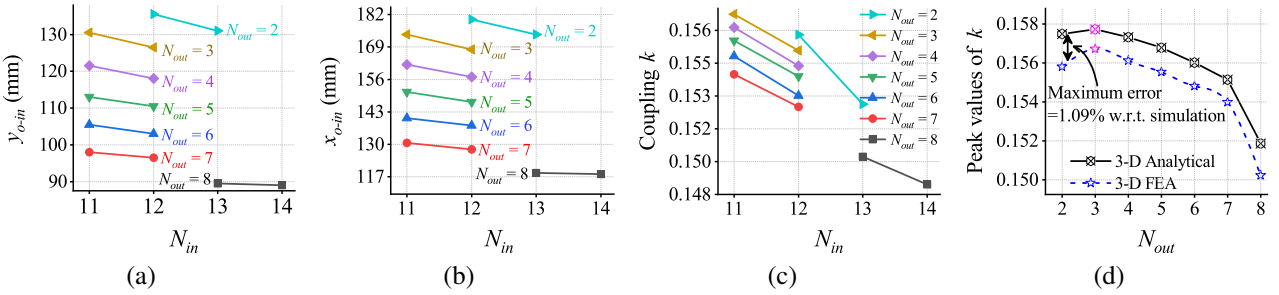

Figure 4.16: Coil parameters variations for finding the maximum value of k for case 8 coil structure. [(a) y_{o-in} versus N_{in}, (b) x_{o-in} versus N_{in}, (c) k versus N_{in}] for different N_{out} to get L_{req}. (d) Peak values of k [obtained from Figure 4.16(c)] versus N_{out}.

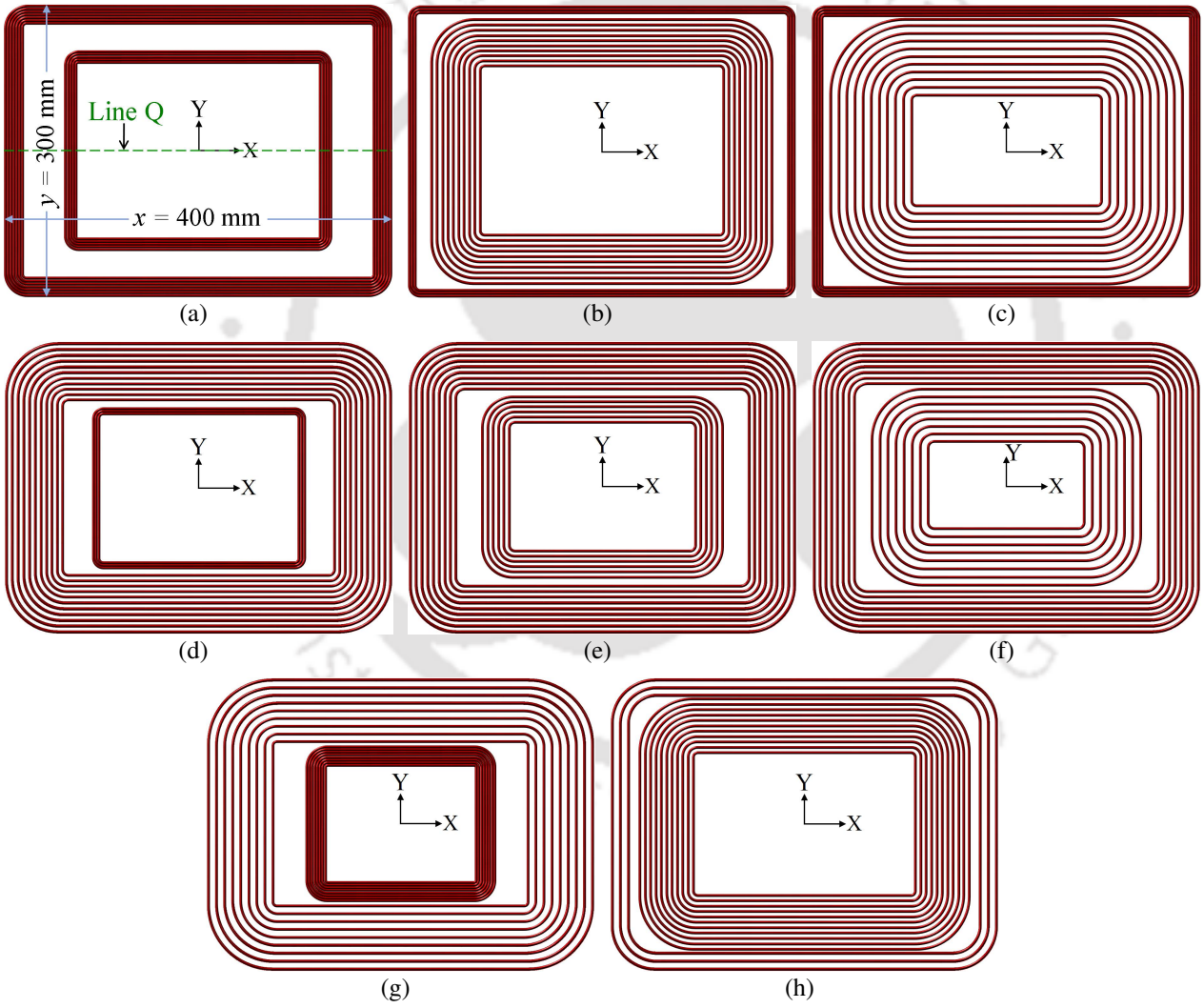

Figure 4.17: Illustration of the coil structures obtained using the coil parameters given in Table 4.2 for (a) case 1, (b) case 2, (c) case 3, (d) case 4, (e) case 5, (f) case 6, (g) case 7, and (h) case 8. It should be noted that InC and OuC are connected in series, and each coil structure ends with two terminals.

Table 4.3: Improvement in k of coil structures obtained from the proposed UCAM with respect to type-I, type-II, and type-H at the 150-mm air gap.

Improvement with respect to	Improvement in k (%) of different coil structures							
	case 1	case 2	case 3	case 4	case 5	case 6	case 7	case 8
type-I	11.65	19.19	**27.04**	19.27	20.54	23.60	10.16	17.03
type-II	–	2.11	**8.83**	2.18	3.26	5.89	–	0.26
type-H	–	0.19	**6.78**	0.25	1.32	3.89	–	–

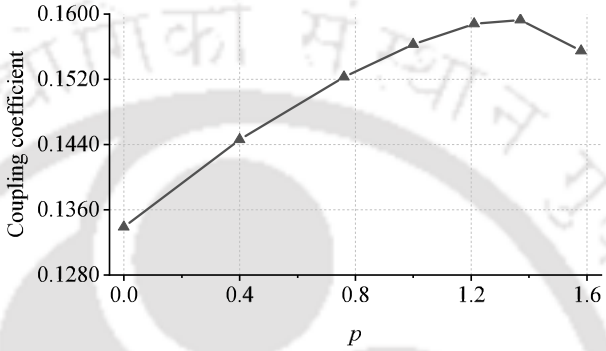

Figure 4.18: Factor k versus p plot to find the highest k conventional coil design.

possible k, then do the obtained coil structures still show improvement in k? In this context, different conventional coils are designed by using the noninteger value of p as well for the constraints given in (3.34) (and the values are in Table 3.2). Figure 4.18 shows the variation of obtained k for different values of p at which the constraints are fulfilled. From Figure 4.18, it can be seen that the highest k (0.1593) is obtained at p = 1.37 and N = 15, and this coil system is named type-H. For analysing the improvement in k of type-H coil system with k of the obtained coil systems (given in Table 4.2), the results are summarised in Table 4.3. From Table 4.3, it is found that the cases 2–6 coil systems still show improvement in k with respect to type-H coil system. Among these coil systems, the case 3 coil system shows the highest improvement (6.78%) in k. From the discussions, it can be said that the coils obtained using the proposed UCAM improve the factor k compared with those designed from CCAM (by using integer or noninteger p). Since the highest k conventional coil is obtained using the noninteger p-value, the type-H coil is also included in the upcoming theoretical analysis. However, due to winding ease in the prototyping (explained in Section 4.3.1), the coils designed using the integer p-value are considered for the experimental verification. In the next subsection, interoperability between the proposed and conventional coils, and among the different proposed coils

Table 4.4: Factor k of the coil system having the conventional coil structures and the obtained coil structures using the proposed UCAM.

Rx \ Tx	case 1	case 2	case 3	case 4	case 5	case 6	case 7	case 8
type-I	0.1409	0.1446	**0.1480**	0.1441	0.1444	0.1452	0.1352	0.1417
type-II	0.1528	0.1580	**0.1630**	0.1580	0.1586	0.1606	0.1502	0.1564
type-H	0.1532	0.1584	**0.1644**	0.1592	0.1598	0.1620	0.1526	0.1577

Table 4.5: Factor k of the coil system having different combinations of Tx and Rx coil structures obtained using the proposed UCAM.

Tx \ Rx	case 1	case 2	case 3	case 4	case 5	case 6	case 7	case 8
case 1	0.1495	0.1540	0.1585	0.1539	0.1544	0.1562	0.1457	0.1526
case 2	0.1540	0.1596	0.1642	0.1595	0.1601	0.1618	0.1515	0.1578
case 3	0.1585	0.1642	**0.1701**	0.1646	0.1656	0.1676	0.1574	0.1630
case 4	0.1539	0.1595	0.1646	0.1597	0.1604	0.1622	0.1524	0.1579
case 5	0.1544	0.1601	0.1656	0.1604	0.1614	0.1634	0.1533	0.1591
case 6	0.1562	0.1618	0.1676	0.1622	0.1634	0.1655	0.1556	0.1609
case 7	0.1457	0.1515	0.1574	0.1524	0.1533	0.1556	0.1475	0.1513
case 8	0.1526	0.1578	0.1630	0.1579	0.1591	0.1609	0.1513	0.1567

is studied.

4.2.4 Interoperability

In this subsection, interoperability between the proposed and conventional coils is studied. In a coil system, if the type-I, type-II, or type-H coil is used as an Rx and one of the obtained coil structures (from the proposed UCAM) is used as a Tx, k of such coil systems has been summarised in Table 4.4 at the 150-mm air gap. From Table 4.4, it can be seen that the maximum k for type-I, type-II, or type-H Rx coil is achieved with case 3 Tx coil among the cases 1–8 Tx coils. Since the unipolar coils have been taken identical, k of the coil system remains the same if the type-I, type-II, or type-H coil is used as a Tx, while one of the obtained coil structures as an Rx.

Furthermore, k of various coil systems is studied, which can have different combinations (using cases 1–8) of Tx and Rx coil structures. The factor k of such coil systems is summarised in Table 4.5. From Table 4.5, it is seen that the maximum k obtained from the coil system having identical Tx and Rx coil structures (here, case 3 coil system) is the highest among k obtained from the coil systems

Table 4.6: Comparison of required length and weight of the Litz wire along with calculated AC resistance of the coils, $\eta_{t,uc}$, and S_{max} at the 100-kHz operating frequency for different coils.

Parameter	type-I	type-II	type-H	case 1	case 2	case 3	case 4	case 5	case 6	case 7	case 8
Total wire length (m)	25.38	27.87	28.64	27.80	28.94	30.00	28.92	29.68	30.31	29.39	28.58
Total weight (Kg)	0.717	0.788	0.810	0.785	0.818	0.848	0.817	0.839	0.857	0.831	0.808
ⓐ $R_{dc,P} = R_{dc,S}$ ($m\Omega$)	78.33	86.03	88.41	85.80	89.32	92.58	89.26	91.62	93.57	90.73	88.23
ⓑ $R_{pe,P} = R_{pe,S}$ ($m\Omega$)	30.82	17.35	16.30	30.74	20.22	21.09	18.98	18.02	17.53	22.01	17.05
(ⓐ + ⓑ) $R_P = R_S$ ($m\Omega$)	109.15	103.38	104.71	116.54	109.54	113.67	108.24	109.64	111.10	112.74	105.28
$\eta_{t,uc}$ (%) at $R_{L,\text{eq}} = 10\ \Omega$	60.69	68.95	69.45	64.14	68.52	70.28	68.83	69.00	69.74	64.46	68.61
S_{max} (VA)	90.46	124.47	128.19	112.50	129.09	145.55	128.90	131.51	138.56	109.70	123.87

having different combinations of Tx and Rx coil structures.

The next subsection investigates the effect of the different number of turns for the obtained coil structures on the required length of the wire. After that, it calculates the coil AC resistance for each case based on the obtained length of the wire and compares them with the AC resistance of the conventional coils. Finally, it examines the impact of increased k and obtained coil AC resistance simultaneously on the transmission efficiency and power transfer capability of each coil system.

4.2.5 Impact of Improved k on Transmission Efficiency and Power Transfer Capability

Different coil structures obtained here (see Table 4.2) possess different gaps between the turns along with the number of turns in OuC and InC. These combinations may increase the length of the Litz wire used in the obtained coil structures and, hence, the AC resistance of these coils, compared with the conventional coils. In this context, the total required length of the Litz wire used in a coil system (both Tx and Rx) is calculated using (4.14) for each case and is summarised in Table 4.6. The total weight of the Litz wire for each case is also included in Table 4.6, which is calculated by measuring the weight of a unit length Litz wire used. The dc resistance, proximity-effect resistance, and AC resistance of the Tx and Rx coils for each case are calculated using (3.28), (3.30), and (3.27), respectively, and are summarsied in Table 4.6. From Table 4.6, it can be seen that all the presented coil structures require different wire lengths, and their dc resistance varies in proportional to the wire length. However, the proximity-effect resistance may increase or decrease in proportional to the wire length because it also depends on the different winding arrangements (spacing between the turns and number of turns) and the selected operating frequency. Therefore, the variation in AC resistance of

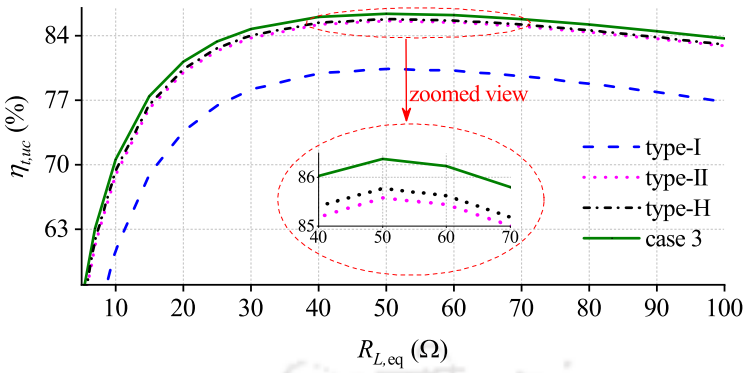

Figure 4.19: Comparison of transmission efficiency of different uncompensated coils for a wide variation of $R_{L,\mathrm{eq}}$.

the coil at 100-kHz operating frequency need not be in proportional to the wire length. From Tables 4.3 and 4.6, it can be seen that with maximum improvement in k of 27.04%, 8.83%, and 6.78% (for case 3 coil system), the total used wire length is increased by 18.20%, 7.64%, and 4.75% with respect to type-I, type-II, and type-H coil systems, respectively. As a result, the AC resistance of the case 3 coil system is increased by 4.14%, 9.95%, and 8.56% with respect to type-I, type-II, and type-H coil systems, respectively. Hence, it is essential to investigate the simultaneous effect of improvement in k and increment in resistance of the obtained coil structures with respect to conventional coils on transmission efficiency and power transfer capability of each coil system.

The $\eta_{t,uc}$ expression (3.33) shows that for a fixed value of ω, $R_{L,\mathrm{eq}}$, R_P, R_S, L_P, and L_S, higher k results in higher $\eta_{t,uc}$ [25, 33]. However, with the increment in coil resistance, does the improved k increase $\eta_{t,uc}$? In this context, equation (3.33) is used to examine the effect of both. In (3.33), $R_{L,\mathrm{eq}}$ is kept 10 Ω (for an example; also used in the previous chapter), while remaining parameters are taken from Tables 4.2 and 4.6 for each case and the results are included in Table 4.6. From Table 4.6, it can be seen that despite an increase in resistance along with improvement in k, $\eta_{t,uc}$ of case 3 coil system is increased to 15.80%, 1.93%, and 1.20% with respect to type-I, type-II, and type-H coil systems, respectively. Furthermore, to verify the improvement in $\eta_{t,uc}$ over a wide range of $R_{L,\mathrm{eq}}$ for the case 3 coil system compared with type-I, type-II, and type-H coil systems, $R_{L,\mathrm{eq}}$ in (3.33) is varied from 5 to 100 Ω, as shown in Figure 4.19. From Figure 4.19, it can be seen that the case 3 coil system has improved $\eta_{t,uc}$ throughout the $R_{L,\mathrm{eq}}$ variation compared with type-I, type-II, and type-H coil systems.

Furthermore, the effect of increment in coil AC resistance on power transfer capability can be

investigated using (4.15). The expression of the active power transferred to the Rx coil (P_{load}) in (4.15) is obtained using (2.27) and (2.32).

$$P_{load} = S_{max} Q_S = (\omega {I_P}^2 k^2 L_P) Q_S \tag{4.15}$$

Here, the meaning of each symbol is the same as explained in Chapter 2. In (4.15), Q_S is the only parameter which contains the term of coil AC resistance because Q_S is $\{\omega L_S/(R_S + R_{L,\text{eq}})\}$ for series and $\{(R_S + R_{L,\text{eq}})/\omega L_S\}$ for parallel compensations. Here, the total resistance in both the compensations is $(R_S + R_{L,\text{eq}})$. Usually, $R_{L,\text{eq}}$ is much higher than R_S [here, 10 Ω ($R_{L,\text{eq}}$) ≫ 0.1267 Ω (R_S of case 3)]. Therefore, the impact of increment in coil AC resistance R_S (given in Table 4.6) on Q_S is insignificant and, hence, on P_{load}. Further, with the considered constraints for improving the factor k, Q_S remains the unchanged irrespective of the compensation circuits (as discussed in the previous chapter). Thus, P_{load} increases in proportion to S_{max}. S_{max} for each case is summarised in Table 4.6, which is calculated from (3.32) at I_P = 10 A and the operating frequency of 100 kHz. From Table 4.6, it is observed that S_{max} of case 3 system is enhanced by 60.90%, 16.94%, and 13.54% compared with type-I, type-II, and type-H coil systems, respectively.

Now, the question is; does the case 3 coil structure has a lower peak B_{leak} nearby coil as well, compared with other obtained cases? In this context, the peak leakage magnetic field of different coil structures is studied in the subsequent subsection.

4.2.6 Leakage Magnetic Field

According to the International Commission on Non-Ionizing Radiation Protection (ICNIRP) guidelines for the general public, the human body should not be exposed to a peak B_{leak} greater than 27 μT [69]. In this context, to determine the safe operating zone while charging, the peak B_{leak} is calculated at various distances in the X- and Y-axis directions away from the centre of the Tx coil, as shown in Figure 4.20. Figure 4.20 shows a 3-D FEA model that is developed by considering the worst possible case of misalignment (i.e., $k \approx 0$ or can say the Tx coil is in operation without Rx coil). With this model, the peak B_{leak} generated by the Tx coil at $10\sqrt{2}$ A (peak) current is calculated for different coil structures (proposed and conventional) at various distances (marked in Figure 4.20). The obtained results are summarised in Table 4.7, and the variation in peak B_{leak} at various distances

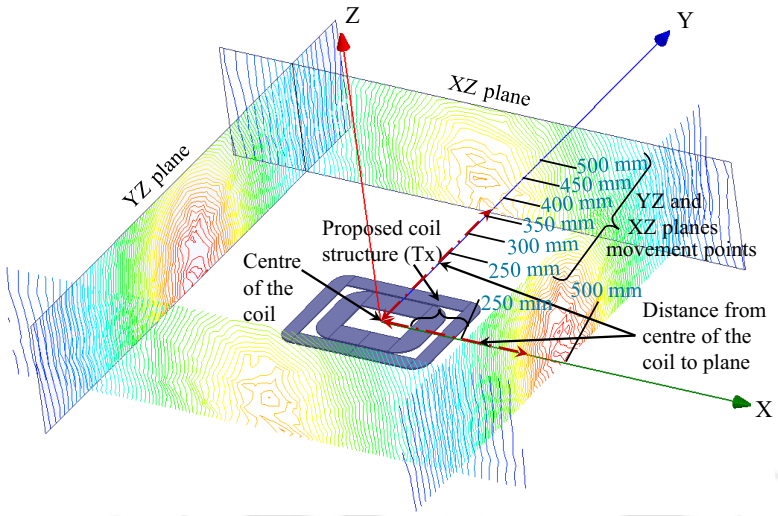

Figure 4.20: 3-D FEA model for calculation of peak B_{leak} generated by Tx coil.

Table 4.7: Peak leakage magnetic field comparison.

Distance of XZ & YZ planes from the centre of coil	Peak B_{leak} (μT)										
	type-I	type-II	type-H	case 1	case 2	case 3	case 4	case 5	case 6	case 7	case 8
250 mm	288.63	255.48	225.83	264.35	244.55	252.30	251.28	239.74	240.90	193.11	215.99
300 mm	110.07	101.06	90.78	104.40	100.36	101.22	100.05	96.66	100.77	81.65	92.69
350 mm	56.81	51.62	48.10	54.85	52.81	53.61	53.43	51.75	51.74	43.54	48.91
400 mm	33.40	31.11	28.77	32.65	31.72	31.87	31.83	31.57	30.91	26.55	29.50
450 mm	21.62	20.41	19.10	20.98	20.60	20.71	21.14	20.13	20.38	17.47	19.41
500 mm	14.70	14.04	13.14	14.53	14.17	14.35	14.25	14.03	13.94	12.12	13.44

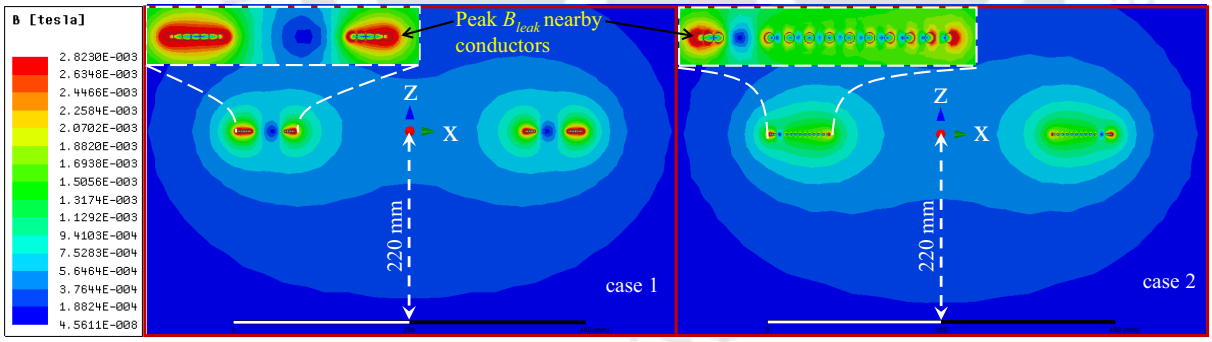

Figure 4.21: Magnetic field distribution on the XZ plane along Line Q [shown in Figure 4.17(a)] of case 1 and case 2 coils for the excitation current of $10\sqrt{2}$ A (peak).

can be found for each case.

In the proposed coil structure, the cancellation of peak B_{leak} nearby conductors in the OuC or InC happens according to the different spacings between the turns (as in type-I and type-II). Further, the cancellation of peak B_{leak} also happens between the OuC and InC due to the total number of turns in OuC and InC. Furthermore, a total number of turns in OuC and InC helps to cancel the peak B_{leak}

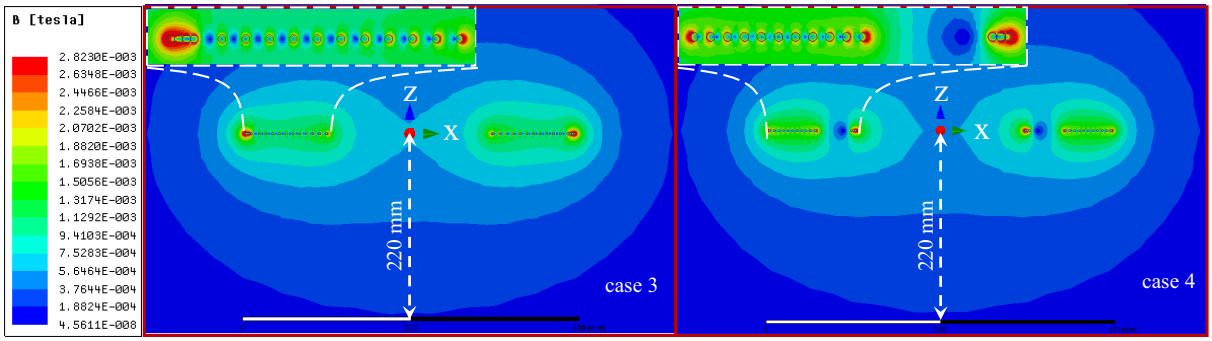

Figure 4.22: Magnetic field distribution on the XZ plane along Line Q of case 3 and case 4 coils for the excitation current of $10\sqrt{2}$ A (peak).

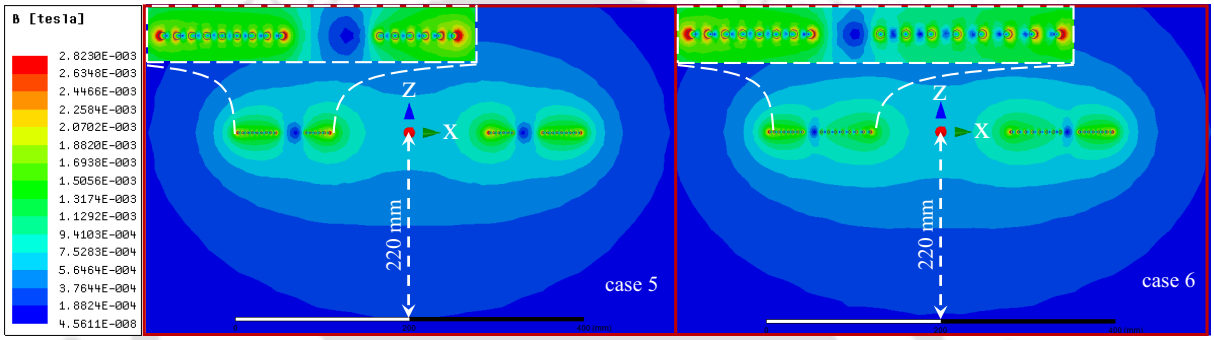

Figure 4.23: Magnetic field distribution on the XZ plane along Line Q of case 5 and case 6 coils for the excitation current of $10\sqrt{2}$ A (peak).

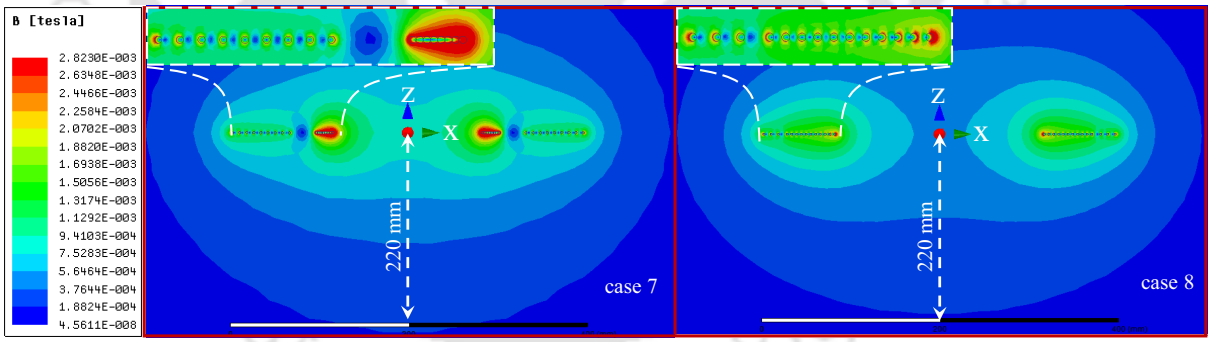

Figure 4.24: Magnetic field distribution on the XZ plane along Line Q of case 7 and case 8 coils for the excitation current of $10\sqrt{2}$ A (peak).

between the OuC and InC. Thus, the simultaneous effect of the different number of turns and the spacing between the turns used in the InC and OuC, and the space between the InC and OuC of the obtained cases 1–8 on the peak B_{leak} nearby the conductors can be well understood from Figures 4.21 to 4.24. The magnetic field distribution of each case, as shown in Figures 4.21 to 4.24, is obtained from the 2-D simulation in ANSYS Maxwell. From the magnetic field distribution of cases 1–8 (Figures 4.21 to 4.24), it can be seen that the case 1 has a higher peak B_{leak} nearby OuC compared

with the other cases. The higher peak B_{leak} is due to the use of a higher number of turns with $0 \cdot d_w$ space between the turns in the OuC of case 1 compared with the other cases. Whereas, case 7 has a lower peak B_{leak} nearby OuC (a weak magnetic field distribution nearby OuC can be seen) compared with the other cases. The numerical difference in the peak B_{leak} of each case can be seen in 4.7. From Table 4.7, it is also seen that at 250 mm (nearby coil structure), the value of peak B_{leak} for all the cases is lower than the type-I and type-II (except for case 1 compared with type-II). However, in comparison to type-H with the obtained coils, cases 7 and 8 have a lower value of peak B_{leak}. Among all the obtained cases, case 3 has a higher peak B_{leak} than the other obtained cases (except from case 1). Nevertheless, the next improved k coil structure (i.e., case 6) has a lower peak B_{leak} than the cases 1–4. In the next subsection, the impact of different misalignments on improvement in k is investigated for both case 3 and case 6 coil systems.

4.2.7 Impact of Different Misalignments on Improvement in k

Usually, the vertical and horizontal (in both X- and Y-directions) misalignments occur in EV charging [59, 67, 70]. Hence, to investigate the impact of these misalignments on improvement in k, k of case 3 and case 6 coil systems are compared with type-I and type-H coil systems, as shown in Figure 4.25. From Figure 4.25(a)–(c), it is seen that case 3 and case 6 coil systems have improved k compared with type-I and type-H coil systems throughout displacements. In Figure 4.25(a), k is plotted for the movement of the Rx coil from 60 to 200 mm in the Z-axis direction. Here, the maximum increase in k is observed for case 3 and case 6 coil systems as 30.51% and 28.60% at the 70-mm air gap in comparison to type-I coil system while 8.81% and 5.05% at the 200-mm air gap with respect to the type-H coil system. Furthermore, in Figure 4.25(b) and (c), k is plotted for the displacement of the Rx coil from 0 to 200 mm in the X-direction and 0 to 150 mm in the Y-direction, respectively, at an air gap of 150 mm. In both horizontal misalignments, the maximum improvement in k is observed for case 3 and case 6 coil systems as 27.06% and 23.62% (at the 0 mm) compared with the type-I coil system. Furthermore, compared with the type-H coil system, case 3 and case 6 coil systems show the maximum improvement in k of 11.86% and 9.06% at the 200 mm in the X-direction while 15.24% and 9.06% at the 150 mm in the Y-direction, respectively. The results in Figure 4.25(b) and 4.25(c) further show that case 3 coil system maintains improvement in k of 6.80%–11.85% and

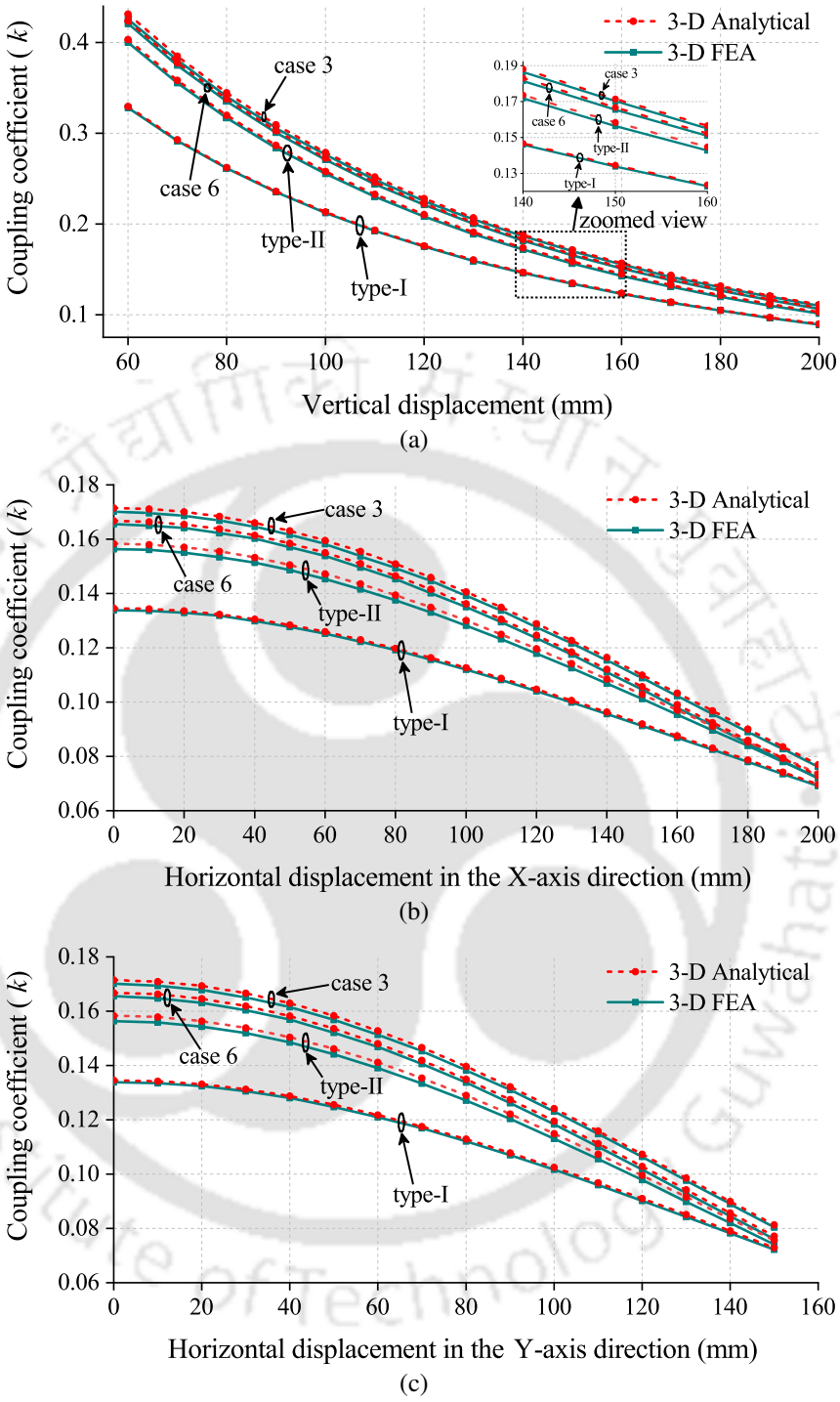

Figure 4.25: Comparison of k (obtained from 3-D analytical and 3-D FEA) among the type-I, type-II, case 6, and case 3 coil systems for (a) vertical displacement of Rx coil in the Z-axis direction, and horizontal displacement of Rx coil in the ((b) X-axis direction and (c) Y-axis direction) at the 150-mm air gap.

6.80%–15.24% for 0%–50% misalignment of the Rx coil in the X- and Y-directions, respectively, compared with the type-H coil system. Thus, from Figure 4.25, it is verified that the improvement in k is achieved even for different misalignments with the selected coil structures (i.e., case 3 and case

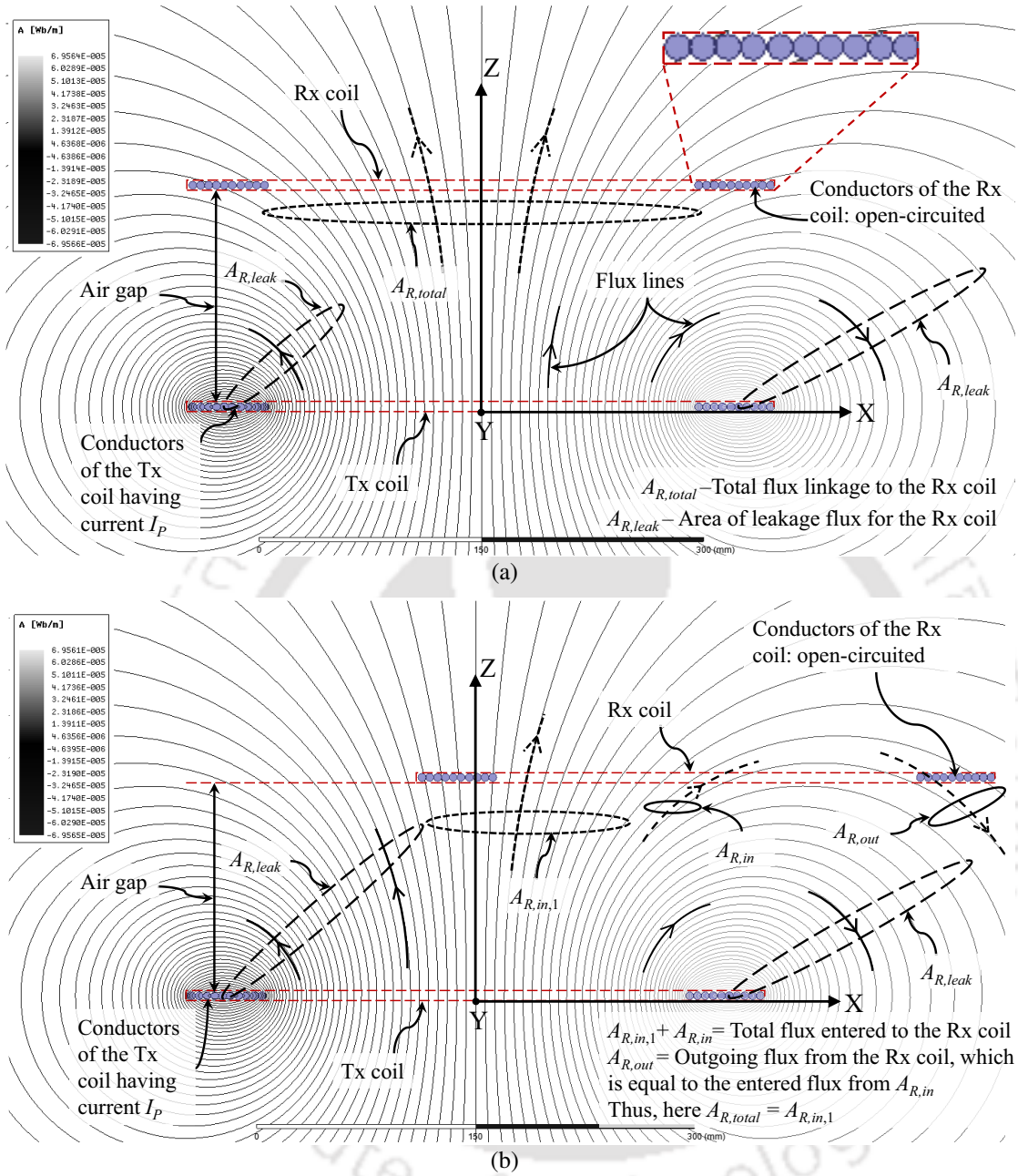

Figure 4.26: XZ plane view of type-I (for example) coil system along Line Q to understand the effect of displacement of Rx coil in (a) vertical and (b) horizontal directions on the magnetic flux linkage to the Rx coil.

6).

Furthermore, Figure 4.25 verifies that k, calculated from 3-D analytical model, is in good agreement with those obtained from 3-D FEA throughout the misalignments. The maximum errors of 1.08%, 3.09%, 1.48%, and 1.47% are noticed in comparison to 3-D FEA results among the presented misalignments for type-I, type-H, case 3, and case 6 coil systems, respectively.

From Figure 4.25, it is seen that the value of k decreases for each coil system with an increase

in displacement of the Rx coil. To understand this decrease in k, Figure 4.26 is used. Figure 4.26 illustrates how does the magnetic flux generated by a Tx coil link to the Rx coil for different misalignments between them. For the vertical displacement of the Rx coil, Figure 4.26(a) shows the scenario of flux linkage to the Rx coil at the 150-mm air gap. Here, the generated flux lines passing through the Rx coil is the total flux linkage (encircled as $A_{R,total}$), whereas the remaining flux lines are the leakage flux for the Rx coil (shown by $A_{R,leak}$). This leakage flux does not contribute to M. As the air gap increases, the amount of flux linkage and its intensity starts decreasing, whereas the leakage flux (i.e., $A_{R,leak}$) increases and vice versa. Thus, M between the coils decreases with the increase in the air gap. As a result, the value of k decreases. Note that in the air-core coil system, the change in the value of L_P and L_S is negligible due to the displacement of the Rx coil [71]).

For the horizontal displacement of Rx coil (in any of the directions; X- or Y-axis), Figure 4.26(b) explains the scenario of flux linkage to the Rx coil at the 150-mm air gap with horizontal misalignment in the X-direction. As the Rx coil is displaced in the X-axis direction, the flux lines passing through the Rx coil starts decreasing compared with the aligned position (i.e., no horizontal displacement). Here, the total flux entering through the Rx coil is encircled as $A_{R,in,1}$ and $A_{R,in}$. However, the flux lines that entered through $A_{R,in}$, leave the Rx coil from $A_{R,out}$ (the net flux is zero). As a result, the flux lines entering through $A_{R,in}$ does not contribute in the total flux linkage to the Rx coil. Hence, the flux lines encircled as $A_{R,in,1}$ only gives the total flux linkage to the Rx coil. Further, as the horizontal displacement of the Rx coil increases, the leakage flux $A_{R,leak}$ increases and the total flux linkage decreases. Accordingly, M between the coils decreases. Thus, it can be concluded that the value of k decreases as the Rx coil displaced in the X- and Y-axis directions.

It should be noted that the direction of the flux lines shown in Figure 4.26 is, for instance, to explain the reason for the decrement in k against the displacement of the Rx coil in the X-, Y-, and Z-axis directions. Practically, the direction of flux lines gets changed continuously due to the alternating action of the current I_P, supplied in the conductor(s) of a Tx coil. However, the above explanation remains the same for other direction of the flux lines and other coil structures also. The upcoming section presents the experimental results of the discussed coil systems. Here, in place of the type-H coil, the type-II coil is considered due to winding ease in the prototyping (as discussed in Section

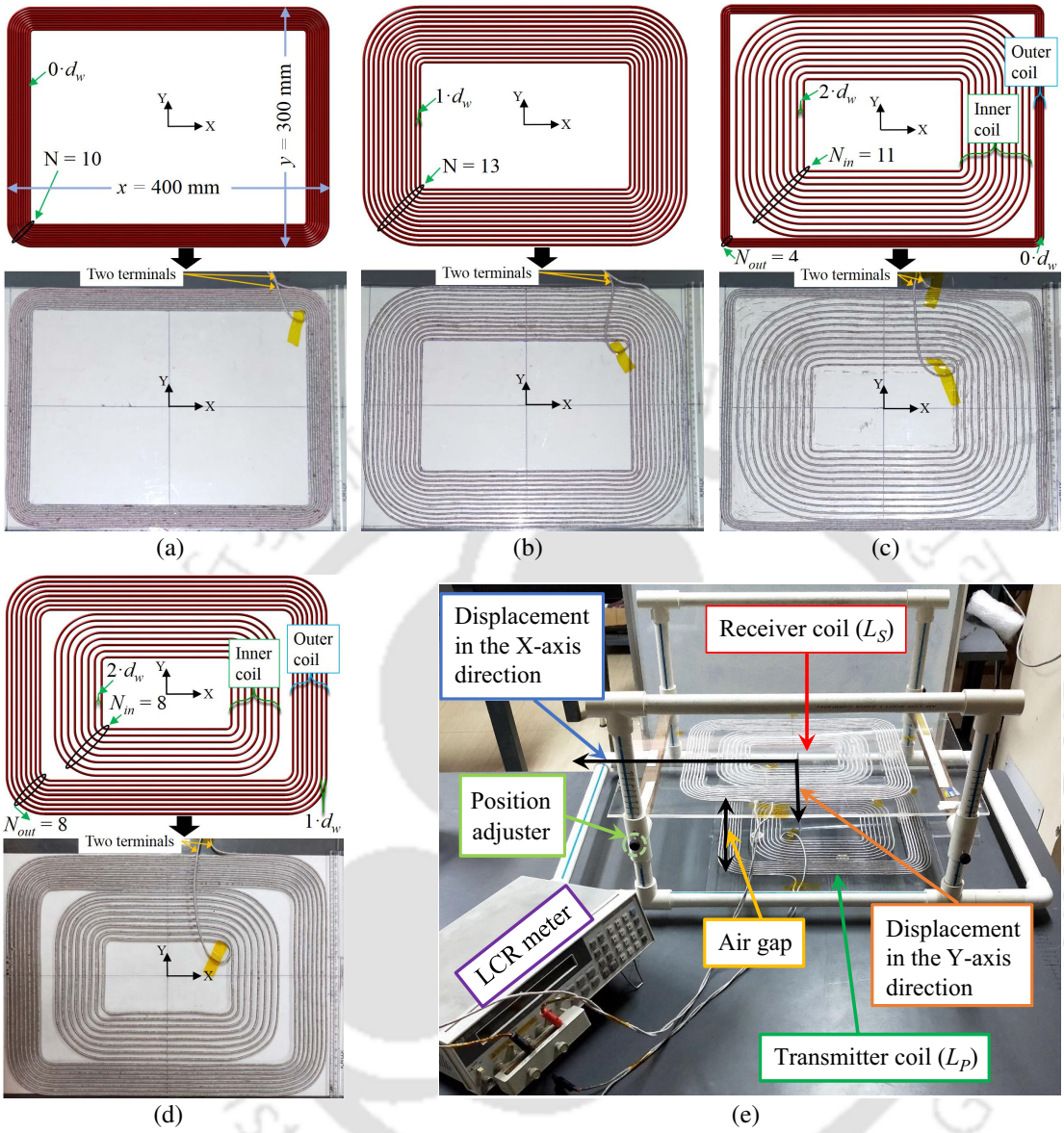

Figure 4.27: Prototypes of the constructed (a) type-I, (b) type-II, (c) case 3, and (d) case 6 coils with schematic. (e) Experimental setup.

4.2.3).

4.3 Experimental Verification

This section discusses the development of different coils' prototype along with the experimental setup. Further, it verifies the self-inductance, k, coil resistance, and $\eta_{t,uc}$ of different coil systems at the 150-mm air gap, followed by k for vertical and horizontal misalignments of the coils.

Table 4.8: Comparison of calculated and simulated L_P, L_S, and k at 150-mm air gap with the measurement.

Coil	3-D Analytical		3-D FEA		Measurement	
system	$L_P = L_S$ (μH)	k	L_P, L_S (μH)	k	L_P, L_S (μH)	k
type-I	80.50	0.1345	80.30, 80.80	0.1339	80.68, 80.85	0.1343
type-II	80.80	0.1581	81.09, 81.11	0.1563	80.84, 80.93	0.1571
case 3	80.85	0.1710	80.06, 80.66	0.1701	80.48, 80.75	0.1706
case 6	81.18	0.1667	80.51, 80.69	0.1655	80.70, 80.77	0.1667

Table 4.9: Comparison between the calculated (with extra wire used) and measured $R_{dc,P}$, $R_{dc,S}$, R_P, R_S, $\eta_{t,uc}$, and S_{max}.

Parameter		type-I	type-II	case 3	case 6
$R_{dc,P}$, $R_{dc,S}$	Cal.	87.90, 89.75	95.60, 97.46	102.15, 104.00	103.14, 104.99
($m\Omega$)	Meas.	90.73, 92.48	95.65, 97.69	102.95, 104.75	103.91, 105.96
R_P, R_S	Cal.	123.76, 126.59	117.99, 120.82	128.28, 131.11	125.71, 128.53
($m\Omega$)	Meas.	138.02, 141.15	128.60, 130.10	143.60, 146.80	142.50, 145.70
$\eta_{t,uc}$ (%)	Cal.	57.64	66.04	67.68	67.06
	Meas.	55.20	64.29	65.38	64.59
S_{max} (VA)	Cal.	90.46	124.47	145.55	138.51
	Meas.	91.43	125.36	147.17	140.90

4.3.1 Prototypes of Different Coils and Experimental Setup

Prototypes of type-I, type-II, case 3, and case 6 coils, as shown in Figure 4.27(a)–(d), are built using the obtained parameters given in Tables 3.7 and 4.2 to verify improvement in k. A transparent acrylic sheet is used as a base for winding. During the winding of coil structure, the same Litz wire (details are mentioned in Section 3.5) is used to maintain the different spacings between the turns (i.e., to create $1{\cdot}d_w$ gap (having integer p), a single wire of d_w is placed between the turns) and is removed after that ((it gives ease in prototyping). In the WPT system, this coil can be connected to a power supply when used as a Tx coil and a load when used as an Rx coil. An experimental setup, as shown in Figure 4.27(e), is designed to obtain k for vertical and horizontal misalignments. In Figure 4.27(e), a wooden made table (for coils placement) is used to avoid the interference of metal during the measurements of self-inductance and factor k. Hewlett Packard 4263B LCR meter is used to measure the coil's dc resistance and the self-inductances, k, and AC resistance of coils at the 100-kHz operating frequency.

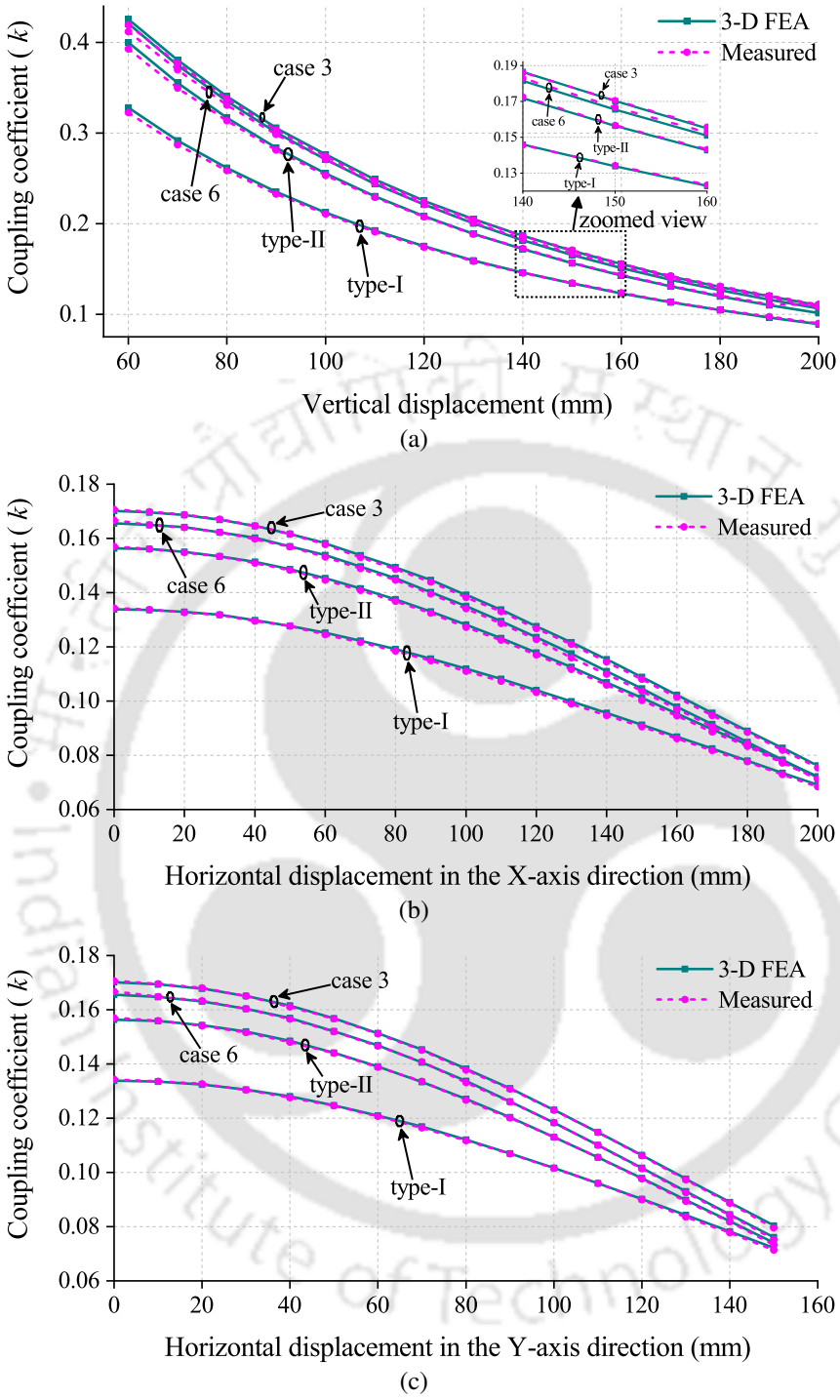

Figure 4.28: Comparison of simulated (3-D FEA) and measured values of k for type-I, type-II, case 6, and case 3 coil systems for (a) vertical displacement of Rx coil in the Z-axis direction, and horizontal displacement of Rx coil in the ((b) X-axis direction and (c) Y-axis direction) at the 150-mm air gap.

4.3.2 Experimental Results

Table 4.9 compares the calculated and measured values of $R_{dc,P}$, $R_{dc,S}$, R_P, R_S, $\eta_{t,uc}$ (measured $\eta_{t,uc}$ is obtained from (3.33) using the measured values of L_P, L_S, R_P, R_S, and k), and S_{max} for different coil

systems. The calculated results in Table 4.9 include the effect of extra wire (1.55 m in Tx and 1.85 m in Rx), which is used in the prototypes to make the connections. From Table 4.9, it can be seen that the measured dc resistance of each coil system is in agreement with the calculated results. However, about 8.90%–13.36% difference between the measured and calculated values of the AC resistance of the different coil systems is observed. As a result, the difference in measured $\eta_{t,uc}$ compared with the calculated $\eta_{t,uc}$ in each coil system is also observed. However, the improvement in measured $\eta_{t,uc}$ of case 3 and case 6 coil systems (compared with the conventional coils) is almost similar as in the calculated $\eta_{t,uc}$. In the measured $\eta_{t,uc}$, 18.44% and 1.70% improvements for case 3 coil system and 17.01% and 0.47% improvements for case 6 coil system are observed with respect to type-I and type-II coil systems, respectively. Moreover, the value of the measured S_{max} for each coil system is found in agreement with the calculated S_{max}.

Figure 4.28 shows the variation of k obtained from 3-D FEA and measurement for different coil systems during vatical and horizontal misalignments. As shown in Figure 4.28(a)–(c), all the curves are in good agreement throughout the displacement of the Rx coil in the Z-, X-, and Y-axis directions, respectively. Here, the maximum errors of 1.61%, 1.81%, 2.12%, and 1.40% are observed in the measurement of k compared with 3-D FEA for type-I, type-II, case 6, and case 3 coil systems, respectively. This error is within acceptable limit (i.e., $< 5\%$). Thus, the improvement in k for practical coils is verified.

4.4 Improvement in k for the Unipolar Coils Having Equal Length and Width

With the proposed UCAM, for verifying the improvement in k of the coil structures of equal length and width ($x = y$), square and circular (here, $x = y$ = radius) geometry is selected. Considering the same area as occupied by the rectangular coil, outer dimensions of the square and circular coils are chosen as 350 mm × 350 mm and 400 mm × 400 mm, respectively, for the same L_{req} value. Figure 4.29 shows the square-shaped coils, which are designed using the CCAM and proposed UCAM (as an example, only one proposed coil structure is presented). Similarly, Figure 4.30 shows the circular-shaped coils designed using the CCAM and proposed UCAM. Table 4.10 summarises the value of coil parameters, self-inductance, and k of these coil structures. For the square coils, the parameters given in Table 4.10 are calculated from 3-D analytical model and 3-D FEA both. However, for the

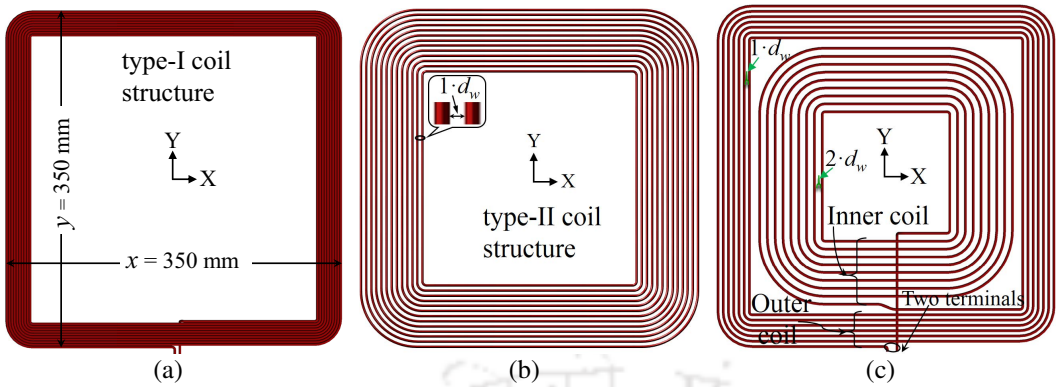

Figure 4.29: Illustration of square shaped coil structures designed using (a) CCAM (b) CCAM, and (c) proposed UCAM.

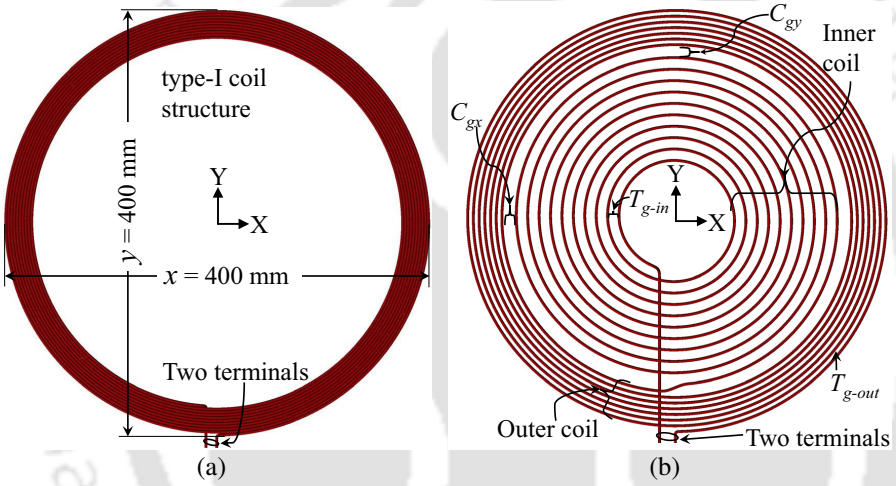

Figure 4.30: Illustration of circular shaped coil structures designed using (a) CCAM and (b) proposed UCAM.

circular coils, only 3-D FEA is used because using the proposed 3-D analytical model (can be used by approximating circular coil as a square coil [48]) results in an unacceptable error. From Table 4.10, for the proposed square coil system, 26.02% and 6.77% improvements in k are observed at the 150-mm air gap with respect to type-I and type-II square coil systems, respectively. Similarly, for the proposed circular coil system, 26.41% and 6.33% improvements in k are observed at the 150-mm air gap with respect to type-I and type-II circular coil systems, respectively. Moreover, the values of L_P and L_S of the coils shown in Figure 4.29 are close to L_{req} value when designed using the proposed UCAM, whereas the same does not achieve when designed using CCAM (for integer value of p).

Table 4.10: Coil parameters' value of different coil geometries.

Coil system	Calculated using	T_{g-out} $(m \cdot d_w)$	T_{g-in} $(n \cdot d_w)$	N_{out}	N_{in}	x_{o-in} (mm)	y_{o-in} (mm)	C_{gx} (mm)	C_{gy} (mm)	N	L_P, L_S (μH)	k at 150 mm
Square coil (350 mm × 350 mm)												
type-I	3-D Anyl	–	–	–	–	–	–	–	–	10	81.02, 81.02	0.1383
	3-D FEA	–	–	–	–	–	–	–	–	10	80.88, 81.43	0.1376
type-II	3-D Anyl	–	–	–	–	–	–	–	–	13	81.98, 81.98	0.1643
	3-D FEA	–	–	–	–	–	–	–	–	13	82.15, 82.21	0.1624
Proposed	3-D Anyl	$1{\cdot}d_w$	$2{\cdot}d_w$	7	9	131.4	131.4	8.5	8.5	–	80.97, 80.97	0.1747
	3-D FEA	$1{\cdot}d_w$	$2{\cdot}d_w$	7	9	131.4	131.4	8.5	8.5	–	80.65, 80.73	0.1734
Circular coil (400 mm × 400 mm)												
type-I	3-D FEA	–	–	–	–	–	–	–	–	10	80.12, 80.23	0.1503
type-II	3-D FEA	–	–	–	–	–	–	–	–	12	77.57, 77.60	0.1732
Proposed	3-D FEA	$1{\cdot}d_w$	$3{\cdot}d_w$	7	10	155.6	155.6	9.5	9.5	–	80.72, 80.74	0.1900

4.5 Improvement in k of Nonidentical Unipolar Coils

This section investigates the improvement in k using the proposed UCAM for nonidentical unipolar coils. Here, the nonidentical unipolar coils are divided into the following three categories (C-1–C-3), which can be used according to the suitability in EV applications.

C-1: Tx and Rx coils having different outer dimensions with the same coil geometries and self-inductance values;

C-2: Tx and Rx coils having different outer dimensions and self-inductance values with the same coil geometries;

C-3: Tx and Rx coils having different outer dimensions, coil geometries, and self-inductance values.

For the verification of improvement in k of the coils defined in categories C-1–C-3, the specifications of nonidentical coils as an example for each category are summarised in Table 4.11. However, according to the designer's requirement, the different values can be chosen. Based on the specifications given in Table 4.11, the different possible conventional coils for C-1–C-3 are designed with the constraints given in (3.34). In the design, integer p-value is considered. The factor k of these

Table 4.11: Specifications (as an example) of nonidentical unipolar coils for improving k at the 150-mm air gap.

Parameter		Different categories		
		C-1	C-2	C-3
x mm × y mm	Tx coil	400 × 300	400 × 300	400 × 400
	Rx coil	360 × 270	360 × 270	250 × 250
Geometry of	Tx coil	Rectangular	Rectangular	Circular
	Rx coil	Rectangular	Rectangular	Square
L_P (μH)		80.50	80.50	80.50
L_S (μH)		80.50	68.00	50.00

Table 4.12: Coil parameters' value of nonidentical unipolar coils.

Coil system	T_{g-out} ($m \cdot d_w$)	T_{g-in} ($n \cdot d_w$)	N_{out}	N_{in}	x_{o-in} (mm)	y_{o-in} (mm)	T_g (mm)	N Tx	N Rx	AIA*(%) (Tx, Rx)	L_P (μH)	L_S (μH)	k at 150 mm
Improvement in k for C-1													
type-I	–	–	–	–	–	–	$0{\cdot}d_w$	10	11	(70.9, 65.1)	80.47	80.59	0.1259
type-II	–	–	–	–	–	–	$1{\cdot}d_w$	13	16	(36.4, 20.3)	80.96	81.62	0.1435
Proposed Tx	$0{\cdot}d_w$	$2{\cdot}d_w$	4	11	182.5	137.5	–	–	–	(4.4, –)	80.23	–	0.1564
Proposed Rx	$0{\cdot}d_w$	$2{\cdot}d_w$	6	11	153.5	115.5	–	–	–	(–, 2.3)	–	80.15	
Improvement in k for C-2													
type-I	–	–	–	–	–	–	$0{\cdot}d_w$	10	10	(70.9, 68.0)	80.54	69.47	0.1246
type-II	–	–	–	–	–	–	$1{\cdot}d_w$	13	13	(36.4, 31.3)	81.03	66.78	0.1443
Proposed Tx	$0{\cdot}d_w$	$2{\cdot}d_w$	4	11	182.5	137.5	–	–	–	(4.4, –)	80.29	–	0.1566
Proposed Rx	$0{\cdot}d_w$	$2{\cdot}d_w$	5	9	158.5	119.5	–	–	–	(–, 1.2)	–	68.26	
Improvement in k for C-3													
type-I	–	–	–	–	–	–	$0{\cdot}d_w$	10	10	(74.8, 61.5)	80.38	49.49	0.1069
type-II	–	–	–	–	–	–	$1{\cdot}d_w$	12	16	(47.5, 10.9)	77.85	49.02	0.1154
type-III Tx	–	–	–	–	–	–	$2{\cdot}d_w$	18	–	(8.9, –)	81.68	–	0.1264
type-II Rx	–	–	–	–	–	–	$1{\cdot}d_w$	–	16	(–, 10.9)	–	49.44	
Proposed Tx	$0{\cdot}d_w$	$3{\cdot}d_w$	4	12	188.5	188.5	–	–	–	(11.2, –)	80.12	–	0.1367
Proposed Rx	$0{\cdot}d_w$	$2{\cdot}d_w$	6	8	105.6	105.6	–	–	–	(–, 13.7)	–	49.93	

* Available inner area (AIA). Here, d_w = 2.7.

conventional coils are tabulated in Table 4.12 along with their coil parameters. Then, the proposed UCAM is applied to design the coils with the same specifications (given in Table 4.11) for C-1–C-3. The coil parameters of the obtained Tx and Rx coils for C-1–C-3 are also summarised in Table 4.12 for the comparison. The 3-D illustration of the obtained coil structures using the proposed UCAM for

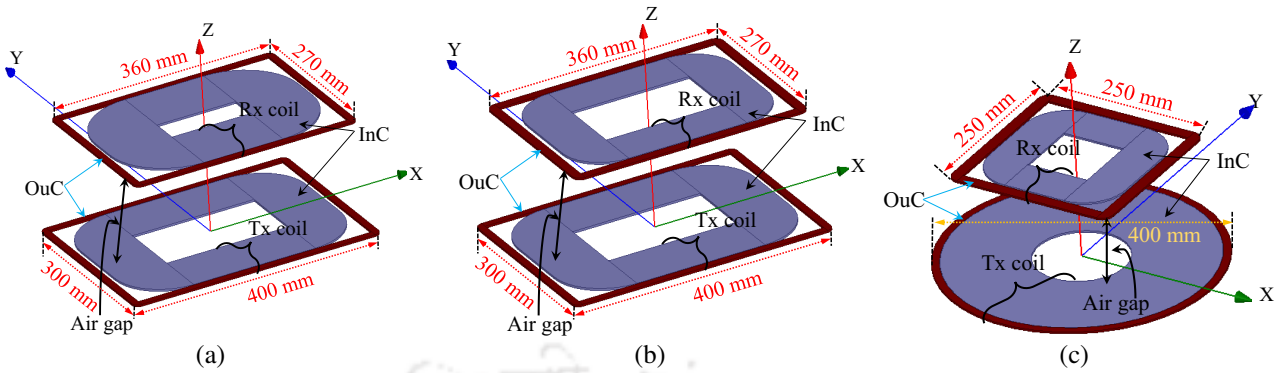

Figure 4.31: 3-D illustration of the nonidentical coil structures designed the using proposed UCAM for (a) C-1 (b) C-2, and (c) C-3. The coil parameters can be seen in Table 4.12.

C-1–C-3 can be seen in Figure 4.31. From Table 4.12, it can be seen that for C-1, 24.22% and 8.99% improvements in k are observed for the proposed nonidentical coils compared with type-I and type-II nonidentical coils, respectively. Similarly, for C-2, 25.68% and 8.52% improvements in k are seen for the proposed nonidentical coils with respect to type-I and type-II nonidentical coils, respectively. Further, for C-3, it is noticed that the proposed nonidentical coils improve the factor k to 27.87%, 18.46%, and 8.15% compared with the type-I, type-II, and type-III (having type-II Rx) nonidentical coils, respectively.

4.6 Summary of the Chapter

In this chapter, UCAM is presented to improve the factor k compared with conventional coils of the same self-inductance and outer dimensions in the WPT system. The steps involved in the proposed UCAM are explained through flowcharts. The developed 3-D analytical model in Chapter 3 is extended to calculate k for the proposed coil structures. The extended 3-D analytical model is also valid for the square and rectangular coil structures obtained using the proposed UCAM. 3-D FEA software ANSYS Maxwell has been used for simulations and verification of the extended 3-D analytical model. For a rectangular coil system (outer dimensions of 400 mm × 300 mm), a maximum of 27.04%, 8.83%, and 6.78% improvements in k is obtained for the case 3 coil system at the 150-mm air gap, which resulted in 60.90%, 16.94%, and 13.54% enhancements in S_{max} compared with type-I, type-II, type-H coil systems, respectively. It is also found that, with the maximum improvement in k of 27.04%, 8.83%, and 6.78% (obtained for case 3 coil system), the total used wire length is increased by 18.20%, 7.65%, and 4.75%, which resulted in 4.14%, 9.95%, and 8.56% increments in the coil's AC

resistance with respect to type-I, type-II, and type-H coil systems, respectively. Despite increment in AC resistance along with improvement in k, increase in $\eta_{t,uc}$ of 15.80%, 1.93%, and 1.20% is obtained for the case 3 coil system in comparison to type-I, type-II, and type-H coil systems, respectively. Moreover, interoperability between the proposed and conventional coils is studied. Furthermore, the peak B_{leak} nearby coil structures are studied for the coils designed using both CCAM and proposed UCAM. Here, it is found that with improved k, case 3 and case 6 coils have lower peak B_{leak} than both type-I and type-II coils. However, compared with the type-H coil, case 3 and case 6 coils have a higher peak B_{leak} nearby. Moreover, the impact of different misalignments on improvement in k is examined for case 3 and case 6 coil systems, and up to 30.51% and 28.60% improvements in k have been found, respectively, with respect to conventional coils. Besides that, prototypes of type-I, type-II, case 3, and case 6 coil systems are built to verify the obtained k from 3-D analytical model and 3-D FEA for vertical and horizontal misalignments. Results show a good agreement among analytical model, simulation, and measurement, which verifies improvement in k of the obtained coil system using the proposed UCAM. Furthermore, for the square and circular coil systems, up to 26.02% and 26.41% improvements in k at the 150 mm air gap have been found with the proposed UCAM for the outer dimensions of 350 mm × 350 mm and 400 mm × 400 mm, respectively, compared with type-I and type-II coil systems. Besides that, improvement in k of nonidentical unipolar coils is investigated using the proposed UCAM. An improvement of 8.14%–27.87% in k is seen for the proposed nonidentical unipolar coils compared with the different conventional coils.

Thus, the presented UCAM provides a platform for the systematic design of unipolar coils of different geometries for improving k compared with conventional coils having the same self-inductance and outer dimensions. Besides that, to further improve k of the proposed coil system(s) using the second resort (i.e., ferrite material), the ferrite core is optimised in the next chapter.

Note: *The method presented in this chapter has been applied for Indian Patent "201931003386," Jan. 28, 2019. Moreover, the research findings of this chapter have been published in "IEEE Transactions on Transportation Electrification".*

भारतीय प्रौद्योगिकी संस्थान गुवाहाटी
Indian Institute of Technology Guwahati

5

A New Ferrite Arrangement of Unipolar Rectangular Coils for Minimising the use of Ferrites in WPT Systems

Contents

5.1 Introduction

In the previous chapter, k of the unipolar air-cored coils has been improved by doing modification in the coil design (the first resort). For this, the UCAM was developed and analysed in Chapter 4. Using the proposed UCAM, the improvement in k at the 150-mm air gap (of the designed coil systems) compared with the different conventional unipolar rectangular coil systems is summarised in Table 4.3.

For further improving the factor k of the unipolar air-cored coils, the second resort is generally used. The second resort, which is one of the simplest ways for improving k, is to use the ferrite core [24, 27, 39]. Due to space limitation in EV charging, the size of the ferrite core is kept approximately equal to the coil dimensions, which is a traditional ferrite arrangement [39]. This arrangement gives the maximum possible k. However, the use of uniform ferrite core throughout the coil dimensions increases the weight and cost of the coil system. Therefore, there is a need to find a ferrite arrangement of the unipolar coil system, which has the minimal use of ferrite core and can maintain k obtained from the traditional ferrite arrangement.

The coil's geometry plays a critical role to minimise the use of ferrites. In the literature, the ferrite arrangement for the unipolar circular coil has been extensively researched and well optimised by using different shapes of ferrite bars [27, 42, 43]. But, the same ferrite arrangement (obtained for circular coils) may not be optimal for the unipolar rectangular (or square) coils because of the corners' effect [44].

In this context, this chapter attempts to find a novel and simple ferrite arrangement (magnetic structure) of the unipolar rectangular (or square) coils to minimise the volume of ferrite used while maintaining the maximum k (obtained from the traditional ferrite arrangement). The organisation of the rest of the chapter is as follows. Section 5.2 gives the details of the ferrites used and presents the assumption taken for simplifying the 3-D simulation models. Section 5.3 presents the traditional ferrite arrangement, discusses the improvement in k for the different horizontal misalignments of the Rx coil arrangement compared with the obtained air-cored coils using the proposed UCAM, and examines the impact of further improved k on the power transfer and transmission efficiency. Section 5.4 discusses and analyses the proposed ferrite arrangement. Furthermore, the various possible fer-

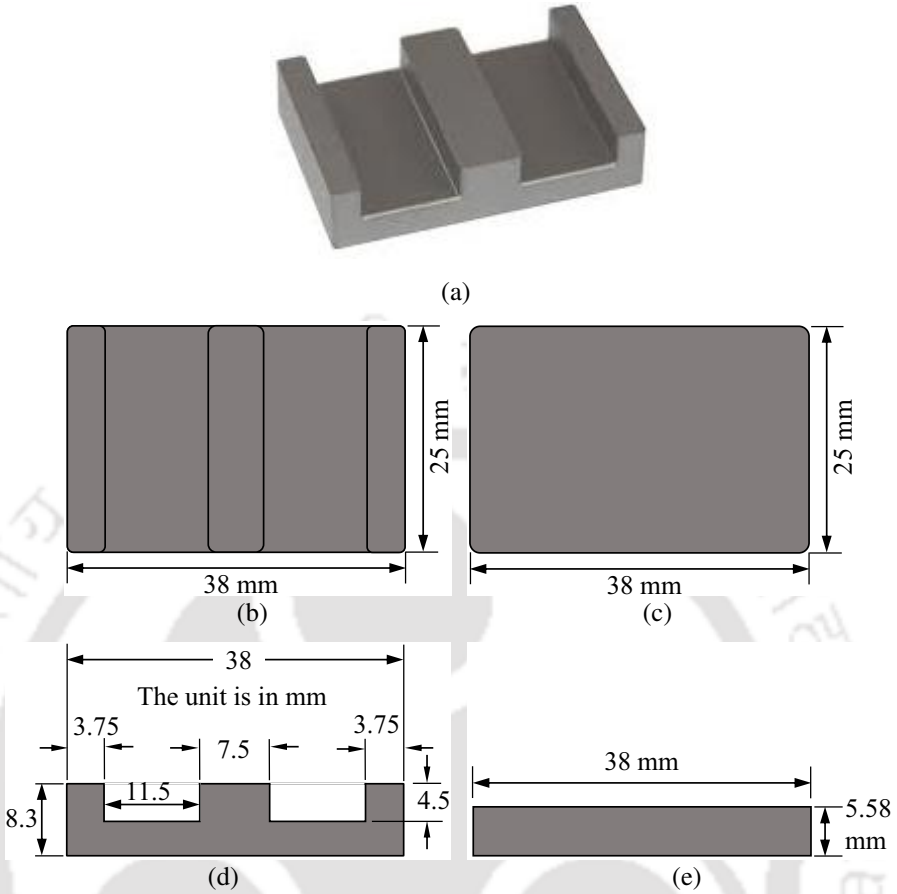

Figure 5.1: (a) Photo of E38/8/25 (planar E-core). Schematic of E38/8/25 showing (b) front, (c) rear, and (d) side views. (e) The calculated average height of the core in Figure 5.1(d) (used to make 3-D simulation models).

rite arrangements are also presented and are compared with the proposed ferrite arrangement for the obtained k and ferrite saved. Section 5.5 shows the constructed prototype of the proposed ferrite arrangement and verifies the obtained results. Section 5.6 investigates the proposed ferrite arrangement with the different rectangular air-cored coils (proposed and conventional) along with the conventional square coils. Finally, Section 5.7 gives a summary of this chapter.

5.2 Ferrite Details and Assumption for Simplifying the 3-D Simulation Models

In this section, the details of the used ferrite core are presented, followed by the assumption made for simplifying the 3-D simulation models.

As per the availability in the laboratory, Ferroxcube E38/8/25-3F4 (planar E-core) [72], as shown in Figure 5.1(a), is used to make the presented ferrite arrangements (in this chapter). However, planar

I-core can also be used for the same. The schematic of E38/8/25 ferrite core with its different views is shown in Figure 5.1(b)–(d). The volume of a single planar E-core is calculated as 5.329 cm^3, which is used to determine the number of required planar E-core in the presented ferrite arrangements. The operating frequency is taken the same as in the previous chapter (i.e., 100 kHz). For this frequency, the relative permeability and the saturation flux of the core are 900 and 100 mT, respectively [72].

For making 3-D simulation models easier (for simulation study; performed in ANSYS Maxwell), the average height of E38/8/25 is used, as shown in Figure 5.1(e). This average height is calculated by equating the total volume of both cores (shown in Figure 5.1(d) and (e)), and it is 5.58 mm. Doing this does not affect the obtained results and makes the 3-D model designing more accessible (and also saves time). However, the final ferrite arrangement is simulated using the planar E-core, which verifies the assumption.

With the abovementioned core details and assumption, the presented ferrite arrangements in Sections 5.3–5.5 are discussed and analysed with case 6 coil system. However, the other proposed and conventional rectangular (or square) coils can also be selected for the same, discussed in Section 5.6. The next section discusses the traditional ferrite arrangement and examines the impact of improved k (using traditional ferrite arrangement) on the power transfer capability and transmission efficiency compared with the (case 6) air-cored coil system.

5.3 Traditional (Uniform) Ferrite Arrangement of Unipolar Rectangular Coils

In the WPT system, the magnetic core partially provides a low reluctance path for the magnetic flux while the remaining of its path passes through the air gap. The cumulative effect of using this core reduces the reluctance or enhances the effective permeability of the flux path; therefore, it increases both the self- and mutual inductance of the Tx and Rx coils [27].

Figure 5.2(a) shows the geometrical details of the selected air-core coil (i.e., case 6; other coils can also be taken). An isometric and front views of the traditional (uniform) ferrite arrangement (UFA) are shown in Figure 5.2(b) and (c), respectively. In UFA, the ferrite size is kept similar to the coil dimensions (due to space restriction in EV application, as discussed in the previous chapters), as shown in Figure 5.2(b) and (c). The total ferrite volume used in case 6 UFA coil system is 1338.31 cm^3,

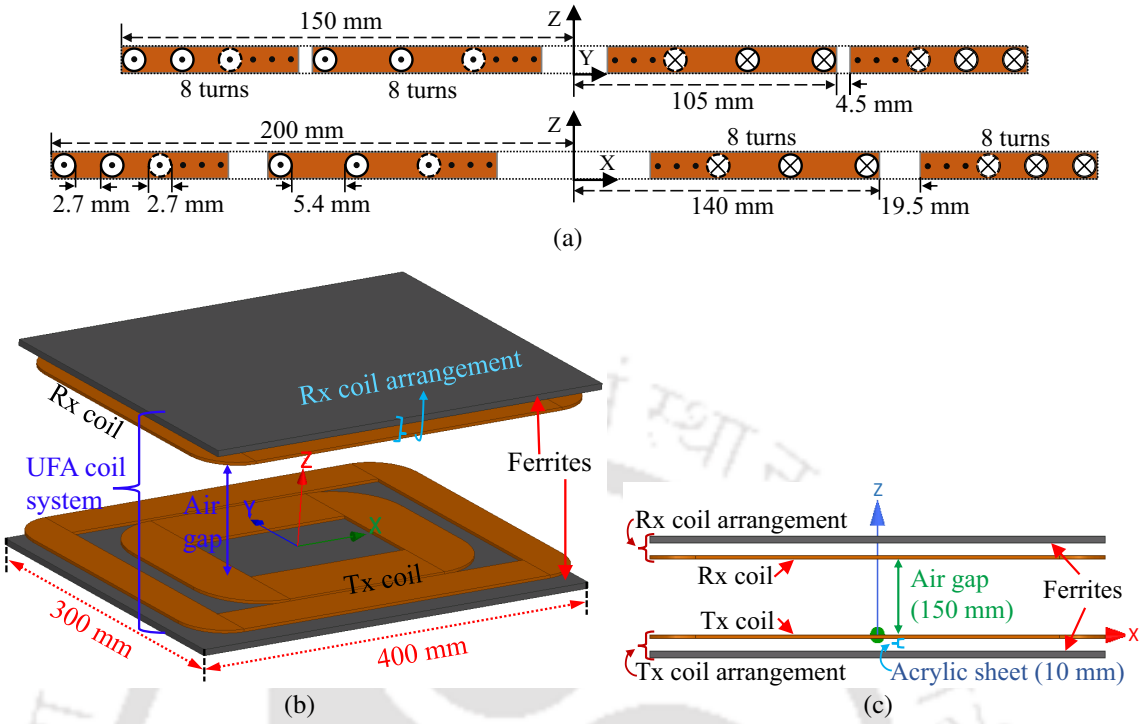

Figure 5.2: (a) Geometrical information of case 6 air-core coil(s) showing the YZ and XZ planes view. Case 6 coils with UFA: (b) an isometric view and (c) front (XZ plane) view.

which requires approx 252 planar E-cores. For the 150-mm air gap, the value of L_P, L_S, M, and k of the case 6 UFA coil system is 117.26 μH, 117.29 μH, 24.543 μH, and 0.2093, respectively. Compared with the case 6 air-cored coil system, the self-inductances, M, and k (of case 6 UFA coil system) are increased by 45.50%, 84.00%, and 26.47%, respectively. Here, it can be seen that the increment in M is more than double to the increment in self-inductance. This increment in self-inductance increases the voltage stress across the coils, which leads to a higher cost of compensation capacitors and insulation of coils (it is undesired) [25, 42, 73]. Therefore, during the ferrite arrangement, the attention should also be given on reducing the increment in self-inductance while maintaining k (obtained in UFA coil system).

Figure 5.3 shows the maximum possible improvement in k of the case 6 UFA coil system for the horizontal misalignment of the Rx coil arrangement in the X- and Y-directions at the 150-mm air gap. Compared with the air-core coil system, UFA coil system improves k throughout the misalignment of the Rx coil arrangement in both directions, as shown in Figure 5.3(a) and (b), respectively. In Figure 5.3(a) and (b), the maximum improvement in k is observed at the 0 mm position of the Rx coil

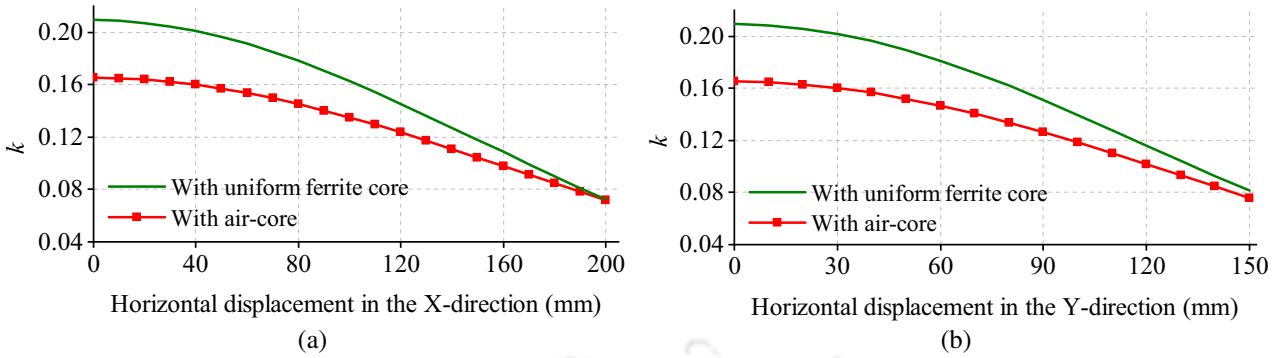

Figure 5.3: Comparison of k (obtained from 3-D FEA simulation) between case 6 air-core and case 6 UFA coil systems for horizontal displacement of the Rx coil arrangement in the (a) X-axis and (b) Y-axis directions at the 150-mm air gap.

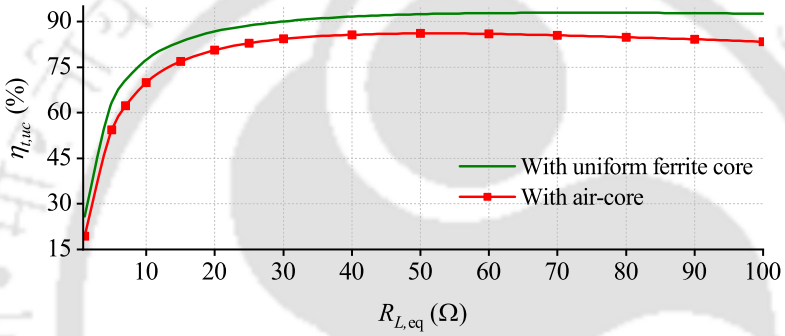

Figure 5.4: Comparison of $\eta_{t,uc}$ at different values of $R_{L,eq}$ for case 6 air-core and case 6 UFA coil systems at the 150-mm air gap.

arrangement, which is 26.47% in comparison to the air-core coil system.

Furthermore, the impact of this improved k on $\eta_{t,uc}$ and S_{max} is examined using (3.33) and (4.15), respectively, throughout the horizontal misalignments of the Rx coil arrangement. For case 6 UFA coil system, the value of R_P (= R_S) is calculated from (3.27), which is 120.41 $m\Omega$, and it is used in (3.33) to determine $\eta_{t,uc}$. At first, $\eta_{t,uc}$ is calculated for different values of $R_{L,eq}$ at the 150-mm air gap for both air-core and with UFA coils, as shown in Figure 5.4. Here, $R_{L,eq}$ is varied from 1 to 100 Ω. From Figure 5.4, it can be seen that $\eta_{t,uc}$ of case 6 UFA coil system has improved throughout $R_{L,eq}$ variation with respect to case 6 air-core coil system. Moreover, in Figure 5.4, it is also seen that with the increase in $R_{L,eq}$ values, the difference between both the curves increases (almost). Now, $\eta_{t,uc}$ is calculated at a fixed value of $R_{L,eq}$ (= 10 Ω) for the horizontal misalignment of the Rx coil arrangement in the X- and Y-directions (i.e., varying the factor k), as shown in Figure 5.5. From Figure 5.5(a) and (b), $\eta_{t,uc}$ curves follow the similar pattern as obtained in Figure 5.3(a) and (b); even the variation in

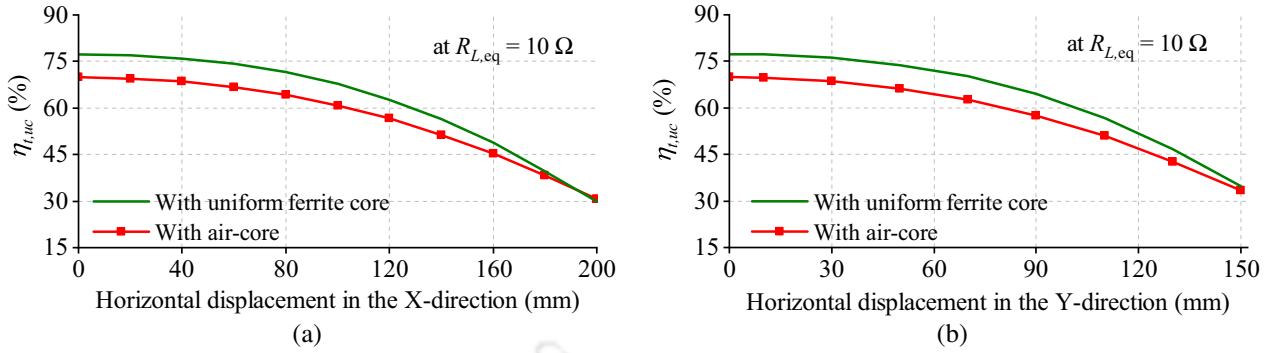

Figure 5.5: Comparison of $\eta_{t,uc}$ at $R_{L,eq}$ = 10 Ω between case 6 air-core and case 6 UFA coil systems when the Rx coil arrangement is horizontally displaced in the (a) X-axis and (b) Y-axis directions at the 150-mm air gap.

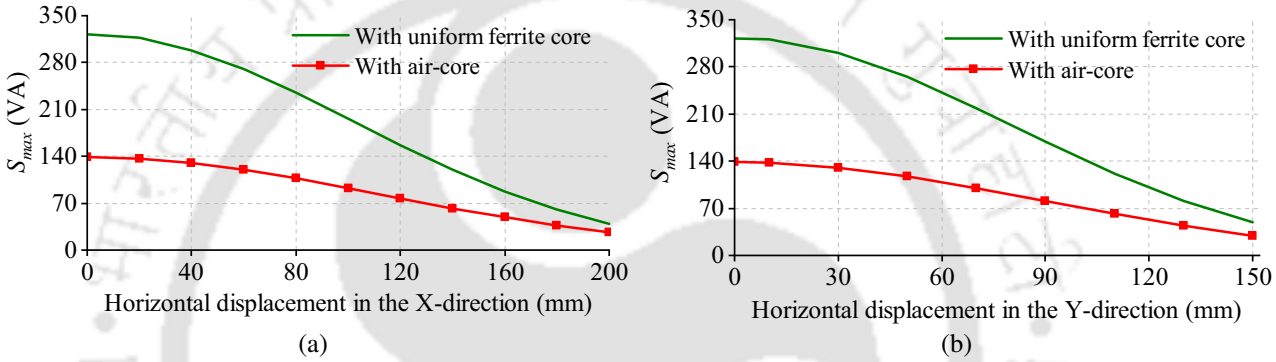

Figure 5.6: Comparison of S_{max} at I_P = 10 A between case 6 air-core and case 6 UFA coil systems when the Rx coil arrangement is horizontally displaced in the (a) X-axis and (b) Y-axis directions at the 150-mm air gap.

improvement in $\eta_{t,uc}$ throughout the misalignment of the Rx coil arrangement. In Figure 5.5(a), the maximum improvement in $\eta_{t,uc}$ of UFA coil system is obtained 11.38% at 80 mm, whereas in Figure 5.5(b), it is 11.95% at 90 mm displacement of the Rx coil arrangement compared with air-core coil system. Moreover, the enhancement in S_{max} for the displacement of the Rx coil arrangement in the X- and Y-directions is shown in Figure 5.6(a) and (b), respectively. From Figure 5.6(a) and (b), it can be seen that S_{max} of case 6 UFA coil system is enhanced throughout the misalignments in the X- and Y-directions compared with the case 6 air-core coil system. A maximum of 132.93% and 133.67% enhancement in S_{max} of case6 UFA coil system (w.r.t. air-core) is obtained at the 0 mm and 10 mm position of the Rx coil arrangement in the X- and Y-directions, respectively.

Thus, the objective of the new ferrite arrangement is to minimise the total ferrite used while maintaining k (obtained from UFA), so that the cost and weight of the coil system can be reduced while maintaining the abovementioned enhancements (Figures 5.4–5.6). Keeping this objective in

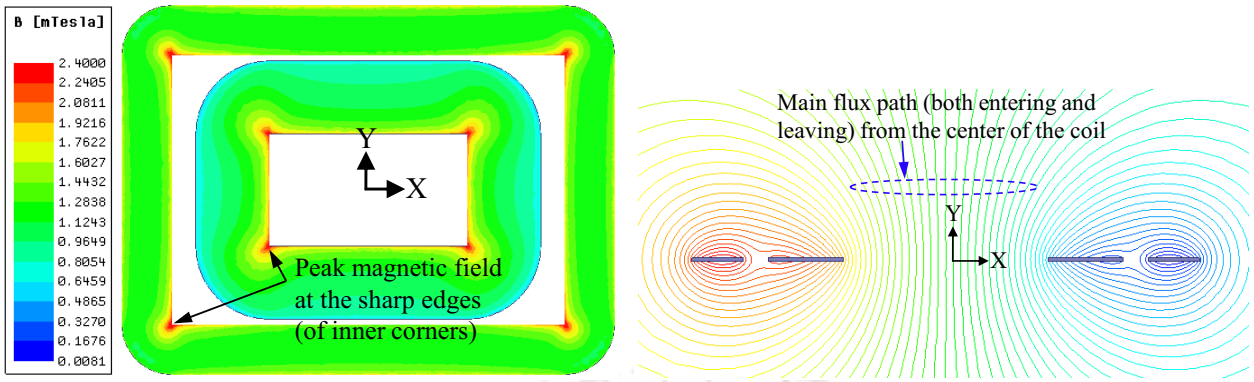

(a) (b)

Figure 5.7: (a) Flux density distribution in case 6 air-core coil showing peak magnetic field at the inner corners. (b) Flux lines distribution of Figure 5.7(a) on the XZ plane illustrating the path of main flux (entering and leaving).

mind, the next section explains the proposed ferrite arrangement and discusses the various other possible ferrite arrangements for comparison.

5.4 Proposed Ferrite Arrangement

In this section, a new and simple ferrite arrangement (PFA) for the unipolar rectangular (and square) air-core coils is presented and analysed. Then, the PFA is compared with various other possible ferrite arrangements along with the reported one in the literature. Moreover, to show the utilisation of ferrites in all the presented ferrite arrangements, the flux density distribution is given.

For minimizing the ferrite volume while maintaining k, prior knowledge of magnetic flux density distribution in the air-core coil is essential. In this context, the flux density distribution in the case 6 air-core coil is shown in Figure 5.7(a). In Figure 5.7(a), peak magnetic field is observed at the inner corners (sharp edges). Moreover, the path of the main flux goes toward the centre part of the coil, as shown in Figure 5.7(b). With these observations, the proposed ferrite arrangement attempts to find a low reluctance path for the peak magnetic flux (at corners) towards the path of the main flux so that the ferrite volume can be minimized while maintaining k.

The fundamental concept of PFA is explained in Figure 5.8(a). Considering the restriction of outer dimensions in EV application (as discussed in Chapters 3 and 4), the length of the ferrite bar of any width (as shown in Figure 5.8) can be calculated using the Pythagoras' theorem as

$$\text{Ferrite bar length} = 0.5\sqrt{x^2 + y^2} - \text{ferrite bar width} \tag{5.1}$$

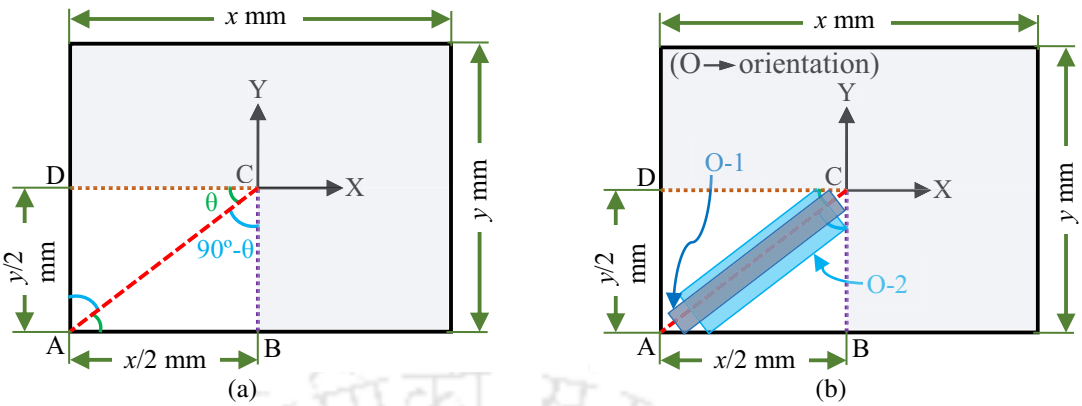

Figure 5.8: Conceptual diagram of the proposed ferrite arrangement. (a) The line (red) and angle for the placement of the ferrite bar (formed by the planar E-cores) in a quarter of the rectangle, calculated using Pythagoras' theorem. This arrangement provides a low reluctance path to most of the flux generated by the neighbor conductors, located on path AD and AB along with the peak flux at the corner(s), while minimising the ferrite used (the same applied to other three parts of the rectangle). (b) Illustration of two different ferrite bar widths formed by interchanging the width and length of each planar E-core.

where x and y are the outer dimensions of the coil. Similarly, the angle (θ) for placing the ferrite bar, as shown in Figure 5.8(a), is given as

$$\theta = \tan^{-1}(y/x) \text{ where } y \leq x. \tag{5.2}$$

Furthermore, to investigate the effect of different ferrite bar widths on k and ferrite volume required, two different orientations (O-1 and O-2) of ferrite bar (obtained by interchanging the width and length of each planar E-core) is taken, as shown in Figure 5.8(b). In the O-1 coil system, the length of the ferrite bar and θ are 225 mm and 36.9° [calculated using (5.1) and (5.2)], respectively, that uses 251.10 cm^3 of ferrite volume (~48 planar E-cores) and gives k = 0.1948 at the 150-mm air gap. Whereas, in the O-2 coil system, the length and θ are 212 mm and 36.9°, respectively, that uses 359.62 cm^3 of ferrite volume (~68 planar E-cores) and gives k = 0.1972 at the 150-mm air gap. On comparing these two coil systems, it is found that increasing the width of the ferrite bar (in O-2) increases the ferrite volume by 43.22% (~10 planar E-cores), that improves k of only 1.23% in comparison to O-1, which is insignificant. Thus, the O-1 coil system is selected for further analysis. The 3-D representation and front view of this coil system can be seen in Figure 5.9(a) and (b), respectively.

For the O-1 coil system, the impact of variation in angle θ with respect to the obtained one [θ = 36.9°; from (5.2)] on k is examined in Figure 5.10. With respect to the reference line shown in Figure

Table 5.1: Comparison among PFA, other possible (and reported) ferrite arrangements, and UFA.

Parameters	UFA	case A	case B	case C	case D	Proposed
3-D representation of the coil system with various types of ferrite arrangements	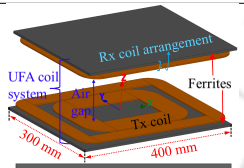	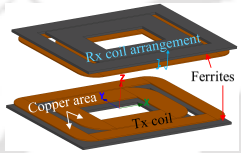	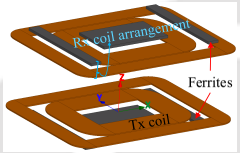	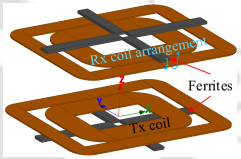	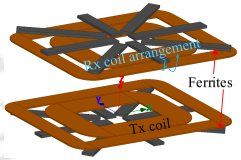	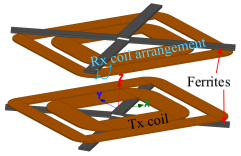
Front view of the ferrite arrangement	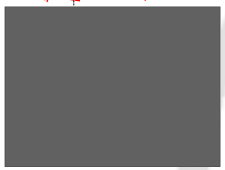	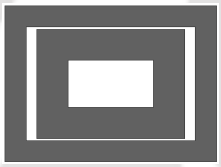	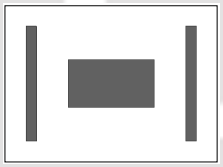	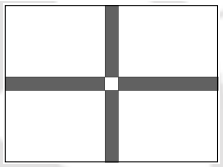	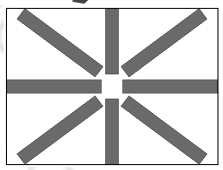	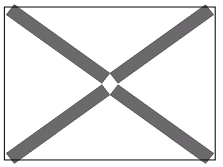
Description of various presented cases	Ferrite is placed on entire coil dimensions	Ferrite is placed only on the copper area	Ferrite is placed at the area where copper is absent	Ferrite bars are placed at the centre of each side of copper area	Radial arrangement of the ferrite bars (widely used [39])	Ferrite bars are placed according to the proposed technique
Ferrite volume used in coil system (cm^3)	1338.31	1050.99	291.29	181.35	377.21	251.11
Ferrite volume saved with respect to UFA	–	21.47%	78.23%	86.45%	71.81%	81.24%
k at 150-mm air gap	0.2093	0.1901	0.1703	0.1782	0.1937	0.1948
Reduction in k with respect to UFA	–	9.17%	18.63%	14.86%	7.45%	6.93%
Increment in self-inductance with respect to air-core	45.50%	27.86%	2.12%	15.38%	25.20%	19.81%
Increment in M with respect to air-core	84.00%	46.90%	5.10%	24.25%	46.55%	41.08%

TH-2585_136102005

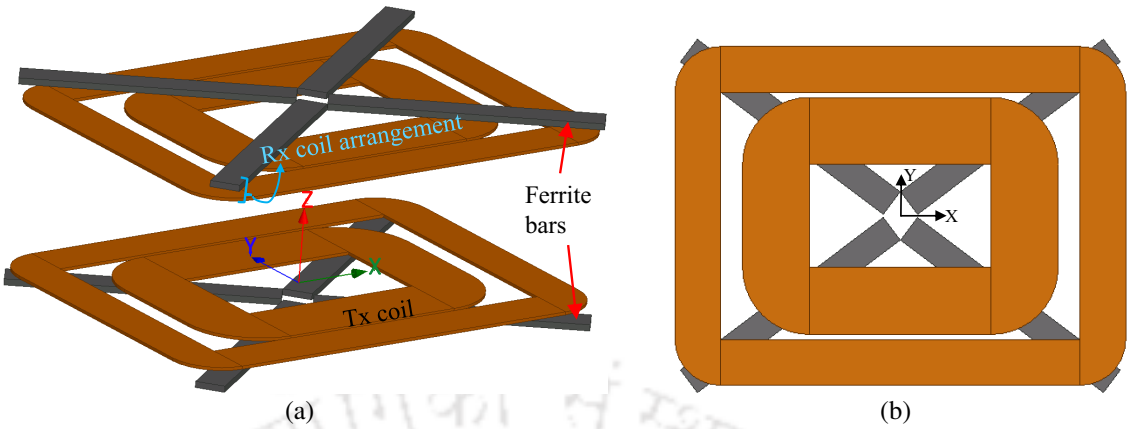

Figure 5.9: PFA with O-1 illustrates (a) an isometric view and (b) front view.

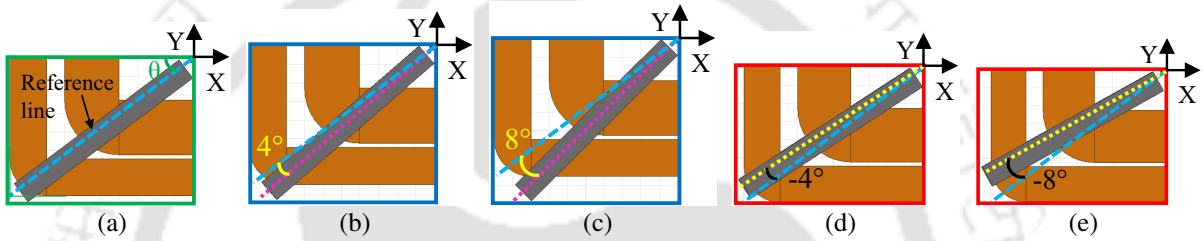

Figure 5.10: Illustration of angle variation of ferrite bar placement. (a) Reference position of ferrite bar obtained from Figure 5.8(a) (k = 0.1948). (b) Position of ferrite bar is varied by 4° (k = 0.1949) and (c) 8° (k = 0.1952) compared with Figure 5.10(a). (d) Position of ferrite bar is varied by -4° (k = 0.1945) and (e) -8° (k = 0.1943) compared with Figure 5.10(a).

5.10(a), θ is varied in Figure 5.10(b)–(e) with a difference of 4° in both sides (keeping the used ferrite volume unchanged). From Figure 5.10(b)–(e), it is seen that the factor k increases by varying θ from -8° to 8°, but requires more outer dimensions in both X- and Y-directions for ferrite bar placement in comparison to those in Figure 5.10(a). However, the outer dimensions are restricted in the EV application. Therefore, the calculated θ [in Figure 5.10(a)] provides a good balance between the obtained k and used outer dimensions (by the ferrite bars). Thus, the ferrite arrangement, as shown in Figure 5.9, is selected for comparison with the various possible ferrite arrangements.

Table 5.1 summarises the various possible ferrite arrangements (cases A–C) including the widely used in the literature (case D) and compare it with PFA for ferrite used, ferrite saved with respect to UFA, k, reduction in k with respect to UFA, increment in self-inductance and M with respect to air-core. The 3-D representation, front view, and the design description of each ferrite arrangement are given in Table 5.1. From the comparison in Table 5.1, it is seen that PFA gives the highest k and uses the second-lowest ferrite volume among all the cases. With respect to UFA, PFA saves 81.24%

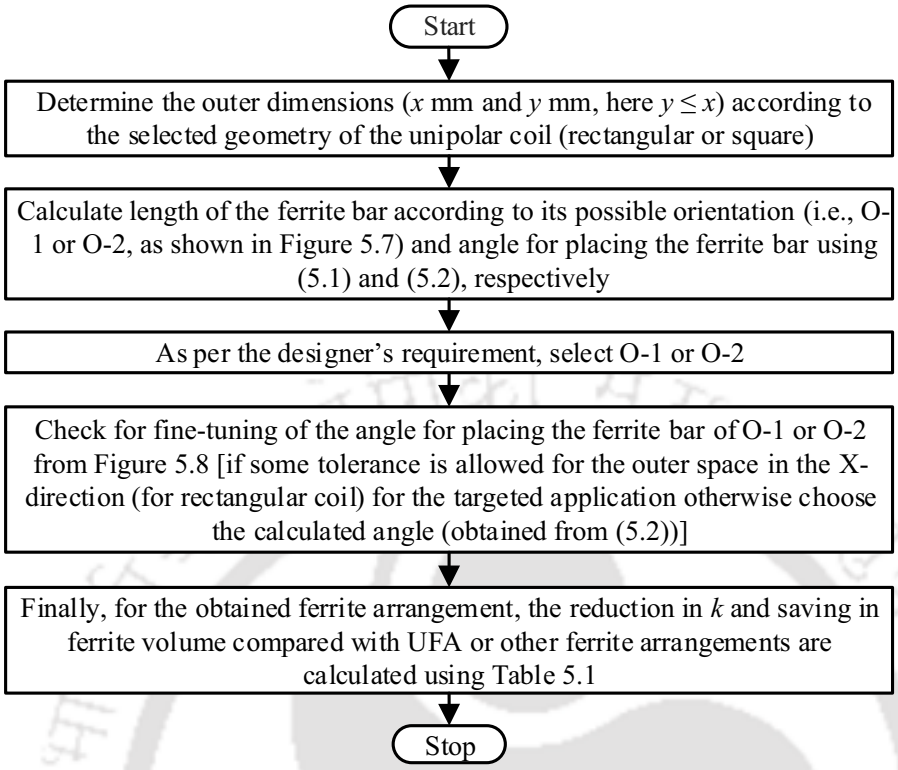

Figure 5.11: Flowchart for finding the PFA for the unipolar rectangular (and square) air-core coils of different outer dimensions.

ferrite volume (second-highest) with a reduction in k of only 6.93% (lowest). The increment in self-inductance and M for PFA are 19.81% and 41.08% with respect to air-core. These increments are more than half (an advantage) compared with the UFA while maintaining k (only 6.93% reduction). The abovementioned process (or steps) explained in this section are summarised in flowchart, as shown in Figure 5.11. With the help of this flowchart, the PFA for the unipolar rectangular (and square) air-core coils of different outer dimensions can be designed (discussed in Section 5.6).

Moreover, the flux density distribution in UFA, cases A–D, and PFA is shown in Figure 5.12 at the current of $10\sqrt{2}$ A. From Figure 5.12(a)–(c), it can be seen that the core utilisation is low in comparison to case C, case D, and PFA. However, case C and case D show similar core utilisation but are lower than PFA, as shown in Figure 5.12(d)–(f). Thus, it can be said that the core utilisation in PFA is maximum among all the presented ferrite arrangements and has the maximum flux density below the saturation point (i.e., 100 mT). In addition, the flux density in all the presented ferrite arrangements remains the below to saturation, as shown in Figure 5.12.

Now, the final simulation of PFA is performed with the ferrite bars made using planar E-cores, as

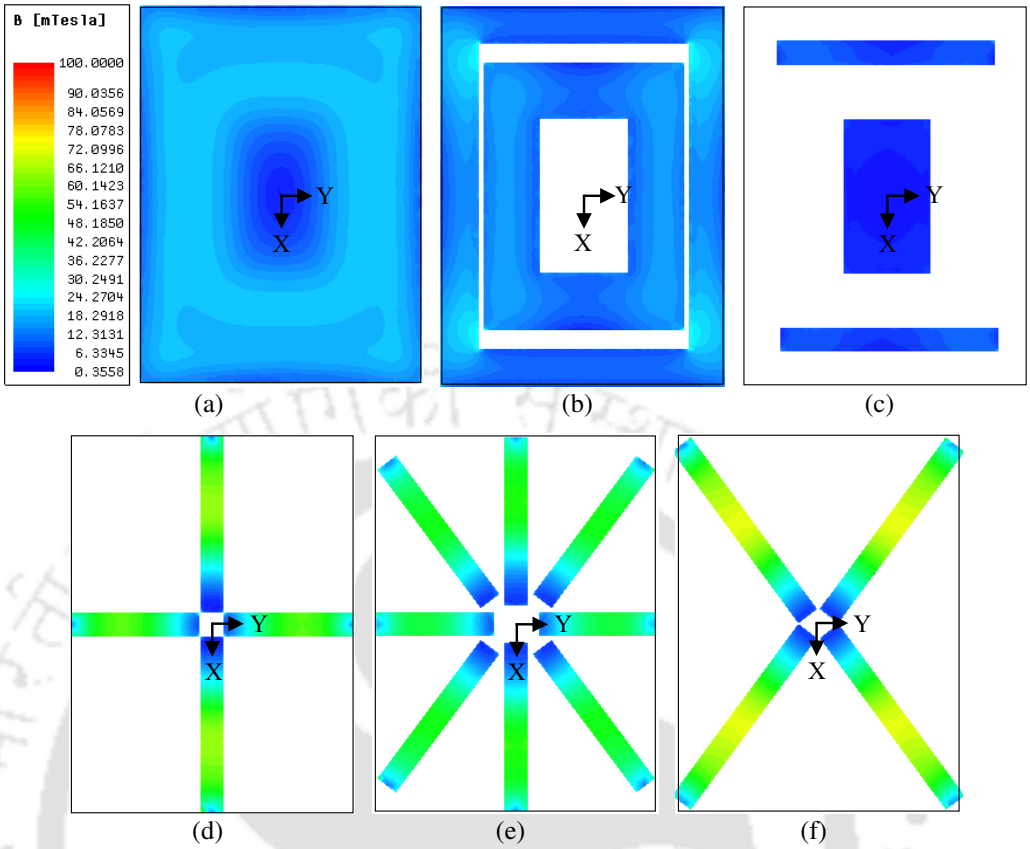

Figure 5.12: Flux density distribution [at $I_P = 10\sqrt{2}$ A (peak)] in (a) UFA, (b) case A, (c) case B, (d) case C, (e) case D, and (f) PFA, to show core utilisation.

shown in Figure 5.13. Here, each ferrite bar contains six planar E-core, which gives 228 mm (6×38) as the length of each ferrite bar. With this ferrite bars, k is 0.1949 at the 150-mm air gap, which is just 0.05% higher than those obtained using the approximated ferrite bars. This difference is due to the increased length of 3 mm (i.e., 228 mm - 225 mm) in each ferrite bar made using planar E-cores, which is reasonable, and it verifies the assumption made in Section 5.2.

The next section presents the prototype of PFA (with case 6 coils) and verifies the calculated (and simulated) results with measurement. Moreover, it also verifies the simulated k obtained for different horizontal misalignments of the Rx coil arrangement at the 150-mm air gap.

5.5 Experimental Verification

The prototype of PFA (with case 6 coil system) is shown in Figure 5.14(c). The same experimental setup, as shown in the Chapter 4 [Figure 4.27(e)], is used for measuring k in different horizontal misalignments of the Rx coil arrangement. The measured value of k is 0.1922 at the 150-mm air gap,

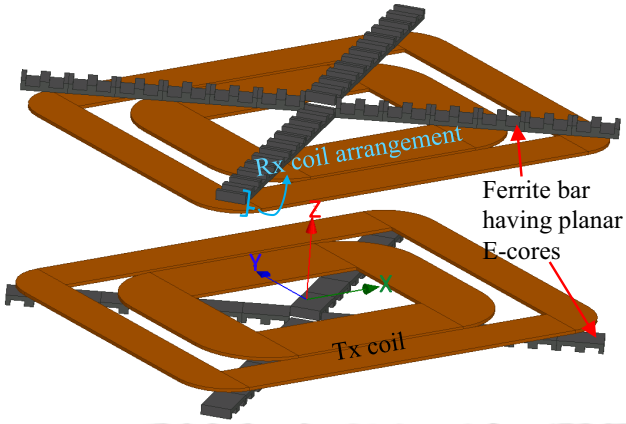

Figure 5.13: 3-D representation of case 6 PFA coil system using planar E-cores in the ferrite bar.

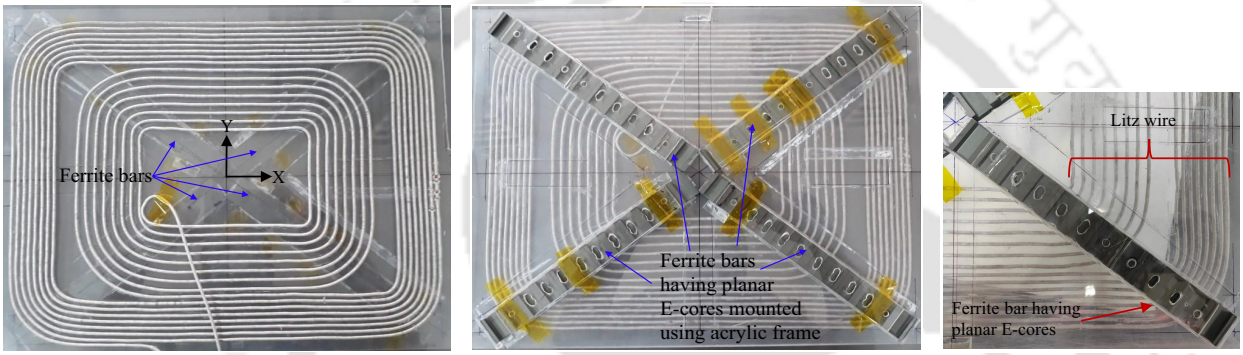

(a) (b) (c)

Figure 5.14: Prototype of PFA with case 6 coil system. (a) Top view (b) Rear view. (c) A fourth part of the rear view.

which is very close to the simulated k (0.1949) with the error of 1.39%. Moreover, the measured value of L_P, L_S, and M is 96.10 μH, 96.23 μH, and 18.479 μH, respectively, which is almost similar to those obtained from simulation (96.60 μH, 97.02 μH, and 18.864 μH). Furthermore, the measured k (of the PFA) for different horizontal misalignments is compared with the simulated k and k of the UFA coil system, as shown in Figure 5.15. From Figure 5.15(a) and (b), it can be seen that the measured and simulated curves of the PFA agree well throughout the misalignments of the Rx coil arrangement in the X- and Y-directions. It is also observed that as the displacement of the Rx coil arrangement increases in both directions [as shown in Figure 5.15(a) and (b)], the difference between k of PFA and UFA coil systems decreases (i.e., reduction in k decreases). Thus, the PFA saves the ferrite volume (81.24% compared with UFA) and maintains k of the UFA coil system (with only 6.93% decrement). In the next section, the PFA is tested with the conventional and other proposed unipolar rectangular coils for different horizontal misalignments of the Rx coil arrangement at the 150-mm air gap.

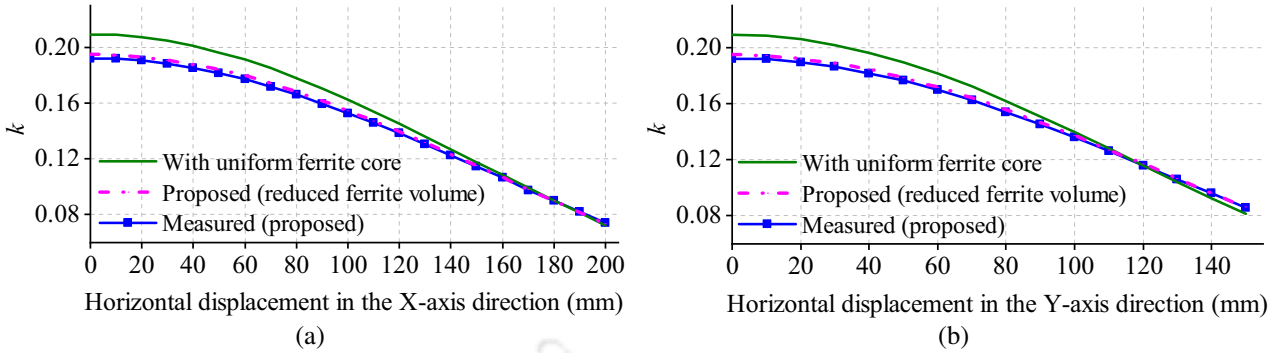

Figure 5.15: Verification of simulated k of case 6 PFA coil system with measurement and its comparison with k of UFA coil systems for horizontal displacement of the Rx coil arrangement in the (a) X-axis and (b) Y-axis directions at the 150-mm air gap.

5.6 Investigation of PFA for the Conventional and Other Proposed Rectangular Coils and Different Outer Dimensions of the Coil

In this section, conventional and proposed unipolar rectangular coils are tested with PFA and are compared with UFA and air-core coils. In the conventional coils, type-I (initial or reference design) and type-H (highest k) coil systems are selected. Whereas, in the proposed coils, case 3 (highest among all) coil system is selected. Since the outer dimensions of type-I, type-H, and case 3 are the same as in case 6, the calculation of the ferrite length, angle, and ferrite volume used is also the same here for PFA. The ferrite dimensions and volume used in UFA are also kept the same as in case 6. Thus, the impact of UFA and PFA on k of the type-I, type-H, and case 3 coil systems can be investigated fairly. Thereafter, PFA is investigated with different outer dimensions of the coil.

Figure 5.16(a) and (b) illustrates the top view (XY plane view) of the type-I coil with UFA and PFA, respectively. In the type-I UFA coil system, the value of L_P, L_S, M, and k at the 150-mm air gap is obtained 102.48 μH, 102.58 μH, 16.590 μH, and 0.1618, respectively. Whereas, in the type-I PFA coil system, these values are 86.61 μH, 86.98 μH, 13.000 μH, and 0.1498, respectively. With the type-I PFA coil system, 7.42% reduction in k is observed compared with type-I UFA coil system (PFA saves 81.24% ferrite volume). Furthermore, k of the type-I UFA and type-I PFA coil systems is compared for different horizontal misalignments of the Rx coil arrangement in the X- and Y-axis directions at the 150-mm air gap, as shown in Figure 5.17(b). In Figure 5.17(b), k of the type-I air-core coil system is also presented, which provides a consolidated comparison. From Figure 5.17(a) and (b), it can be seen that the type-I PFA and type-I UFA coil systems improve k throughout displacement

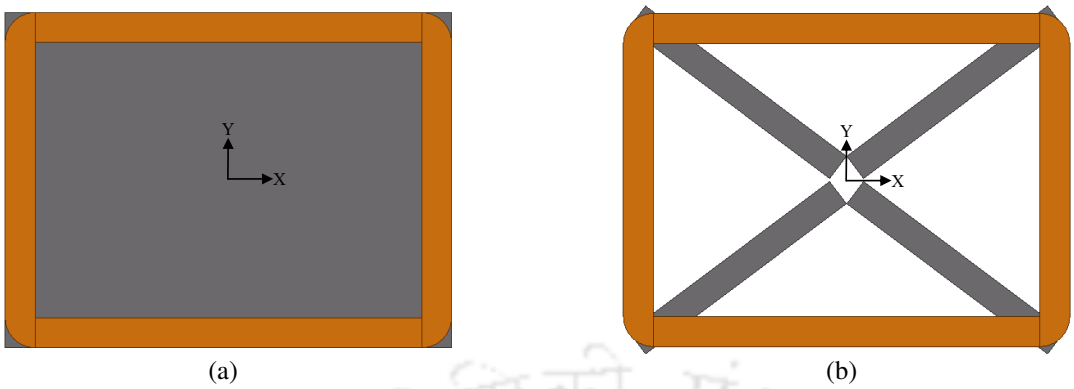

Figure 5.16: Top view (XY plane view) of the type-I coil with (a) UFA and (b) PFA.

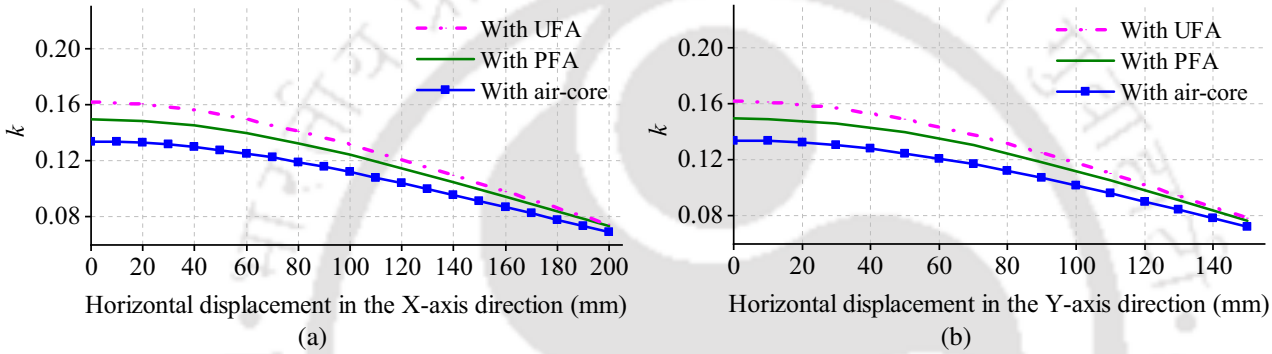

Figure 5.17: Comparison of simulated *k* of the type-I air-core, type-I UFA, and type-I PFA coil systems for horizontal displacement of the Rx coil arrangement in the (a) X-axis and (b) Y-axis directions at the 150-mm air gap.

of the Rx coil arrangement in both directions compared with the type-I air core coil system. It is also observed that the difference between *k* curves of the PFA and UFA becomes narrower with an increase in horizontal misalignment in both directions, and it remains about 2% at the end of the horizontal displacements (i.e., 200 mm for X-axis and 150 mm for Y-axis). Moreover, the maximum improvement in *k* of the type-I PFA and type-I UFA coil systems is obtained at the 0 mm position of the Rx coil arrangement for both misalignments compared with the type-I air-core coil system, which is 11.88% and 20.84%, respectively. These improvements in *k* with the PFA and UFA coil systems are obtained at an additional cost of about 48 and 252 planar E-cores, respectively. Thus, to achieve 75.42% more improvement in *k* with respect to the type-I PFA coil system (obtained in the type-I UFA coil system), an additional cost of 425% in planar E-cores needs to invest (compared with type-I PFA).

Similarly, Figure 5.18(a) and (b) shows the top view of the type-H coil with UFA and PFA, re-

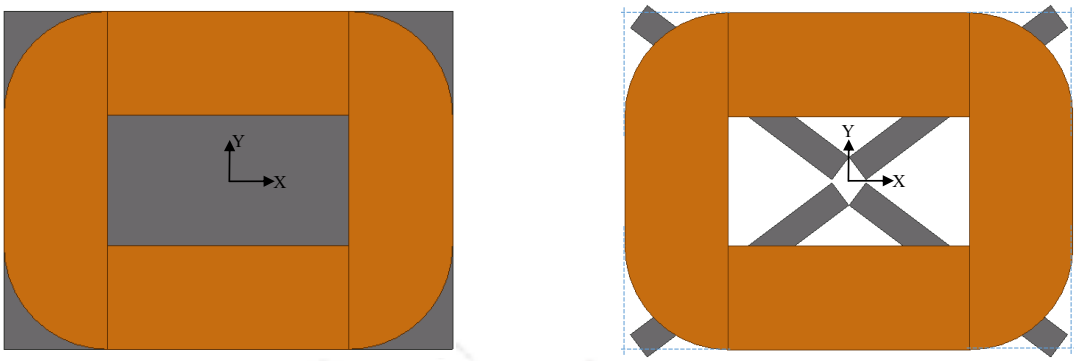

(a) (b)

Figure 5.18: Top view (XY plane view) of the type-H coil with (a) UFA and (b) PFA.

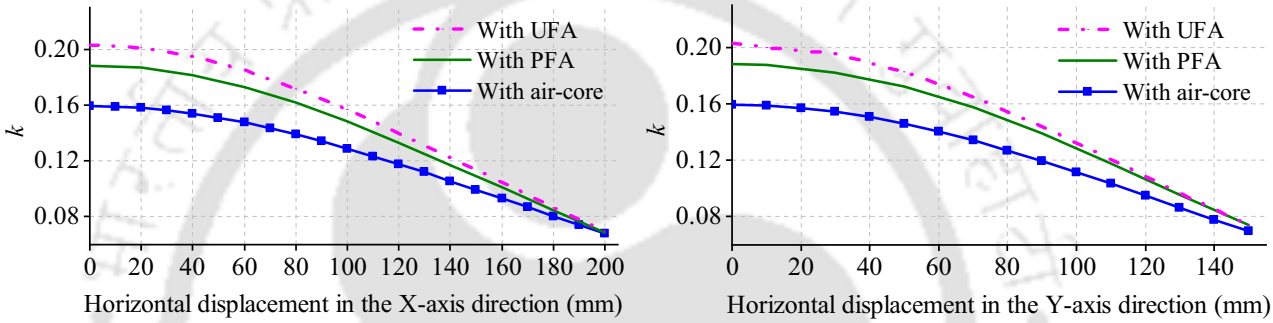

(a) (b)

Figure 5.19: Comparison of simulated k of the type-H air-core, type-H UFA, and type-H PFA coil systems for horizontal displacement of the Rx coil arrangement in the (a) X-axis and (b) Y-axis directions at the 150-mm air gap.

spectively. In the type-H UFA coil system, the value of L_P, L_S, M, and k at the 150-mm air gap is obtained 121.23 μH, 121.30 μH, 24.700 μH, and 0.2033, respectively. Whereas, in the type-H PFA coil system, these values are 98.79 μH, 98.81 μH, 18.626 μH, and 0.1885, respectively. Here, 7.28% reduction in k is seen for type-H PFA coil system with 81.24% saving in ferrite volume compared with type-H UFA coil system. Moreover, k of the type-H UFA, type-H PFA, and type-H air-core coil systems is compared for different horizontal misalignments of the Rx coil arrangement in both directions at the 150-mm air gap, as shown in Figure 5.17(b). From Figure 5.17(a) and (b), it is seen that the type-H PFA and type-H UFA coil systems improve k throughout displacement of the Rx coil arrangement in the X- and Y-axis directions compared with the type-H air core coil system. In Figure 5.17(a) and (b), the difference between k curves of the PFA and UFA becomes narrower with an increase in horizontal misalignment in both directions, and it remains about 1% at 200 mm for X-axis and 150 mm for Y-axis. Furthermore, in the type-H PFA and type-H UFA coil systems, the

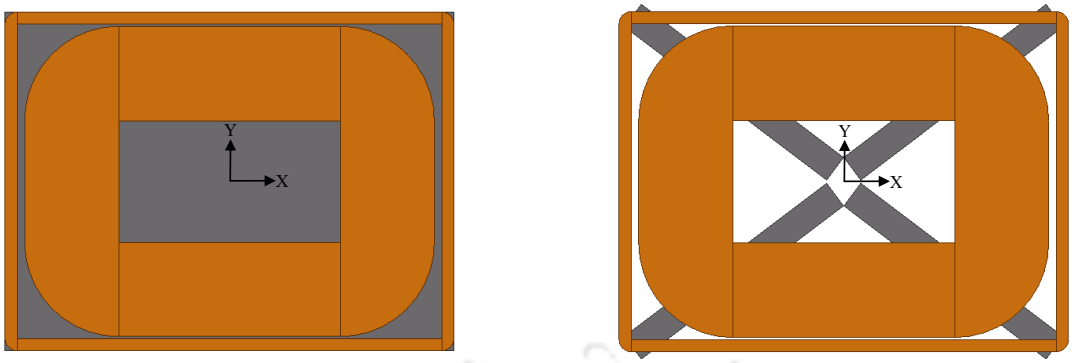

(a) (b)

Figure 5.20: Top view (XY plane view) of the type-I coil with (a) UFA and (b) PFA.

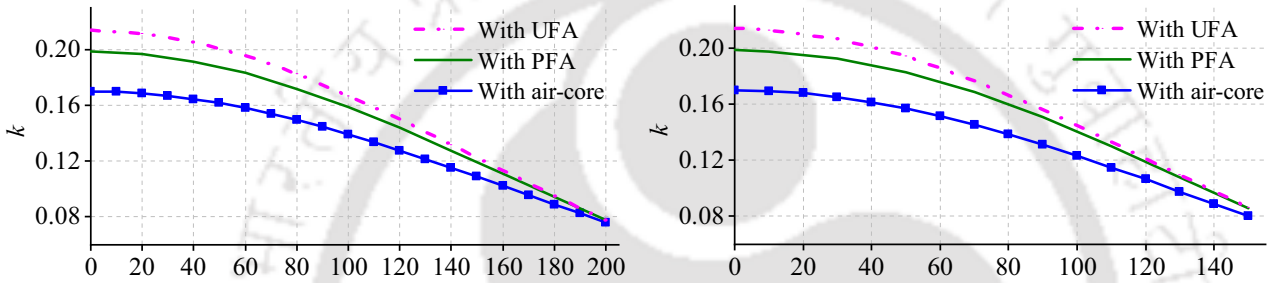

(a) (b)

Figure 5.21: Comparison of simulated k of the case 3 air-core, case 3 UFA, and case 3 PFA coil systems for horizontal displacement of the Rx coil arrangement in the (a) X-axis and (b) Y-axis directions at the 150-mm air gap.

maximum improvement in k of 18.34% and 27.60%, respectively, is obtained at the 0 mm position of the Rx coil arrangement for both misalignments compared with the type-H air-core coil system. Here also, the PFA and UFA coil systems require about 48 and 252 planar E-cores, respectively. Thus, to achieve 50.48% more improvement in k with respect to the type-H PFA coil system (obtained in the type-H UFA coil system), an additional cost of 425% in planar E-cores needs to invest (compared with type-H PFA).

Figure 5.20(a) and (b) illustrates the XY plane view of the case 3 coil with UFA and PFA, respectively. In the case 3 UFA coil system, the value of L_P, L_S, M, and k at the 150-mm air gap is obtained 114.64 μH, 114.72 μH, 24.517 μH, and 0.2138, respectively. Whereas, in the case 3 PFA coil system, these values are 94.93 μH, 94.70 μH, 18.821 μH, and 0.1985, respectively. With the case 3 PFA coil system, 7.15% reduction in k is observed with 81.24% saving in ferrite volume compared with case 3 UFA coil system. Furthermore, k of the case 3 UFA, case 3 PFA, and case 3 air-core coil

systems is compared for different horizontal misalignments of the Rx coil arrangement in the X- and Y-axis directions at the 150-mm air gap, as shown in Figure 5.17(b). From Figure 5.17(a) and (b),it is seen that the case 3 PFA and case 3 UFA coil systems improve k throughout displacement of the Rx coil arrangement in both directions compared with the case 3 air core coil system. Moreover, in Figure 5.17(a) and (b), the difference between k curves of the PFA and UFA becomes narrower with an increase in horizontal misalignment in both directions. This difference is less than 0.9% from 180 mm onwards for X-axis and at 150 mm for Y-axis. Furthermore, the maximum improvement in k of the case 3 PFA and case 3 UFA coil systems is obtained 16.70% and 25.69%, respectively, at the 0 mm position of the Rx coil arrangement for both misalignments compared with the case3 air-core coil system. Here again, the PFA and UFA coil systems use about 48 and 252 planar E-cores, respectively. Thus, to achieve 53.83% more improvement in k with respect to the case 3 PFA coil system (obtained in the case 3 UFA coil system), an additional cost of 425% in planar E-cores needs to invest (compared with case 3 PFA).

Finally, by comparing the type-I, type-H, case 3, and case 6 PFA coil system, it is found that the case 3 PFA coil system has improved the highest k (0.1985) among all the selected PFA coil systems, followed by case 6 PFA coil system.

For showing the example of different dimensions of the coil, type-I square coil system is selected. The specifications of the type-I (square) air-core coils are the same as used in the previous chapter (given in Table 4.10). Figure 5.22(a) and (b) show the type-I (square) UFA and PFA coils, respectively. The ferrite dimensions in Figure 5.22(a) are the same as the dimensions of coil, and it uses 1367.1 cm^3 of ferrite volume. In Figure 5.22(b), the shown length of ferrite bars and θ are calculated using (5.1) and (5.2), respectively. In PFA, the ferrite volume used is only 251.67 cm^3 (i.e., 81.6% saving in ferrite volume compared with UFA). For the 150 mm-air gap, L_P, L_S, M, and k of the UFA and PFA coil systems are obtained (103.28 μH, 103.37 μH, 17.233 μH, and 0.1668) and (86.80 μH, 87.13 μH, 13.317 μH, and 0.1531), respectively. With respect to the air-core coil system, the increment in self-inductance and M are obtained 27.32% and 54.32% for UFA, whereas 7.16% and 19.25% for PFA while maintaining k (only 8.21% deviation compared with UFA). However, at 50% misalignment of the Rx coil arrangement in X- (or Y-) direction (i.e., 175 mm), the difference

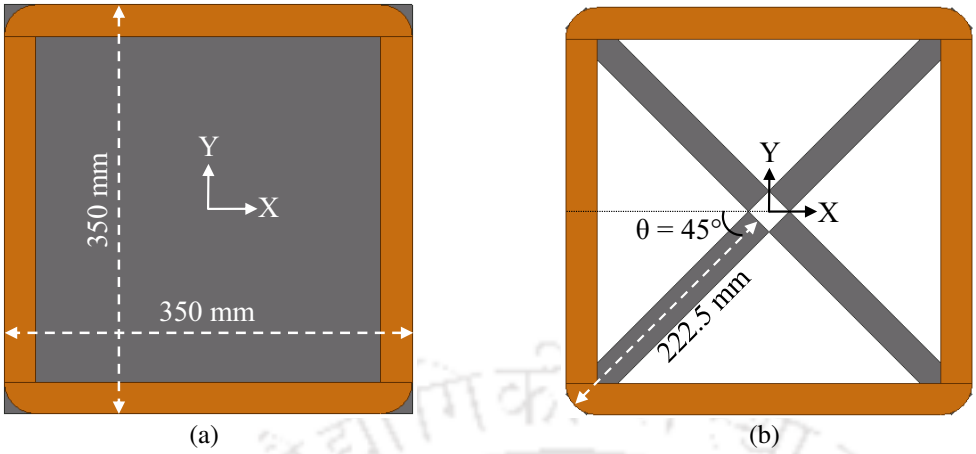

Figure 5.22: Top view (XY plane view) of type-I square coil of 350 mm × 350 mm with (a) UFA, and (b) PFA.

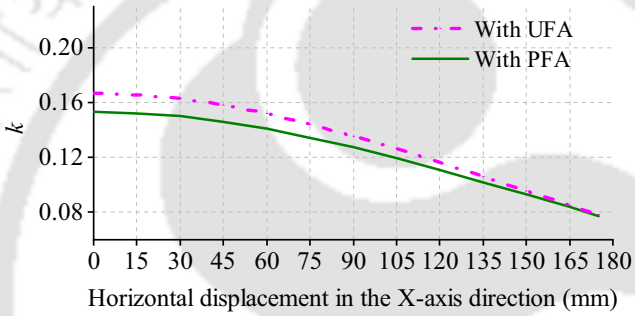

Figure 5.23: Simulated k of type-I (square) UFA and PFA coil systems for horizontal displacement of the Rx coil arrangement in the X- (or Y-) direction.

between k of UFA (0.0783) and PFA (0.0774) becomes only 1.15%, as shown in Figure 5.23. Thus, PFA saves 81.6% ferrite volume while maintaining k in comparison to UFA for the scenario of the different outer dimensions of the coil system as well.

5.7 Summary of the Chapter

In this chapter, the factor k of the air-cored coils (conventional and proposed, presented in the previous chapters) has been improved using the second resort (i.e., with ferrites). In the beginning, the traditional (uniform) ferrite arrangement has been discussed. In the UFA, the ferrite dimensions have been kept equal to the coil outer dimensions due to space limitation in EV. Furthermore, the impact of improved k (using UFA) on the power transfer capability and transmission efficiency is investigated for different horizontal misalignments. For both misalignments, at the 150-mm air gap, the maximum enhancement in S_{max} (of case 6 UFA coils) is obtained 132.30% at the 0 mm position of the Rx coil arrangement compared with case 6 air-core coils. Besides that, the maximum improvement

in transmission efficiency is obtained about 12% in both misalignments. Then, a new and simple ferrite arrangement of the unipolar rectangular (and square) coils has been presented to minimise the volume of ferrite used while maintaining the maximum k (obtained from the UFA), so that the obtained enhancement in S_{max} and transmission efficiency can be maintained, and the cost and weight of the coil system can be reduced. Pythagoras' theorem is used to determine the position and length of the ferrite bars. PFA saves 81.24% volume of the ferrite used with a decrement of only 6.93% in k (for case 6) in comparison to the UFA. Moreover, various possible ferrite arrangements have been investigated and are compared with PFA. From the comparison, it is found that the PFA gives the lowest reduction in k (with respect to UFA) and the second-highest saving in the used ferrite volume. Finally, a prototype of PFA is constructed, and the results are verified.

Furthermore, the PFA has been tested for the type-I, type-H, and case 3 coil systems and compared with UFA and air-core coil systems for different horizontal misalignments. From the comparison, it is found that the case 3 PFA coil system has improved the highest k (0.1985) among all the selected PFA coil systems (including case 6), followed by case 6 PFA coil system. In the selected coil system, PFA saves 81.24% volume of the ferrite used with a decrement of only 6.93%–7.42% in k in comparison to the UFA. Similar results are obtained for PFA with different outer dimensions of the coil (for example, square-shaped). The presented method is elegant and obviates the need for computationally expensive optimisation.

Note: *The research findings of this chapter have been published in "IEEE Transactions on Circuits and Systems II: Express briefs".*

6

Conclusion and Future Works

Contents

This thesis has presented various approaches to improve transmission efficiency and power transfer capability in the WPT system for EV charging applications, which are simple and cost-effective. In the first approach, the transmission efficiency has been improved by operating the WPT system (SP compensated) at the derived optimum frequency, as discussed in Chapter 2. Another approach to improve the transmission efficiency and enhancing the power transfer capability is based on the factor k. By improving k, both transmission efficiency and power transfer capability can be increased. To understand the improvement in k of coils and improving the factor k from different possible ways are discussed in Chapters 3–5. At the end of each chapter, a summary of the individual findings has been given. Therefore, only the key points and conclusions of the work are presented in the upcoming section, followed by the suggestions for future works.

6.1 Key Points of the Work

The key points and conclusions of this thesis are as follows:

- An open-loop control for battery charging using the SP compensated WPT system has been studied. The expression of load phase angle, optimum operating frequency, and $\eta_{t,cc_{max}}$ has been derived (using different equivalent circuits of the SP compensated WPT system) to examine the system performance in the charging process.

- Experimental setup of the SP compensated WPT system has been built for charging the lead-acid battery bank. Measured charging profile and the equivalent resistance profile of the lead-acid battery bank have been presented in the CC and CV modes. Moreover, the derived expressions to examine the system performance have been verified.

- Operating the SP compensated WPT system at the derived optimum frequency has provided proper ZVS in both CC and CV charging modes whereas, at the resonant frequency, proper ZVS is obtained in only CV charging mode.

- Furthermore, the impact of k on transmission efficiency and transferred power has been studied in the CC and CV charging modes, and it is found that to enhance the power transfer capability and transmission efficiency of the WPT system, k should be enhanced.

- Investigation for improving k of unipolar conventional coils has been presented. For the analyses of coils' parameters (magnetic field, self- and mutual inductance, and k), a 3-D analytical model has been developed, which is applicable to square- and rectangular-shaped coils. The presented 3-D analytical model has been verified with 3-D FEA software (ANSYS Maxwell) and measurement. Moreover, the expression for calculating the AC resistance of the coil is presented.

- From the investigation (of improving k), it has been found that improving k by keeping the self-inductance constant while increasing the mutual inductance improves both transmission efficiency and power transfer capability of the WPT system.

- Based on the observations of improving k, the UCAM has been developed and analysed. The proposed UCAM improves k compared with conventional coils of the same self-inductance and outer dimensions in the WPT systems, and it is applicable for different popular shapes (rectangular, square, and circular) of unipolar coils. Moreover, the developed 3-D analytical model (for conventional coil) has been extended to calculate k of coils designed using the proposed UCAM.

- The impact of improved k (of rectangular coils; obtained using the proposed UCAM) on transmission efficiency and power transfer capability has been studied. Furthermore, the impact of different misalignments (vertical and horizontal) on improvement in k has also been investigated.

- Prototypes of conventional (type-I and type-II) and proposed (case 3 and case 6) coil systems have been constructed and the improvement in k and enhancement in power transfer capability and transmission efficiency are verified.

- Interoperability between the proposed and conventional coils has been studied. Moreover, the leakage magnetic field of each coil has been calculated at different distances away from the centre of the Tx coil and compared.

- With the proposed UCAM, the improvement in k for rectangular, square, and circular coils has been shown. For these geometries, both identical and nonidentical unipolar Tx and Rx coils have been considered.

- To further improve the factor k of air-core coils (proposed and conventional), a novel and simple ferrite arrangement of unipolar rectangular (and square) coils has been proposed to minimise the volume of ferrite used while maintaining the maximum k (obtained from the traditional ferrite arrangement). In the proposed arrangement, Pythagoras' theorem has been used to determine the position and length of the ferrite bars. The presented method is elegant and obviates the need for computationally expensive optimisation.

- The proposed ferrite arrangement has been tested with both conventional (type-I and type-H) and proposed (case 3 and case 6) coil systems and compared with the traditional ferrite arrangement. Form the comparison, it has been found that the proposed arrangement saved 81.24% volume of the ferrite used with a decrement of only 6.93%–7.42% in k in comparison to the traditional ferrite arrangement for the conventional and proposed coil systems. Moreover, the improvement in k has also been investigated for different horizontal misalignments of the Rx coil arrangement as well. Finally, the results have been verified with the developed prototype of the proposed ferrite arrangement.

6.2 Suggestions for Future Research

Based on the presented work in the thesis, the following suggestions are given for future research:

- In Chapter 2, an optimum operating frequency for SP compensated WPT system has been derived and analysed, which gives maximum transmission efficiency and maintains ZVS in both CC and CV charging modes. However, the impact of maintaining ZVS in both charging modes on system efficiency is not examined, which can be a further work.

- In continuation of the previous point, the impact of obtained maximum transmission efficiency (at the optimum operating frequency) on system efficiency can also be investigated.

- Moreover, in Chapter 2, the SP compensated WPT system has been analysed in open-loop where the control parameters have also been identified. With these control parameters, one can implement a suitable closed-loop controller for this system (for example, rule-based controller).
- The presented 3-D analytical model in Chapter 3 is for the rectangular-and square-shaped coils. However, when this model is applied to the circular-shaped coil (by doing approximation to a square shape), the obtained error is unacceptable. Therefore, this analytical model can be modified for the circular-shaped coil as well. The modifications may be done by changing the co-coordinate system of the modelling and by changing the current density definitions.
- The proposed UCAM can be extended for more than two sub-coils. Moreover, the impact of including multi-sub-coils can be studied for increasing complexity versus obtained improvement in k compared with two sub-coils.
- Thermal analysis of the proposed coils (cases 1–8) in long hours of use can be performed. Along with this, a comparison with the conventional coils can be done.
- The extended 3-D analytical model in Chapter 4 (for designing the coils using the proposed UCAM) can also be modified for the circular-shaped coils.
- The active and (or) passive shieldings can be investigated for PFA.

भारतीय प्रौद्योगिकी संस्थान गुवाहाटी
Indian Institute of Technology Guwahati

A

Derivation of R_{ac}

A cut section of Figure 2.1 is shown in Figure A.1. Here, it shows the input terminals of the rectifier to the load R_L (with filter) and its equivalent circuit. This appendix give the derivation of $R_{L,eq}$ to get this equivalent circuit.

In the parallel resonant circuit, the rectifier at secondary side is driven by the nearly sinusoidal

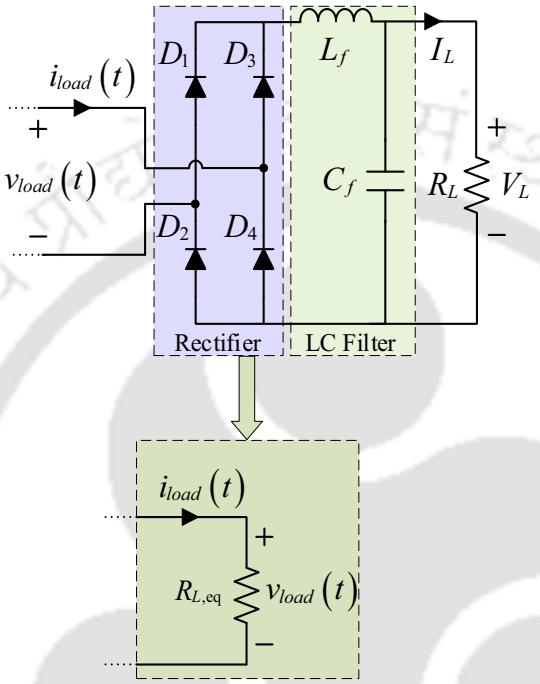

Figure A.1: Cut section of the Figure 2.1, showing circuit of input terminals of the rectifier to the load R_L (with filter) and its equivalent circuit.

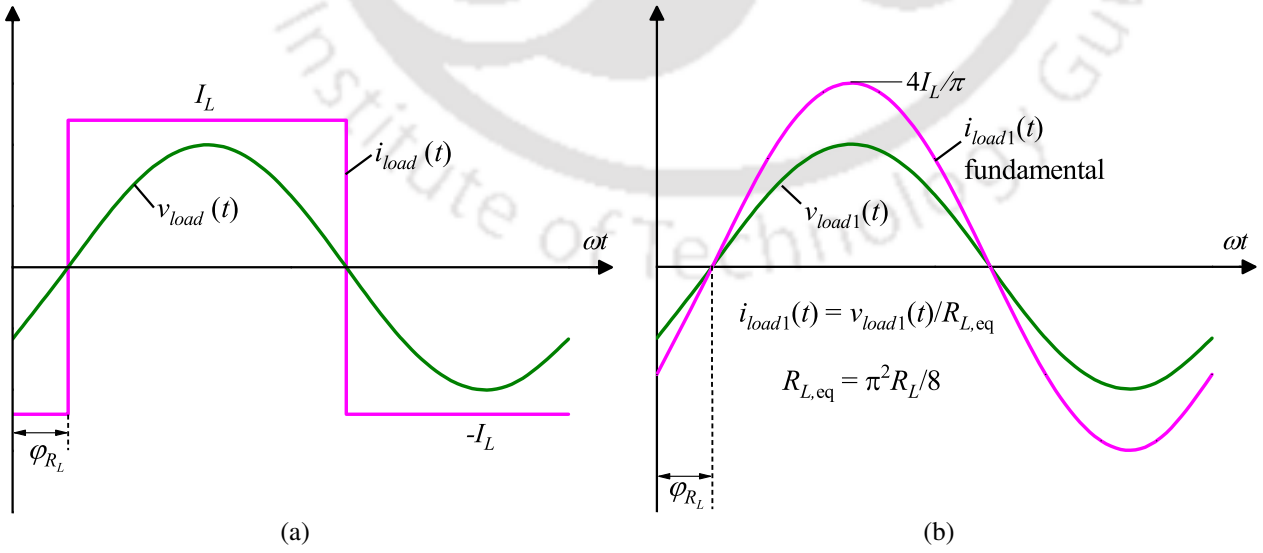

Figure A.2: Waveforms at the input terminals of rectifier for the parallel resonant converter [74]. (a) Actual waveform of current and voltage. (b) fundamental components of Figure A.2(a).

secondary compensation capacitor voltage ($v_{load}(t)$), and the diode rectifiers switch when $v_{load}(t)$ passes through zero as in Figure A.2. If the filter inductor current ripple is small, then in steady-state the filter inductor current is essentially equal to the dc load current I_L. The rectifier input current $i_{load}(t)$ is, therefore, a square wave of amplitude I_L, and is in phase with the secondary compensation capacitor voltage $v_{load}(t)$:

$$i_{load}(t) = \frac{4I_L}{\pi} \sum_{h=1,3,5,..}^{\infty} \frac{1}{h} \sin(h\omega t - \varphi_{R_L}) \tag{A.1}$$

where φ_{R_L} is the phase shift of $v_{load}(t)$.

The fundamental component of $i_{load}(t)$ is

$$i_{load1}(t) = \frac{4I_L}{\pi} \sin(\omega t - \varphi_{R_L}) \tag{A.2}$$

Hence, the rectifier again presents an effective resistive load to the secondary compensation capacitor circuit, equal to

$$R_{L,\text{eq}} = \frac{v_{load1}(t)}{i_{load1}(t)} = \frac{\pi V_{load1}}{4I_{load1}} \tag{A.3}$$

The ac components of the rectified secondary compensation capacitor voltage $|v_{load}(t)|$ are removed by the output filter (low-pass). In steady-state, the output voltage V_L is equal to the DC-components of $|v_{load}(t)|$:

$$V_L = \frac{2}{T_S} \int_0^{T_S/2} V_{load1} \left|\sin(\omega t - \varphi_{R_L})\right| dt = \frac{2}{\pi} V_{load1} \tag{A.4}$$

So the load voltage V_L and the secondary compensation capacitor voltage $v_{load}(t)$ are directly related in steady-state. Substitution of (A.4) and resistive load characteristics $V_L = I_L R_L$ into (A.3) gives:

$$R_{L,\text{eq}} = \frac{\pi^2}{8} R_L \tag{A.5}$$

B

FPGA Programming Code and 3-D model of a Coil for FEA Simulations

B.1 FPGA Programming Code for Generation of Gate Pulses

The following FPGA code is developed to generate 150-kHz square wave pulses (50% duty-cycle), and have a 180° phase shift between two pulses (used in a single inverter leg). Here, a dead-time is also included in the program. The dead-time prevents on-state overlapping and cross-conduction currents through the inverter leg due to the non-ideal nature of switches. The program is based on the clock division concept. The cyclone-II FPGA have 50-Mhz clock frequency. Here, for 50% duty cycle, the counter value is calculated by dividing the FPGA clock frequency to the two times of the required frequency (i.e., 2×150-kHz) and taken the nearest even number of the quotient. For 50% duty-cycle of 150-kHz, the counter value is 166.

```
////////////////////////////////////// Start ////////////////////////////////
 module pwm150Khz_dead(Clock,rst,Pxo,Pyo);
  //port declaration;
  output wire Pxo,Pyo;
  input Clock, rst;
  wire pw15,pw16;

  PWM_150khz_old m1 (Clock,rst,pw5,pw6);
  PWM_150khz_oldd m2(Clock,pw1);
  PWM_150khz_and m3(pw15,pw16,pw1,pw5,pw6);
  PWM_150khz_not m4 (Pxo,Pyo,pw15,pw16);
 endmodule

//////////////////////////////////////////////////////////////////////////////

 module PWM_150khz_not(Pxo,Pyo,pw15,pw16);
  //port declaration;
  output Pxo, Pyo;
  input pw15, pw16;

  not n1(Pxo,pw15);
  not n2(Pyo,pw16);
endmodule

//////////////////////////////////////////////////////////////////////////////

 module PWM_150khz_and(pw15,pw16,pw1,pw5,pw6);
  //port declaration;
  output pw15, pw16;
```

```
 input pw1, pw5, pw6;

 and a1(pw15,pw1,pw5);
 and a2(pw16,pw1,pw6);
endmodule

////////////////////////////////////////////////////////////////////////////////

module PWM_150khz_old(Clock,rst,pw5,pw6);
 //port declaration;
 input Clock;
 input rst;
 output pw5, pw6;

 reg [16:0] r_reg;
 wire [16:0] r_nxt;
 reg clk_track;

 always @(posedge Clock or posedge rst)
    begin
        if (rst)
           begin
              r_reg <= 16'd0;
              clk_track <= 15'd0;
           end

        else if (r_nxt == 16'd166)
           begin
              r_reg <= 0;
              clk_track <=  clk_track;
           end
        else
          r_reg <= r_nxt;
    end

   assign r_nxt = r_reg+1;
   assign pw5 = clk_track;
   assign pw6 = (!pw5);
endmodule

////////////////////////////////////////////////////////////////////////////////

module PWM_150khz_oldd(Clock,pw1);
 //port declaration;
```

```
input Clock;
output reg pw1;
reg [15:0] ct_1=0;

//pwm generation;
always @ (posedge Clock)
  begin
      ct_1=ct_1+1;
        if(ct_1<=166)
          begin
            if(ct_1<=10)  //counter for dead-time;
              begin
                pw1=0;
              end
            else if ((ct_1>11) & (ct_1<=166))
              begin
                pw1=1;
              end
          end
        else
    ct_1=0;
  end
endmodule
```

////////////////////////////////////// End ////////////////////////////////////

The texts written in blue color are the syntax of verilog (a hardware description language).

B.2 Equations based on the Boundary Conditions

By applying the boundary conditions, given in (3.21), the following six equations are given as

$$k_Z\left(c_4^{II}-c_3^{II}\right)-\mu_0 c_I k_X=0 \quad \text{(B.1)}$$

$$k_Z\left(c_2^{II}-c_1^{II}\right)-\mu_0 c_I k_Y=0 \quad \text{(B.2)}$$

$$k_Z^3 c_I\mu_0+\left(\left(c_4^{II}+c_3^{II}\right)k_X+\left(c_2^{II}+c_1^{II}\right)k_Y\right)k_Z^2+\mu_0\left(k_X j_Y^{total}+k_Y j_X^{total}\right)=0 \quad \text{(B.3)}$$

$$k_Z\left(c_4^{II}e^{-k_Z d_w}-c_3^{II}e^{k_Z d_w}\right)-\mu_0 c_{III}k_X e^{-k_Z d_w}=0 \quad \text{(B.4)}$$

$$k_Z\left(c_2^{II}e^{-k_Z d_w}-c_1^{II}e^{k_Z d_w}\right)-\mu_0 c_{III}k_Y e^{-k_Z d_w}=0 \quad \text{(B.5)}$$

$$k_Z^3 c_{III}\mu_0 e^{-k_Z d_w}+\left(\left(c_1^{II}k_Y+c_3^{II}k_X\right)e^{k_Z d_w}-\left(c_2^{II}k_Y+c_4^{II}k_X\right)e^{-k_Z d_w}\right)k_Z^2+\mu_0\left(k_X j_Y^{total}+k_Y j_X^{total}\right)=0. \quad \text{(B.6)}$$

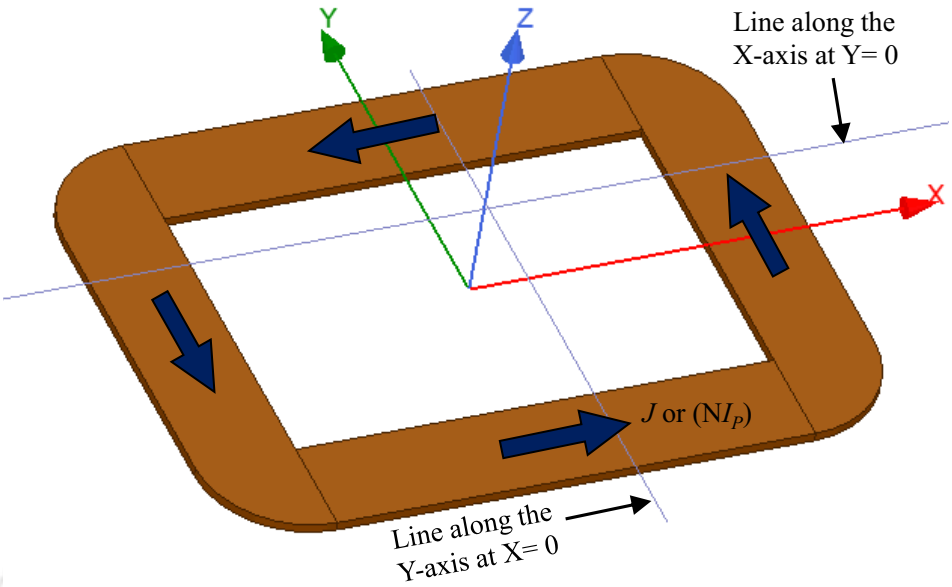

Figure B.1: 3-D model of rectangular coil with circular corners used in 3-D FEA simulation.

B.3 3-D Model of a Coil for FEA Simulations

3-D FEA software ANSYS Maxwell has been used for simulations. Figure B.1 shows the developed 3-D model of a rectangular coil in Maxwell 3D environment. Here, the coil is made with four rectangular bars and circular corners. In each bar, the stranded conductor type is chosen in the current or current density excitation. For the current excitation, the total current is assigned according to the total number of turns. For example, if a single conductor has current I_P and the total number of turns in a coil is N, then the total current in a bar is NI_P (amp-turns). For the current density excitation, a current density terminal is made inside the bar, and then the value of current density is assigned with a sign (+ or -) according to its direction. The magnetostatic solver is used for the (magnetic) simulation. Length based mesh operation is assigned in this model. The maximum length of elements is restricted to 25 mm. Two nonmodel lines, as shown in Figure B.1 are created to obtain the B-fields. Multiple such lines are created to obtain the B-field at different coordinates for a 3-D graph.

B.4 Explanation of the Flowchart in Figure 3.9

The flowchart in Figure 3.9 shows the calculation of B-field at a point (X, Y). At first, record the waveform of the induced EMF at each point. Then, find the waveform of induced EMF for a cycle at a point (X, Y). At point (X, Y), the induced EMF waveform has been integrated over a cycle. This integration gives the waveform of magnetic flux, which has passed through the cross-sectional area of

a pickup coil. Then, the RMS value of this magnetic flux has been divided by the total cross-sectional area of a pickup coil that gives the RMS value of B-field. The same procedure has been applied for the induced EMF measurement at other points.

C

Derivation of Total Required Length of Wire in a Coil Structure (l_{coil})

C. Derivation of Total Required Length of Wire in a Coil Structure (l_{coil})

Figure C.1 shows the geometrical parameters of an example coil structure obtained using the proposed UCAM, and it is used for the calculation of total required length of wire in a coil structure (l_{coil}). The l_{coil} is calculated by adding the length of wire used in OuC and InC, which can be written as

$$l_{coil} = l_{\text{OuC}} + l_{\text{InC}} \tag{C.1}$$

where l_{OuC} is the total length of wire used in OuC, and l_{InC} is the total length of wire used in InC. From Figure C.1(a), l_{OuC} is expressed as

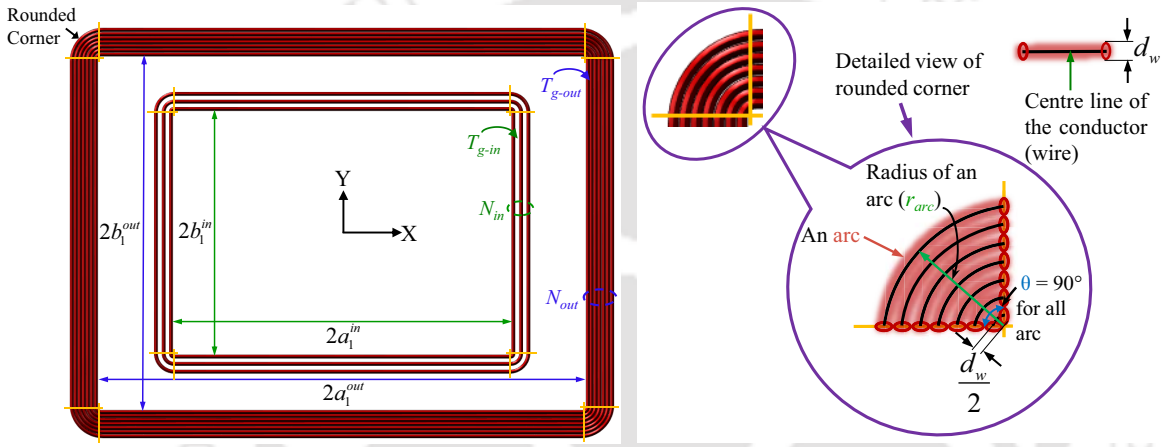

Figure C.1: Illustration of a coil structure (an example of the proposed UCAM) showing (a) geometrical parameters in OuC and InC and (b) detailed view of a rounded corner (shown in Figure C.1(a)) for the calculation of total wire length.

$$l_{\text{OuC}} = 2\left(2a_1^{out}N_{out}\right) + 2\left(2b_1^{out}N_{out}\right) + 4l_{arc}^{out} \tag{C.2}$$

where l_{arc}^{out} is the total length of wire (contributed by all the turns) used in a rounded corner of OuC, forming many arcs due to multiple turns. Traditionally, the length of an arc (l_{arc}) is calculated as

$$l_{arc} = \pi r_{arc}\left(\frac{\theta}{180}\right) \tag{C.3}$$

where θ is the angle of an arc ($^\circ$). From Figure C.1(b), it can be seen that $\theta = 90^\circ$ for all arcs in a rounded corner. Hence, from (C.3), l_{arc}^{out} is expressed as

$$l_{arc}^{out} = \sum_{q_t=1}^{N_{out}} \frac{\pi}{2} G_{out} = \sum_{q_t=1}^{N_{out}} \frac{\pi}{2}\left(\left(T_{g-out} + d_w\right)(q_t - 1) + \frac{d_w}{2}\right) \tag{C.4}$$

where $q_t = 1$ represents the innermost turn of OuC. Substituting (C.4) in (C.2), l_{OuC} can be represented as

$$l_{\mathrm{OuC}} = 4\left[\left(a_1^{out} + b_1^{out}\right) N_{out} + \sum_{q_t=1}^{N_{out}} \frac{\pi}{2}\left(\left(T_{g-out} + d_w\right)(q_t - 1) + \frac{d_w}{2}\right)\right]. \tag{C.5}$$

Similarly, l_{InC} is written as

$$l_{\mathrm{InC}} = 4\left[\left(a_1^{in} + b_1^{in}\right) N_{in} + \sum_{q_t=1}^{N_{in}} \frac{\pi}{2}\left(\left(T_{g-in} + d_w\right)(q_t - 1) + \frac{d_w}{2}\right)\right] \tag{C.6}$$

where $q_t = 1$ represents the innermost turn of InC. Substituting (C.5) and (C.6) in (C.1), the expression of l_{coil} is

$$\begin{aligned} l_{\mathrm{coil}} \;=\; & 4\left[\left(a_1^{out} + b_1^{out}\right) N_{out} + \sum_{q_t=1}^{N_{out}} \frac{\pi}{2}\left(\left(T_{g-out} + d_w\right)(q_t - 1) + \frac{d_w}{2}\right)\right] + 4\left[\left(a_1^{in} + b_1^{in}\right) N_{in} + \sum_{q_t=1}^{N_{in}} \frac{\pi}{2}\right. \\ & \left.\left(\left(T_{g-in} + d_w\right)(q_t - 1) + \frac{d_w}{2}\right)\right]. \end{aligned} \tag{C.7}$$

Here, all the terms used in (C.7) are defined in Chapter 4. For the identical Tx and Rx coil structures, the total required length of Litz wire in a coil system (l_{cs}) is calculated by (such calculations can be seen in Table 4.4)

$$l_{cs} = 2l_{coil}. \tag{C.8}$$

For **conventional coils**, l_{coil} can be calculated by modifying (C.7). In (C.7), the modifications are done by putting $N_{in} = 0$ and replacing the remaining geometrical parameters with the geometrical parameters of conventional coil structure. Thus, the expression of l_{coil} for conventional coil is

$$l_{coil} = 4\left[\left(a_1 + b_1\right) \mathrm{N} + \sum_{q_t=1}^{\mathrm{N}} \frac{\pi}{2}\left(\left(T_g + d_w\right)(q_t - 1) + \frac{d_w}{2}\right)\right]. \tag{C.9}$$

where $q_t = 1$ represents the innermost turn of the coil, and the remaining terms, such as a_1, b_1, N, T_g, and d_w are defined in Chapter 3.

C. Derivation of Total Required Length of Wire in a Coil Structure (l_{coil})

Bibliography

[1] D. Patil, M. K. McDonough, J. M. Miller, B. Fahimi, and P. T. Balsara, "Wireless power transfer for vehicular applications: Overview and challenges," *IEEE Trans. Transport. Electrific.*, vol. 4, no. 1, pp. 3–37, March 2018.

[2] E. R. Joy, B. K. Kushwaha, G. Rituraj, and P. Kumar, "Analysis and comparison of four compensation topologies of contactless power transfer system," in *2015 4th Int. Conf. Electric Power Energy Convers. Syst. (EPECS)*, Nov 2015, pp. 1–6.

[3] V. Shevchenko, O. Husev, R. Strzelecki, B. Pakhaliuk, N. Poliakov, and N. Strzelecka, "Compensation topologies in ipt systems: Standards, requirements, classification, analysis, comparison and application," *IEEE Access*, vol. 7, pp. 120 559–120 580, 2019.

[4] W. Zhang and C. C. Mi, "Compensation topologies of high-power wireless power transfer systems," *IEEE Trans. Veh. Technol.*, vol. 65, no. 6, pp. 4768–4778, June 2016.

[5] G. A. Covic and J. T. Boys, "Modern trends in inductive power transfer for transportation applications," *IEEE J. Emerg. Sel. Topics Power Electron.*, vol. 1, no. 1, pp. 28–41, March 2013.

[6] S. Li and C. C. Mi, "Wireless power transfer for electric vehicle applications," *IEEE J. Emerg. Sel. Topics Power Electron.*, vol. 3, no. 1, pp. 4–17, March 2015.

[7] T. M. Fisher, K. B. Farley, Y. Gao, H. Bai, and Z. T. H. Tse, "Electric vehicle wireless charging technology: a state-of-the-art review of magnetic coupling systems," *Wireless Power Transfer*, vol. 1, no. 2, pp. 87–96, 2014.

[8] J. Sallan, J. Villa, A. Llombart, and J. Sanz, "Optimal design of icpt systems applied to electric vehicle battery charge," *IEEE Trans. Ind. Electron.*, vol. 56, no. 6, pp. 2140–2149, June 2009.

[9] C. Zheng, R. Chen, E. Faraci, Z. U. Zahid, M. Senesky, D. Anderson, J. S. Lai, W. Yu, and C. Y. Lin, "High efficiency contactless power transfer system for electric vehicle battery charging," in *2013 IEEE Energy Conv. Congr. Expo.*, Sept 2013, pp. 3243–3249.

[10] J. D. Jackson, *Classical Electrodynamics*. Hoboken, NJ, USA: Wiley, 1999.

[11] C.-S. Wang, G. A. Covic, and O. H. Stielau, "Power transfer capability and bifurcation phenomena of loosely coupled inductive power transfer systems," *IEEE Trans. Ind. Electron.*, vol. 51, no. 1, pp. 148–157, Feb 2004.

[12] G. Rituraj, E. R. Joy, B. K. Kushwaha, and P. Kumar, "Analysis and comparison of series-series and series-parallel topology of contactless power transfer systems," in *TENCON 2014 - IEEE Region 10 Conf.*, Oct 2014, pp. 1–6.

[13] B. K. Kushwaha, G. Rituraj, P. Kumar, and P. Bauer, "Mathematical model for the analysis of series-parallel compensated wireless power transfer system for different misalignments," *IET Circuits, Devices & Systems*, vol. 13, no. 7, pp. 970–978, 2019.

[14] A. Khaligh and Z. Li, "Battery, ultracapacitor, fuel cell, and hybrid energy storage systems for electric, hybrid electric, fuel cell, and plug-in hybrid electric vehicles: State of the art," *IEEE Trans. Veh. Technol.*, vol. 59, no. 6, pp. 2806–2814, July 2010.

[15] Y. Chen, Z. Kou, Y. Zhang, Z. He, R. Mai, and G. Cao, "Hybrid topology with configurable charge current and charge voltage output-based wpt charger for massive electric bicycles," *IEEE J. Emerg. Sel. Topics Power Electron.*, vol. 6, no. 3, pp. 1581–1594, Sep. 2018.

[16] G. Buja, M. Bertoluzzo, and K. N. Mude, "Design and experimentation of wpt charger for electric city car," *IEEE Trans. Ind. Electron.*, vol. 62, no. 12, pp. 7436–7447, Dec 2015.

[17] G. Monti, A. Costanzo, F. Mastri, and M. Mongiardo, "Optimal design of a wireless power transfer link using parallel and series resonators," *Wireless Power Transfer*, vol. 3, no. 2, pp. 105–116, 2016.

[18] K. Aditya and S. S. Williamson, "Comparative study of series-series and series-parallel topology for long track ev charging application," in *2014 IEEE Transport. Electrific. Conf. and Expo (ITEC)*, June 2014, pp. 1–5.

[19] Y. H. Chao, J. J. Shieh, C. T. Pan, and W. C. Shen, "A closed-form oriented compensator analysis for series-parallel loosely coupled inductive power transfer systems," in *2007 IEEE Power Electron. Specialists Conf. (PESC)*, June 2007, pp. 1215–1220.

[20] N. Liu and T. G. Habetler, "Design of a universal inductive charger for multiple electric vehicle models," *IEEE Trans. Power Electron.*, vol. 30, no. 11, pp. 6378–6390, Nov 2015.

[21] B. Jiang, J. g. Wang, L. j. Chen, B. Wang, and Q. Wang, "A efficient control method for series-parallel cpt system," in *2014 33rd Chinese Control Conf. (CCC)*, July 2014, pp. 3500–3504.

[22] S. J. Huang, Y. J. Li, B. G. Huang, T. H. Huang, and T. S. Lee, "Contactless energy-transfer system design for lithium iron phosphate battery-charging circuits," in *2013 IEEE 10th Int. Conf. Power Electron. Drive Syst. (PEDS)*, April 2013, pp. 217–220.

[23] C. Zheng, J. S. Lai, R. Chen, W. E. Faraci, Z. U. Zahid, B. Gu, L. Zhang, G. Lisi, and D. Anderson, "High-efficiency contactless power transfer system for electric vehicle battery charging application," *IEEE J. Emerg. Sel. Topics Power Electron.*, vol. 3, no. 1, pp. 65–74, March 2015.

[24] B. K. Kushwaha, G. Rituraj, and P. Kumar, "3-d analytical model for computation of mutual inductance for different misalignments with shielding in wireless power transfer system," *IEEE Trans. Transport. Electrific.*, vol. 3, no. 2, pp. 332–342, June 2017.

[25] B. R. Long, J. M. Miller, A. Daga, P. C. Schrafel, and J. Wolgemuth, "Which way for wireless power: High q or high k?" in *2016 IEEE PELS Workshop Emerg. Tech.: Wireless Power Transfer (WoW)*, Oct 2016, pp. 6–10.

[26] Z. Zhang, H. Pang, A. Georgiadis, and C. Cecati, "Wireless power transfer-an overview," *IEEE Trans. Ind. Electron.*, vol. 66, no. 2, pp. 1044–1058, Feb. 2019.

[27] M. Mohammad, S. Choi, Z. Islam, S. Kwak, and J. Baek, "Core design and optimization for better misalignment tolerance and higher range of wireless charging of phev," *IEEE Trans. Transport. Electrific.*, vol. 3, no. 2, pp. 445–453, Jun. 2017.

[28] H. Li, K. Wang, L. Huang, J. Li, and X. Yang, "Coil structure optimization method for improving coupling coefficient of wireless power transfer," in *2015 IEEE Applied Power Electron. Conf. Expo. (APEC)*, March 2015, pp. 2518–2521.

[29] Z. Luo and X. Wei, "Analysis of square and circular planar spiral coils in wireless power transfer system for electric vehicles," *IEEE Trans. Ind. Electron.*, vol. 65, no. 1, pp. 331–341, Jan. 2018.

[30] A. Zaheer, G. A. Covic, and D. Kacprzak, "A bipolar pad in a 10-khz 300-w distributed ipt system for agv applications," *IEEE Trans. Ind. Electron.*, vol. 61, no. 7, pp. 3288–3301, Jul. 2014.

[31] M. Budhia, J. T. Boys, G. A. Covic, and C. Huang, "Development of a single-sided flux magnetic coupler for electric vehicle ipt charging systems," *IEEE Trans. Ind. Electron.*, vol. 60, no. 1, pp. 318–328, Jan. 2013.

[32] A. Zaheer, H. Hao, G. A. Covic, and D. Kacprzak, "Investigation of multiple decoupled coil primary pad topologies in lumped ipt systems for interoperable electric vehicle charging," *IEEE Trans. Power Electron.*, vol. 30, no. 4, pp. 1937–1955, Apr. 2015.

[33] A. A. S. Mohamed, S. An, and O. Mohammed, "Coil design optimization of power pad in ipt system for electric vehicle applications," *IEEE Trans. Magn.*, vol. 54, no. 4, pp. 1–5, Apr. 2018.

[34] S. Moon and G. W. Moon, "Wireless power transfer system with an asymmetric four-coil resonator for electric vehicle battery chargers," *IEEE Trans. Power Electron.*, vol. 31, no. 10, pp. 6844–6854, Oct 2016.

[35] D. H. Tran, V. B. Vu, and W. Choi, "Design of a high-efficiency wireless power transfer system with intermediate coils for the on-board chargers of electric vehicles," *IEEE Trans. Power Electron.*, vol. 33, no. 1, pp. 175–187, Jan 2018.

[36] S. Kim, G. A. Covic, and J. T. Boys, "Tripolar pad for inductive power transfer systems for ev charging," *IEEE Trans. Power Electron.*, vol. 32, no. 7, pp. 5045–5057, July 2017.

[37] K. L. H. A. B. Kurs, M. P. Kesler and A. J. Campanella, "High frequency pcb coils," US Patent 2013/0 069 753 A1, 2013.

[38] Z. Zhang, H. Pang, C. H. T. Lee, X. Xu, X. Wei, and J. Wang, "Comparative analysis and optimization of dynamic charging coils for roadway-powered electric vehicles," *IEEE Trans. Magn.*, vol. 53, no. 11, pp. 1–6, Nov. 2017.

[39] Y. Zhang, L. Wang, Y. Guo, and C. Tao, "Design and optimization of asymmetrical spiral rectangular pads for ev wireless charging," in *2018 IEEE 4th Southern Power Electron. Conf. (SPEC)*, 2018, pp. 1–5.

[40] F. Lu, H. Zhang, H. Hofmann, and C. C. Mi, "A dynamic charging system with reduced output power pulsation for electric vehicles," *IEEE Trans. Ind. Electron.*, vol. 63, no. 10, pp. 6580–6590, Oct 2016.

[41] V. Prasanth, S. Bandyopadhyay, P. Bauer, and J. A. Ferreira, "Analysis and comparison of multi-coil inductive power transfer systems," in *2016 IEEE Int. Power Electron. Motion Control Conf. (PEMC)*, Sep. 2016, pp. 993–999.

[42] M. Budhia, G. A. Covic, and J. T. Boys, "Design and optimization of circular magnetic structures for lumped inductive power transfer systems," *IEEE Trans. Power Electron.*, vol. 26, no. 11, pp. 3096–3108, 2011.

[43] Y. Hsieh, Z. Lin, M. Chen, H. Hsieh, Y. Liu, and H. Chiu, "High-efficiency wireless power transfer system for electric vehicle applications," *IEEE Trans. Circuits Syst. II, Exp. Briefs*, vol. 64, no. 8, pp. 942–946, 2017.

[44] C. Panchal, S. Stegen, and J. Lu, "Review of static and dynamic wireless electric vehicle charging system," *An Int. J. Eng. Sci. Tech.*, vol. 21, no. 5, pp. 922 – 937, 2018.

[45] J. P. C. Smeets, T. T. Overboom, J. W. Jansen, and E. A. Lomonova, "Inductance calculation nearby conducting material," *IEEE Trans. Magn.*, vol. 50, no. 11, pp. 1–4, Nov 2014.

[46] T. Lubin and A. Rezzoug, "3-d analytical model for axial-flux eddy-current couplings and brakes under steady-state conditions," *IEEE Trans. Magn.*, vol. 51, no. 10, pp. 1–12, Oct 2015.

[47] J. P. C. Smeets, T. T. Overboom, J. W. Jansen, and E. A. Lomonova, "Three-dimensional magnetic field modeling for coupling calculation between air-cored rectangular coils," *IEEE Trans. Magn.*, vol. 47, no. 10, pp. 2935–2938, Oct 2011.

[48] J. P. C. Smeets, T. T. Overboom, J. W. Jansen, and E. A. Lomonova, "Three-dimensional analytical modeling technique of electromagnetic fields of air-cored coils surrounded by different ferromagnetic boundaries," *IEEE Trans. Magn.*, vol. 49, no. 12, pp. 5698–5708, Dec 2013.

[49] J. P. C. Smeets, T. T. Overboom, J. W. Jansen, and E. A. Lomonova, "Mode-matching technique applied to three-dimensional magnetic field modeling," *IEEE Trans. Magn.*, vol. 48, no. 11, pp. 3383–3386, Nov 2012.

[50] A. Dalal, T. P. E. R. Joy, and P. Kumar, "Mutual inductance computation method for coils of different geometries and misalignments," in *2015 IEEE Power Energy Soc. Gen. Meeting*, July 2015, pp. 1–5.

[51] K. J. Meessen, B. L. J. Gysen, J. J. H. Paulides, and E. A. Lomonova, "General formulation of fringing fields in 3-d cylindrical structures using fourier analysis," *IEEE Trans. Magn.*, vol. 48, no. 8, pp. 2307–2323, Aug 2012.

[52] E. R. Joy, A. Dalal, and P. Kumar, "Accurate computation of mutual inductance of two air core square coils with lateral and angular misalignments in a flat planar surface," *IEEE Trans. Magn.*, vol. 50, no. 1, pp. 1–9, Jan 2014.

[53] "Electric vehicles inindia and its impact on grid," NSGM-PMU, Tech. Rep. [Online]. Available: https://www.nsgm.gov.in/sites/default/files/EV_in_India_and_its_Impact_on_Grid.pdf

[54] X. Qu, H. Han, S. Wong, C. K. Tse, and W. Chen, "Hybrid ipt topologies with constant current or constant voltage output for battery charging applications," *IEEE Trans. Power Electron.*, vol. 30, no. 11, pp. 6329–6337, Nov 2015.

[55] K. Aditya and S. S. Williamson, "Comparative study of series-series and series-parallel compensation topologies for electric vehicle charging," in *2014 IEEE 23rd Int. Symp. Ind. Electron. (ISIE)*, June 2014, pp. 426–430.

[56] C. T. Rim and C. Mi, *Wireless Power Transfer for Electric Vehicles and Mobile Devices*, 1st ed. Wiley-IEEE Press, Jun. 2017, no. 53-65.

[57] TDK, "Equivalent series resistance (esr) of metallized polypropylene film capacitors." [Online]. Available: https://www.tdk-electronics.tdk.com/inf/20/20/db/fc_2009/MKP_B32674_678.pdf

[58] H. Li, Y. Liu, K. Zhou, Z. He, W. Li, and R. Mai, "Uniform power ipt system with three-phase transmitter and bipolar receiver for dynamic charging," *IEEE Trans. Power Electron.*, vol. 34, no. 3, pp. 2013–2017, March 2019.

[59] Y. Li, T. Lin, R. Mai, L. Huang, and Z. He, "Compact double-sided decoupled coils-based wpt systems for high-power applications: Analysis, design, and experimental verification," *IEEE Trans. Transport. Electrific.*, vol. 4, no. 1, pp. 64–75, March 2018.

[60] E. R. Joy, A. Dalal, and P. Kumar, "Accurate computation of mutual inductance of two air core square coils with lateral and angular misalignments in a flat planar surface," *IEEE Trans. Magn.*, vol. 50, no. 1, pp. 1–9, Jan 2014.

[61] A. Ahmad, M. S. Alam, and A. A. S. Mohamed, "Design and interoperability analysis of quadruple pad structure for electric vehicle wireless charging application," *IEEE Trans. Transport. Electrific.*, vol. 5, no. 4, pp. 934–945, Dec 2019.

[62] J. P. C. Smeets, "Contactless transfer of energy : 3d modeling and designof a position-independent inductive coupling integrated ina planar motor," Ph.D. dissertation, Eindhoven: Technische Universiteit Eindhoven., 2015.

[63] G. Rituraj, B. K. Kushwaha, and P. Kumar, "3-d analytical modeling of magnetic field for air core rectangular coil in contactless power transfer system," in *IECON 2016 - 42nd Annu. Conf. IEEE Ind. Electron.Soc.*, Oct. 2016, pp. 4459–4464.

[64] K. Raeen, "A study of the gibbs phenomenon in fourier series and wavelets," Master's thesis, The University of New Mexico, August 2008.

[65] M. Lu and K. D. T. Ngo, "Analytical calculation of proximity-effect resistance for planar coil with litz wire and ferrite plate in inductive power transfer," *IEEE Trans. Ind. Appl.*, vol. 55, no. 3, pp. 2984–2991, May 2019.

[66] C. R. Sullivan, "Computationally efficient winding loss calculation with multiple windings, arbitrary waveforms, and two-dimensional or three-dimensional field geometry," *IEEE Trans. Power Electron.*, vol. 16, no. 1, pp. 142–150, Jan 2001.

[67] J. M. Miller, O. C. Onar, and M. Chinthavali, "Primary-side power flow control of wireless power transfer for electric vehicle charging," *IEEE J. Emerg. Sel. Topics Power Electron.*, vol. 3, no. 1, pp. 147–162, March 2015.

[68] S. Hasanzadeh, S. Vaez-Zadeh, and A. H. Isfahani, "Optimization of a contactless power transfer system for electric vehicles," *IEEE Trans. Veh. Technol.*, vol. 61, no. 8, pp. 3566–3573, Oct 2012.

[69] "Guidelines for limiting exposure to time-varying electric, magnetic, and electromagnetic fields (up to 300 ghz). icnirp." *Health phys.*, vol. 74, no. 4, pp. 494–522, Apr. 1998.

[70] L. Zhao, D. J. Thrimawithana, U. K. Madawala, A. P. Hu, and C. C. Mi, "A misalignment-tolerant series-hybrid wireless ev charging system with integrated magnetics," *IEEE Trans. Power Electron.*, vol. 34, no. 2, pp. 1276–1285, Feb 2019.

[71] Y. Chen, Z. Kou, Y. Zhang, Z. He, R. Mai, and G. Cao, "Hybrid topology with configurable charge current and charge voltage output-based wpt charger for massive electric bicycles," *IEEE J. Emerg. Sel. Topics Power Electron.*, vol. 6, no. 3, pp. 1581–1594, Sep. 2018.

[72] *Soft Ferrites and Accessories, Data Handbook, 2013. [Online]. Available: http://www.ferroxcube.com.*

[73] G. Rituraj, B. K. Kushwaha, and P. Kumar, "A unipolar coil arrangement method for improving the coupling coefficient without ferrite material in wireless power transfer systems," *IEEE Trans. Transport. Electrific.*, vol. 6, no. 2, pp. 497–509, 2020.

[74] R. W. Erickson and D. Maksimovic, *Fundamentals of Power Electronics*. Kluwer Academic Publishers, 2001.

List of Publications

In this thesis, various parts of the presented research findings have been published or will be published in international journals and conference proceedings, or have been protected by patents. Those patents, journal papers, and conference papers are listed below.

Patents

1. **G. Rituraj** and P. Kumar, "Unipolar coil arrangement method for improving the coupling factor and reducing the electromagnetic emissions in wireless power transfer systems and a coil thereof," **Indian Patent** 201931003386, filed on 28 Jan **2019**, published on 01 Mar **2019** (supported provided by Patent Information Centre–ASTEC Guwahati-Assam).

Journal Papers

1. **G. Rituraj** and P. Kumar, "A new magnetic structure of unipolar rectangular coils in wpt systems to minimize the ferrite volume while maintaining maximum coupling," in ***IEEE Transactions on Circuits and Systems II: Express briefs***, DOI:10.1109/TCSII.2020.3044585.

2. **G. Rituraj**, B. K. Kushwaha, and P. Kumar, "A unipolar coil arrangement method for improving the coupling coefficient without ferrite material in wireless power transfer systems," in ***IEEE Transactions on Transportation Electrification***, vol. 6, no. 2, pp. 497–509, June **2020**.

3. **G. Rituraj**, B. K. Kushwaha, and P. Kumar,"Contactless power transfer system for sealed lead acid battery charging," in ***Wireless Power Transfer (Cambridge University Press)***, vol. 5, no. 1, pp. 20–26, March **2018**.

4. **G. Rituraj** and P. Kumar, "Which ways improving coupling coefficient of coils to enhance the power transfer capability and transmission efficiency in wpt systems," **(Under preparation)**.

Conference Paper

1. **G. Rituraj**, B. K. Kushwaha, and P. Kumar, "3-d analytical modeling of magnetic field for air core rectangular coil in contactless power transfer system," in ***IECON 2016 - 42nd Annual Conference of the IEEE Industrial Electronics Society***, pages 4459–4464, Oct. **2016**.

Further Contributions

Apart from the aforementioned publications, the following publications are listed below in which the contributions are made as an author and co-author (in the field of WPT) but have not been included in this thesis.

Journal Papers

1. B. K. Kushwaha, **G. Rituraj**, and P. Kumar, "A subdomain analytical model of coil system with magnetic shields of finite dimensions and finite permeability for wpt systems," in ***IEEE Transactions on Magnetics***, vol. 56, no. 12, pp. 1–11, December 2020.

2. B. K. Kushwaha, **G. Rituraj**, P. Kumar, and P. Bauer, "Mathematical Model for the Analysis of Series-Parallel Compensated Wireless Power Transfer System for Different Misalignments," in ***IET Circuits, Devices & Systems***, vol. 13, no. 7, pp. 970–978, October **2019**.

3. B. K. Kushwaha, **G. Rituraj**, and P. Kumar, "3-d analytical model for computation of mutual inductance for different misalignment of a rectangular coil with shielding in wireless power transfer system," in ***IEEE Transactions on Transportation Electrification***, vol. 3, no. 2, pp. 332–342, June **2017**.

Conference Papers

1. B. K. Kushwaha, **G. Rituraj**, P. Kumar, and P. Bauer, "Mathematical model of series-parallel compensation for contactless power transfer system," in ***2016 IEEE International Power Electronics and Motion Control Conference (PEMC)***, pages 1020–1025, Sept. **2016**.

2. B. K. Kushwaha, **G. Rituraj**, and P. Kumar, "Mathematical model of series-series compensation for contactless power transfer system," in ***IECON 2015 - 41st Annual Conference of the IEEE Industrial Electronics Society***, pages 001321–001326, Nov. **2015**.

3. B. K. Kushwaha, **G. Rituraj**, and P. Kumar, "Modeling and analysis of inductively coupled power transfer system," in ***2015 IEEE International Transportation Electrification Conference (ITEC)***, pages 1–4, Aug. **2015**.

4. E. R. Joy, B. K. Kushwaha, **G. Rituraj**, and P. Kumar, "Analysis and comparison of four compensation topologies of contactless power transfer system," in ***2015 4th International Conference on Electric Power and Energy Conversion Systems (EPECS)***, pages 1–6, Nov. **2015**.

5. E. R. Joy, B. K. Kushwaha, **G. Rituraj**, and P. Kumar, "Impact of circuit parameters in contactless power transfer system," in ***2014 IEEE International Conference on Power Electronics, Drives and Energy Systems (PEDES)***, pages 1–6, Dec. **2014**.

6. **G. Rituraj**, B. K. Kushwaha, and P. Kumar, "Analysis and comparison of series-series and series-parallel topology of contactless power transfer systems," in ***TENCON 2014 - 2014 IEEE Region 10 Conference***, pages 1–6, Oct. **2014**.

भारतीय प्रौद्योगिकी संस्थान गुवाहाटी
Indian Institute of Technology Guwahati